ANALYSIS AND DESIGN OF POST-WALL WAVEGUIDES FOR APPLICATION IN SIW

Teis Coenen

De promotiecommissie is als volgt samengesteld:

voorzitter en secretaris	
prof. dr. ir. A.J. Mouthaan	Universiteit Twente
promotoren	
prof. J.L. Tauritz, MSc	Universiteit Twente
prof. dr. ir. F.E. van Vliet	Universiteit Twente
assistent-promotor	
dr. ir. D.J. Bekers, PDEng	TNO Defensie en Veiligheid
leden	
dr. M. Hammer	Universiteit Twente
prof. dr. A.G. Tijhuis	Technische Universiteit Eindhoven
prof. ir. A.J.M. van Tuijl	Universiteit Twente
prof. dr. H.P. Urbach	Technische Universiteit Delft
prof. dr. ir. D. De Zutter	Universiteit Gent

Keywords: microwaves / microwave components / electromagnetics / substrate-integrated waveguides / post-wall waveguides / computational electromagnetics / electromagnetic modeling.

ISBN 978-90-365-2974-7
DOI 10.3990/1.9789036529747

Cover page „*Posts and Waves*" designed by Teis Coenen

Printed by Ipskamp Drukkers BV, Enschede, The Netherlands

The work leading to this thesis has been performed in the Transceivers department of the business unit Observation Systems of TNO Defence, Safety and Security in The Hague, The Netherlands. The author is also affiliated with the Telecommunication Engineering group of the Faculty of Electrical Engineering, Mathematics and Computer Science of the University of Twente, Enschede, The Netherlands.

This work was supported by the Dutch Ministry of Economic Affairs within the scope of the WiComm project as part of the Freeband Communication program.

ANALYSIS AND DESIGN OF POST-WALL WAVEGUIDES FOR APPLICATION IN SIW

PROEFSCHRIFT

ter verkrijging van
de graad van doctor aan de Universiteit Twente,
op gezag van de rector magnificus,
prof. dr. H. Brinksma,
volgens besluit van het College voor Promoties
in het openbaar te verdedigen
op vrijdag 29 januari 2010 om 13:15 uur

door

Teis Johan Coenen

geboren op 18 september 1978

te Nijmegen

Dit proefschrift is goedgekeurd door

de promotoren:	prof. J.L. Tauritz, MSc prof. dr. ir. F.E. van Vliet
de assistent-promotor:	dr. ir. D.J. Bekers, PDEng

ISBN 978-90-365-2974-7

Preface

This thesis is the result of over four years of work performed at TNO Defence, Safety and Security in The Hague during the period from April 2005 until the autumn of 2009. However, the first step that eventually resulted in this PhD project was made quite some time before. I can't remember the exact date anymore, but it must have been during my internship period at Thales in 2003 that Joe Tauritz inquired whether I was interested in a PhD position. Joe's enthusiasm made me increasingly enthusiastic for such a position. It was Joe again who brought me into contact with Frank van Vliet and Frank van den Bogaart at what was at that time still named TNO-FEL. As a result I was offered a position at TNO in September 2004. Thanks to the effort of both Franks and to the help of Marcel van der Graaf, this PhD project was initiated and I was offered a PhD position in April 2009. During the project Dave Bekers gradually took the task of the daily supervision, resulting in a close cooperation between me and him.

Four and a half years of work is a substantial period: it is about 14 percent of my life so far. Now, looking back at the period, I can only conclude that it was an extremely valuable experience. The life of a PhD student involves numerous ups and downs during the course of the project: after working for weeks on the same problem without solving it you can get slightly desperate, while on the contrary the joy of finally solving the problem is great. Why do I mention this? Because, in my opinion, this is very specific to PhD students: a PhD student *can* spend these weeks working on the same problem trying to arrive at a solution. It is toward the end of the project that you realize that all investigations that did not lead to solutions, and you at first thought of as being pointless, might be the essential result of the project. Not only did these investigations contribute to the actual result of solving the problem that was formulated at the start of the project, they also were an invaluable contribution to my personal education and greatly increased my knowledge. To me this is the true result of my work and therefore I am extremely thankful to everybody that supported me before and during the project.

Then, at last, the final version of the thesis must arrive and after a long period the work must be concluded. Of course I have new ideas about how to improve the work and it would also be nice if some procedures would have been implemented in, but this is future work: the thesis has to be printed. Probably also this conclusion is part of the PhD process.

Teis Coenen
Den Haag, December 2009

Notation

Roman Symbols

a	post radius
$d_{\text{port}(i)}$	width of port i
d_x	post spacing orthogonal to the direction of propagation
d_z	post spacing along the direction of propagation
$\boldsymbol{E}$	time-harmonic electric field
$\mathscr{E}$	strength of the electric field
f	frequency
f_{co}	cut-off frequency of the TE_{10} mode
f_{stop}	lowest frequency of the first stop band due to the periodicity
h_s	substrate height
$\boldsymbol{H}$	time-harmonic magnetic field
$\mathscr{H}$	strength of the magnetic field
$\boldsymbol{i}_x$, $\boldsymbol{i}_y$, $\boldsymbol{i}_z$	vectors of unit length, pointing in the x, y and z directions (Cartesian coordinates)
$\boldsymbol{i}_r$, $\boldsymbol{i}_\varphi$, $\boldsymbol{i}_z$	vectors of unit length, pointing in the radial, angular and axial direction (cylindrical coordinates)
$\boldsymbol{J}$	time-harmonic electric current
$\boldsymbol{J}^{\text{surf}}$	electric surface current
$\mathscr{J}$	current density
j	imaginary unit
k	propagation constant or wave number
N_{exp}	number of (rooftop) expansion functions on a port
N_{int}	number of integration points per (rooftop) expansion functions
P_{rad}	radiated power
S	scattering parameter matrix
$\tan\delta$	loss tangent
T	current matrix *or* wave-transmission matrix
w_g	waveguide width
$w_{g,\text{eff}}$	effective waveguide width
w_s	strip width

Greek Symbols

α	attenuation constant, $\alpha = \operatorname{Im} k$
β	phase constant, $\beta = \operatorname{Re} k$
ε	complex permittivity

ε_r	relative permittivity
ζ	wave impedance
λ	wavelength
λ_d	wavelength in a dielectric medium
μ	complex permeability
ρ	volume charge
ϱ	charge density
σ	conductivity
ω	angular frequency, $\omega = 2\pi f$

Other

$\times$	product (scalar operator) *or* cross product (vector operator)
$\bullet$	dot product
$\langle \cdot, \cdot \rangle$	inner product
curl	curl of a vector field
det	matrix determinant
div	divergence of a vector field
$\mathcal{F}\{\cdot\}$	Fourier transform of $\cdot$
grad	gradient of a vector field
Im	imaginary part
Δ	Laplace operator
Re	real part
$\mathbb{Z}$	set of whole numbers

Abbreviations

ABC	absorbing boundary condition
APAR	active phased array radar
BI-RME	boundary integral-resonant mode expansion
BLUE	best linear unbiased estimator
CPW	co-planar waveguide
DUT	device under test
EBG	electromagnetic band gap
FDFD	finite-difference frequency-domain
FBW	fractional bandwidth, FBW = $(f_2 - f_1)/\sqrt{f_1 f_2}$
FEM	finite element method
FMCW	frequency-modulated continuous wave
GCPW	grounded co-planar waveguide
IF	intermediate frequency
IL	insertion loss
LHS	left-hand side
MoM	method of moments

NRD	non-radiative dielectric (guide)
PCB	printed circuit board
PMCHW	Poggio Miller Chang Harrington Wu
PTFE	polytetrafluoroethylene (Teflon)
PWWG	post-wall waveguide
RF	radio frequency
RL	return loss
RHS	right-hand side
SISW	substrate-integrated slab waveguide
SIW	substrate-integrated waveguide
SMA	subminiature version A
SMART-L	Signaal multi-beam acquisition radar for tracking, L band
SMP	subminiature push-on
SOLT	short-open-load-through
TE	transverse electric: the electric field is perpendicular to the direction of propagation (H-type)
TEM	transverse electromagnetic: *both* the electric and magnetic fields are perpendicular to the direction of propagation
TM	transverse magnetic: the magnetic field is perpendicular to the direction of propagation (E-type)
T/R	transmit/receive
TRL	through-reflect-line
TRT	transverse resonance technique
VNA	vector network analyzer
WLAN	wireless local area network
WPAN	wireless personal area network

Contents

CHAPTER 1

Introduction

In the last decades, the use of electronic components operating at microwave frequencies has grown tremendously. Commonly known applications are related to satellite-based TV transmission, navigation based on GPS, mobile telephony, radar, and wireless local area networks. Also in the areas of defense and security, microwave technology has acquired a prominent position. The enabling technologies at the basis of this growth appear to be a wide variety of microwave components: antennas, feed networks, MMICs, amplifiers, mixers, filters, etc. Moreover, the level of integration of these technologies has evolved significantly. As component size continues to diminish, the need for innovation in the area of transmission-line structure conceptualization, design, and realization is apparent, in particular because intrinsic physical limitations such as proximity effects and loss become more and more manifest. Beside these constraints, cost and integration aspects led in recent years to the introduction of new concepts, materials, and production techniques. In Section 1.1 we describe the impact of these aspects and constraints on the antennas and front-ends of wireless systems. Subsequently, we consider these aspects in relation to the classical feed structures of wireless systems, i.e., planar transmission lines and waveguides, in Section 1.2. The discussion in these two sections reveals that new solutions for the transmission-line structure itself are needed. A promising alternative for the classical structures is the post-wall waveguide. We give a brief overview of its short history in Section 1.3. Based on this historical review and the corresponding literature reviews, we formulate in Section 1.4 the aims of this thesis related to the characteristics, analysis, design, and manufacturing of post-wall waveguides. Finally we summarize the contents of the thesis in Section 1.6.

1.1 Wireless Systems: Antennas and Front-Ends

Many wireless systems consist of a receiver and a transmitter chain. Figure 1.1 depicts this chain in a block diagram. The transmitter / receiver block in the figure typically consists of one or more integrated circuits that are realized on a small piece of semiconductor wafer. Classically the integrated circuit, or chip, is mounted on a printed circuit board (PCB) with its circuit side facing away from the PCB. Thin gold wires (bond wires) are used to connect the chip to the board, as shown in Figure 1.2(a). The series inductance of the bond wires, together with the shunt capacitance of the bond pads, exhibits in general a low-pass behavior. Consequently,

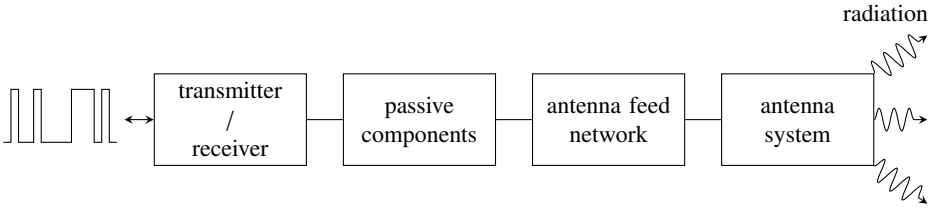

Figure 1.1 — Block schematic of a general wireless system chain.

(a) bond wire interconnection (b) flip-chip interconnection

Figure 1.2 — Schematic side view of two types of wafer to printed circuit board interconnection methods.

the connection to the board will be band-limited, which can be alleviated by applying shorter or thicker bonds. Nevertheless the losses of the bond wire transition become in general unacceptably high at millimeter wave frequencies. Alternatively, the flip-chip mounting method depicted in Figure 1.2(b) employs small metal bumps on the PCB to which the wafer's pads are attached directly. In this way a short connection with low self-inductance can be achieved and measurements show that this technique can be used up to at least 100 GHz [1].

On the PCB, a transmission line network may connect the chip to additional microwave components, e.g., a (low-loss) filter or a circulator. In turn these components are connected through an antenna feed network to the antenna itself, which often consists of multiple antennas constituting an antenna array. The feed network, which should be of low-loss and of a prescribed phase and amplitude response, connects the PCB to one or several antenna elements, which convert the microwave signal into a space wave.

The large-scale application of PCBs in microwave front-ends has been triggered by cost cutting incentives and aspects of weight, integration, and ease of manufacturing. Although relatively cheap, PCBs offer a high level of integration of all parts of the microwave front-end. Therefore, PCBs have become the substrate of choice for building microwave front-ends. However, higher component packaging densities and an upward shift in operating frequency in search for more bandwidth have led to new complications. Firstly, substrate and parallel-plate modes can be excited in planar (PCB-based) structures, often causing strong parasitic coupling between components and a reduction of efficiency due to the leakage of power. In the literature, a number of possible solutions have been proposed to eliminate these modes, for example by introducing electromagnetic bandgap (EBG) materials [2], [3], [4], [5]. Secondly, classical planar transmission-line configurations suffer from increased losses at higher frequencies. In the next section we discuss some classical transmission lines and discuss their losses.

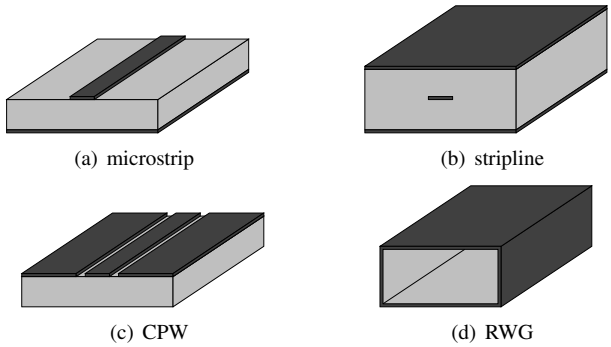

Figure 1.3 — Transverse view of four types of transmission lines that are commonly used in antenna feed networks: microstrip line, stripline, co-planar waveguide and rectangular waveguide.

1.2 Classical Antenna Feed Structures

We distinguish two types of transmission lines that are commonly used in antenna feed networks: waveguides and planar transmission lines. At the end of the nineteenth century Lord Rayleigh found that electromagnetic waves could propagate through a hollow conducting tube. The solutions to Maxwell's equations that represented these waves formed a set of well-defined normal modes. In the forty years following, the work received no particular attention. It was not until the mid 1930's that G.C. Southworth and W.L. Barrow independently rediscovered the concept and applied the theory to construct waveguide prototypes [6]. The first strip transmission lines were used in antenna systems that were developed during World War II. In 1949 R.M. Barrett realized that not only transmission lines, but also a variety of components could be constructed with these strips, and that the same technique that was already used to manufacture low-frequency printed circuits could be used to manufacture microwave printed circuits [7].

Planar transmission lines include the microstrip line, the stripline and the co-planar waveguide (CPW), as depicted in Figure 1.3(a)–1.3(c). In these transmission lines conducting strips support electric currents and the strips are isolated by dielectric material. The orientation of the strips is parallel and, hence, these transmission lines are well-adapted to PCB technology. The dominant propagation mode in these planar transmission lines is the transverse electromagnetic (TEM) mode. To ensure that interfering (TE and TM) modes are sufficiently suppressed, the transverse dimensions (e.g. strip width and substrate height) need to be small with respect to the wavelength. Consequently high losses may occur, in particular in the narrow signal strip.

A planar feed network is used for example in the long-range surveillance radar SMART-L developed and produced by Thales Nederland [8,9]. The system operates between 1 and 2 GHz and the feed network consists of 24 distributed stripline networks that allow for scanning in azimuth and that together feed a total of around 1000 elements. A second example is a traffic radar system developed by TNO Defence, Safety and Security. This system is a FMCW sensor that detects traffic movement on roads, e.g., to provide data to smart traffic lights. The antenna, as shown in the photograph in Figure 1.4, is a circularly polarized array with 16 microstrip patch

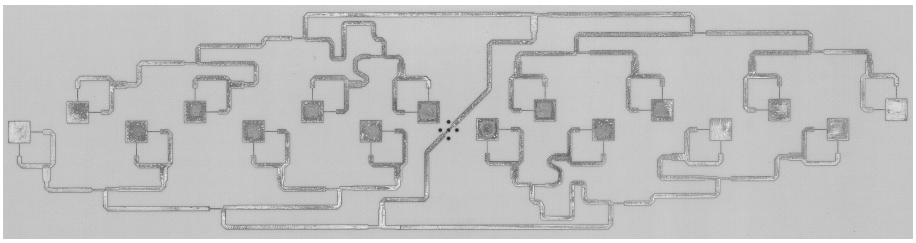

Figure 1.4 — Top view of the traffic radar antenna panel with a microstrip line feeding network.

elements and a distributed microstrip line feed network operating around 14 GHz. Thirdly, we mention the aperture-coupled microstrip-line fed patch array proposed in [10] for gigabit-WLAN applications as an example of a planar antenna feed network operating at 60 GHz. The antenna consists of 16 elements fed by a microstrip line distribution network.

Waveguides such as the rectangular waveguide in Figure 1.3(d) cannot support TEM modes; they only support TE and TM modes. To ensure that these modes are sufficiently transmitted, the transverse dimensions of the waveguide need to be of the order of the wavelength and are, therefore, larger than in the case of planar transmission lines. Consequently, the electric current is distributed over a larger volume and the conductor loss in waveguides is much lower than in planar transmission lines. The bandwidth of the dominant mode (commonly the TE_{10} mode) is at most about 40 percent, which limits the overall bandwidth of the feed network. Large feed networks based on waveguides are often bulky and production costs are in general high. Moreover, their non-planar nature complicates easy integration with PCB technology. These aspects make waveguide antenna feed networks mainly suited for specialized high-performance systems. An example of an application with a waveguide feed network is the APAR radar system developed and produced by Thales Nederland [11, 12]. This multi-function naval radar operates around 10 GHz. The antenna feed network consists of about 3200 separate open-ended waveguides that are each fed directly by a T/R-module. In the system no power combination is performed in the antenna feed network. For other examples of waveguide feed networks see [13, 14].

In Figure 1.5 the losses (in dB per wavelength) of a planar transmission line are compared to the losses of a hollow waveguide and a waveguide filled with a dielectric material. For the set of hollow waveguides, the dimensions are those the standard rectangular waveguides WR-770, WR-284, WR-90, WR-28, WR-15 and WR-10 covering, at least in part, the L-, S-, X-, Ka-, V- and W-band, respectively (see also Appendix A). In the case of waveguides with dielectric filling, we choose the dimensions such that the cut-off frequencies of the TE_{10} modes coincide with the equivalent air-filled waveguides; this choice results in equal operational bands for both cases. For the planar transmission line, we choose a microstrip line with a strip width $w_s = \lambda_d/10$ at the highest usable frequency of each waveguide, where $\lambda_d = c_0/f\sqrt{\epsilon_r}$ is the wavelength in the substrate. The thickness of the substrate is chosen such that the characteristic impedance is 50 Ohms. For all configurations we ensure that $h_s < \lambda_d/10$. The simulations have been performed with Ansoft HFSS [15]. The results in the figure show that the loss per wavelength in the hollow waveguide is much lower than the loss per wavelength in the filled waveguide and

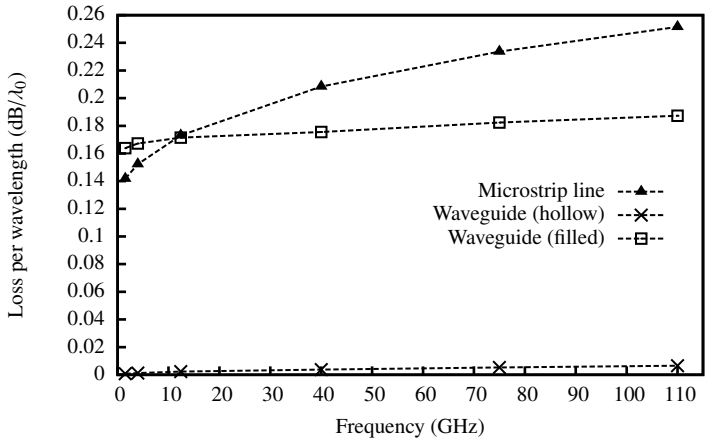

Figure 1.5 — Comparison of transmission line losses per free-space wavelength as a function of the frequency. Dielectric material with $\epsilon_r = 3.55$, $\tan\delta_1 = 0.0027$ and all metal with $\sigma = 58 \cdot 10^6$ S/m.

the microstrip line. We also observe that the loss per wavelength increases with frequency, the fastest in the case of the microstrip line, and that the loss of the microstrip line exceeds the loss of the filled waveguide for frequencies around X-band and above. It goes without saying that the loss per meter increases much more rapidly. Since not all dimensions in an antenna feed network are wavelength-related, the dimensions of the complete feed network are less than linearly proportional to the wavelength, and thus the total loss of antenna feed networks will increase more rapidly with the operating frequency. This demonstrates clearly the need for PCB technology integrable transmission lines with lower loss than planar transmission lines. Furthermore, we observe that, at least for this particular example, filled waveguides exhibit lower loss than microstrip lines above a certain frequency and therefore transmission lines based on filled waveguides could pose a solution to the problem of loss at higher frequencies.

1.3 A Promising Alternative: Post-Wall Waveguides

An alternative to the classical transmission lines of the previous section is the post-wall waveguide as depicted in Figure 1.6. The post-wall waveguide (PWWG) is a substrate-integrated waveguide (SIW): a waveguide transmission line that can be embedded in a PCB. Rows of cylindrical posts constitute the side walls and together with an optional top and bottom plate they enclose a rectangular cross section similar to the waveguide in Figure 1.3(d). The posts can be either conducting (metallic posts) or insulating (dielectric posts with a permittivity different from the background medium).

PWWGs for application at microwave frequencies were first mentioned in 1994 in a Japanese patent [16]. The first application of these PWWGs is described in a paper by Hirokawa and Ando from the Tokyo Institute of Technology [17] where they employ the waveguides to feed a

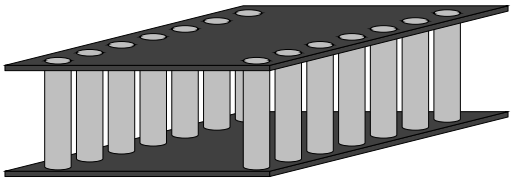

Figure 1.6 — Concept of the post-wall waveguide.

slotted waveguide array at 40 GHz. A first investigation of PWWG components at microwave frequencies is presented in [18]. In 2001 Deslandes and Wu from the École Polytechnique de Montréal present work on PWWGs with metal posts [19, 20]. From then on the number of publications slowly increases as more groups target PWWGs.

Parallel to this development, PWWGs with dielectric posts evolved from the field of photonic bandgap (PBG) materials introduced in the late eighties by Yablonovitch to the optical community [21]. The PBGs are combined in such a way that a central guiding region between rows of dielectric posts emerges [22–25]. At first the literature was solely focused on optical applications. To the best of our knowledge the first use of PWWGs with dielectric posts (sometimes referred to as substrate-integrated slab waveguide, SISW) at microwave frequencies was reported in 2003 [26–28].

Assessing the literature on PWWGs, we perceive four major foci: electromagnetic analysis, PWWG excitation, PWWG components, and PWWG antenna systems. Most often, a mix of two or more of these foci is treated and, over time, a shift from the first two foci to the last two can be distinguished as the technology matures. A variety of approaches have been proposed for the electromagnetic modeling of PWWGs. Most of the approaches aim at a fast semi-analytical tool, because general-purpose simulators are as a rule too slow for design optimization. Moreover, the accurate estimation of the losses in PWWGs is an important issue. Due to their low value, they are rather difficult to estimate. An overview of the most important analysis approaches in the literature is presented in Section 2.1. Suitable excitation of PWWGs is crucial to their adoption, since this defines the connection with other (existing) circuitry. We systematically discuss a variety of excitation structures in the literature in Section 5.1. The design of post-wall waveguides as described in the literature is often based on the similarity between rectangular waveguide components and PWWG components. The types of components with PWWGs as a basis is large and includes splitters, bends, couplers, circulators, and filters. Design is most often performed with the aid of general-purpose simulators and, therefore, optimization is a laborious task. Section 6.1 provides an overview of the key PWWG components. The last focus, PWWG antenna systems, concerns the literature in which complete antenna (array) systems with PWWG feed structures are considered. Examples may be found in [17] and [29].

1.4 Aims of the Thesis

We formulate the following three aims of this thesis:

1. to systematically inventory the key PWWG characteristics,

2. to develop a model to link subsystem specifications directly to PWWG characteristics and design, and

3. to work out issues related to implementation and manufacturing.

The first aim stems from the observation that –at the time of the initialization of this PhD project– the literature on PWWGs was fragmented and, therefore, PWWG characteristics needed to be inventoried. Several approximations for PWWG characteristics such as propagation constant, losses, and (effective) waveguide width existed in the literature, and these approximations needed to be judged on their merits [30, 31].

The second aim refers in particular to the focus of the literature at that time. Most of the work was aimed at specific design cases, while we desired a modular component-based CAD tool that could eventually be integrated in extant circuit simulators, such as Agilent's ADS or Ansoft's Designer. Such a tool requires a model and analysis approach suited for fast execution.

The third aim refers to the limited knowledge on performance determining aspects of PWWGs and the effects of the manufacturing process on these aspects. Therefore, the corresponding limits and limitations needed to be worked out in a clear way.

1.5 Applications and Methodology

Beside these aims, two additional aspects played a key role in the definition and realization of the project. First, the following primary applications of PWWGs were identified:

- antenna feed networks,
- electromagnetic guiding structures, or transmission lines,
- coupling structures,
- resonating structures,
- (compact) filters,
- interlayer transmission line transitions, and
- the miniaturization of microwave components.

Several of these are addressed in this thesis and the publications stemming from this work [30–35], both from the point-of-view of analysis and simulation as well as that of design, manufacturing, and measurement.

Secondly, as mentioned in the previous section, the analysis and application of PWWGs with dielectric posts only entered the microwave field in 2003. These PWWGs were considered promising, because the metalization step may lead to additional manufacturing difficulties, in particular for complicated PCB stacks. To obtain sufficient isolation of the walls of PWWGs with dielectric posts, one could employ post diameters that are not small with respect to the wavelength. The presence of such (resonant) structures is one of our reasons for employing a reduced full-wave model, see Chapter 2. By 'reduced' we mean that specific assumptions regarding the geometry are made through which 1D, 2D, or 2.5D models emerge. Alternatively

one could employ circuit models by first identifying a reasonable layout for the lumped-element circuit and subsequently fitting its parameters either with analytical methods [36,37], numerical simulation tools [38], or measurements. While such models may be computationally faster than (reduced) full-wave models, their flexibility in terms of geometrical variations are more limited, since suitable models have to be determined for many variations of the PWWG geometry. Furthermore, for circular metallic and dielectric posts, the literature reveals that reduced full-wave models can provide, to a great extent, an analytic description of the electromagnetic-field behavior [39–41], which may lead to fast simulations. Finally, reduced full-wave models seem to provide a more solid basis for determining accurately the relatively low PWWG losses.

We note that reduced full-wave models have in recent years led to succesful tools for the design of antennas and microwave structures at TNO Defence, Security and Safety, see [5,42–46]. The stratified-medium model described in the first two references and the Multi-mode Equivalent Network approach described in the third and fourth assume periodicity or uniformity in two orthogonal directions and assume a layered medium in the third (orthogonal) direction. As we will show, straight PWWGs can under certain assumptions be modeled as periodic in the direction of propagation and uniform along the axes of the posts, but they are truncated structures perpendicular to these two directions. The Boundary Integral-Resonant Mode Expansion (BI-RME) method [47, Ch. 5] developed in the eighties and nineties could be an alternative. The advantage of this full-wave method in comparison to other full-wave and circuit models is that it permits the direct determination of the layout and the parameters of the equivalent circuit model without a fitting procedure [48]. The method has been applied to PWWGs structures, but the main disadvantage is the need for enclosing the structure by a waveguide with certain dimensions. This method is inaccurate for higher PWWG losses. Alternatives are described in Section 2.1. In particular the recently developed LEGO approach described in [49, 50] and employed to characterize an EBG power splitter implemented using dielectric posts deserves mention. While this approach employs an embedding step to transfer the equivalent sources describing the domain to its *entire* boundary, we will only consider the field behavior at designated ports, see Chapter 3, to facilitate the integration of transmission-line components in a circuit simulator, as mentioned in our aims. The principles that we employ to characterize such components are the same as those underlying LEGO, namely Lorentz's reciprocity theorem, Love's equivalence principle, and Oseen's extinction theorem.

1.6 Outline of the Thesis

In Chapter 2 we establish our analysis approach and the formulation of an electromagnetic model for PWWGs. In this chapter we give an overview of analysis approaches in the literature on PWWG structures (Section 2.1), present a short review of electromagnetic theory (Section 2.2), and apply this theory to model wave propagation in PWWGs (Section 2.3). We focus on wave behavior that is similar to the TE_{m0} modal behavior of rectangular waveguides and we solve the field equations by means of a modal representation (Section 2.4) and an integral equation formulation that follows from Lorentz's reciprocity theorem (Section 2.5). We characterize the propagation in uniform infinitely long periodic PWWGs (Section 2.6) and treat the (spatial) evaluation of the electric field in a PWWG (Section 2.7).

The next chapter focuses on specific wave-propagation characteristics of PWWGs. It dis-

cusses the propagation constant of transmission lines (Section 3.1), the equivalence of rectangular waveguides and PWWGs (Section 3.2), and the different loss mechanisms of PWWGs (Section 3.3). To determine the losses and scattering parameters of PWWGs, we introduce excitation at specified ports and construct a current matrix. This concept has proved to be a powerful tool for characterizing the behavior of PWWG components and through derivation of the scattering parameters this paves the way to calculating the losses of uniform PWWGs.

In Chapter 4 in order to determine the characteristics of PWWGs, i.e., losses, effective width, phase dispersion, and scattering parameters, we measure a set of PWWG transmission lines with uniform post spacing. We consider the design (Section 4.1) of PWWG transmission lines, the multi-line calibration measurement procedure to extract the propagation constant from scattering-parameter measurements (Section 4.2) and we present the results from measurements (Section 4.4). We compare these results with results obtained from simulations (Section 4.5).

The excitation of PWWGs through transmission line transitions is discussed in Chapter 5. The transitions presumably limit the overall bandwidth so that specific attention must be paid to the design. The chapter starts with an overview of the transitions described in the literature (Section 5.1) and subsequently we treat the design of a grounded co-planar waveguide (GCPW) (Section 5.3) and a microstrip line (Section 5.2) to PWWG transition, and finally a transition from a PWWG with metallic posts to a PWWG with dielectric posts (Section 5.4).

The design and measurement of PWWG components is treated in Chapter 6. The theory developed in Chapter 2 and 3 is used to evaluate the scattering parameters of PWWG components. The chapter starts with a concise overview of the PWWG components that have been described in the literature (Section 6.1). Next, the design of a set of components –including phase-shifting lines, bends, a Tee-junction, couplers and a Butler-matrix– is discussed (Section 6.2) followed by a comparison with the measurement results (Section 6.3). The chapter concludes with an outlook for future requirements, that enhance the flexibility and enable the integration of our numerical method with a circuit simulator (Section 6.5).

Chapter 7 concludes with a review of the results presented in this thesis. In Section 7.2 we discuss which applications present the largest potential for PWWG structures followed by a number of recommendations for the extension of this work are to be found in Section 7.3.

CHAPTER 2

Modeling and Analysis of Post-Wall Waveguides

Figure 2.1 shows the top view of a PWWG with three arrays of posts per side-wall. In a classical rectangular waveguide the dominant TE_{10} mode can be thought of as a plane wave reflecting at the side-walls. Similarly, the two side-walls of a PWWG act as reflecting surfaces, and a perturbed TE_{10} mode is able to propagate along the guide, i.e., in the z-direction. In Section 2.1 we provide an overview of analysis approaches reported in the literature for PWWG structures. In Section 2.2 we present a brief review of electromagnetic theory. In Section 2.3 we apply this theory to model wave propagation in PWWGs. We focus on wave behavior that is similar

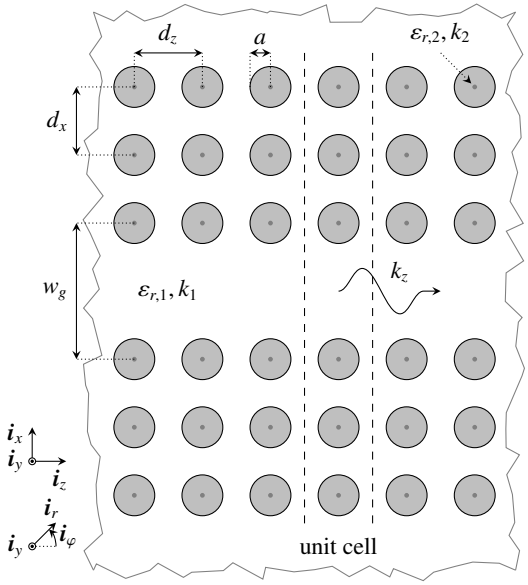

Figure 2.1 — Top view of a section of PWWG with three parallel rows of posts per sidewall. We note that the post positioning inside the unit cell does not need to be regular and can be arbitrary, under the conditions that the periodicity is in the z-direction and posts never overlap.

to the TE_{m0} modal behavior of rectangular waveguide. The resulting field equations are solved in Section 2.4 by means of a modal representation and in Section 2.5 by means of an integral-equation formulation that follows from Lorentz's reciprocity theorem. The integral-equation formulation is only solved for metallic posts and this solution is equivalent to the corresponding modal solution. To characterize the propagation in uniform PWWGs, the modeling of infinitely long periodic PWWGs is described in Section 2.6. This modeling involves the summation of an infinite series for which we introduce an acceleration procedure. Section 2.7 treats the (spatial) evaluation of the electric field in a PWWG for both the integral and modal formulations.

2.1 Analysis Approaches in the Literature

In this section, we provide an overview of the approaches cited in the literature for PWWG analysis distinguishing between the different methodologies. Most of the literature focuses on PWWGs with conducting posts. There is little in the way of literature that addresses waveguides with dielectric posts and in almost all cases the analysis of metal and dielectric posts is treated separately.

- In [17, 51] metallic posts are represented by several uniform, y-directed, electric currents on the post surface. Through the expansion of the Green's function and the application of Poisson's summation, the authors arrive at a method-of-moments formulation to determine the propagation constant of a PWWG with metallic posts.
- The method in [52] is a finite-difference frequency-domain method (FDFD) algorithm, where the electric and magnetic fields are imposed periodically in the z-direction. In the x- and y-directions absorbing boundary conditions are chosen to prevent interference from reflection of the leakage. The complex propagation constants of the waveguide modes are the eigenvalues of a matrix, that is derived from the FDFD matrices.
- In [37] the TE modes in a rectangular waveguide are regarded as two interfering plane waves, reflecting at the waveguide walls. The post-walls are modeled as a surface impedance by a LC-model consisting of capacitively coupled inductive posts. This model is mapped onto an equivalent rectangular waveguide and an iterative procedure finds the appropriate angle of propagation of the plane waves. This method is not used to determine the losses in PWWGs.
- The boundary integral-resonant mode expansion (BI-RME) method is used in [53] to determine the admittance matrix of a PWWG unit cell. The BI-RME method is based on the analysis of a PWWG section inside a rectangular waveguide section. Since the rectangular waveguide is a bounded structure, the leakage loss from the PWWG needs to be sufficiently low in order not to distort the accuracy by reflections at the rectangular waveguide walls. Under the assumption of periodic boundary conditions for modes propagating in an infinite concatenation of unit cells, the propagation constants are extracted as the eigenvalues of a system matrix. From this method, the authors derive an approximate expression that determines the dimensions of an equivalent rectangular waveguide.
- To analyze a PWWG with perfectly conducting posts, the authors of [54] use a Fourier expansion of the currents at the cylinder surface. By requiring that the scattered field at the

cylindrical surface vanishes and by applying the Bloch-Floquet theorem, the elements of the moment matrix $Z(k_p)$ are found. From the requirement $\det[Z(k_p)] = 0$, the propagation constants k_p are determined.

- In [55] the transverse resonance technique (TRT) is used to calculate the propagation constant from the reflection coefficient of a plane wave incident to the side wall. This method requires knowledge of the surface impedance of the side walls, which the authors calculate by discretizing the posts in a number of current filaments at the post surface and subsequently solving the resulting matrix system with the method-of-moments (MoM).

- In [56], PWWGs with metallic posts are also analyzed with the transverse resonance technique, where the impedance of the walls is calculated via an integral formulation of the discretized posts. Dielectric PWWGs are studied by regarding waveguides with side walls that consists of uniform and parallel dielectric slabs of different permittivity; the transverse resonance technique is used to determine the propagation constant. For specific choices of the slab dimensions, the geometry behaves similarly to a PWWG with dielectric posts.

- The method discussed in [57], discretizes the spatial permittivity and conductivity of a PWWG with rectangular posts. The resulting differential equation, are the telegraphist's equations and are solved for the propagation constant.

- Post-wall waveguides with dielectric posts are analyzed in [22] using a plane-wave expansion method, combined with the Bloch-Floquet theorem.

- In [58] a volumetric average of the permittivity is calculated to model a PWWG with dielectric posts as an equivalent uniform structure. In [59] a similar approach is used, where an effective average permittivity is used to find the dimensions of an equivalent non-radiative dielectric guide (NRD guide).

As discussed in Section 1.4, we will model the electromagnetic behavior of collections of metallic or dielectric posts in ways similar to those described in [39–41].

2.2 General EM Theory

To facilitate the modeling of the electromagnetic behavior of PWWGs we present a brief review of general electromagnetic theory. Throughout this work we assume that all media are passive, linear, time-invariant, instantaneously reacting, locally reacting, homogeneous and isotropic [60, Ch. 19]. The electromagnetic field in such media with permittivity ε and permeability μ is governed by Maxwell's equations

$$\operatorname{curl} \mathscr{E} = -\mu \frac{\partial \mathscr{H}}{\partial t}, \qquad \operatorname{curl} \mathscr{H} = \varepsilon \frac{\partial \mathscr{E}}{\partial t} + \mathscr{J}, \tag{2.1}$$

and by the conservation of charge

$$\frac{\partial \varrho}{\partial t} + \operatorname{div} \mathscr{J} = 0. \tag{2.2}$$

Here $\mathscr{E}$ and $\mathscr{H}$ are the electric and magnetic field strengths, $\mathscr{J}$ and ϱ are the current and charge densities, and t is the time. We assume time harmonic behavior of the current,

$$\mathscr{J}(\boldsymbol{x}, t) = \mathrm{Re}\left[\boldsymbol{J}(\boldsymbol{x})e^{j\omega t}\right]. \tag{2.3}$$

Consequently, the electric and magnetic fields assume the same time behavior and Maxwell's equations reduce to

$$\mathrm{curl}\,\boldsymbol{E} = -j\omega\mu\boldsymbol{H}, \tag{2.4a}$$

$$\mathrm{curl}\,\boldsymbol{H} = j\omega\varepsilon\boldsymbol{E} + \boldsymbol{J}, \tag{2.4b}$$

$$j\omega\rho + \mathrm{div}\,\boldsymbol{J} = 0. \tag{2.4c}$$

Applying the divergence to (2.4a) and (2.4b), we find $\mathrm{div}\,\boldsymbol{H} = 0$ and $\mathrm{div}\,\boldsymbol{E} = \rho/\varepsilon$. Applying the curl to the same equations, we find

$$\mathrm{curl\,curl}\,\boldsymbol{E} = k^2\boldsymbol{E} - j\omega\mu\boldsymbol{J}, \tag{2.5a}$$

$$\mathrm{curl\,curl}\,\boldsymbol{H} = k^2\boldsymbol{H} + \mathrm{curl}\,\boldsymbol{J}, \tag{2.5b}$$

where $k^2 = \omega^2\varepsilon\mu$. Introducing the identity $\Delta = \mathrm{grad\,div} - \mathrm{curl\,curl}$, we obtain

$$\Delta\boldsymbol{E} + k^2\boldsymbol{E} = j\omega\mu\boldsymbol{J} + \mathrm{grad\,div}\,\boldsymbol{E}, \tag{2.6a}$$

$$\Delta\boldsymbol{H} + k^2\boldsymbol{H} = -\mathrm{curl}\,\boldsymbol{J}. \tag{2.6b}$$

In the absence of free charges $\rho = 0$ and (2.6a) simplifies to

$$\Delta\boldsymbol{E} + k^2\boldsymbol{E} = j\omega\mu\boldsymbol{J}. \tag{2.7}$$

In absence of volume current, the equations of (2.6) become the homogeneous equations

$$\Delta\boldsymbol{E} + k^2\boldsymbol{E} = \boldsymbol{0}, \qquad \Delta\boldsymbol{H} + k^2\boldsymbol{H} = \boldsymbol{0}. \tag{2.8}$$

In order to solve Maxwell's equations (2.4) they should be supplemented by boundary or transition conditions and, eventually, by a constitutive relation for the current. We consider two different situations. In case there are no perfect conductors, the tangential electric and magnetic fields and the normal components of electric ($\varepsilon\boldsymbol{E}$) and magnetic ($\mu\boldsymbol{H}$) flux densities are continuous across all transitions and the current satisfies Ohm's law $\boldsymbol{J} = \sigma\boldsymbol{E}$, where σ is the conductivity.
In case all conductors are perfect, the volume current $\boldsymbol{J}$ and the volume charge ρ vanish. Moreover, the jumps in $\boldsymbol{n} \times \boldsymbol{H}$ and $\boldsymbol{n} \cdot \varepsilon\boldsymbol{E}$ (with $\boldsymbol{n}$ the normal) across a perfectly conducting transition equal the surface current and the surface charge, respectively.

2.3 Model Setup for Post-Wall Waveguides

In classical rectangular waveguides the height is much smaller than the width and the electromagnetic field is described by the first few TE_{m0} modes. The TM_{m0} modes do not propagate and the other TE and TM modes are significantly attenuated. To investigate wave propagation in PWWGs, we focus therefore on modal behavior similar to that of the TE_{m0} modes in a classical rectangular waveguide. For such modal behavior

1. $E_z = 0$,
2. the fields do not depend on the y-coordinate, and
3. E_x vanishes at the top and bottom plates, provided that they are perfectly conducting.

The consequence of the second and third condition is that $E_x = 0$ and, hence,

$$\boldsymbol{E} = E_y(x, z)\boldsymbol{i}_y. \tag{2.9}$$

Consequently,

$$\operatorname{div} \boldsymbol{E} = 0, \qquad \Delta E_y + k^2 E_y = j\omega\mu J_y, \qquad J_x = J_z = 0. \tag{2.10}$$

We describe the surfaces of the posts by the parameter representation

$$\boldsymbol{x}(\varphi, y) = \boldsymbol{c}_p + a_p \cos\varphi\, \boldsymbol{i}_z + a_p \sin\varphi\, \boldsymbol{i}_x + y\boldsymbol{i}_y, \quad -\infty < y < \infty, -\pi < \varphi < \pi, \tag{2.11}$$

where $\boldsymbol{c}_p$ is the center of the post p in the xz-plane. This parameter representation can straightforwardly be extended to a global (cylindrical) coordinate description

$$\boldsymbol{x}(r, \varphi, y) = \boldsymbol{c}_p + r\cos\varphi\, \boldsymbol{i}_z + r\sin\varphi\, \boldsymbol{i}_x + y\boldsymbol{i}_y, \tag{2.12}$$

with corresponding unit vectors

$$\boldsymbol{i}_r(\varphi) = \cos\varphi\, \boldsymbol{i}_z + \sin\varphi\, \boldsymbol{i}_x, \qquad \boldsymbol{i}_\varphi(\varphi) = -\sin\varphi\, \boldsymbol{i}_z + \cos\varphi\, \boldsymbol{i}_x, \tag{2.13}$$

and $\boldsymbol{i}_y$. In this system all fields depend only on r and φ. Expressing the curl in cylindrical coordinates and using $\boldsymbol{E} = E_y(r, \varphi)$ we obtain from (2.4a)

$$-j\omega\mu H_r = \frac{1}{r}\frac{\partial E_y}{\partial \varphi}, \tag{2.14a}$$

$$j\omega\mu H_\varphi = \frac{\partial E_y}{\partial r}, \tag{2.14b}$$

$$H_y = 0. \tag{2.14c}$$

Expressing also the Laplace operator Δ in cylindrical coordinates, reduces the Helmholtz equations for the y-component of the electric field as

$$\frac{1}{r}\frac{\partial}{\partial r}\left(r\frac{\partial E_y}{\partial r}\right) + \frac{1}{r^2}\frac{\partial^2 E_y}{\partial \varphi^2} + k^2 E_y = j\omega\mu J_y. \tag{2.15}$$

Note that $k = k_1$ outside the posts and $k = k_2$ inside the posts, as Figure 2.1 shows.

The posts are excited by an electromagnetic excitation field $\{\boldsymbol{E}^{\text{exc}}, \boldsymbol{H}^{\text{exc}}\}$ in medium 1. This field satisfies Maxwell's equations, with possibly an associated current, and induces a field $\{\boldsymbol{E}^{\text{int}}, \boldsymbol{H}^{\text{int}}\}$ in medium 2 (the posts) and a scattered field $\{\boldsymbol{E}^{\text{sct}}, \boldsymbol{H}^{\text{sct}}\}$ in medium 1 (outside the posts as) visualized in Figure 2.2. Furthermore, the fields satisfy Maxwell's equations in the respective media 1 and 2, possibly with associated currents. The total electromagnetic field

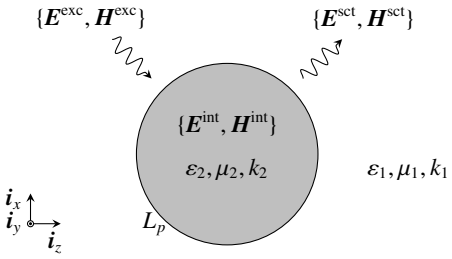

Figure 2.2 — Electromagnetic field representation in the presence of a cylindrical post.

satisfies the boundary conditions described in Section 2.2 at the post surfaces. Hence, the tangential components of the electric and magnetic field satisfy

$$E_y^{\text{exc}} + E_y^{\text{sct}} = E_y^{\text{int}}, \tag{2.16a}$$

$$H_\varphi^{\text{exc}} + H_\varphi^{\text{sct}} = H_\varphi^{\text{int}}, \tag{2.16b}$$

at each L_p, where L_p is the surface of post p in the xz-plane described by (2.13) with $y = 0$. In case the posts are perfectly conducting, $E_y^{\text{int}} = 0$ and H_φ^{int} should be replaced by the surface current J_y^{surf}.

2.4 Modal Representation

To determine the electromagnetic field in a PWWG we consider here the case that the dielectric media are lossless and the metal is perfectly conducting. Then, the volume current J_y is zero everywhere (except for the boundary). Thus we need to solve (2.15) with $J_y = 0$, i.e. the homogeneous 2D Helmholtz equation in polar coordinates,

$$\frac{1}{r}\frac{\partial}{\partial r}\left(r\frac{\partial E_y}{\partial r}\right) + \frac{1}{r^2}\frac{\partial^2 E_y}{\partial \varphi^2} + k^2 E_y = 0. \tag{2.17}$$

Applying separation of variables, $E_y(r, \varphi) = R(r)\Phi(\varphi)$, we obtain

$$\frac{r^2}{R(r)}\left[\frac{d^2R}{dr^2} + \frac{1}{r}\frac{dR}{dr}\right] + k^2 r^2 = -\frac{1}{\Phi(\varphi)}\frac{d^2\Phi}{d\varphi^2} = \nu^2, \tag{2.18}$$

with ν a constant with nonnegative real part. Then,

$$\frac{d^2\Phi}{d\varphi^2} + \nu^2\Phi(\varphi) = 0, \tag{2.19a}$$

$$\frac{d^2R}{dr^2} + \frac{1}{r}\frac{dR}{dr} + \left(k^2 - \frac{\nu^2}{r^2}\right)R(r) = 0. \tag{2.19b}$$

The solutions of (2.19a) are linear combinations of $e^{\pm j\nu\varphi}$ or $\cos\nu\varphi$ and $\sin\nu\varphi$. Since all field quantities are periodic in φ with period 2π, E_y and $\partial E_y/\partial\varphi$ are periodic in φ with period 2π. The

periodicity of $\partial E_y/\partial\varphi$ follows from (2.14) and, hence, the same is valid for Φ and its derivative: $\Phi(\pi) = \Phi(-\pi)$, $\Phi'(\pi) = \Phi'(-\pi)$. Then, we obtain non-trivial solutions of (2.19a), provided that $\sin\nu\pi = 0$, or, $\nu = n$ with $n \geq 0$. Substituting $\nu = n$ in (2.19b) and transforming the variable of differentiation $\hat{r} = kr$ we obtain Bessel's equation for functions of order ν [61, p. 38]. The solutions of (2.19b) with $\nu = n$ are therefore linear combinations of the Bessel functions of the first and the second kind $J_n(kr)$ and $Y_n(kr)$, respectively. Thus E_y is a linear combination of $J_n(kr)e^{\pm jn\varphi}$ and $Y_n(kr)e^{\pm jn\varphi}$ with $n \geq 0$. Since $J_{-n} = (-1)^n J_n$ and $Y_{-n} = (-1)^n Y_n$, we note that E_y is a linear combination of $J_n(kr)e^{jn\varphi}$ and $Y_n(kr)e^{jn\varphi}$ with $n \in \mathbb{Z}$.

The derivations so far are general in the sense that they apply to any field $\boldsymbol{E} = E_y(r,\varphi)\boldsymbol{i}_y$ that satisfies Maxwell's equations. For the excitation-field component E_y^{exc} and the interior-field component E_y^{int}, the solutions $Y_n(k_1 r)$ and $Y_n(k_2 r)$ of (2.19b) with $\nu = n$ are not admissible since both fields should be bounded at $r = 0$. Hence, these components are described by the functions $J_n(k_1 r)e^{jn\varphi}$ and $J_n(k_2 r)e^{jn\varphi}$, $n \in \mathbb{Z}$, respectively. For the scattered field component E_y^{sct}, we apply the radiation condition that for $r \to \infty$ its expression should represent outgoing waves. From the asymptotes of the Hankel function $H_n^{(1)}(k_1 r)$ and $H_n^{(2)}(k_1 r)$, and our choice $e^{j\omega t}$ for the time dependence, it follows that only the functions $H_n^{(2)}$ are admissible. Hence, E_y^{sct} is described by the functions $H_n^{(2)}(k_1 r)e^{jn\varphi}$, $n \in \mathbb{Z}$. In conclusion, we formulate the field solutions

$$E_y^{\text{exc}}(r,\varphi) = \sum_{n=-\infty}^{\infty} B_n^{\text{exc}} J_n(k_1 r)e^{jn\varphi}, \tag{2.20a}$$

$$E_y^{\text{sct}}(r,\varphi) = \sum_{n=-\infty}^{\infty} A_n H_n^{(2)}(k_1 r)e^{jn\varphi}, \tag{2.20b}$$

$$E_y^{\text{int}}(r,\varphi) = \sum_{n=-\infty}^{\infty} B_n^{\text{int}} J_n(k_2 r)e^{jn\varphi}. \tag{2.20c}$$

We note that the differential operators in (2.19a) and (2.19b) are both of Sturm-Liouville type [62, Ch. 7]. The differential equation (2.19a) for Φ equipped with the boundary conditions stated above is a Sturm-Liouville problem and, hence, the solutions $e^{jn\varphi}$ constitute a complete orthogonal set in the space of complex-valued square-integrable functions on $[-\pi,\pi]$. These observations consolidate the validity of the field expansions in (2.20).

By applying the second equation of (2.14) to the electric field expansions of (2.20), we obtain the magnetic-field φ-components

$$H_\varphi^{\text{exc}}(r,\varphi) = -\frac{j\omega\varepsilon_1}{k_1}\sum_{n=-\infty}^{\infty} B_n^{\text{exc}} J_n'(k_1 r)e^{jn\varphi}, \tag{2.21a}$$

$$H_\varphi^{\text{sct}}(r,\varphi) = -\frac{j\omega\varepsilon_1}{k_1}\sum_{n=-\infty}^{\infty} A_n H_n^{(2)\prime}(k_1 r)e^{jn\varphi}, \tag{2.21b}$$

$$H_\varphi^{\text{int}}(r,\varphi) = -\frac{j\omega\varepsilon_2}{k_2}\sum_{n=-\infty}^{\infty} B_n^{\text{int}} J_n'(k_2 r)e^{jn\varphi}. \tag{2.21c}$$

The polar coordinates r and φ in (2.20) and (2.21) correspond to the parametric representation of a specific post. In a system of posts the total scattered field is given by the sum of the scattered

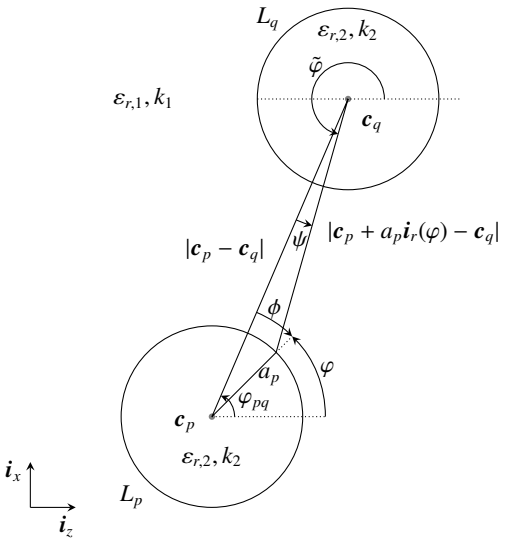

Figure 2.3 — Notation and symbols in a multiple post geometry.

fields of all posts. In the boundary conditions (2.16) this field needs to be evaluated at each post surface L_p. Hence the scattered field of each post q needs to be evaluated at each surface.

Let $\{\boldsymbol{E}_q^{\text{sct}}, \boldsymbol{H}_q^{\text{sct}}\}$ be the electromagnetic field generated by post q. We denote the corresponding expansion coefficients by $A_{q,n}$, $B_{q,n}^{\text{int}}$, and $B_{q,n}^{\text{exc}}$. Then, with reference to Figure 2.3, $E_{q,y}^{\text{sct}}$ at L_p is given by

$$E_{q,y}^{\text{sct}}\Big|_{L_p}(\varphi) = \sum_{n=-\infty}^{\infty} A_{q,n} H_n^{(2)}(k_1|\boldsymbol{c}_p + a_p \boldsymbol{i}_r(\varphi) - \boldsymbol{c}_q|) e^{jn\tilde{\varphi}}. \tag{2.22}$$

With the aid of Graf's addition theorem we can express $\tilde{\varphi} = \pi + \varphi_{pq} + \psi$ in $\varphi = \varphi_{pq} - \phi$. In (B.1) in Appendix B we set

$$r_B = k_1 a_p, \qquad r_A = k_1|\boldsymbol{c}_p - \boldsymbol{c}_q|, \qquad r_{BA} = k_1|\boldsymbol{c}_p + a_p \boldsymbol{i}_r(\varphi) - \boldsymbol{c}_q|, \qquad \nu = -n. \tag{2.23}$$

Then,

$$H_n^{(2)}(k_1|\boldsymbol{c}_p + a_p \boldsymbol{i}_r(\varphi) - \boldsymbol{c}_q|) = (-1)^n e^{jn\psi} \sum_{m=-\infty}^{\infty} H_{m-n}^{(2)}(k_1|\boldsymbol{c}_p - \boldsymbol{c}_q|) J_m(k_1 a) e^{-jm\phi}. \tag{2.24}$$

Substituting $\phi = \varphi_{pq} - \varphi$ and $\psi = \tilde{\varphi} - \pi - \varphi_{pq}$ in (2.24) and substituting (2.24) in (2.22) we obtain

$$E_{q,y}^{\text{sct}}\Big|_{L_p}(\varphi) = \sum_{m=-\infty}^{\infty} \sum_{n=-\infty}^{\infty} A_{q,n} J_m(k_1 a_p) H_{m-n}^{(2)}(k_1|\boldsymbol{c}_p - \boldsymbol{c}_q|) e^{-j(m-n)\varphi_{pq}} e^{jm\varphi}. \tag{2.25}$$

To evaluate $H_{q,\varphi}^{\text{sct}}$ at L_p we replace a_p by r in (2.22)–(2.25), by which (2.25) becomes the expression for $E_{q,y}^{\text{sct}}$ expressed in the (r, φ) coordinates related to L_p. Substituting this expression in

(2.14) and evaluating it at $r = a_p$ we obtain

$$H^{\mathrm{sct}}_{q,\varphi}\big|_{L_p}(\varphi) = -\frac{j\omega\varepsilon_1}{k_1^2}\frac{\partial E^{\mathrm{sct}}_{q,y}}{\partial r}\bigg|_{L_p} \tag{2.26}$$
$$= -\frac{j\omega\varepsilon_1}{k_1}\sum_{m=-\infty}^{\infty}\sum_{n=-\infty}^{\infty} A_{q,n}J'_m(k_1a_p)H^{(2)}_{m-n}(k_1|\boldsymbol{c}_p-\boldsymbol{c}_q|)e^{-j(m-n)\varphi_{pq}}e^{jm\varphi}.$$

2.4.1 Metallic Posts

For metallic posts, we find the coefficients $B^{\mathrm{int}}_{q,n} = 0$ since $E^{\mathrm{int}}_y = 0$. The coefficients $A_{q,n}$ can then be determined from the boundary condition for the electric field, i.e., $E^{\mathrm{sct}}_y = -E^{\mathrm{exc}}_y$ at each L_p, or,

$$E^{\mathrm{sct}}_{p,y}\big|_{L_p} + \sum_{\substack{q=1\\q\neq p}}^{Q} E^{\mathrm{sct}}_{q,y}\big|_{L_p} = -E^{\mathrm{exc}}_y\big|_{L_p}. \tag{2.27}$$

Substituting (2.20a), (2.20b) and (2.25) in this equation, we obtain

$$\sum_{m=-\infty}^{\infty} A_{p,m}H^{(2)}_m(k_1a_p)e^{jm\varphi} + \sum_{\substack{q=1\\q\neq p}}^{Q}\sum_{m=-\infty}^{\infty}\sum_{n=-\infty}^{\infty} A_{q,n}J_m(k_1a_p)H^{(2)}_{m-n}(k_1|\boldsymbol{c}_p-\boldsymbol{c}_q|)e^{-j(m-n)\varphi_{pq}}e^{jm\varphi}$$
$$= -\sum_{m=-\infty}^{\infty} B^{\mathrm{exc}}_{p,m}J_m(k_1a_p)e^{jm\varphi}. \tag{2.28}$$

Since $\{e^{jm\varphi}\}_{m=-\infty}^{\infty}$ constitute an orthogonal system on $[-\pi,\pi]$ with respect to the classical L_2 inner product, we can equate the coefficients of $e^{jm\varphi}$ for each m. Thus we find

$$A_{p,m}\frac{H^{(2)}_m(k_1a_p)}{J_m(k_1a_p)} + \sum_{\substack{q=1\\q\neq p}}^{Q}\sum_{n=-\infty}^{\infty} A_{q,n}H^{(2)}_{m-n}(k_1|\boldsymbol{c}_p-\boldsymbol{c}_q|)e^{j(m-n)\varphi_{pq}} = -B^{\mathrm{exc}}_{p,m}. \tag{2.29}$$

These equations can be cast in the (infinite) matrix equation

$$\begin{pmatrix} C_{11} & C_{12} & \cdots & C_{1Q}\\ C_{21} & C_{22} & & \vdots\\ \vdots & & \ddots & \vdots\\ C_{Q1} & \dots & \dots & C_{QQ}\end{pmatrix}\begin{pmatrix} A_1\\ A_2\\ \vdots\\ A_Q\end{pmatrix} = \begin{pmatrix} -B^{\mathrm{exc}}_1\\ -B^{\mathrm{exc}}_2\\ \vdots\\ -B^{\mathrm{exc}}_Q\end{pmatrix}, \tag{2.30}$$

where $B^{\mathrm{exc}}_p = (\dots, B^{\mathrm{exc}}_{p,-1}, B^{\mathrm{exc}}_{p,0}, B^{\mathrm{exc}}_{p,1}, \dots)^{\mathrm{T}}$, $A_p = (\dots, A_{p,-1}, A_{p,0}, A_{p,1}, \dots)^{\mathrm{T}}$, and

$$C_{pq,mn} = \begin{cases} 0 & (p = q, m \neq n)\\ \dfrac{H^{(2)}_m(k_1a_p)}{J_m(k_1a_p)} & (p = q, m = n)\\ H^{(2)}_{m-n}(k_1|\boldsymbol{c}_p-\boldsymbol{c}_q|)e^{-j(m-n)\varphi_{pq}} & (p \neq q).\end{cases} \tag{2.31}$$

In practice we truncate the infinite matrices C_{pq} by taking $m, n = -N, \ldots, N$. In other words, we replace ∞ in (2.28) by N. Such a truncation is based on the fact that for large values of m $e^{jm\varphi}$ shows many oscillations per wavelength and, hence, corresponds to highly reactive field contributions, which do not contribute to the total field. As a consequence: the smaller the post circumference the smaller the value of N.

2.4.2 Dielectric Posts

For dielectric posts we need to determine the coefficients $A_{q,n}$ *and* $B^{\text{int}}_{q,n}$ from the boundary conditions for both the electric and magnetic field, i.e., (2.16), or,

$$E_y^{\text{exc}}\big|_{L_p} + E_{p,y}^{\text{sct}}\big|_{L_p} + \sum_{\substack{q=1\\q\neq p}}^{Q} E_{q,y}^{\text{sct}}\big|_{L_p} = E_{p,y}^{\text{int}}\big|_{L_p}, \tag{2.32a}$$

$$H_\varphi^{\text{exc}}\big|_{L_p} + H_{p,\varphi}^{\text{sct}}\big|_{L_p} + \sum_{\substack{q=1\\q\neq p}}^{Q} H_{q,\varphi}^{\text{sct}}\big|_{L_p} = H_{p,\varphi}^{\text{int}}\big|_{L_p}, \tag{2.32b}$$

where $E^{\text{int}}_{p,y}$ and $H^{\text{int}}_{p,\varphi}$ are the interior fields of post p. Substituting (2.20a)–(2.20c) and (2.25) in (2.32a) and similarly to the derivation for metallic posts, employing the orthogonality of $\{e^{jm\varphi}\}_{m=-\infty}^{\infty}$ we obtain

$$B^{\text{exc}}_{p,m}\frac{J_m(k_1a_p)}{J_m(k_2a_p)} + A_{p,m}\frac{H_m^{(2)}(k_1a_p)}{J_m(k_2a_p)} + \frac{J_m(k_1a_p)}{J_m(k_2a_p)}\sum_{\substack{q=1\\q\neq p}}^{Q}\sum_{n=-\infty}^{\infty} A_{q,n}H^{(2)}_{m-n}(k_1|\boldsymbol{c}_p-\boldsymbol{c}_q|)e^{-j(m-n)\varphi_{pq}} = B^{\text{int}}_{p,m}. \tag{2.33}$$

Substituting (2.21a)–(2.21c) and (2.26) in (2.32b) and again employing orthogonality we arrive at

$$B^{\text{exc}}_{p,m}\frac{J_m'(k_1a_p)}{J_m'(k_2a_p)} + A_{p,m}\frac{H_m^{(2)'}(k_1a_p)}{J_m'(k_2a_p)} + \frac{J_m'(k_1a_p)}{J_m'(k_2a_p)}\sum_{\substack{q=1\\q\neq p}}^{Q}\sum_{n=-\infty}^{\infty} A_{q,n}H^{(2)}_{m-n}(k_1|\boldsymbol{c}_p-\boldsymbol{c}_q|)e^{-j(m-n)\varphi_{pq}} = \frac{\varepsilon_2k_1}{\varepsilon_1k_2}B^{\text{int}}_{p,m}. \tag{2.34}$$

We substitute this expression for $B^{\text{int}}_{p,m}$ in (2.33). Then,

$$B^{\text{exc}}_{p,m}\left[\frac{J_m(k_1a_p)}{J_m(k_2a_p)} - \frac{\varepsilon_1k_2}{\varepsilon_2k_1}\frac{J_m'(k_1a_p)}{J_m'(k_2a_p)}\right] + A_{p,m}\left[\frac{H_m^{(2)}(k_1a_p)}{J_m(k_2a_p)} - \frac{\varepsilon_1k_2}{\varepsilon_2k_1}\frac{H_m^{(2)'}(k_1a_p)}{J_m'(k_2a_p)}\right] + \left[\frac{J_m(k_1a_p)}{J_m(k_2a_p)} - \frac{\varepsilon_1k_2}{\varepsilon_2k_1}\frac{J_m'(k_1a_p)}{J_m'(k_2a_p)}\right]\sum_{\substack{q=1\\q\neq p}}^{Q}\sum_{n=-\infty}^{\infty} A_{q,n}H^{(2)}_{m-n}(k_1|\boldsymbol{c}_p-\boldsymbol{c}_q|)e^{-j(m-n)\varphi_{pq}} = 0. \tag{2.35}$$

Dividing all terms by the coefficient of $B^{\text{exc}}_{p,m}$ we obtain

$$A_{p,m}\frac{\varepsilon_2 k_1 H_m^{(2)}(k_1 a_p)J'_m(k_2 a_p) - \varepsilon_1 k_2 H_m^{(2)\prime}(k_1 a_p)J_m(k_2 a_p)}{\varepsilon_2 k_1 J_m(k_1 a_p)J'_m(k_2 a_p) - \varepsilon_1 k_2 J'_m(k_1 a_p)J_m(k_2 a_p)} + \sum_{\substack{q=1\\ q\neq p}}^{Q}\sum_{n=-\infty}^{\infty} A_{q,n} H^{(2)}_{m-n}(k_1|\boldsymbol{c}_p - \boldsymbol{c}_q|)e^{-j(m-n)\varphi_{pq}} = -B^{\text{exc}}_{p,m}. \quad (2.36)$$

Since both the posts and their surrounding medium will in general have the same permeability, $\mu_1 = \mu_2$, we can rewrite the coefficient of $A_{p,m}$ by dividing numerator and denominator by $\sqrt{\varepsilon_1\varepsilon_2}$ in the form

$$\frac{k_2 H_m^{(2)}(k_1 a_p)J'_m(k_2 a_p) - k_1 H_m^{(2)\prime}(k_1 a_p)J_m(k_2 a_p)}{k_2 J_m(k_1 a_p)J'_m(k_2 a_p) - k_1 J'_m(k_1 a_p)J_m(k_2 a_p)}. \quad (2.37)$$

The equation (2.36) can be cast in the matrix form (2.30), where

$$C_{pq,mn} = \begin{cases} 0 & (p = q, m \neq n) \\ \dfrac{\varepsilon_2 k_1 H_m^{(2)}(k_1 a_p)J'_m(k_2 a_p) - \varepsilon_1 k_2 H_m^{(2)\prime}(k_1 a_p)J_m(k_2 a_p)}{\varepsilon_2 k_1 J_m(k_1 a_p)J'_m(k_2 a_p) - \varepsilon_1 k_2 J'_m(k_1 a_p)J_m(k_2 a_p)} & (p = q, m = n) \\ H^{(2)}_{m-n}(k_1|\boldsymbol{c}_p - \boldsymbol{c}_q|)e^{-j(m-n)\varphi_{pq}} & (p \neq q). \end{cases} \quad (2.38)$$

We observe that the mutual coupling ($p \neq q$) has the same form as in the case of metallic posts.

2.5 Integral Equation Formulation

As an alternative to the modal formulation we can describe the electromagnetic behavior of PWWGs by integral equations. For such a description it is convenient to use the concept of Lorentz's reciprocity theorem. This concept facilitates in a straightforward manner the description of the electric and magnetic fields in terms of (boundary) integral expressions. Introducing Lorentz's reciprocity theorem and deriving the integral expressions we will draw the links with other important concepts in electromagnetics, such as Oseen's extinction theorem and Love's equivalence principle. The integral expressions so derived are not only used in this section to describe the electromagnetic behavior of PWWGs, but they will also play an important role in connecting PWWG components as we describe in Section 3.4 and Chapter 6. We formulate the concept and integral expressions such that they suit the model setup of Section 2.3, i.e., the fields do not depend on the y-coordinate, which is the axial direction of the posts.

2.5.1 Lorentz's Reciprocity Theorem for Fields Dependent on Two Spatial Coordinates

Let $\boldsymbol{J}$ and $\tilde{\boldsymbol{J}}$ be two different current distributions in the same domain Ω, which comprises a linear homogeneous medium. The corresponding fields $\{\boldsymbol{E}, \boldsymbol{H}\}$ and $\{\tilde{\boldsymbol{E}}, \tilde{\boldsymbol{H}}\}$ are governed by

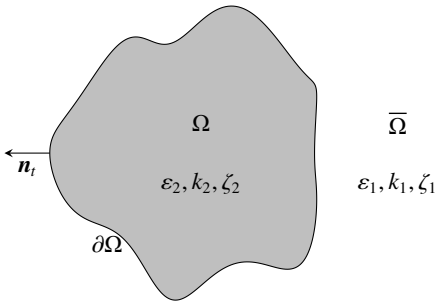

Figure 2.4 — Graphical representation of the setup for Lorentz's reciprocity theorem.

Maxwell's equations (2.4). Then,

$$\tilde{\boldsymbol{H}} \bullet \operatorname{curl} \boldsymbol{E} - \boldsymbol{E} \bullet \operatorname{curl} \tilde{\boldsymbol{H}} = -j\omega\mu\tilde{\boldsymbol{H}} \bullet \boldsymbol{H} - j\omega\varepsilon\boldsymbol{E} \bullet \tilde{\boldsymbol{E}} - \boldsymbol{E} \bullet \tilde{\boldsymbol{J}}. \tag{2.39}$$

The term in the left-hand side equals $\operatorname{div}(\boldsymbol{E} \times \tilde{\boldsymbol{H}})$. A similar equation for $\operatorname{div}(\tilde{\boldsymbol{E}} \times \boldsymbol{H})$ can be obtained from (2.39) by interchanging the fields. Subtracting the resulting equation from (2.39) and integrating over Ω we obtain

$$\int_{\Omega} \operatorname{div}\left(\boldsymbol{E} \times \tilde{\boldsymbol{H}} - \tilde{\boldsymbol{E}} \times \boldsymbol{H}\right) d\Omega = \int_{\Omega} \tilde{\boldsymbol{E}} \bullet \boldsymbol{J}\, d\Omega - \int_{\Omega} \boldsymbol{E} \bullet \tilde{\boldsymbol{J}}\, d\Omega. \tag{2.40}$$

Usually Ω is assumed to be a volume in $\mathbb{R}^3$ and Gauss' theorem is applied to the left-hand side of (2.40). Under the assumption that the fields do not depend on the y-coordinate (and that $\boldsymbol{E} \times \tilde{\boldsymbol{H}} - \tilde{\boldsymbol{E}} \times \boldsymbol{H}$ has a zero y-component), we can define Ω as an area in the xz-plane, with boundary curve $\partial\Omega$, and apply Gauss' theorem in two dimensions to the left-hand side of (2.40); this is depicted in Figure 2.4. Then,

$$\int_{\partial\Omega} \left(\boldsymbol{E} \times \tilde{\boldsymbol{H}} - \tilde{\boldsymbol{E}} \times \boldsymbol{H}\right) \bullet \boldsymbol{n}_t\, d\partial\Omega = \int_{\Omega} \tilde{\boldsymbol{E}} \bullet \boldsymbol{J}\, d\Omega - \int_{\Omega} \boldsymbol{E} \bullet \tilde{\boldsymbol{J}}\, d\Omega, \tag{2.41}$$

where $\boldsymbol{n}_t$ is the outward normal given by $\boldsymbol{n}_t = n_x\boldsymbol{i}_x + n_z\boldsymbol{i}_z$. The fields in the boundary integral are restricted to $\partial\Omega$ from the inside of $\partial\Omega$. The integrals on the right-hand side are called the reactions as introduced by Rumsey [63] and may be interpreted as a measure of correlation between the two sets of fields.

2.5.2 Integral Expressions Derived by Lorentz's Reciprocity Theorem

Let $\tilde{\boldsymbol{J}} = \delta(\tilde{\boldsymbol{x}}_t - \boldsymbol{x}_t)\boldsymbol{i}$, where the subscript t denotes that vectors should be read as $\boldsymbol{x}_t = x\boldsymbol{i}_x + z\boldsymbol{i}_z$ and where $\boldsymbol{i} \in \mathbb{R}^3$ is a fixed vector of length 1. Then, applying Lorentz's reciprocity theorem (2.41) we find

$$\int_{\Omega} \tilde{\boldsymbol{E}} \bullet \boldsymbol{J}\, d\Omega - \int_{\partial\Omega} \left(\tilde{\boldsymbol{E}} \bullet (\boldsymbol{n}_t \times \boldsymbol{H}) + \tilde{\boldsymbol{H}} \bullet (\boldsymbol{n}_t \times \boldsymbol{E})\right) d\partial\Omega = \begin{cases} \boldsymbol{i} \bullet \boldsymbol{E}(\tilde{\boldsymbol{x}}_t), & \tilde{\boldsymbol{x}}_t \in \Omega \setminus \partial\Omega, \\ \boldsymbol{0}, & \tilde{\boldsymbol{x}}_t \in \overline{\Omega} \setminus \partial\Omega, \end{cases} \tag{2.42}$$

with cyclic rotation of the cross and dot products on the left-hand side of (2.41) and where $\overline{\Omega}$ is the complement of Ω. We write explicitly $\setminus\partial\Omega$ to emphasize that the boundary is excluded. We do not discuss here the case that $\tilde{\boldsymbol{x}} \in \partial\Omega$. Expression (2.42) reveals that the electric field $\boldsymbol{E}$ in $\Omega \setminus \partial\Omega$ can be expressed in terms of the volume source $\boldsymbol{J}$ and the tangential components of the electric and magnetic fields on the boundary curve $\partial\Omega$. In $\overline{\Omega} \setminus \partial\Omega$ the contribution of the volume source to $\boldsymbol{E}$ is annihilated by the contribution of the tangential fields at $\partial\Omega$. This property is known as Oseen's extinction theorem.

Analogously to Section 2.3 we introduce $\{\boldsymbol{E}^{\text{exc}}, \boldsymbol{H}^{\text{exc}}\}$ as the excitation field incident on Ω and $\{\boldsymbol{E}^{\text{sct}}, \boldsymbol{H}^{\text{sct}}\}$ and $\{\boldsymbol{E}^{\text{int}}, \boldsymbol{H}^{\text{int}}\}$ as the induced fields outside and inside Ω, respectively. Applying (2.42) to the extinction field $\{\boldsymbol{E}^{\text{exc}}, \boldsymbol{H}^{\text{exc}}\}$ inside Ω we obtain

$$-\int_{\partial\Omega} \Big(\tilde{\boldsymbol{E}} \bullet (\boldsymbol{n}_t \times \boldsymbol{H}^{\text{exc}}) + \tilde{\boldsymbol{H}} \bullet (\boldsymbol{n}_t \times \boldsymbol{E}^{\text{exc}})\Big)\, d\partial\Omega = \begin{cases} \boldsymbol{i} \bullet \boldsymbol{E}^{\text{exc}}(\tilde{\boldsymbol{x}}_t), & \tilde{\boldsymbol{x}}_t \in \Omega \setminus \partial\Omega, \\ \\ \boldsymbol{0}, & \tilde{\boldsymbol{x}}_t \in \overline{\Omega} \setminus \partial\Omega, \end{cases} \tag{2.43}$$

where we assume that there are no volume sources. Applying (2.42) to the induced or scattered field $\{\boldsymbol{E}^{\text{sct}}, \boldsymbol{H}^{\text{sct}}\}$ in $\overline{\Omega}$ we obtain under the same assumption

$$\int_{\partial\Omega} \Big(\tilde{\boldsymbol{E}} \bullet (\boldsymbol{n}_t \times \boldsymbol{H}^{\text{sct}}) + \tilde{\boldsymbol{H}} \bullet (\boldsymbol{n}_t \times \boldsymbol{E}^{\text{sct}})\Big)\, d\partial\Omega = \begin{cases} \boldsymbol{0}, & \tilde{\boldsymbol{x}}_t \in \Omega \setminus \partial\Omega, \\ \\ \boldsymbol{i} \bullet \boldsymbol{E}^{\text{sct}}(\tilde{\boldsymbol{x}}_t), & \tilde{\boldsymbol{x}}_t \in \overline{\Omega} \setminus \partial\Omega. \end{cases} \tag{2.44}$$

Note the sign difference with respect to (2.43), which follows from $\boldsymbol{n}_t$ being the outward normal on $\partial\Omega$. Subtracting (2.43) from (2.44) we arrive at

$$\int_{\partial\Omega} \Big(\tilde{\boldsymbol{E}} \bullet \boldsymbol{J}^{\text{surf}} + \tilde{\boldsymbol{H}} \bullet \boldsymbol{M}^{\text{surf}}\Big)\, d\partial\Omega = \begin{cases} -\boldsymbol{i} \bullet \boldsymbol{E}^{\text{exc}}(\tilde{\boldsymbol{x}}_t), & \tilde{\boldsymbol{x}}_t \in \Omega \setminus \partial\Omega, \\ \\ \boldsymbol{i} \bullet \boldsymbol{E}^{\text{sct}}(\tilde{\boldsymbol{x}}_t), & \tilde{\boldsymbol{x}}_t \in \overline{\Omega} \setminus \partial\Omega, \end{cases} \tag{2.45}$$

with electric and magnetic surface currents $\boldsymbol{J}^{\text{surf}}$ and $\boldsymbol{M}^{\text{surf}}$ defined by

$$\boldsymbol{J}^{\text{surf}} = \boldsymbol{n}_t \times \Big(\boldsymbol{H}^{\text{exc}} + \boldsymbol{H}^{\text{sct}}\Big)\Big|_{\partial\Omega}, \qquad \boldsymbol{M}^{\text{surf}} = \boldsymbol{n}_t \times \Big(\boldsymbol{E}^{\text{exc}} + \boldsymbol{E}^{\text{sct}}\Big)\Big|_{\partial\Omega}, \tag{2.46}$$

where the restriction is applied outside of $\partial\Omega$. We note that in (2.43) the restriction of the fields to $\partial\Omega$ is carried out inside of $\partial\Omega$. Since $\{\boldsymbol{E}^{\text{exc}}, \boldsymbol{H}^{\text{exc}}\}$ exist in an environment without Ω present, the fields in (2.43) are continuous across $\partial\Omega$. Therefore, the restriction to $\partial\Omega$ can be taken from either side. From (2.45) we observe that the excitation field in $\Omega \setminus \partial\Omega$ and the scattered field in $\overline{\Omega} \setminus \partial\Omega$ are both entirely described by the surface currents.

Applying (2.41) to the induced field $\{\boldsymbol{E}^{\text{int}}, \boldsymbol{H}^{\text{int}}\}$ in Ω, we find –in absence of volume sources– the same equations as (2.43) with 'exc' replaced by 'int'. If we assume that the total tangential field is continuous across $\partial\Omega$, we can write this expression as

$$-\int_{\partial\Omega} \Big(\tilde{\boldsymbol{E}} \bullet \boldsymbol{J}^{\text{surf}} + \tilde{\boldsymbol{H}} \bullet \boldsymbol{M}^{\text{surf}}\Big)\, d\partial\Omega = \begin{cases} \boldsymbol{i} \bullet \boldsymbol{E}^{\text{int}}(\tilde{\boldsymbol{x}}_t), & \tilde{\boldsymbol{x}}_t \in \Omega \setminus \partial\Omega, \\ \\ \boldsymbol{0}, & \tilde{\boldsymbol{x}}_t \in \overline{\Omega} \setminus \partial\Omega, \end{cases} \tag{2.47}$$

where $\boldsymbol{J}^{\text{surf}}$ and $\boldsymbol{M}^{\text{surf}}$ equal $\boldsymbol{n} \times \boldsymbol{H}^{\text{int}}\big|_{\partial\Omega}$ and $\boldsymbol{n} \times \boldsymbol{E}^{\text{int}}\big|_{\partial\Omega}$ with the restriction applied from the inside of $\partial\Omega$. Equation (2.47) can be viewed as the interior equivalent state in Love's equivalence principle, where the field in Ω is entirely described by its tangential components on $\partial\Omega$ while the field outside Ω is zero.

2.5.3 Fundamental Solutions and their Application

To calculate the fields from (2.45) and (2.47) we need to evaluate the source fields $\{\tilde{\boldsymbol{E}}, \tilde{\boldsymbol{H}}\}$. Under the model assumption that $\tilde{\boldsymbol{E}} = \tilde{E}_y \boldsymbol{i}_y$, the electric field is determined by the Helmholtz equation in two dimensions

$$\Delta \tilde{E}_y + k^2 \tilde{E}_y = j\omega\mu\delta(\tilde{\boldsymbol{x}}_t - \boldsymbol{x}_t). \tag{2.48}$$

The solution to this equation is a fundamental solution of the Helmholtz operator $\Delta + k^2$. Taking into account the radiation condition mentioned in Section 2.4, we can specify this solution as

$$\tilde{\boldsymbol{E}}(\boldsymbol{x}_t) = \frac{k\zeta}{4} H_0^{(2)}(k|\tilde{\boldsymbol{x}}_t - \boldsymbol{x}_t|)\boldsymbol{i}_y, \tag{2.49}$$

where $\zeta = \sqrt{\mu/\varepsilon}$. Note that $\omega\mu = k\zeta$. The corresponding magnetic field $\tilde{\boldsymbol{H}}$ follows from (2.4a),

$$\tilde{\boldsymbol{H}}(\boldsymbol{x}_t) = \frac{j}{4}\mathrm{curl}_{\boldsymbol{x}} \left(H_0^{(2)}(k|\tilde{\boldsymbol{x}}_t - \boldsymbol{x}_t|)\boldsymbol{i}_y\right) = \frac{j}{4}\mathrm{grad}_{\boldsymbol{x}} \left(H_0^{(2)}(k|\tilde{\boldsymbol{x}}_t - \boldsymbol{x}_t|)\right) \times \boldsymbol{i}_y. \tag{2.50}$$

Here the subscript $\boldsymbol{x}$ on the curl operator means that the curl is taken with respect to $\boldsymbol{x} = (x, y, z)$. Substituting these expressions for $\tilde{\boldsymbol{E}}$ and $\tilde{\boldsymbol{H}}$ in (2.45) and (2.47) and applying cyclic rotation to $\tilde{\boldsymbol{H}} \bullet \boldsymbol{M}^{\mathrm{surf}}$ with $\tilde{\boldsymbol{H}}$ given by the second equation in (2.50), we arrive at

$$\begin{aligned}
&\frac{k_i\zeta_i}{4}\int_{\partial\Omega} H_0^{(2)}(k_i|\boldsymbol{x}_t - \boldsymbol{x}_t'|)J_y^{\mathrm{surf}}(\boldsymbol{x}_t')\,d\partial\Omega' + \frac{j}{4}\int_{\partial\Omega} \boldsymbol{i}_y \bullet \left(\boldsymbol{M}^{\mathrm{surf}}(\boldsymbol{x}_t') \times \mathrm{grad}_{\boldsymbol{x}'} H_0^{(2)}(k_i|\boldsymbol{x}_t - \boldsymbol{x}_t'|)\right) d\partial\Omega' \\
&\qquad = \begin{cases} E_y^{\mathrm{exc}}(\boldsymbol{x}_t)\ (i=1), \quad E_y^{\mathrm{int}}(\boldsymbol{x}_t)\ (i=2), & \boldsymbol{x}_t \in \Omega \setminus \partial\Omega, \\ E_y^{\mathrm{sct}}(\boldsymbol{x}_t)\ (i=1), \quad 0\ (i=2), & \boldsymbol{x}_t \in \overline{\Omega} \setminus \partial\Omega. \end{cases}
\end{aligned} \tag{2.51}$$

Here we replaced $\tilde{\boldsymbol{x}}_t$ by $\boldsymbol{x}_t$. Moreover, $\{k_i, \zeta_i, \varepsilon_i\}$ are the medium parameters in Ω and $\overline{\Omega}$ for $i = 1$ and $i = 2$ respectively, as depicted in Figure 2.4. We note that the medium parameters are chosen according to the restriction of the fields in (2.45) and (2.47) from the outside and inside to $\partial\Omega$. If $k_1 = k_2$ and $\zeta_1 = \zeta_2$, (2.51) shows that $E_y^{\mathrm{sct}} = 0$ and $E_y^{\mathrm{int}} = E_y^{\mathrm{exc}}$. The cross product in the second integral of (2.51) only has a y-component and, hence, in the expression for the electric field $\boldsymbol{E} = E_y \boldsymbol{i}_y$ we only need to omit the dot product with $\boldsymbol{i}_y$. Taking the curl of (2.51) we find expressions for the magnetic fields,

$$\begin{aligned}
&\frac{j}{4}\mathrm{curl}_{\boldsymbol{x}} \left[\int_{\partial\Omega} H_0^{(2)}(k_i|\boldsymbol{x}_t - \boldsymbol{x}_t'|)J_y^{\mathrm{surf}}(\boldsymbol{x}_t')\,d\partial\Omega' \boldsymbol{i}_y\right] \\
&\qquad - \frac{1}{4k_i\zeta_i}\mathrm{curl}_{\boldsymbol{x}} \left[\int_{\partial\Omega} \boldsymbol{i}_y \bullet \left(\boldsymbol{M}^{\mathrm{surf}}(\boldsymbol{x}_t') \times \mathrm{grad}_{\boldsymbol{x}'} H_0^{(2)}(k_i|\boldsymbol{x}_t - \boldsymbol{x}_t'|)\right) d\partial\Omega'\right] \\
&\qquad\qquad = \begin{cases} \boldsymbol{H}_y^{\mathrm{exc}}(\boldsymbol{x}_t)\ (i=1), \quad \boldsymbol{H}_y^{\mathrm{int}}(\boldsymbol{x}_t)\ (i=2), & \boldsymbol{x}_t \in \Omega \setminus \partial\Omega, \\ \boldsymbol{H}_y^{\mathrm{sct}}(\boldsymbol{x}_t)\ (i=1), \quad \boldsymbol{0}\ (i=2), & \boldsymbol{x}_t \in \overline{\Omega} \setminus \partial\Omega. \end{cases}
\end{aligned} \tag{2.52}$$

The curl operations in these expressions are not easy to handle computationally. Therefore we rewrite (2.52). The first curl in the left-hand side can be rewritten by the vector identity $\operatorname{curl}(f\boldsymbol{v}) = f\operatorname{curl}\boldsymbol{v} + \operatorname{grad} f \times \boldsymbol{v}$,

$$\text{first curl in (2.52)} = \operatorname{grad}_{\boldsymbol{x}} \int_{\partial\Omega} H_0^{(2)}(k_i|\boldsymbol{x}_t - \boldsymbol{x}_t'|) J_y^{\text{surf}}(\boldsymbol{x}_t')\, d\partial\Omega' \times \boldsymbol{i}_y. \tag{2.53}$$

Reversing the gradient and the integral, moving the cross product inside the integral, and applying the gradient to $\boldsymbol{x}'$ instead of $\boldsymbol{x}$, we obtain

$$\text{first curl in (2.52)} = \int_{\partial\Omega} J_y^{\text{surf}}(\boldsymbol{x}_t')\boldsymbol{i}_y \times \operatorname{grad}_{\boldsymbol{x}'} H_0^{(2)}(k_i|\boldsymbol{x}_t - \boldsymbol{x}_t'|)\, d\partial\Omega'. \tag{2.54}$$

To rewrite the second curl in the left-hand side of (2.52) we first apply the vector identity $\boldsymbol{v} \times \operatorname{grad} f = f\operatorname{curl}\boldsymbol{v} - \operatorname{curl}(f\boldsymbol{v})$ to the cross product. Thus we obtain

$$\text{second curl in (2.52)} = \operatorname{curl}_{\boldsymbol{x}} \int_{\partial\Omega} \operatorname{curl}_{\boldsymbol{x}} \left(H_0^{(2)}(k_i|\boldsymbol{x}_t - \boldsymbol{x}_t'|) \boldsymbol{M}^{\text{surf}}(\boldsymbol{x}_t') \right) d\partial\Omega', \tag{2.55}$$

where we use $\operatorname{curl}_{\boldsymbol{x}} \boldsymbol{M}^{\text{surf}}(\boldsymbol{x}_t') = \boldsymbol{0}$. Taking the curl out of the integral and applying the vector identity $\operatorname{curl}\operatorname{curl} = \operatorname{grad}\operatorname{div} - \Delta$ we rewrite this expression as

$$\begin{aligned}\text{second curl in (2.52)} = \operatorname{grad}_{\boldsymbol{x}} \operatorname{div}_{\boldsymbol{x}} \int_{\partial\Omega} H_0^{(2)}(k_i|\boldsymbol{x}_t - \boldsymbol{x}_t'|) \boldsymbol{M}^{\text{surf}}(\boldsymbol{x}_t')\, d\partial\Omega' \\ - \Delta_{\boldsymbol{x}} \int_{\partial\Omega} H_0^{(2)}(k_i|\boldsymbol{x}_t - \boldsymbol{x}_t'|) \boldsymbol{M}^{\text{surf}}(\boldsymbol{x}_t')\, d\partial\Omega'.\end{aligned} \tag{2.56}$$

Moving $-\Delta_{\boldsymbol{x}}$ inside the second integral we can, for $\boldsymbol{x} \notin \partial\Omega$, replace $-\Delta_{\boldsymbol{x}}$ of the Hankel function by k^2 times the Hankel function. Then, substituting this result and (2.54) in (2.52) we obtain

$$\begin{aligned} -\frac{k_i}{4\zeta_i}\left(1 + \frac{1}{k_i^2}\operatorname{grad}_{\boldsymbol{x}}\operatorname{div}_{\boldsymbol{x}}\right) \int_{\partial\Omega} H_0^{(2)}(k_i|\boldsymbol{x}_t - \boldsymbol{x}_t'|) \boldsymbol{M}^{\text{surf}}(\boldsymbol{x}_t')\, d\partial\Omega' + \\ \frac{j}{4} \int_{\partial\Omega} J_y^{\text{surf}}(\boldsymbol{x}_t')\boldsymbol{i}_y \times \operatorname{grad}_{\boldsymbol{x}'} H_0^{(2)}(k_i|\boldsymbol{x}_t - \boldsymbol{x}_t'|)\, d\partial\Omega' \\ = \begin{cases} \boldsymbol{H}_y^{\text{exc}}(\boldsymbol{x}_t)\ (i=1), \quad \boldsymbol{H}_y^{\text{int}}(\boldsymbol{x}_t)\ (i=2), & \boldsymbol{x}_t \in \Omega \setminus \partial\Omega, \\ \boldsymbol{H}_y^{\text{sct}}(\boldsymbol{x}_t)\ (i=1), \quad \boldsymbol{0}\ (i=2), & \boldsymbol{x}_t \in \overline{\Omega} \setminus \partial\Omega. \end{cases} \end{aligned} \tag{2.57}$$

In Appendix C we show how the divergence in the first term of (2.56) can be transferred to the surface current.

2.5.4 Boundary Integral Equations for Dielectric and Perfectly Conducting Objects

Before we can compute the electric and magnetic fields from (2.51) and (2.52), the magnetic and electric surface currents need to be calculated. These currents are determined by boundary integral equations that follow from the boundary conditions for the tangential components of the electric and magnetic fields. Let us consider the case that Ω and $\overline{\Omega}$ consist of dielectric media. The tangential components of the electric and magnetic fields are continuous across $\partial\Omega$, where tangential components should be interpreted as components perpendicular to $\boldsymbol{n}_t$. Then, by (2.51) the boundary condition for the tangential electric field is written as

$$-E_y^{\mathrm{exc}}\big|_{\partial\Omega}\,\boldsymbol{i}_y = \left(\frac{k_1\zeta_1}{4}\mathcal{K}_1 + \frac{k_2\zeta_2}{4}\mathcal{K}_2\right) J_y^{\mathrm{surf}}\boldsymbol{i}_y\Big|_{\partial\Omega} + \frac{j}{4}\left(\mathcal{L}_1 + \mathcal{L}_2\right)\boldsymbol{M}^{\mathrm{surf}}\Big|_{\partial\Omega}, \tag{2.58}$$

where

$$\mathcal{K}_i\boldsymbol{v} = \int_{\partial\Omega} H_0^{(2)}(k_i|\boldsymbol{x}_t - \boldsymbol{x}_t'|)\boldsymbol{v}(\boldsymbol{x}_t')\,d\partial\Omega', \tag{2.59a}$$

$$\mathcal{L}_i\boldsymbol{v} = \int_{\partial\Omega} \boldsymbol{v}\times\mathrm{grad}_{x'}\, H_0^{(2)}(k_i|\boldsymbol{x}_t - \boldsymbol{x}_t'|)\,d\partial\Omega', \tag{2.59b}$$

for vector functions $\boldsymbol{v}$ defined on $\partial\Omega$. Moreover, by (2.57) the boundary condition for the tangential magnetic field is written as

$$\begin{aligned}-(\boldsymbol{H}^{\mathrm{exc}})_{\tan} = &-\left(\left(\frac{k_1}{4\zeta_1}\mathcal{K}_1 + \frac{k_2}{4\zeta_2}\mathcal{K}_2\right)\boldsymbol{M}^{\mathrm{surf}}\right)_{\tan}\\ &-\left(\left(\frac{1}{4k_1\zeta_1}\mathrm{grad\,div}\,\mathcal{K}_1 + \frac{2}{4k_2\zeta_2}\mathrm{grad\,div}\,\mathcal{K}_2\right)\boldsymbol{M}^{\mathrm{surf}}\right)_{\tan} + \frac{j}{4}\left(\left(\mathcal{L}_1 + \mathcal{L}_2\right)J_y^{\mathrm{surf}}\boldsymbol{i}_y\right)_{\tan}.\end{aligned} \tag{2.60}$$

The operator $(\,\cdot\,)_{\tan}$ restricts vector fields $\boldsymbol{v}$ to $\partial\Omega$ and gives the tangential component, i.e.

$$(\boldsymbol{v})_{\tan} = \boldsymbol{v}|_{\partial\Omega} - (\boldsymbol{n}_t \bullet\, \boldsymbol{v}|_{\partial\Omega})\,\boldsymbol{n}_t. \tag{2.61}$$

The set of equations (2.58),(2.60) determine the surface currents $\boldsymbol{J}^{\mathrm{surf}}$ and $\boldsymbol{M}^{\mathrm{surf}}$. In these equations both the interior and the exterior fields are present. It is possible to derive separate equations for the fields in Ω and $\overline{\Omega}$. To this end the surface currents on the inside and outside of $\partial\Omega$ should be defined as different quantities. Hence, in (2.47) we should have given $\boldsymbol{J}^{\mathrm{surf}}$ and $\boldsymbol{M}^{\mathrm{surf}}$ different names. The derivation of the separate equations relies in general on two additional ingredients that we have avoided, namely the introduction of the magnetic volume current in Maxwell's equation to make them symmetric and to invoke duality, and the evaluation of the fields in (2.45) and (2.47) on $\partial\Omega$, which requires a dedicated limiting process [64]. If in the resulting separate sets of equations, the surface currents on the inside and outside of $\partial\Omega$ are set equal, as we have done at an earlier stage, one speaks of the Poggio, Miller, Chang, Harrington and Wu (PMCHW) formulation. In this respect, our set of equations can be viewed as a special case of this formulation.

Next we consider the case that $\partial\Omega$ is a perfectly conducting transition. In that case we consider only the field in $\overline{\Omega}$. The tangential component of the sum of the excitation and scattered fields vanishes at the boundary and, hence, $\boldsymbol{M}^{\mathrm{surf}} = \boldsymbol{0}$. Then, the electric surface current can be determined from this boundary condition only, which by (2.51) can be written as

$$-\boldsymbol{E}^{\mathrm{exc}}\big|_{\partial\Omega}\,\boldsymbol{i}_y = \frac{k_1\zeta_1}{4}\mathcal{K}_1 J_y^{\mathrm{surf}}\boldsymbol{i}_y\Big|_{\partial\Omega} = \frac{k_1\zeta_1}{4}\int_{\partial\Omega} H_0^{(2)}(k_i|\boldsymbol{x}_t-\boldsymbol{x}_t'|)J_y^{\mathrm{surf}}(\boldsymbol{x}_t')\,d\partial\Omega'\Bigg|_{\partial\Omega}\boldsymbol{i}_y. \tag{2.62}$$

2.5.5 Metallic Posts

Based on the derivation above, the scattered electric field for an array of metallic posts is given by $\boldsymbol{E}^{\mathrm{sct}} = E_y^{\mathrm{sct}}\boldsymbol{i}_y$, where

$$E_y^{\mathrm{sct}}(\boldsymbol{x}_t) = \sum_{q=1}^{\infty} E_{q,y}^{\mathrm{sct}}(\boldsymbol{x}_t), \tag{2.63}$$

$$E_{q,y}^{\mathrm{sct}}(\boldsymbol{x}_t) = \frac{k_1\zeta_1}{4}\int_{L_q} H_0^{(2)}(k_1|\boldsymbol{x}_t-\boldsymbol{x}_t'|)J_{q,y}^{\mathrm{surf}}(\boldsymbol{x}_t')\,dL_q, \tag{2.64}$$

where $J_{q,y}^{\mathrm{surf}}$ is the surface current on the qth post. With the parameter representation we can write (2.64) as

$$E_{q,y}^{\mathrm{sct}}(\boldsymbol{x}_t) = \frac{k_1\zeta_1 a_q}{4}\int_{-\pi}^{\pi} H_0^{(2)}(k_1|\boldsymbol{x}_t-\boldsymbol{c}_q-a_q\boldsymbol{i}_r(\varphi')|)J_{q,y}^{\mathrm{surf}}(\varphi')\,d\varphi'. \tag{2.65}$$

In the boundary condition for the scattered field, i.e., $E_y^{\mathrm{sct}} = -E_y^{\mathrm{exc}}$ on each L_p, we need to evaluate E_y^{sct} at each L_p,

$$E_{q,y}^{\mathrm{sct}}\big|_{L_p}(\varphi) = \frac{k_1\zeta_1 a_q}{4}\int_{-\pi}^{\pi} H_0^{(2)}(k_1|\boldsymbol{c}_p+a_p\boldsymbol{i}_r(\varphi)-\boldsymbol{c}_q-a_q\boldsymbol{i}_r(\varphi')|)J_{q,y}^{\mathrm{surf}}(\varphi')\,d\varphi', \tag{2.66}$$

where $|_{L_p}$ denotes the restriction of a quantity to L_p. We define the vector functions $\boldsymbol{w}$ and $\boldsymbol{v}^{\mathrm{exc}}$ from $[-\pi,\pi]$ to $\mathbb{C}^Q$ by $w_q = J_{q,y}^{\mathrm{surf}}$ and $v_q^{\mathrm{exc}} = -E_y^{\mathrm{surf}}\big|_{L_q}$. Thus, $\boldsymbol{w}$ and $\boldsymbol{v}^{\mathrm{exc}}$ add to each $\varphi\in[-\pi,\pi]$ the tangential components of the currents and excitation fields of the posts. Then, we can interpret the boundary condition as the operator equation

$$\mathcal{Z}\boldsymbol{w} = \boldsymbol{v}^{\mathrm{exc}}, \tag{2.67}$$

where the pth component of $\mathcal{Z}\boldsymbol{w}$ is defined by

$$(\mathcal{Z}\boldsymbol{w})_p(\varphi) = \frac{k_1\zeta_1}{4}\sum_{q=1}^{Q} a_q\int_{-\pi}^{\pi} H_0^{(2)}(k_1|\boldsymbol{c}_p+a_p\boldsymbol{i}_r(\varphi)-\boldsymbol{c}_q-a_q\boldsymbol{i}_r(\varphi')|)w_q(\varphi')\,d\varphi'. \tag{2.68}$$

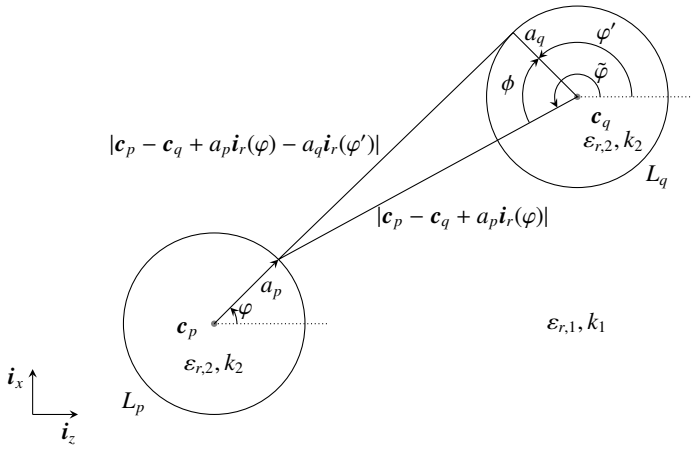

Figure 2.5 — Notation and symbols in a multiple post geometry as used in the integral formulation.

To solve (2.67) we apply a moment method of Galerkin type, based on the classical inner product

$$\langle \boldsymbol{v}, \boldsymbol{w} \rangle = \int_{-\pi}^{\pi} \boldsymbol{v}^*(\varphi) \bullet \boldsymbol{w}(\varphi)\, d\varphi \tag{2.69}$$

and the basis functions $w_{q,n}$, which are zero on all the posts except the qth one, where they equal w_n. Subsequently, the moment-matrix component $\langle \boldsymbol{w}_{p,m}, \mathcal{Z}\boldsymbol{w}_{q,n} \rangle$ is given by

$$\langle \boldsymbol{w}_{p,m}, \mathcal{Z}\boldsymbol{w}_{q,n} \rangle = \frac{k_1\zeta_1 a_q}{4} \int_{-\pi}^{\pi} w_m^*(\varphi) \int_{-\pi}^{\pi} H_0^{(2)}(k_1|\boldsymbol{c}_p - \boldsymbol{c}_q + a_p\boldsymbol{i}_r(\varphi) - a_q\boldsymbol{i}_r(\varphi')|) w_n(\varphi')\, d\varphi' d\varphi. \tag{2.70}$$

To calculate the integral with respect to φ' we apply Graf's addition theorem. In (B.1) in Appendix B we set

$$r_B = k_1 a_q, \quad r_A = k_1|\boldsymbol{c}_p + a_p\boldsymbol{i}_r(\varphi) - \boldsymbol{c}_q|, \quad r_{BA} = k_1|\boldsymbol{c}_p - \boldsymbol{c}_q + a_p\boldsymbol{i}_r(\varphi) - a_q\boldsymbol{i}_r(\varphi')|, \quad \nu = 0. \tag{2.71}$$

Then, with reference to Figure 2.5,

$$H_0^{(2)}(k_1|\boldsymbol{c}_p - \boldsymbol{c}_q + a_p\boldsymbol{i}_r(\varphi) - a_q\boldsymbol{i}_r(\varphi')|) = \sum_{s=-\infty}^{\infty} J_s(k_1 a_q) H_s^{(2)}(k_1|\boldsymbol{c}_p - \boldsymbol{c}_q + a_p\boldsymbol{i}_r(\varphi)|) e^{-js(\tilde{\varphi}-\varphi')}. \tag{2.72}$$

To calculate the integral with respect to φ, we apply once again Graf's addition theorem. In (B.1) in Appendix B we set

$$r_B = k_1 a_p, \qquad r_A = k_1|\boldsymbol{c}_p - \boldsymbol{c}_q|, \qquad r_{BA} = k_1|\boldsymbol{c}_p - \boldsymbol{c}_q + a_p\boldsymbol{i}_r(\varphi)|, \qquad \nu = s. \tag{2.73}$$

It follows, with reference to Figure 2.3 that

$$H_s^{(2)}(k_1|\boldsymbol{c}_p - \boldsymbol{c}_q + a_p\boldsymbol{i}_r(\varphi)|) = e^{js(\tilde{\varphi}-\pi-\varphi_{pq})} \sum_{t=-\infty}^{\infty} J_t(k_1a_p)H_{t+s}^{(2)}(k_1|\boldsymbol{c}_p - \boldsymbol{c}_q|)e^{-jt(\varphi_{pq}-\varphi)}. \tag{2.74}$$

We note that the angles $\tilde{\varphi}$ in Figure 2.5 and in Figure 2.3 are the same. They are the angular position of a point on L_p expressed in the coordinate system of L_q. Substituting (2.74) in (2.72) and (2.72) in (2.70), we arrive at

$$\langle \boldsymbol{w}_{p,m}, \mathcal{Z}\boldsymbol{w}_{q,n}\rangle = \frac{k_1\zeta_1 a_q}{4} \sum_{s=-\infty}^{\infty}\sum_{t=-\infty}^{\infty} J_s(k_1a_q)J_t(k_1a_p)H_{s+t}^{(2)}(k_1|\boldsymbol{c}_p - \boldsymbol{c}_q|) \times e^{-js\pi}e^{-j\varphi_{pq}(s+t)}\mathcal{F}_t\{w_m^*\}\mathcal{F}_s\{w_n\}, \tag{2.75}$$

where

$$\mathcal{F}_s\{w\} = \int_{-\pi}^{\pi} w(\varphi)e^{js\varphi}\,d\varphi. \tag{2.76}$$

We introduce the basis functions

$$w_n(\varphi) = \frac{1}{2\pi}e^{-jn\varphi}, \qquad n = -N, \ldots, N. \tag{2.77}$$

Then,

$$\mathcal{F}_s\{w_n\} = \begin{cases} 1, & n-s=0 \\ 0, & n-s\neq 0 \end{cases} \tag{2.78}$$

Based on this result, $J_{-m} = (-1)^m J_m$ and $w_m^* = w_{-m}$, (2.75) turns into

$$\langle \boldsymbol{w}_{p,m}, \mathcal{Z}\boldsymbol{w}_{q,n}\rangle = \frac{k_1\zeta_1 a_q}{4} J_n(k_1a_q)J_m(k_1a_p)H_{n-m}^{(2)}(k_1|\boldsymbol{c}_p - \boldsymbol{c}_q|)(-1)^{n+m}e^{-j\varphi_{pq}(n-m)}. \tag{2.79}$$

Note that $(-1)^{n+m}e^{-j\varphi_{pq}(n-m)} = e^{-j(\varphi_{pq}+\pi)(n-m)}$. While φ_{pq} is the angle between $\boldsymbol{c}_q - \boldsymbol{c}_p$ and $\boldsymbol{i}_x$, $\varphi_{pq}+\pi$ is the angle between $\boldsymbol{c}_p - \boldsymbol{c}_q$ and $\boldsymbol{i}_x$. Up to now we have assumed that $p \neq q$. In case $p = q$, (2.70) turns into

$$\langle \boldsymbol{w}_{q,m}, \mathcal{Z}\boldsymbol{w}_{q,n}\rangle = \frac{k_1\zeta_1 a_q}{4} \int_{-\pi}^{\pi} w_m^*(\varphi) \int_{-\pi}^{\pi} H_0^{(2)}(k_1a_q|\boldsymbol{i}_r(\varphi) - \boldsymbol{i}_r(\varphi')|)w_n(\varphi')\,d\varphi'\,d\varphi. \tag{2.80}$$

Substituting (2.72) with $p = q$ and $\tilde{\varphi} = \varphi$ in (2.80) we obtain

$$\langle \boldsymbol{w}_{q,m}, \mathcal{Z}\boldsymbol{w}_{q,n}\rangle = \frac{k_1\zeta_1 a_q}{4} \sum_{s=-\infty}^{\infty} J_s(k_1a_q)H_s^{(2)}(k_1a_q)\mathcal{F}_{-s}\{w_m^*\}\mathcal{F}_s\{w_n\}. \tag{2.81}$$

With the choice of basis functions of (2.77) this expression turns into

$$\langle \boldsymbol{w}_{q,m}, \mathcal{Z}\boldsymbol{w}_{q,n}\rangle = \begin{cases} \frac{k_1\zeta_1 a_q}{4} J_n(k_1a_q)H_n^{(2)}(k_1a_q), & m=n \\ 0, & m\neq n \end{cases} \tag{2.82}$$

The entire moment matrix is established by (2.79) and (2.82). For the right-hand side we consider as specific excitation field $\boldsymbol{E}^{\text{exc}} = E_y^{\text{exc}} \boldsymbol{i}_y$ a plane wave, defined by

$$E_y^{\text{exc}}(\boldsymbol{x}) = e^{-j\boldsymbol{k}^{\text{inc}}\cdot\boldsymbol{x}}, \qquad \frac{\boldsymbol{k}^{\text{inc}}}{k_1} = -\cos\varphi_{\text{inc}}\,\boldsymbol{i}_z - \sin\varphi_{\text{inc}}\,\boldsymbol{i}_x, \tag{2.83}$$

where φ_{inc} is the angle of incidence with respect to the positive z-axis. Subsequently

$$\begin{aligned} v_p^{\text{exc}}(\varphi) &= -\left. E_y^{\text{exc}} \right|_{L_p}(\varphi) \\ &= -e^{jk_1(c_{p,z}\cos\varphi_{\text{inc}} + c_{p,x}\sin\varphi_{\text{inc}})} e^{jk_1 a_p \cos(\varphi-\varphi_{\text{inc}})}, \end{aligned} \tag{2.84}$$

and

$$\begin{aligned} \langle \boldsymbol{w}_{p,m}, \boldsymbol{v}^{\text{exc}} \rangle &= -\frac{1}{2\pi} e^{jk_1(c_{p,z}\cos\varphi_{\text{inc}} + c_{p,x}\sin\varphi_{\text{inc}})} \int_{-\pi}^{\pi} e^{jm\varphi} e^{jk_1 a_p \cos(\varphi-\varphi_{\text{inc}})} d\varphi \\ &= -j^m J_m(k_1 a_p) e^{jk_1(c_{p,z}\cos\varphi_{\text{inc}} + c_{p,x}\sin\varphi_{\text{inc}})}. \end{aligned} \tag{2.85}$$

2.6 Linear Periodic Arrays

We consider a linear array of identical unit cells. We number the cells

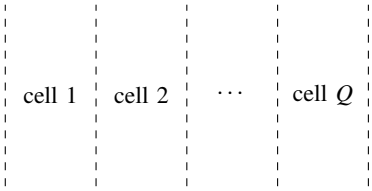

from 1 to Q. The matrix C_{pq} describes the mutual coupling of the objects in cell q to the objects in cell p. Since the cells are equally spaced, the mutual coupling depends only on the differences between the cells $q - p$ and we can write $C_{pq} = C_{q-p}$. The matrices C_{1-m} describe the coupling from cell 1 to cell m and the matrices C_{m-1} describe the coupling from cell m on cell 1. The moment-matrix equation is then

$$\begin{pmatrix} C_0 & C_1 & \cdots & \cdots & C_{N-1} \\ C_{-1} & C_0 & \ddots & & \vdots \\ \vdots & C_{-1} & \ddots & \ddots & \vdots \\ \vdots & & \ddots & \ddots & C_1 \\ C_{-N+1} & \cdots & \cdots & C_{-1} & C_0 \end{pmatrix} \begin{pmatrix} A_1 \\ \vdots \\ \vdots \\ \vdots \\ A_N \end{pmatrix} = \begin{pmatrix} -B_1^{\text{exc}} \\ \vdots \\ \vdots \\ \vdots \\ -B_Q^{\text{exc}} \end{pmatrix}. \tag{2.86}$$

We consider an array of unit cells, with elements numbered from $-Q$ to Q. Multiplying row p ($p = -Q, \ldots, Q$) of the moment matrix and the expansion vector $\boldsymbol{A}$ yields

$$\sum_{q=-N}^{N} C_{pq} A_q = \sum_{q=-N}^{N} C_{q-p} A_q = -B_p^{\text{exc}}. \tag{2.87}$$

We assume a linear phase progression $B_p^{\text{exc}} = B_0^{\text{exc}} e^{-jp\psi}$ over the unit cells, so that

$$\sum_{q=-Q}^{Q} C_{q-p} A_q = -B_0^{\text{exc}} e^{-jp\psi}. \tag{2.88}$$

If we assume an infinite array and let $Q \to \infty$, then

$$\sum_{q=-\infty}^{\infty} C_{q-p} A_q = -B_0^{\text{exc}} e^{-jp\psi}. \tag{2.89}$$

Substitution of $q' = q - p$ gives

$$\sum_{q'=-\infty}^{\infty} C_{q'} A_{p+q'} = -B_0^{\text{exc}} e^{-jp\psi}. \tag{2.90}$$

If the expansion vector $\boldsymbol{A}$ has the same phase progression as the right-hand side, i.e. $A_p = A_0 e^{-jp\psi}$, this equation turns into

$$\sum_{q'=-\infty}^{\infty} C_{q'} e^{-jq'\psi} A_0 e^{-jp\psi} = -B_0^{\text{exc}} e^{-jp\psi}. \tag{2.91}$$

This reduces to

$$C(\psi) A_0 = -B_0^{\text{exc}}, \tag{2.92}$$

with

$$C(\psi) = \sum_{q=-\infty}^{\infty} C_q e^{-jq\psi}. \tag{2.93}$$

This equation is independent of the row index p. The matrix $C(\psi)$ exists if the infinite system converges per matrix component and the (homogeneous) solutions to (2.92) A_0 correspond to (homogeneous) solutions $A_p = A_0 e^{-j\psi}$ of the infinite matrix equation

$$\begin{pmatrix} \ddots & \ddots & & & \\ \ddots & C_0 & C_1 & & \\ & C_{-1} & C_0 & C_1 & \\ & & C_{-1} & C_0 & \ddots \\ & & & \ddots & \ddots \end{pmatrix} \begin{pmatrix} \vdots \\ A_{-1} \\ A_0 \\ A_1 \\ \vdots \end{pmatrix} = \begin{pmatrix} \vdots \\ -B_0^{\text{exc}} e^{j\psi} \\ -B_0^{\text{exc}} \\ -B_0^{\text{exc}} e^{-j\psi} \\ \vdots \end{pmatrix}. \tag{2.94}$$

2.6.1 Series Convergence and Acceleration

Each component of the infinite-array moment matrix $C(\psi)$ is the infinite sum of the coupling terms of a linear array of posts to a post in the zeroth cell. Thus, for the modal formulation each component assumes the form

$$(q = 0 \text{ term}) + \sum_{\substack{q=-\infty \\ q \neq 0}}^{\infty} H_{m-n}^{(2)}(k_1 r_q) e^{-j(m-n)\varphi_q} e^{-jq\psi}, \tag{2.95}$$

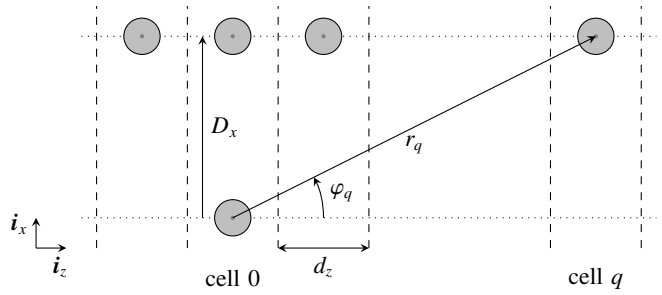

Figure 2.6 — Schematic view of the coupling of a linear array to a post in the zeroth cell. We note that D_x is the difference between the x-coordinates of the posts in the linear array and that of the posts in the zeroth cell: D_x can be negative!

where

$$r_q(D_x) = \sqrt{q^2 d_z^2 + D_x^2}, \qquad \varphi_q(D_x) = \arctan\left(\frac{D_x}{q d_z}\right) \tag{2.96}$$

and D_x is the difference between the x-coordinates of the posts in the linear array and that of the posts in the zeroth cell, as depicted in Figure 2.6. We introduce the series

$$S(n, \psi, D_x) = \sum_{q=1}^{\infty} H_{m-n}^{(2)}(k_1 r_q(D_x)) e^{-jn\varphi_q(D_x)} e^{-jq\psi}. \tag{2.97}$$

Now, (2.95) can be written as

$$(q = 0 \text{ term}) + S(n, \psi, D_x) + S(n, -\psi, -D_x), \tag{2.98}$$

where we use $\varphi_{-q}(D_x) = \varphi_q(-D_x)$. In our study of the matrix components of $C(\psi)$ we therefore focus on the series S.

For propagation in a PWWG, the parameter ψ equals $k_z d_z$, where k_z is the propagation constant of the mode under consideration and d_z is the spacing of the unit cells. If we assume both the PWWG and the dielectric in medium 1 to be lossless, k_1 and ψ are real-valued. In that case the convergence of S is extremely slow since the value of the Hankel function is proportional to $1/\sqrt{q}$ for $q \to \infty$. To accelerate the convergence we apply the concept of accelerating sequences. We replace the sequence $\{S_q\}_{Q=1}^{\infty}$ of partial sums (S_Q is defined by (2.97) with ∞ replaced by Q) by a sequence $\{S_Q^{\text{acc}}\}_{Q=Q_0}^{\infty}$ that exhibits the same limit S and converges faster in the sense that $(S_Q^{\text{acc}} - S)/(S_Q - S) \to 0, Q \to 0$. We construct the accelerating sequence using Aitken's delta-squared process,

$$S_Q^{\text{acc}} = S_Q - \frac{(S_Q - S_{Q-1})^2}{S_Q - 2S_{Q-1} + S_{Q-2}}, \qquad Q \geq 3. \tag{2.99}$$

This expression can also be written as

$$S_Q^{\text{acc}} = S_Q - \frac{\Delta_Q}{1 - \Delta_Q}(S_{Q-1} - S_Q), \qquad \Delta_Q = \frac{S_Q - S_{Q-1}}{S_{Q-1} - S_{Q-2}}. \tag{2.100}$$

In the literature, proofs demonstrating that $\{S_Q^{\text{acc}}\}_{Q=3}^{\infty}$ converges to S and that it converges faster than $\{S_Q\}_{Q=1}^{\infty}$, generally rely on the assumption that the limit of $(S_Q - S)/(S_{Q-1} - S)$ is not one for $Q \to \infty$. In our specific case, this can be shown as follows. For Δ_Q we have

$$\Delta_Q = \frac{H_n^{(2)}(k_1 r_Q(D_x))}{H_n^{(2)}(k_1 r_{Q-1}(D_x))} e^{-jn(\varphi_Q(D_x)-\varphi_{Q-1}(D_x))} e^{-j\psi}. \tag{2.101}$$

Since $\varphi_Q(D_x) \to \pm\pi/2, Q \to \infty$, the first exponential in this expression tends to 1 as $Q \to \infty$. The asymptotic expansion of the Hankel function in (2.101) is given by

$$H_n^{(2)}(k_1 r_Q(D_x)) = \sqrt{\frac{2}{\pi k_1}} \frac{1}{\sqrt{Q}} \frac{1}{\left(1 + \frac{D_x^2}{Q^2 d_z^2}\right)^{1/4}} \exp\left\{-j\left(k_1 Q d_z \sqrt{1 + \frac{D_x^2}{Q^2 d_z^2}} - \frac{1}{2}n\pi - \frac{1}{4}\pi\right)\right\} \times \left(1 + O\left(\frac{1}{Q}\right)\right), \quad Q \to \infty. \tag{2.102}$$

It follows that the fraction in (2.101) tends to $\exp(-jk_1 d_z)$ as $Q \to \infty$. Hence,

$$\Delta_Q \to e^{-j(k_1 d_z + \psi)}. \tag{2.103}$$

Thus S_Q^{acc} converges to S provided that $\psi \neq -k_1 d_z + 2m\pi$. For $\psi = -k_1 d_z + 2m\pi$ the series S does not converge so that we cannot calculate the series.

In case the dielectric is lossy, $k_1 = k_0\sqrt{\varepsilon_{r,1}(1 - j\tan\delta_1)}$, where the complex square root is defined by

$$\sqrt{1 - j\tan\delta_1} = |1 - j\tan\delta_1|^{1/2} \exp\left(-\frac{1}{2}j\delta_1\right). \tag{2.104}$$

Then, it follows from the asymptotes of the Hankel function (2.102) that the terms in S tend as $\exp(qd_z \text{Im}\, k_1)/\sqrt{q}$ for $q \to \infty$ and since $\text{Im}\, k_1 < 0$, S converges faster than in the lossless case.

In case we wish to consider the PWWG as lossy with a complex propagation constant k_z, we need to be careful with the series. In that case, the terms in S tend as $\exp(q(d_z \text{Im}\, k_1 + \text{Im}\, \psi))/\sqrt{q}$ for $q \to \infty$. Thus for $\text{Im}\, \psi > -d_z \text{Im}\, k_1$ the terms in the series grow exponentially and consequently the series is divergent. This observation implies that the components of the infinite-array matrix $C(\psi)$ given by (2.95) and (2.98) are defined, provided that

$$|\text{Im}\, \psi| \leq -d_z \text{Im}\, k_1 = d_z k_0 \sqrt{\varepsilon_{r,1}} \sqrt{1 + \tan^2\delta_1} \sin\left(\frac{1}{2}\delta_1\right). \tag{2.105}$$

The considerations (2.101)–(2.103) for the accelerating sequence are also valid for k_1 and ψ complex, provided that S converges, or (2.105) is satisfied. We note that in case S is calculated with ψ replaced by $-\psi$ as in the third term of (2.98) the condition $\psi \neq -k_1 d_z + 2m\pi$ is replaced by $\psi \neq k_1 d_z + 2m\pi$ to have $S_Q^{\text{acc}} \to S$ for $Q \to \infty$.

2.7 Field Calculation

To calculate the scattered field of an arbitrary collection of posts we need to calculate the scattered fields $\boldsymbol{E}_q^{\text{sct}}$ of each post q at position $\boldsymbol{x}_t$. For a fixed q we can write $\boldsymbol{x}_t = \boldsymbol{c}_q + r\boldsymbol{i}_r(\varphi)$,

where

$$r_q = |\boldsymbol{x} - \boldsymbol{c}_q|, \qquad \varphi_q = \begin{cases} \arccos \frac{(\boldsymbol{x}_t - \boldsymbol{c}_q)\bullet \boldsymbol{i}_z}{|\boldsymbol{x}_t - \boldsymbol{c}_q|}, & (\boldsymbol{x}_t - \boldsymbol{c}_q)\bullet \boldsymbol{i}_x \geq 0, \\ 2\pi - \arccos \frac{(\boldsymbol{x}_t - \boldsymbol{c}_q)\bullet \boldsymbol{i}_z}{|\boldsymbol{x}_t - \boldsymbol{c}_q|}, & (\boldsymbol{x}_t - \boldsymbol{c}_q)\bullet \boldsymbol{i}_x \leq 0. \end{cases} \tag{2.106}$$

We calculate the fields $\boldsymbol{E}_q^{\mathrm{sct}}$ both for the modal formulation and for the integral equation formulation for arrays of metallic posts.

2.7.1 Integral Equation Formulation for Arrays of Metallic Posts

The y-component of $\boldsymbol{E}_q^{\mathrm{sct}}$ is given by (2.65). Let the current $J_{q,y}^{\mathrm{surf}}$ be described by

$$J_{q,y}^{\mathrm{surf}} = \sum_{n=-N}^{N} A_{q,n} w_n, \tag{2.107}$$

where the coefficients $A_{q,n}$ are computed from the moment-matrix system. Substituting this expression and $\boldsymbol{x}_t = \boldsymbol{c}_q + r_q \boldsymbol{i}_r(\varphi_q)$ in (2.65) we obtain

$$E_{q,y}^{\mathrm{sct}}(\boldsymbol{x}_t) = \frac{k_1 \zeta_1 a_q}{4} \sum_{n=-N}^{N} A_{q,n} \int_{-\pi}^{\pi} H_0^{(2)}(k_1 |r_q \boldsymbol{i}_r - a_q \boldsymbol{i}_r(\varphi')|) w_n(\varphi')\, d\varphi'. \tag{2.108}$$

From (2.72) with $\boldsymbol{c}_p = \boldsymbol{c}_q$, $a_p = r_q$ and $\tilde{\varphi} = \varphi_q$, we obtain

$$E_{q,y}^{\mathrm{sct}}(\boldsymbol{x}_t) = \frac{k_1 \zeta_1 a_q}{4} \sum_{n=-N}^{N} A_{q,n} \sum_{s=-\infty}^{\infty} J_s(k_1 a_q) H_s^{(2)}(k_1 r_q) e^{-js\varphi_q} \mathcal{F}_s\{w_n\}. \tag{2.109}$$

For the specific basis-function choice (2.77) we arrive at

$$E_{q,y}^{\mathrm{sct}}(\boldsymbol{x}) = \frac{k_1 \zeta_1 a_q}{4} \sum_{n=-N}^{N} A_{q,n} J_n(k_1 a_q) H_n^{(2)}(k_1 r_q) e^{-jn\varphi_q}. \tag{2.110}$$

2.7.2 Modal Formulation

The y-component of $\boldsymbol{E}_q^{\mathrm{sct}}$ is given by (2.20b) with A_n replaced by $A_{q,n}$ and ∞ replaced by N. The coefficients $A_{q,n}$ are computed from the matrix system (2.30) with N the truncation index of these blocks. Hence,

$$E_{q,y}^{\mathrm{sct}}(\boldsymbol{x}_t) = \sum_{n=-N}^{N} A_{q,n} H_n^{(2)}(k_1 r_q) e^{jn\varphi_q}. \tag{2.111}$$

For a linear periodic array, as described in Section 2.6, the field computation needs some modification. Firstly we note that only the field in the zeroth cell needs to be computed. The fields in the other cells follow by multiplication of this field with $e^{-jq\psi}$ where $q \in \mathbb{Z}$ is the cell index (see also Section 2.6). The linear periodic PWWG array is composed of several rows of posts.

Therefore, the total electric field at a position $\boldsymbol{x}_t$ is the sum of the electric fields at $\boldsymbol{x}_t$ generated by these rows of posts. For one such row, the field at $\boldsymbol{x}_t$ is of the form

$$\sum_{n=-N}^{N} A_n \sum_{q=-\infty}^{\infty} H_n^{(2)}(k_1 r_q) e^{jn\varphi_q} e^{-jq\psi}, \tag{2.112}$$

where A_n are the field expansion coefficients of the post in the zeroth cell and r_q and φ_q are defined by (2.106) with $\boldsymbol{c}_0$ the center of the post in the zeroth cell and $\boldsymbol{c}_q = \boldsymbol{c}_0 + qd_z\boldsymbol{i}_z$, $q \in \mathbb{Z}$. The series with summation index q is of the same form as the series (2.95). As a result, we can apply Aitken's delta-squared process to the sum from $q = 1$ to ∞ and to the sum from $q = -\infty$ to -1.

Chapter 3

Post-Wall Waveguide Characteristics

This chapter focuses on characteristics of PWWGs with respect to wave-propagation. Section 3.1 discusses the propagation constant of transmission lines and of PWWGs in particular. The propagation constant of uniform PWWGs is determined by applying an optimization procedure to the periodic-array model described in Section 2.6. The advantages and disadvantages of this approach are discussed. The equivalence of rectangular waveguides and PWWGs is addressed in Section 3.2. Since this equivalence is often discussed in the literature, we compare the results of several models. PWWG loss mechanisms are discussed in Section 3.3 and approximate expressions for the loss terms are derived. With respect to Section 3.1 and 3.3 we conclude that the periodic-array model described in Section 2.6 together with the optimization procedure is suitable for determining the phase constant of PWWGs, but not for determining the attenuation constant or loss. Section 3.4 relates the electromagnetic modeling of Chapter 2 to the excitation at specified ports, facilitating the determination of losses and scattering parameters of PWWGs. A current matrix is constructed that describes the output electric and magnetic currents at the ports in terms of prescribed input electric and magnetic currents. In Section 3.5 the scattering parameters of PWWGs are derived from their current matrices. The current-matrix concept is a powerful tool for characterizing the behavior of PWWG components and calculating the scattering parameters paves the way to determining the losses of uniform PWWGs when using a multi-line calibration method as described in the next chapter.

3.1 Propagation Constant and Dispersion

In Section 2.6 we modeled uniform PWWG transmission lines of infinite length. We consider these waveguides to be composed of a cascade of identical unit cells along the z-axis. Let us assume that such a structure supports a uniform wave propagating in the positive z-direction and with a voltage distribution

$$V(z) = V_0^+ e^{-jk_z z}, \tag{3.1}$$

where k_z is the wavenumber. Under the condition of linear phase progression, the voltage along the guide can be expressed as a function of the voltage in a single unit cell at $z = 0$ as

$$V(z) = V_0^+ e^{-jk_z(z+qd_z)}, \qquad 0 \le z < d_z \tag{3.2}$$

with q the number of unit cells from the origin. Rewriting expression (3.2)

$$V(z) = V_0^+ e^{-jk_z z} e^{-jq\psi}, \qquad 0 \leq z < d_z \tag{3.3}$$

where the first exponential term accounts for the voltage in the unit cell and the second exponential term dictates the phase progression between the unit cells with $\psi = k_z d_z$. The propagation constant k_z is a complex quantity, defined by

$$k_z = \beta_z - j\alpha_z. \tag{3.4}$$

Here, the real part β_z is the *phase constant* of the wave. Modes for which the phase constant is a function of frequency, are called dispersive; the dispersion is expressed by the relation between the phase constant and the frequency. The (negative) imaginary part α_z is the *attenuation constant*, which describes the decrease of the wave's voltage along the direction of propagation. It is therefore a measure of loss.

To determine the propagation constant of uniform PWWG transmission lines, we consider in this section the matrix $C(\psi)$ defined by (2.93), where $\psi = k_z d_z$ with k_z the propagation constant of the mode of interest. Alternative approaches to determine this constant are discussed in the other sections of this chapter. The eigenvectors $\boldsymbol{x}_n$ and corresponding eigenvalues λ_n of C are the nontrivial solutions of the equation

$$C(k_z d_z)\boldsymbol{x}_n = \lambda_n \boldsymbol{x}_n. \tag{3.5}$$

The eigenvalues are solutions of the characteristic equation

$$\det(C - \lambda I) = 0. \tag{3.6}$$

In case an eigenvalue λ_n is zero, the corresponding eigenvector $\boldsymbol{x}_n$ is a source-free solution, i.e., $C\boldsymbol{x}_n = 0$. The corresponding expansion of the scattered fields in the unit cell represents a characteristic mode of the PWWG with propagation constant k_z. Hence, the determination of the propagation constant of a PWWG is equivalent to finding the values ψ, for which $C(\psi)$ exhibits a zero-valued eigenvalue. In order to determine these values, a minimization problem in the complex variable ψ and a real-valued objective function $f(\psi)$, depending on the eigenvalues of $C(\psi)$ is solved.

If the determinant of C vanishes, at least one of its eigenvalues is zero. Thus $f(\psi)$ can be defined by

$$f(\psi) = |\det C(\psi)|. \tag{3.7}$$

A disadvantage of this objective function, is that if none of the eigenvalues is zero, the determinant is in general large with respect to the smallest eigenvalue. This is of particular concern if the number of cylinders and expansion terms in the unit cell becomes large, i.e. in case the number of eigenvalues of the matrix is large, because the determinant is the product of the eigenvalues. To decrease the extreme contrast of the objective function in (3.7) we introduce the alternative definition

$$f(\psi) = \min_n |\lambda_n|, \tag{3.8}$$

which selects the smallest absolute eigenvalue as its function value. Figure 3.1 shows this objective function as a function of $\psi/k_0 d_z$, where the imaginary part of ψ is bounded by (2.105)

in order to have a convergent infinite-array series. Considering Figure 3.1(a) and the table of Figure 3.1(d) for 10 GHz, we observe one pair of zeros. These zeros represent the propagation of the TE_{10} mode. At 15 GHz the second pair of zeros corresponds to the TE_{20} mode, that is also above its cut-off frequency. For increasing frequency, all zeros follow a trajectory that is first parallel to the imaginary axis and then bends parallel to the real axis in the direction of $\psi/k_0 d_z \approx \pm\sqrt{\varepsilon_{r,1}}(1 - j(\tan\delta_1)/2) = \pm(+1.88 - 0.09\,j)$. We note that the zeros of propagating modes, $|\mathrm{Re}\,\psi| \gg |\mathrm{Im}\,\psi|$, especially in low-loss dielectric materials. Therefore, the objective function will have local minima for real argument ψ in case ψ is close to the real part of the zero location. In Figure 3.2(a) and 3.2(b) $\ln(f(\psi))$ is plotted as a function of the real argument ψ and the frequency with $f(\psi)$ defined in (3.7) and (3.8), respectively. The plots demonstrate that the zeros of the objective function move from $\mathrm{Re}\,\psi = 0$ at the cut-off frequency of each mode to $\mathrm{Re}\,\psi = \sqrt{\varepsilon_{r,1}}$ for increasing frequency. For fixed frequencies Figure 3.3 shows $\ln(f(\psi))$ as a function of the real argument ψ. The (near) zeros of $\ln(f(\psi))$ are clearly distinguishable.

In order to find the zeros of the objective function $f(\psi)$ automatically, we need to choose an optimization algorithm. To a limited extent the behavior of the objective function is predictable, since the zeros of the propagating modes are located in a partially bounded region close to the real axis. We can, therefore, identify the number of optima and get a rough estimation of their locations. These estimates are useful as initial states for local deterministic optimization algorithms that determine the multiple optima or the global optimum of the objective function, see e.g. [65, Ch. 10] for an overview. We limit ourselves to such algorithms. By deterministic we mean that for a given initial value these algorithms always yield the same result as opposed to stochastic optimization algorithms, see e.g. [66] for an overview. In our case the optimization method must be able to find an optimum in the complex plane and is thus a multiple variable optimization. Since the numerical computation of the derivative of the objective function is not straightforward, we prefer optimization algorithms that use only the objective function itself, i.e., direct search techniques. Moreover, since we will encounter multiple optima, we prefer hybrid algorithms, where a first optimization step determines roughly the location of the optima and a second optimization step determines their exact locations. In the first step we only search for the minima of the objective function for real values of ψ by means of the bracketing method. This method tries to enclose all the minima in the interval $0 \le \psi \le \sqrt{\varepsilon_{r,1}}$. The bracketing algorithm distinguishes the multiple propagating modes and thus simplifies the task of the second step, since it provides starting points that are close to the optima in the complex plane. For the second step we choose the Nelder-Mead or downhill simplex method. This method is a simple direct search method, which does not use derivative information. It optimizes a single objective function for N real variables. The algorithm is fairly sensitive to the choice of the initial state, but is robust in convergence towards an optimum.

Discussing the example we noted that the imaginary part of ψ is bounded by (2.105) in order to have a convergent infinite-array series. Consequently, the attenuation constant α_z, determined by our optimization procedure will never be larger than this bound. Since the bound is dictated by the dielectric loss, we will never determine losses larger than the dielectric losses, even in case large leakage losses occur. In fact, we will in general find losses equal to the dielectric losses. Despite this deficiency of the periodic-array model presented in Section 2.6, the described optimization procedure in combination with Aitken's delta-squared process applied to the infinite-array series provides reasonable and fast approximations of the phase constant β_z. We note that since the minimum of the objective function is in general found for α_z equal to

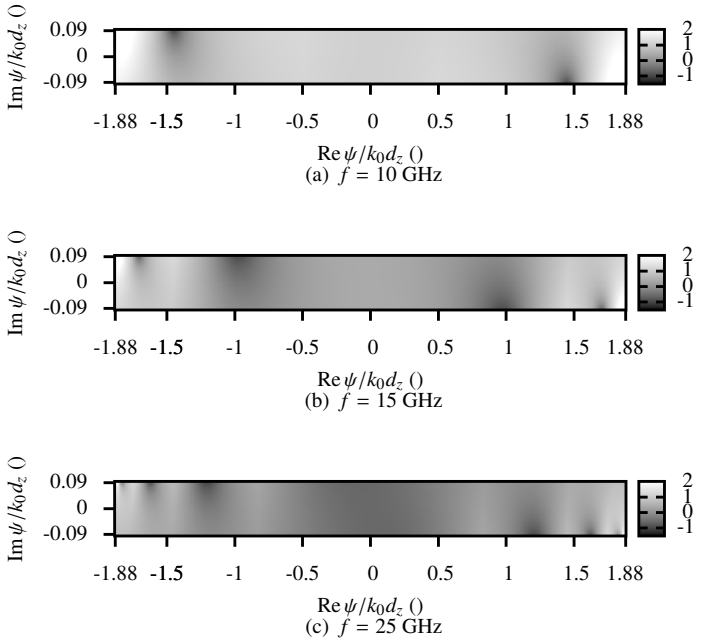

Frequency (GHz)	Mode	$\psi/k_0 d_z$ ()	
10.0	TE_{10}	$-1.45+0.09j$	$1.45-0.09j$
15.0	TE_{10}	$-1.71+0.09j$	$1.71-0.09j$
	TE_{20}	$-1.45+0.09j$	$1.45-0.09j$
25.0	TE_{10}	$-1.83+0.09j$	$1.83-0.09j$
	TE_{20}	$-1.62+0.09j$	$1.62-0.09j$
	TE_{30}	$-1.21+0.09j$	$1.21-0.09j$

(d) Minima locations

Figure 3.1 — Plots of the natural logarithm of the objective function (3.8) in the complex plane at f = 10 GHz, f = 15 GHz and f = 25 GHz. Medium parameters: $\varepsilon_{r,1}$ = 3.55 and $\tan\delta$ = 0.1. Geometry parameters: two posts per unit cell, a = 0.50 mm, w_g = 12.63 mm, one constant expansion function per post, d_z = 2.00 mm, and 101 unit cells in the summation (Aitken's delta-squared process with Q = 50, see Section 2.6.1).

the bound (2.105), one could also consider a single optimization parameter, i.e., β_z. In case the dielectric loss is small, one can even set α_z equal to zero to obtain a reasonable approximation of β_z. For a single optimization parameter we select the Golden Section Search, since it does not require any derivatives.

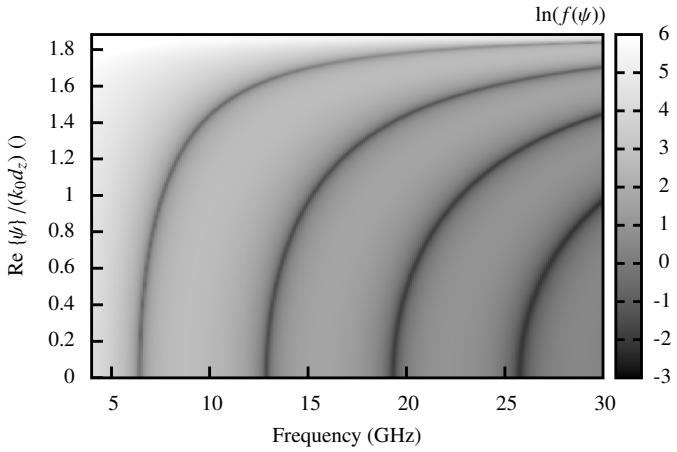

(a) Determinant

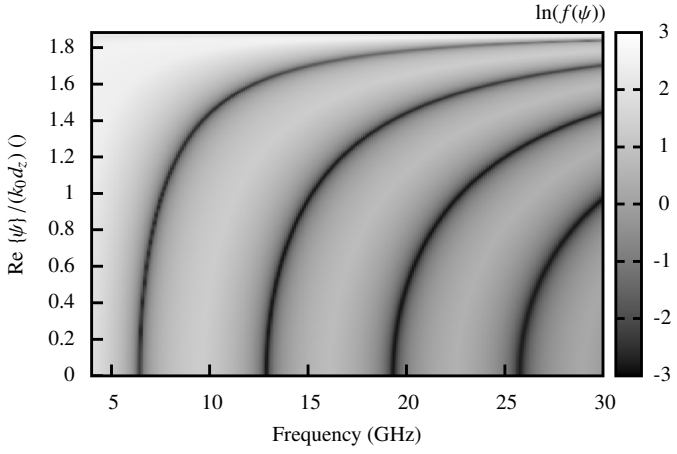

(b) Smallest eigenvalue

Figure 3.2 — Landscape plot of the natural logarithm $\ln(f(\psi))$ as a function of the *normalized* real propagation constant and the frequency. (a) f in (3.7) and (b) f in (3.8). Medium parameters: $\varepsilon_{r,1} = 3.55$, $\tan\delta = 0.0027$. Geometry parameters: two posts per unit cell, $a = 0.50$ mm, $w_g = 12.63$ mm, one constant expansion coefficient per post, $d_z = 2.00$ mm and 101 unit cells in the summation (Aitken's delta-squared process with $Q = 50$, see Section 2.6.1).

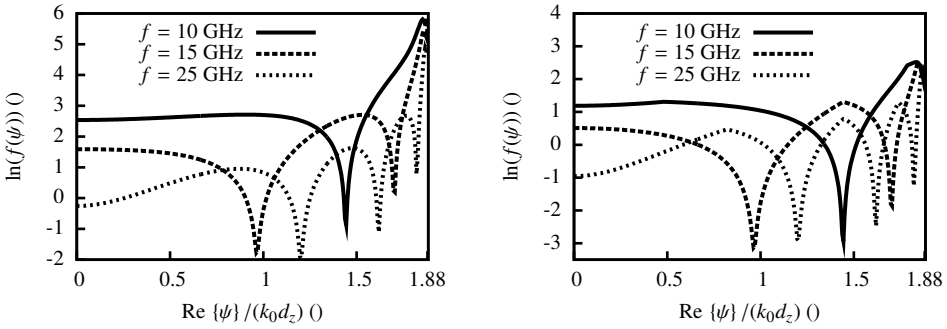

(a) Determinant

(b) Smallest eigenvalue

Figure 3.3 — The natural logarithm $\ln(f(\psi))$ as a function of $\operatorname{Re}\psi$ at different frequencies. Figure 3.3(a): f in (3.7). Figure 3.3(a): f in (3.8). Medium parameters: $\varepsilon_{r,1} = 3.55$, $\tan\delta = 0.0027$. Geometry parameters: two posts per unit cell, $a = 0.50$ mm, $w_g = 12.63$ mm, one constant expansion coefficient per post, $d_z = 2.00$ mm and 101 unit cells in the summation (Aitken's delta-squared process with $Q = 50$, see Section 2.6.1).

3.2 Effective Width

The effective width of a PWWG has been introduced by Hirokawa and Ando in [17]. It is defined as the width of a rectangular waveguide with perfectly conducting walls, which has the same dielectric filling and the same (real part of the) propagation constant as the PWWG. This definition implies that the dispersion of the TE_{10} mode in a PWWG is equal to the dispersion of the TE_{10} mode in a rectangular waveguide. A graphical representation of the definition in Figure 3.4 shows the top view of two sections of waveguide: on the left a rectangular waveguide and on the right a PWWG. A propagating mode can be thought of as a wave reflecting at the side walls. For the rectangular waveguide the planes of reflection are the waveguide walls. If the post-walls are highly reflective, their planes of reflection can be thought of as two effective planes that coincide with the rectangular waveguide walls. We note that the concept of effective width is not necessarily limited to the characterization of PWWGs: in [67] the effective width is used to improve the measurement accuracy for imperfectly rectangular waveguides.

We can calculate the effective width of a PWWG from the propagation constant k_z of the dominant mode. To this end, we equate the (real part of the) propagation constant and the dispersion of the TE_{10} waveguide mode,

$$\operatorname{Re} k_z = \sqrt{\varepsilon_{r,1} k_0^2 - \left(\frac{\pi}{w_{g,\mathrm{eff}}}\right)^2}, \tag{3.9}$$

of a rectangular waveguide with width $w_{g,\mathrm{eff}}$ and dielectric constant $\varepsilon_{r,1}$. Consequently, the effective width is given by

$$w_{g,\mathrm{eff}} = \frac{\pi}{\sqrt{\varepsilon_{r,1} k_0^2 - \operatorname{Re} k_z{}^2}}. \tag{3.10}$$

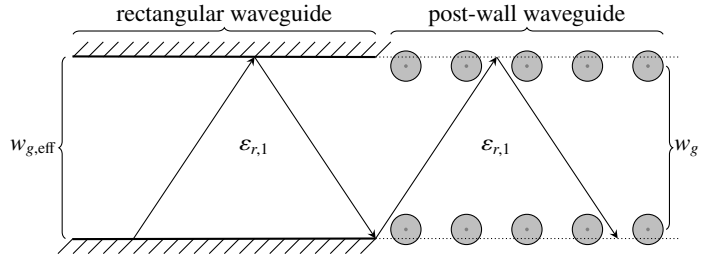

Figure 3.4 — Illustration of the characteristic *equivalent width* of a PWWG. The width of the rectangular waveguide on the left is such that its walls and the virtual reflection planes of the PWWG (dotted lines) coincide. The diagonal arrowed lines depict the propagating mode that reflects at the side walls.

A fixed effective width corresponds to a fixed position of the effective planes of reflection. Intuitively we expect the reflection at the post-walls to decrease with increasing frequency, since the post spacing relative to the wavelength increases. Consequently, the effective planes of reflection will move outward and hence the effective width will increase. In [68] the authors analyze the frequency dependence of the effective width by simulations and measurements. The results show that, for PWWGs with broad walls, consisting of multiple parallel rows of posts, the effective width varies more with frequency than in the case of single-row side walls. Moreover, for walls with fixed numbers of parallel posts, the frequency dependence is in general more pronounced in PWWGs with less reflective side walls, e.g., with dielectric, very small, or widely spaced posts. For widely spaced posts, a *grating effect* may be discernible in which the fields no longer are confined to the inside of the PWWG resulting in severe leakage. This effect strongly influences the propagation of the modes in the PWWG. It occurs in case $d_z \geq \pi/\mathrm{Re}\, k_z$ for the dominant mode and $d_z = \pi/\mathrm{Re}\, k_z$ is called the grating condition. Since $\mathrm{Re}\, k_z \leq \mathrm{Re}\, k_1$, the grating effect cannot occur in case

$$d_z < \frac{\lambda_1}{2}, \tag{3.11}$$

where λ_1 is the wavelength in the medium under consideration. We note that in antenna parlance the grating effect is identified as the grating lobe. In conclusion, the assumption of a fixed effective width to model wave propagation in PWWGs is not valid in case

- the posts are widely spaced (in particular if $d_z \geq \lambda_1/2$),
- multiple parallel rows of posts are used per side wall,
- the PWWG supports multiple modes or,
- very small or dielectric posts are used.

Since the effective width defines the matching between the dominant modes in PWWGs and rectangular waveguides, the case for which the effective width is constant for variations of the geometry is of particular interest. In [17, Fig. 5] the results of an analysis based on a Floquet

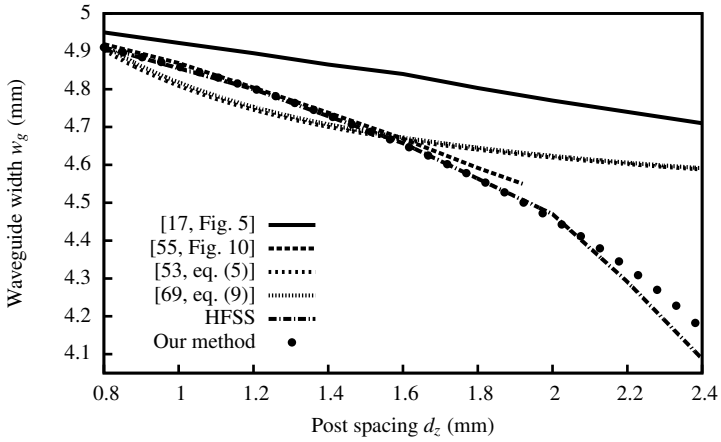

(a) Waveguide width

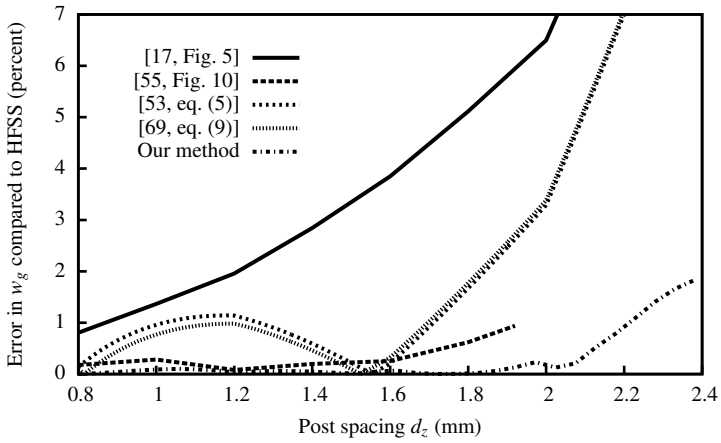

(b) Difference with HFSS

Figure 3.5 — Waveguide width w_g as a function of the post spacing d_z for a constant equivalent width ($w_{g,\text{eff}} = 4.43$ mm). Specifications as in [17]: $f = 40.0$ GHz, $\varepsilon_r = 2.17$ and $a = 0.30$ mm. Top graph: comparison between [17, Fig. 5], [55, Fig. 10], the approximations in [53, eq. (5)] and [69, eq. 9], the results extracted with the multi-line calibration from simulations with Ansoft HFSS, and our own method from Chapter 2 with $N = 101$ terms (Aitken's delta-squared process with $Q = 50$, see Section 2.6.1) and $M = 5$ expansion coefficients. Bottom graph: difference of the methods compared to HFSS.

wave expansion are discussed, where the PWWG width w_g is calculated for different post spacings d_z and a constant effective width $w_{g,\text{eff}}$. The results are plotted in Figure 3.5(a). The same PWWG geometry as used for [17, Fig. 5] (effective width $w_{g,\text{eff}} = 4.43$ mm, dielectric with

$\varepsilon_{r,1} = 2.17$, post radius $a = 0.3$ mm, and frequency 40 GHz) was chosen in [55] for comparison. The results of the surface impedance method, combined with a method-of-moments technique to calculate the surface impedance of the side walls, as presented in [55, Fig. 10] are also plotted in Figure 3.5(a). We present now four other methods to calculate w_g for different post spacings d_z in the PWWG geometry of [17, Fig. 5]. The results of these methods are also plotted in Figure 3.5(a).

The authors of [53] use a boundary integral-resonant mode expansion (BI-RME) method combined with Floquet's theorem to derive the simple approximate expression

$$w_{g,\text{eff}} = w_g - \frac{4a^2}{0.95 d_z}. \tag{3.12}$$

Thus the expression for the waveguide width is

$$w_g = w_{g,\text{eff}} + 4.21 \frac{a^2}{d_z}\,. \tag{3.13}$$

In [69] an extra correction term is added to the expression of (3.12), to obtain the more accurate expression

$$w_{g,\text{eff}} = w_g - 1.08 \frac{4a^2}{d_z} + 0.1 \frac{4a^2}{w_g}. \tag{3.14}$$

Thus the expression for the waveguide width is

$$w_g = \frac{1}{2}\left[w_{g,\text{eff}} + 4.32 \frac{a^2}{d_z} + \sqrt{w_{g,\text{eff}}^2 + 8.64 \frac{a^2}{d_z}\left(w_{g,\text{eff}} + 2.16 \frac{a^2}{d_z} \right) - 0.16 a^2} \right], \tag{3.15}$$

which is obtained by solving the quadratic equation of (3.14) for w_g.

With our model presented in Section 2.4 we determine the PWWG width w_g for the fixed effective width of the PWWG geometry in [17, Fig. 5]. To this end we apply a minimization procedure to the absolute difference of the real part of k_z and the dispersion of the TE_{10} waveguide mode as given by the right-hand side of (3.9). As discussed in the previous section we use the Golden Section Search and we set the imaginary part of k_z equal to zero.

Finally, we determine the w_g, d_z-relationship with the electromagnetic solver Ansoft HFSS [15] that is based on the finite-element method (FEM). We compute the propagation constant k_z by applying the multi-line calibration to the simulation results of HFSS for the scattering parameters of a set of uniform PWWG transmission lines. The method of multi-line calibration discussed in Section 4.2 enables us to calculate $w_{g,\text{eff}}$ for a given value of k_z. If we perform a number of simulations for different values of w_g, we can use interpolation to determine the waveguide width for which $w_{g,\text{eff}}$ attains the desired value. We repeat these steps for several post spacings. This procedure requires a large number of simulations.

Figure 3.5(b) shows deviations in the results obtained with different methods with respect to the HFSS results. We select Ansoft HFSS as a reference, since it is a full-wave 3D simulator while all the results are based on reduced models or curve-fitted expressions derived from reduced models. The deviations are (in percent) defined by

$$e_{\text{HFSS}} = 100 \left| \frac{w_g - w_{g,\text{ref}}}{\sqrt{w_g w_{g,\text{ref}}}} \right|, \tag{3.16}$$

where w_g is the width obtained with the respective methods and $w_{g,\text{ref}}$ is the width obtained by HFSS and the multi-line calibration.

The HFSS results in Figure 3.5(a) show that w_g decreases with increasing d_z and that the decrease is faster for larger values of d_z. The upper bound of 2.4 mm is chosen based on the grating condition (3.11), which by substitution of $\lambda_1 = c_0/(f\sqrt{\varepsilon_{r,1}\mu_{r,1}})$ turns into

$$d_z < \frac{c_0}{2f\sqrt{\varepsilon_{r,1}\mu_{r,1}}} \tag{3.17}$$

and which evaluates to $d_z < 2.54$ mm for this specific case. Since the effective width is chosen constant, the faster decrease towards the grating condition is due to the extension of the fields outside the central region of the PWWG. Consequently, the leakage increases to a maximum at the grating condition. This effect is not observed in the results of Hirokawa and Ando. In fact, in [17, Fig. 5] the relation between w_g and d_z extends almost linearly until $d_z = 3.00$ mm. Figure 3.5(b) shows a difference with HFSS that is monotonically increasing and exceeds 1 percent for almost the entire range of d_z.

The approximate expressions of Cassivi et.al. [53] and Xu and Wu [69] exhibit similar behavior. The first paper claims an accuracy of (3.13) better than 5 percent relative to the BI-RME method for $d_z < \lambda_0\sqrt{\varepsilon_{r,1}}/2$ and $d_z < 8a$, which in this example leads to $d_z < 2.40$ mm. The second paper claims that (3.15) is "very accurate" for $d_z/a < 6$ (and $a/w_g < 0.1$), which implies that $d_z < 1.80$ mm. Figure 3.5(b) shows that the expression of [69] is marginally more accurate for $d_z < 1.50$ mm. We observe for both expressions that $e_{\text{HFSS}} < 1.8$ percent for $d_z < 1.80$ mm and $e_{\text{HFSS}} > 5$ percent for $d_z > 2.1$ mm. Thus, the claimed accuracy of 5 percent for $d_z < 2.40$ mm is overly optimistic with respect to HFSS.

The results of the transverse resonance technique used by Deslandes and Wu exhibit very little difference with HFSS: $e_{\text{HFSS}} < 1$ percent for $d_z < 1.9$ mm. The results that we obtained with the approach of Chapter 2 are in very good agreement with HFSS: $e_{\text{HFSS}} < 0.5$ percent for $d_z < 2.1$ mm. For larger d_z tending to the grating condition the results start to deviate minimally, with $e_{\text{HFSS}} < 2$ percent for $d_z < 2.40$ mm. In conclusion, for the configuration presented in [17] our method demonstrates the smallest difference with respect to HFSS for the w_g, d_z-relationship of the investigated methods.

3.3 Losses

Different mechanisms contribute to the losses in a PWWG. We distinguish three categories:

1. dielectric loss, $\alpha_{z,d}$,
2. conductor loss, $\alpha_{z,c}$, and
3. radiation or leakage loss, $\alpha_{z,r}$.

In this section we derive separate approximate formulas for these losses and we comment on their applicability and the possibility of calculating the total loss, or attenuation constant, α_z as the sum of the separate loss constituents. We note that the unit of the attenuation constant is

Np/m, but in most cases the attenuation is expressed in dB/m. The conversion between neper and decibel is linear with

$$1\ \text{Np} \equiv \frac{20}{\ln(10)}\ \text{dB}. \tag{3.18}$$

3.3.1 Dielectric Loss

In our model of Chapter 2, the dielectric loss is embodied in the complex propagation constant

$$k_1 = k_0\sqrt{\varepsilon_{r,1}(1 - j\tan\delta_1)}\,, \tag{3.19}$$

see Section 2.6.1, where $\varepsilon_{r,1}$ and $\tan\delta_1$ are the relative permittivity and the loss tangent of the dielectric material in the PWWG. Considering a waveguide filled with such a material, and ignoring loss in dielectric posts, we can write according to [70, p. 340, Eq. (36)]

$$k_z^2 = k_1^2 - k_{\text{co}}^2\,, \tag{3.20}$$

where k_{co} is the modal cutoff wavenumber. Substituting (3.19) and (3.4) in this equation and equating the real and imaginary parts we obtain

$$\beta_z^2 - \alpha_z^2 = k_0^2\varepsilon_{r,1} - k_{\text{co}}^2\,, \qquad \alpha_z = \frac{k_0^2\varepsilon_{r,1}\tan\delta_1}{2\beta_z}\,. \tag{3.21}$$

We note that $\beta_z = \alpha_z$ at the cut-off frequency f_{co}. Substituting the second equation in the first we obtain a second-order equation for β_z^2. Under the assumption that $k_0^2\varepsilon_{r,1} - k_{\text{co}}^2 \gg k_0^2\varepsilon_{r,1}\tan\delta_1 \geq 0$, i.e., the frequency is sufficiently above the cutoff frequency, the equation has one non-zero solution,

$$\beta_z^2 = k_0^2\varepsilon_{r,1} - k_{\text{co}}^2\,. \tag{3.22}$$

For increasing frequency β_z tends asymptotically to $\operatorname{Re} k_1 = \sqrt{\varepsilon_{r,1}}k_0$ and

$$\lim_{\beta_z \to \sqrt{\varepsilon_{r,1}}k_0} \alpha_z = \frac{1}{2}k_0\sqrt{\varepsilon_{r,1}}\tan\delta_1. \tag{3.23}$$

Finally we observe that the dielectric loss $\alpha_{z,d}$ of a PWWG can be approximated by the second equation of (3.21). The phase constant can be approximated by the optimization procedure described in Section 3.1, where α_z is temporarily set equal to zero or set equal to the bound (2.105).

3.3.2 Conductor Loss

If we consider imperfectly conducting posts, the ohmic loss in the posts will attribute to the attenuation of the propagating wave. The attenuation constant $\alpha_{z,c}$ relates to the power loss in a unit cell of the PWWG P_{uc} and the power dissipated at the posts P_c as

$$\alpha_{z,c} = \frac{P_c}{2P_{\text{uc}}}. \tag{3.24}$$

The power loss of the unit cell consists of leaked or radiated power and dissipated power terms: $P_{\text{uc}} = P_{\text{rad}} + P_c$. To assess the dissipated power P_c, we assume that the metallic posts are

good conductors and that the effect of the finite conductivity on the electric current density is negligible. We represent the finite conductivity by an equivalent surface impedance

$$Z^{\text{surf}} = R^{\text{surf}} + jX^{\text{surf}} = \sqrt{\frac{j\omega\mu}{\sigma + j\omega\varepsilon}}, \tag{3.25}$$

and for good conductors ($\sigma \gg \omega\varepsilon$) we approximate $Z^{\text{surf}} \approx (1 + j)\sqrt{\omega\mu/2\sigma}$. The power dissipated in post q is

$$P_{c,q} = \frac{R^{\text{surf}}}{2} \int\limits_{L_q} \boldsymbol{J}_q^{\text{surf}} \bullet (\boldsymbol{J}_q^{\text{surf}})^* dL_q, \tag{3.26}$$

where L_q is the circumference of post q. With $\boldsymbol{J}_q^{\text{surf}} = \boldsymbol{n} \times H_{q,\phi}^{\text{sct}} \boldsymbol{i}_\phi$ and $\boldsymbol{n} = \boldsymbol{i}_r$ this results in

$$P_{c,q} = \frac{R^{\text{surf}}}{2} \int\limits_{L_q} H_{q,\phi}^{\text{sct}} (H_{q,\phi}^{\text{sct}})^* dL_q. \tag{3.27}$$

Evaluating (2.21b) at the cylinder surface and summing up the dissipation of all cylinders $q = 1, \ldots, Q$ in the unit cell, we find

$$P_c = \pi R^{\text{surf}} \left(\frac{\omega\varepsilon_1}{k_1}\right)^2 \sum_{q=1}^{Q} \sum_{n=-\infty}^{\infty} |A_{q,n}|^2 |H_n^{(2)\prime}(k_1 a_q)|^2. \tag{3.28}$$

Next, we consider the power radiated by a unit cell

$$P_{\text{rad}} = \tfrac{1}{2} \int\limits_{\partial\Omega} \boldsymbol{E} \times \boldsymbol{H}^* \bullet \boldsymbol{n} d\partial\Omega, \tag{3.29}$$

where $\partial\Omega$ is the boundary of the unit cell in the xz-plane defined by $-\infty \le x \le \infty, z = \pm d_z/2$ and $\boldsymbol{n}$ is the outward normal at the boundary. Because of the Sommerfeld radiation condition at infinity [71, pp.21,22], we can express the radiated power as

$$P_{\text{rad}} = -\tfrac{1}{2} \int\limits_{-\infty}^{\infty} E_y H_x^*\big|_{z=-d_z/2}^{d_z/2} \, dx. \tag{3.30}$$

3.3.3 Leakage Loss and Total Loss

Unlike rectangular waveguides, PWWGs are open structures. Thus the electromagnetic fields are not bound to a closed region. The objective of PWWG designs is to confine the fields of the propagating mode to the central guiding region – as much as possible. Nevertheless, through the slots between the posts, and in the case of dielectric posts also through the posts themselves, energy will leak away from the guide. Intuitively we feel that a small post radius and a large post spacing will give rise to high leakage loss. Moreover, the if the grating condition of (3.17) is fulfilled leakage loss can be extremely high. From this expression we see that the

Description	f_{stop} (GHz)	$\varepsilon_{r,1}$ ()	a (mm)	d_z (mm)
PTFE based, normal	112	2.2	0.15	0.90
PTFE based, special	184	2.2	0.125	0.55
RO4003C based, normal	88.4	3.55	0.15	0.90
RO4003C based, special	145	3.55	0.125	0.55

Table 3.1 — Overview of practical frequency limitations as caused by the grating condition for typical PCB design rules. The design rules are based on the capabilities of Thales Nederland's facilities [72]; other manufacturers state similar values.

minimum frequency at which the grating condition is satisfied is determined by the post spacing d_z and the material properties. In general, PCB manufactures formulate design rules based on the capabilities of their PCB processing facilities. Often a distinction between 'standard' and 'special' design rules is made, where standard means that no additional effort has to be put in the manufacturing process to obtain a large yield. Typical design rules relate the minimum allowed d_z to the radius a of the posts. To give an idea of the minimum stop band frequencies f_{stop} (originating from the grating condition) for typical design rules and circuit boards, Table 3.1 gives an overview for different combinations. Polytetrafluoroethylene (PTFE) substrates exhibit a very low permittivity but cannot be processed with standard, FR-4 based, techniques; Rogers RO4003C substrates have a slightly higher permittivity, but can be processed using standard PCB facilities.

In PWWGs with dielectric posts, a high contrast between the permittivity of the cylinders and the background medium, will lower the leakage loss. Also the use of multiple parallel rows of posts reduces the loss from leakage, as the field is better confined to the waveguide. In our full-wave model of Chapter 2, leakage loss is automatically accounted for, however, as explained in Section 3.1, we cannot determine the attenuation constant from the infinite-array model described in Section 2.6. Therefore we can neither say anything about the contribution of the leakage loss to the attenuation constant nor can we compute the total attenuation constant as the sum of the three mentioned loss terms,

$$\alpha_z = \alpha_{z,d} + \alpha_{z,c} + \alpha_{z,r}, \tag{3.31}$$

an approximation that is valid provided that all loss contributions are small. It is for this reason that we need to find another way to determine the attenuation constant or the losses. In Section 3.2 we indicated that a multi-line calibration was used for sets of uniform PWWG transmission lines simulated by HFSS to determine the propagation constant. A similar procedure could be carried out with our model provided that we can calculate the scattering parameters of PWWG components. An electromagnetic model, based on current matrices, for such a procedure is described in the next section and the calculation of scattering parameters is discussed in Section 3.5.

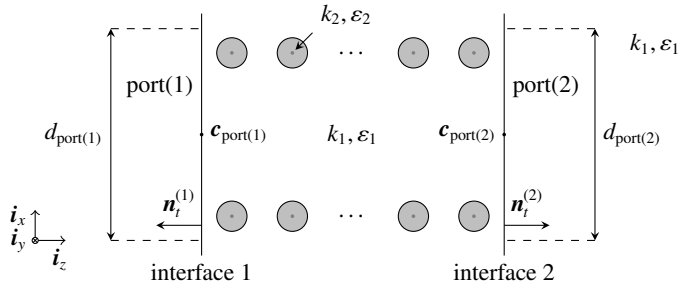

Figure 3.6 — Top view of a section of uniform PWWG with a single row of posts per sidewall and the notation used to specify the ports.

3.4 The Description of Post-Wall Waveguide Components by Current Matrices

In this section we introduce a description of the electromagnetic behavior of PWWG components in terms of current matrices. Such a matrix describes the component behavior entirely in terms of the electric and magnetic surface currents at ports. The current matrix is a scattering matrix in the sense that it relates input quantities to output quantities, which are in this case the electric and magnetic currents. We limit ourselves here to components that can be described with two parallel interfaces, such as a uniform line or an iris. Other types of components are briefly discussed in Section 6.5. Figure 3.6 illustrates the case of a uniform line with only one row of posts per side wall. We assume that the leakage of the component is such that the tangential fields at the two interfaces are only significant in (bounded) segments, which we denote by port(i), $i = 1, 2$. Let $\boldsymbol{c}_{\text{port}(i)}$ be the centers of these segments in the xz-plane and let $d_{\text{port}(i)}$ be their lengths. Then their parametric representations are

$$\boldsymbol{x}_{\text{port}(i)}(s) = \boldsymbol{c}_{\text{port}(i)} + \boldsymbol{i}_x s d_{\text{port}(i)}/2, \qquad -1 \le s \le 1. \tag{3.32}$$

The normals $\boldsymbol{n}_t^{(i)}$, $i = 1, 2$, on port(1) and port(2) are $-\boldsymbol{i}_z$ and $\boldsymbol{i}_z$, respectively. Hence, the magnetic surface currents on these interfaces are vectors along $\boldsymbol{i}_x$ according to their definition in 2.46. We write $\boldsymbol{M}^{\text{surf}} = M_x^{\text{surf}} \boldsymbol{i}_x$ and for the electric surface current we know that $\boldsymbol{J}^{\text{surf}} = J_y^{\text{surf}} \boldsymbol{i}_y$. Since we deal in this section only with the surface currents and not with the volume currents, we omit the superscript 'surf' in the remainder of this chapter.

Let $\{\boldsymbol{J}^{\text{in}(i)}, \boldsymbol{M}^{\text{in}(i)}\}$ be prescribed (input) surface currents at port(i), $i = 1, 2$. These currents generate a field in the PWWG (component) that is scattered by the posts. Consequently, (output) surface currents $\{\boldsymbol{J}^{\text{out}(i)}, \boldsymbol{M}^{\text{out}(i)}\}$ are generated at port(i), $i = 1, 2$. For a fixed port index i, these currents are composed of the scattered fields of the posts and the field generated by the surface currents on the other posts.

The surface currents $\{\boldsymbol{J}^{\text{out}(i)}, \boldsymbol{M}^{\text{out}(i)}\}$, $i = 1, 2$, can be related to the surface currents $\{\boldsymbol{J}^{\text{in}(i)}, \boldsymbol{M}^{\text{in}(i)}\}$ via a current matrix. To construct such a matrix we first consider the fields $\{\boldsymbol{E}^{\text{in}(i)}, \boldsymbol{H}^{\text{in}(i)}\}$, generated by the surface currents $\{\boldsymbol{J}^{\text{in}(i)}, \boldsymbol{M}^{\text{in}(i)}\}$ in between the two interfaces. Considering the domain between these interfaces as the domain Ω in (2.51) and (2.57) in

Section 2.5, we obtain

$$E_y^{\mathrm{in}(i)}(\boldsymbol{x}_t) = -\frac{k_1\zeta_1 d_{\mathrm{port}(i)}}{8}\int_{-1}^{1} H_0^{(2)}(k_1\dagger)J_y^{\mathrm{in}(i)}(s')ds' - \frac{jk_1\zeta_1 d_{\mathrm{port}(i)}}{8}\int_{-1}^{1} M_x^{\mathrm{in}(i)}(s')H_1^{(2)}(k_1\dagger)\frac{z-c_{\mathrm{port}(i),z}}{\dagger}ds', \quad (3.33a)$$

$$\boldsymbol{H}^{\mathrm{in}(i)}(\boldsymbol{x}_t) = \frac{k_1 d_{\mathrm{port}(i)}}{8\zeta_1}\left(\int_{-1}^{1} H_0^{(2)}(k_1\dagger)M_x^{\mathrm{in}(i)}(s')ds'\boldsymbol{i}_x - \frac{2}{k_1^2 d_{\mathrm{port}(i)}}\mathrm{grad}_{\boldsymbol{x}}\int_{-1}^{1} H_0^{(2)}(k_1\dagger)M_x^{\mathrm{in}(i)'}(s')ds'\right)$$
$$-\frac{jk_1 d_{\mathrm{port}(i)}}{8}\int_{-1}^{1} J_y^{\mathrm{in}(i)'}(s')H_1^{(2)}(k_1\dagger)\times\frac{1}{\dagger}\left((x-c_{\mathrm{port}(i),x}-s'd_{\mathrm{port}(i)}/2)\boldsymbol{i}_z-(z-c_{\mathrm{port}(i),x})\boldsymbol{i}_x\right), \quad (3.33b)$$

$$\dagger = |\boldsymbol{x}_t - \boldsymbol{c}_{\mathrm{port}(i)} - \boldsymbol{i}_x s' d_{\mathrm{port}(i)}/2|$$

where $\boldsymbol{x}_t$ is between the two interfaces. Note that $\boldsymbol{J}^{\mathrm{in}(i)}$ has only a y-component and $\boldsymbol{M}^{\mathrm{in}(i)}$ has only a x-component. To arrive at (3.33) we used that

$$\mathrm{grad}_{\boldsymbol{x}'}\, H_0^{(2)}(k_1|\boldsymbol{x}-\boldsymbol{x}_t'|) = -k_1 H_1^{(2)}(k_1|\boldsymbol{x}_t-\boldsymbol{x}_t'|)\frac{1}{|\boldsymbol{x}_t-\boldsymbol{x}_t'|}\left((x-x')\boldsymbol{i}_x+(z-z')\boldsymbol{i}_z\right). \quad (3.34)$$

Moreover, the $\mathrm{grad}_{\boldsymbol{x}}\,\mathrm{div}_{\boldsymbol{x}}$ term in (2.57) is rewritten as follows: the divergence reduces to the derivative with respect to x because $\boldsymbol{M}^{\mathrm{in}(i)}$ has only a x-component. This derivative and the integral are interchanged after which the derivative is transformed by

$$\frac{\partial}{\partial x}H_0^{(2)}(k_1|\boldsymbol{x}_t-\boldsymbol{c}_{\mathrm{port}(i)}-\boldsymbol{i}_x s' d_{\mathrm{port}(i)}/2|) = -\frac{2}{d_{\mathrm{port}(i)}}\frac{\partial}{\partial s'}H_0^{(2)}(k_1|\boldsymbol{x}_t-\boldsymbol{c}_{\mathrm{port}(i)}-\boldsymbol{i}_x s' d_{\mathrm{port}(i)}/2|). \quad (3.35)$$

Next, integration by parts is applied to transfer the derivative with respect to s to the surface current $M_x^{\mathrm{in}(i)}$. The boundary terms resulting from this integration vanish because $M_x^{\mathrm{in}(i)}(\pm 1) = 0$.

The fields in (3.33) are incident on the posts which in turn generate a scattered field. For each post with center $\boldsymbol{c}_p$ we write the incident electric field as in (2.20a). Then, the electric field at the surface of this post is described by

$$E_y^{\mathrm{exc}(i)}\big|_{L_p}(\varphi) = \sum_{\nu=-N}^{N} B_{p,\nu}^{\mathrm{exc}(i)}J_\nu(k_1 a_p)e^{j\nu p}, \quad (3.36)$$

where we have replaced the infinite sum by a finite one as discussed in Section 2.4 and the angle φ is related to the position vector $\boldsymbol{x}_t$ by $\boldsymbol{x}_t = \boldsymbol{c}_p + a_p\boldsymbol{i}_r(\varphi)$. By (3.33b), the inner product (2.69)

and the functions w_n in (2.77), we obtain

$$B_{p,\nu}^{\mathrm{exc}(i)} = \frac{\langle w_n,\, E_y^{\mathrm{in}(i)}\big|_{L_p}\rangle_{[-\pi,\pi]}}{J_n(k_1 a_p)} = -\frac{k_1\zeta_1 d_{\mathrm{port}(i)}}{16\pi J_\nu(k_1 a_p)} \int_{-\pi}^{\pi}\int_{-1}^{1} e^{j\nu\varphi} H_0^{(2)}(k_1 R_p^{(i)}(\varphi, s'))J^{\mathrm{in}(i)}(s')ds'd\varphi$$

$$- \frac{jk_1 d_{\mathrm{port}(i)}}{16\pi J_\nu(k_1 a_p)} \int_{-\pi}^{\pi}\int_{-1}^{1} e^{j\nu\varphi} H_1^{(2)}(k_1 R_p^{(i)}(\varphi, s'))\frac{c_{p,z} + a_p\cos\varphi - c_{\mathrm{port}(i),z}}{R_p^{(i)}(\varphi, s')} M_x^{\mathrm{in}(i)}(s')ds'd\varphi, \quad (3.37)$$

where

$$R_p^{(i)}(\varphi, s') = |\boldsymbol{c}_p + a_p\boldsymbol{i}_r(\varphi) - \boldsymbol{c}_{\mathrm{port}(i)} - \boldsymbol{i}_x s' d_{\mathrm{port}(i)}/2|. \quad (3.38)$$

The coefficients $A_{q,\nu}^{(i)}$ $(q = 1, \ldots, Q)$ of the scattered field are computed by first constructing the matrix system (2.30), where

$$B_p^{\mathrm{exc}} = (B_{p,-N}^{\mathrm{exc}(i)}, B_{p,-N+1}^{\mathrm{exc}(i)}, \ldots, B_{p,N}^{\mathrm{exc}(i)})^T, \qquad A_q = A_q^{(i)} = (A_{q,-N}^{(i)}, A_{q,-N+1}^{(i)}, \ldots, A_{q,N}^{(i)})^T, \quad (3.39)$$

and the matrices C_{pq} are defined by (2.31) for metallic posts and by (2.38) for dielectric posts. Next $A^{(i)} = C^{-1}B^{\mathrm{exc}(i)}$ is computed where

$$A^{(i)} = (A_1^{(i)}, \ldots, A_Q^{(i)}), \qquad B^{\mathrm{exc}(i)} = (B_1^{\mathrm{exc}(i)}, \ldots, B_Q^{\mathrm{exc}(i)}), \quad (3.40)$$

and C is the matrix with blocks C_{pq}. The scattered electric field of post q is then described by (2.20b),

$$E_{q,y}^{\mathrm{sct}(i)}(r, \varphi) = \sum_{\nu=-N}^{N} A_{q,\nu}^{(i)} H_\nu^{(2)}(k_1 r)e^{j\nu\varphi}, \quad (3.41)$$

where the polar coordinates (r, φ) are related to the position vector $\boldsymbol{x}_t$ by $\boldsymbol{x}_t = \boldsymbol{c}_q + r\boldsymbol{i}_r(\varphi)$. The φ component of the scattered magnetic field is described by (2.21b),

$$H_{q,\varphi}^{\mathrm{sct}(i)}(r, \varphi) = -\frac{j\omega\varepsilon_1}{k_1} \sum_{\nu=-N}^{N} A_{q,\nu}^{(i)} H_\nu^{(2)\prime}(k_1 r)e^{j\nu\varphi}. \quad (3.42)$$

Since we need to compute the tangential fields at the interfaces, we also need the r component, which follows from (2.14a) applied to (3.41),

$$H_{q,r}^{\mathrm{sct}(i)}(r, \varphi) = -\frac{\omega\varepsilon_1}{k_1^2 r} \sum_{\nu=-N}^{N} \nu A_{q,\nu}^{(i)} H_\nu^{(2)}(k_1 r)e^{j\nu\varphi}. \quad (3.43)$$

To calculate the output surface currents $\{\boldsymbol{J}^{\mathrm{out}(i)}, \boldsymbol{M}^{\mathrm{out}(i)}\}$, $i = 1, 2$, we consider first the specific case that the input surface currents at port(i_2) are zero. The input surface currents at port(i_1) generate the excitation fields (3.33) with $i = i_1$. The resulting scattered fields $\{\boldsymbol{E}^{\mathrm{sct}(i_1)}, \boldsymbol{H}^{\mathrm{sct}(i_1)}\}$ are given by (3.41)–(3.43) with $i = i_1$. Then, the output surface current are given by

$$J_y^{\mathrm{out}(i)} = \chi(i)\left(\boldsymbol{i}_z \times \left(\boldsymbol{H}^{\mathrm{sct}(i_1)} + \boldsymbol{H}^{\mathrm{in}(i_1)}\right)\Big|_{\mathrm{port}(i)}\right)_y, \quad (3.44a)$$

$$M_x^{\mathrm{out}(i)} = \chi(i)\left(\boldsymbol{i}_z \times \left(\boldsymbol{E}^{\mathrm{sct}(i_1)} + \boldsymbol{E}^{\mathrm{in}(i_1)}\right)\Big|_{\mathrm{port}(i)}\right)_x, \quad (3.44b)$$

where $i = i_1, i_2$. Here, $\{\boldsymbol{E}^{\mathrm{sct}(i_1)}, \boldsymbol{H}^{\mathrm{sct}(i_1)}\}$ are the sums of the scattered fields of the posts and $\chi(i)$ is defined by $\chi(1) = -1$, $\chi(2) = 1$. Note that $\boldsymbol{n}_t^{(i)} = \chi(i)\boldsymbol{i}_z$. The cross product of $\boldsymbol{i}_z$ with the fields $\boldsymbol{E}^{\mathrm{in}(i_1)}$ and $\boldsymbol{H}^{\mathrm{in}(i_1)}$ restricted to port(i) are calculated from (3.33) with $i = i_1$,

$$\left(\boldsymbol{i}_z \times \boldsymbol{E}^{\mathrm{in}(i_1)}\big|_{\mathrm{port}(i)}\right)_x(s) = \frac{k_1\zeta_1 d_{\mathrm{port}(i)}}{8}\int_{-1}^{1} H_0^{(2)}(k_1R^{(i,i_1)}(s,s'))J_y^{\mathrm{in}(i_1)}(s')ds' + \frac{jk_1\zeta_1 d_{\mathrm{port}(i)}}{8}\int_{-1}^{1} H_1^{(2)}(k_1R^{(i,i_1)}(s,s'))\frac{c_{\mathrm{port}(i),z} - c_{\mathrm{port}(i_1),z}}{R^{(i,i_1)}(s,s')}M_x^{\mathrm{in}(i_1)}(s')ds', \quad (3.45a)$$

$$\left(\boldsymbol{i}_z \times \boldsymbol{H}^{\mathrm{in}(i_1)}\big|_{\mathrm{port}(i)}\right)_y(s) = \frac{k_1 d_{\mathrm{port}(i)}}{8\zeta_1}\left(\int_{-1}^{1} H_0^{(2)}(k_1R^{(i,i_1)}(s,s'))M_x^{\mathrm{in}(i_1)}(s')ds' + \frac{4}{k_1^2 d_{\mathrm{port}(i_1)}d_{\mathrm{port}(i)}}\frac{d}{ds}\int_{-1}^{1} H_0^{(2)}(k_1R^{(i,i_1)}(s,s'))M_x^{\mathrm{in}(i_1)'}(s')ds'\right) + \frac{jk_1 d_{\mathrm{port}(i_1)}}{8}\int_{-1}^{1} H_1^{(2)}(k_1R^{(i,i_1)}(s,s'))\frac{c_{\mathrm{port}(i),z} - c_{\mathrm{port}(i_1),z}}{R^{(i,i_1)}(s,s')}J_y^{\mathrm{in}(i_1)'}(s')ds', \quad (3.45b)$$

where s is related to the position vector $\boldsymbol{x}_t$ by $\boldsymbol{x}_t = \boldsymbol{c}_{\mathrm{port}(i)} + \boldsymbol{i}_x s d_{\mathrm{port}(i)}/2$ and

$$R^{(i,i_1)}(s,s') = |\boldsymbol{c}_{\mathrm{port}(i)} + \boldsymbol{i}_x s d_{\mathrm{port}(i)}/2 - \boldsymbol{c}_{\mathrm{port}(i_1)} - \boldsymbol{i}_x s' d_{\mathrm{port}(i_1)}/2|. \quad (3.46)$$

The cross products of $\boldsymbol{i}_z$ with the fields $\boldsymbol{E}^{\mathrm{sct}(i_1)}$ and $\boldsymbol{H}^{\mathrm{sct}(i_1)}$ evaluated at port(i) are given by

$$\left(\boldsymbol{i}_z \times \boldsymbol{E}^{\mathrm{sct}(i_1)}\big|_{\mathrm{port}(i)}\right)_x(s) = -E_y^{\mathrm{sct}(i_1)}\big|_{\mathrm{port}(i)}(s) = -\sum_{q=1}^{Q} E_{q,y}^{\mathrm{sct}(i_1)}\big|_{\mathrm{port}(i)}(s), \quad (3.47a)$$

$$\left(\boldsymbol{i}_z \times \boldsymbol{H}^{\mathrm{sct}(i_1)}\big|_{\mathrm{port}(i)}\right)_y(s) = -H_x^{\mathrm{sct}(i_1)}\big|_{\mathrm{port}(i)}(s) = -\sum_{q=1}^{Q} H_{q,x}^{\mathrm{sct}(i_1)}\big|_{\mathrm{port}(i)}(s), \quad (3.47b)$$

where the electric field is oriented in the y-direction and the magnetic field is parallel to the xz-plane. The parameter s is related to the position vector $\boldsymbol{x}_t$ by $\boldsymbol{x}_t = \boldsymbol{c}_{\mathrm{port}(i)} + \boldsymbol{i}_x s d_{\mathrm{port}(i)}/2$. For a specific value of s, or a specific point $\boldsymbol{x}_t$ on port(i), the components $E_{q,y}^{\mathrm{sct}(i_1)}$ and $H_{q,x}^{\mathrm{sct}(i_1)}$ are evaluated by first calculating $r_q^{(i)}(s)$ and $\varphi_q^{(i)}(s)$ from (2.106). Next, $E_{q,y}^{\mathrm{sct}(i_1)}$ is evaluated from (3.41) with $r = r_q^{(i)}(s)$ and $\varphi = \varphi_q^{(i)}(s)$. Thus,

$$E_{q,y}^{\mathrm{sct}(i_1)}\big|_{\mathrm{port}(i)}(s) = \sum_{\nu=-N}^{N} A_{q,\nu}^{(i_1)} H_\nu^{(2)}(k_1 r_q^{(i)}(s))e^{j\nu\varphi_q^{(i)}(s)}. \quad (3.48)$$

The component $H_{q,x}^{\mathrm{sct}(i_1)}$ is evaluated by taking the x-component of $H_{q,r}^{\mathrm{sct}(i_1)}\boldsymbol{i}_r + H_{q,\varphi}^{\mathrm{sct}(i_1)}\boldsymbol{i}_\varphi$ and next by calculating the r and φ components from (3.43) and (3.42) with $r = r_q^{(i)}(s)$ and $\varphi = \varphi_q^{(i)}(s)$. Thus,

$$H_{q,x}^{\mathrm{sct}(i_1)}\big|_{\mathrm{port}(i)}(s) = -\frac{\omega\varepsilon_1}{k_1^2 r_q^{(i)}(s)} \sum_{\nu=-N}^{N} A_{q,\nu}^{(i_1)} H_\nu^{(2)}(k_1 r_q^{(i)}(s)) e^{j\nu\varphi_q^{(i)}(s)} \sin\varphi_q^{(i)}(s) - \frac{j\omega\varepsilon_1}{k_1} \sum_{\nu=-N}^{N} A_{q,\nu}^{(i_1)} H_\nu^{(2)\prime}(k_1 r_q^{(i)}(s)) e^{j\nu\varphi_q^{(i)}(s)} \cos\varphi_q^{(i)}(s). \quad (3.49)$$

Having calculated the cross products (3.45) and (3.47) we deal with the output surface currents (3.44). To obtain the total output surface currents at the ports we can consider the two cases $(i_1, i_2) = (1, 2), (2, 1)$ and sum up the individual output surface currents.

Up to now we have not specified the exact nature of the input and output surface currents. We expand these fields in terms of rooftop functions, which we define on the interval $[-1, 1]$ by

$$\Lambda_n^{(i)}(s) = \Lambda\left(\frac{s - s_n^{(i)}}{\Delta_{\mathrm{exp}}^{(i)}}\right), \qquad \Lambda(s) = (1 - |s|)1_{[-1,1]}(s), \quad (3.50)$$

where $\Delta_{\mathrm{exp}}^{(i)} = 2/(N_{\mathrm{exp}}^{(i)} + 1)$, $s_n^{(i)} = -1 + n\Delta_{\mathrm{exp}}^{(i)}$, and $n = 1, 2, \ldots, N_{\mathrm{exp}}^{(i)}$, $i = 1, 2$. Then we write $\{J_y^{\mathrm{in}(i)}, M_x^{\mathrm{in}(i)}\}$ and $\{J_y^{\mathrm{out}(i)}, M_x^{\mathrm{out}(i)}\}$ as

$$J_y^{\mathrm{in}(i)} = \sum_{n=1}^{N_{\mathrm{exp}}^{(i)}} D_{\mathrm{el},n}^{\mathrm{in}(i)} \Lambda_n^{(i)}, \qquad M_x^{\mathrm{in}(i)} = \sum_{n=1}^{N_{\mathrm{exp}}^{(i)}} D_{\mathrm{mag},n}^{\mathrm{in}(i)} \Lambda_n^{(i)}, \quad (3.51a)$$

$$J_y^{\mathrm{out}(i)} = \sum_{n=1}^{N_{\mathrm{exp}}^{(i)}} D_{\mathrm{el},n}^{\mathrm{out}(i)} \Lambda_n^{(i)}, \qquad M_x^{\mathrm{out}(i)} = \sum_{n=1}^{N_{\mathrm{exp}}^{(i)}} D_{\mathrm{mag},n}^{\mathrm{out}(i)} \Lambda_n^{(i)}, \quad (3.51b)$$

where $i = 1, 2$, $D_{\mathrm{el},n}^{\mathrm{in}(i)}$ and $D_{\mathrm{mag},n}^{\mathrm{in}(i)}$ are the expansion coefficients of the input surface currents and $D_{\mathrm{el},n}^{\mathrm{out}(i)}$ and $D_{\mathrm{mag},n}^{\mathrm{out}(i)}$ are the expansion coefficients of the output surface currents. Let $D_{\mathrm{el}}^{\mathrm{in}(i)}$, $D_{\mathrm{mag}}^{\mathrm{in}(i)}$, $D_{\mathrm{el}}^{\mathrm{out}(i)}$ and $D_{\mathrm{mag}}^{\mathrm{out}(i)}$ be the corresponding vectors of coefficients. We can construct the current matrix that relates $(D_{\mathrm{el}}^{\mathrm{in}(1)}, D_{\mathrm{mag}}^{\mathrm{in}(1)}, D_{\mathrm{el}}^{\mathrm{in}(2)}, D_{\mathrm{mag}}^{\mathrm{in}(2)})^T$ to $(D_{\mathrm{el}}^{\mathrm{out}(1)}, D_{\mathrm{mag}}^{\mathrm{out}(1)}, D_{\mathrm{el}}^{\mathrm{out}(2)}, D_{\mathrm{mag}}^{\mathrm{out}(2)})^T$. The matrix is a block matrix,

$$\begin{pmatrix} T^{\mathrm{el}(1),\mathrm{el}(1)} & T^{\mathrm{el}(1),\mathrm{mag}(1)} & T^{\mathrm{el}(1),\mathrm{el}(2)} & T^{\mathrm{el}(1),\mathrm{mag}(2)} \\ T^{\mathrm{mag}(1),\mathrm{el}(1)} & T^{\mathrm{mag}(1),\mathrm{mag}(1)} & T^{\mathrm{mag}(1),\mathrm{el}(2)} & T^{\mathrm{mag}(1),\mathrm{mag}(2)} \\ T^{\mathrm{el}(2),\mathrm{el}(1)} & T^{\mathrm{el}(2),\mathrm{mag}(1)} & T^{\mathrm{el}(2),\mathrm{el}(2)} & T^{\mathrm{el}(2),\mathrm{mag}(2)} \\ T^{\mathrm{mag}(2),\mathrm{el}(1)} & T^{\mathrm{mag}(2),\mathrm{mag}(1)} & T^{\mathrm{mag}(2),\mathrm{el}(2)} & T^{\mathrm{mag}(2),\mathrm{mag}(2)} \end{pmatrix}, \quad (3.52)$$

where the first and second number in the superscripts of the blocks refer to the output and input ports, respectively, el and mag refer to the type of current as in (3.51a) and (3.51b), and the numbers between the parentheses refer to the ports. In Appendix D the evaluation of the current matrix blocks based on (3.33), (3.37)–(3.49) is treated in detail.

Let us now consider the cascading of two components, where the second port of the first component feeds the first port of the second component. Both ports require the same geometry and discretization. We write the current relations as

$$\begin{pmatrix} D^{i,\mathrm{out}(1)} \\ D^{i,\mathrm{out}(2)} \end{pmatrix} = \begin{pmatrix} T_{11}^{(i)} & T_{12}^{(i)} \\ T_{21}^{(i)} & T_{22}^{(i)} \end{pmatrix} \begin{pmatrix} D^{i,\mathrm{in}(1)} \\ D^{i,\mathrm{in}(2)} \end{pmatrix}, \tag{3.53}$$

where i is the index of the component ($i = 1, 2$), the block $T_{i_1,i_2}^{(i)}$ of the ith component is given by

$$T_{i_1,i_2}^{(i)} = \begin{pmatrix} T^{i,\mathrm{el}(i_1),\mathrm{el}(i_2)} & T^{i,\mathrm{el}(i_1),\mathrm{mag}(i_2)} \\ T^{i,\mathrm{mag}(i_1),\mathrm{el}(i_2)} & T^{i,\mathrm{mag}(i_1),\mathrm{mag}(i_2)} \end{pmatrix}, \tag{3.54}$$

and $D^{i,u(i_1)} = (D_{\mathrm{el}}^{i,u(i_1)}, D_{\mathrm{mag}}^{i,u(i_1)})^T$ with $u = \mathrm{in}, \mathrm{out}$. Since the current matrices in (3.53) relate the input coefficients to the output coefficients, the current matrix of the two cascaded components is constructed from the current matrices of the individual components using Redheffer's star product as in the case of scattering matrices, see e.g. [73, p. 199]. We can derive this product as follows. Let the current relation of the components be given by

$$\begin{pmatrix} D^{1,\mathrm{out}(1)} \\ D^{2,\mathrm{out}(2)} \end{pmatrix} = \begin{pmatrix} T_{11} & T_{12} \\ T_{21} & T_{22} \end{pmatrix} \begin{pmatrix} D^{1,\mathrm{in}(1)} \\ D^{2,\mathrm{in}(2)} \end{pmatrix}. \tag{3.55}$$

First we consider the case $D^{2,\mathrm{in}(1)} = 1$, $D^{2,\mathrm{in}(2)} = 0$. Then, by (3.53) and $D^{2,\mathrm{in}(1)} = D^{1,\mathrm{out}(1)}$, $D^{2,\mathrm{out}(1)} = D^{1,\mathrm{in}(1)}$,

$$\begin{pmatrix} D^{1,\mathrm{out}(1)} \\ D^{1,\mathrm{out}(2)} \end{pmatrix} = \begin{pmatrix} T_{11}^{(1)} + T_{21}^{(1)} D^{1,\mathrm{in}(2)} \\ T_{21}^{(1)} + T_{22}^{(1)} D^{1,\mathrm{in}(2)} \end{pmatrix}, \qquad \begin{pmatrix} D^{1,\mathrm{in}(1)} \\ D^{2,\mathrm{in}(2)} \end{pmatrix} = \begin{pmatrix} T_{11}^{(2)} D^{1,\mathrm{out}(2)} \\ T_{21}^{(2)} D^{1,\mathrm{out}(2)} \end{pmatrix}. \tag{3.56}$$

From the two relations between $D^{1,\mathrm{out}(2)}$ and $D^{1,\mathrm{in}(2)}$ it follows that

$$D^{1,\mathrm{out}(2)} = \left(I - T_{22}^{(1)} T_{11}^{(2)}\right)^{-1} T_{21}^{(1)}, \tag{3.57a}$$

$$D^{1,\mathrm{in}(2)} = T_{11}^{(2)} \left(I - T_{22}^{(1)} T_{11}^{(2)}\right)^{-1} T_{21}^{(1)}, \tag{3.57b}$$

where I is the identity matrix. Substituting these expressions in the other two relations and employing (3.55) with $D^{1,\mathrm{in}(1)} = 1$ and $D^{2,\mathrm{in}(2)} = 0$ we find

$$T_{11} = T_{11}^{(1)} + T_{12}^{(1)} T_{11}^{(2)} \left(I - T_{22}^{(1)} T_{11}^{(2)}\right)^{-1} T_{21}^{(1)}, \tag{3.58a}$$

$$T_{21} = T_{21}^{(2)} \left(I - T_{22}^{(1)} T_{11}^{(2)}\right)^{-1} T_{21}^{(1)}. \tag{3.58b}$$

The case $D^{1,\mathrm{in}(1)} = 0$ and $D^{2,\mathrm{in}(2)} = 1$ is analogous and we find (3.57) with 1 and 2 interchanged,

$$T_{22} = T_{22}^{(2)} + T_{21}^{(2)} T_{22}^{(1)} \left(I - T_{11}^{(2)} T_{22}^{(1)}\right)^{-1} T_{12}^{(2)}, \tag{3.59a}$$

$$T_{12} = T_{12}^{(1)} \left(I - T_{11}^{(2)} T_{22}^{(1)}\right)^{-1} T_{12}^{(2)}. \tag{3.59b}$$

3.5 Scattering Parameters of Post-Wall Waveguides

To determine the scattering parameters of a PWWG, we couple its ports to (rectangular) waveguides of width $w_g^{(i)}$ described only by the TE_{10} mode. Thus we assume that the frequency is such that higher order modes are evanescent and that we are at sufficient distance from discontinuities in the PWWG to have indeed negligible contribution from these modes. The non-zero components of the TE_{10} mode are

$$E_y(x,z) = E(z)\sin\frac{\pi x}{w_g}, \tag{3.60a}$$

$$H_x(x,z) = -\frac{j\omega\varepsilon}{k^2}E'(z)\sin\frac{\pi x}{w_g}, \tag{3.60b}$$

$$H_z(x,z) = -\frac{j\omega\varepsilon}{k^2 w_g}E(z)\cos\frac{\pi x}{w_g}, \tag{3.60c}$$

where we employed (2.4a) to determine (3.60b) and (3.60c) and where $0 \le x \le w_g$ is the waveguide aperture. Employing (2.4b) with $\boldsymbol{J} = \boldsymbol{0}$ and with the magnetic field given by (3.60b), (3.60c) we find

$$E_y(x,z) = \frac{1}{k^2}\left(-E''(z) + \frac{\pi^2}{w_g^2}E(z)\right)\sin\frac{\pi x}{w_g}. \tag{3.61}$$

Equating (3.60a) and (3.61) we find the following differential equation for E_0,

$$E'' + \left(k^2 - \frac{\pi^2}{w_g^2}\right)E = 0 \tag{3.62}$$

with solutions

$$E(z) = E_0 e^{\pm j\sqrt{k^2-\pi^2/w_g^2}z}, \tag{3.63}$$

where the sign depends on the direction of propagation (+ corresponds to negative z-direction and − corresponds to positive z-direction). For each of the two ports in Section 3.4 we center the waveguide at $\boldsymbol{c}_{\mathrm{port}(i)}$ and we choose the plane $z = 0$ for projection of the surface currents; the direction of propagation is the $-\chi(i)z$ direction. Thus, the non-zero components of the TE_{10} field at $z = 0$ are

$$E_y^{(i)}(s) = E_0^{(i)} f^{(i)}(s), \tag{3.64a}$$

$$H_x^{(i)}(s) = \frac{j\omega\varepsilon_1 E_0^{(i)}}{k_1^2}\chi(i)\sqrt{k_1^2 - \pi^2/(w_g^{(i)})^2}\, f^{(i)}(s), \tag{3.64b}$$

with

$$f^{(i)}(s) = \cos\left(\frac{\pi d_{\mathrm{port}(i)}}{2w_g^{(i)}}s\right)1_{[-w_g^{(i)}/d_{\mathrm{port}(i)},\, w_g^{(i)}/d_{\mathrm{port}(i)}]}, \tag{3.64c}$$

where we omit the z-component of the magnetic field since it does not contribute to the surface currents and where we used that $x = (d_{\mathrm{port}(i)}s + w_g^{(i)})/2$. The projected surface currents at $z = 0$

are then given by

$$J_y^{\mathrm{in}(i)}(s) = \frac{j\omega\varepsilon_1 E_0^{(i)}}{k_1^2}\chi(i)\sqrt{k_1^2 - \pi^2/(w_g^{(i)})^2}\, f^{(i)}(s), \tag{3.65a}$$

$$M_x^{\mathrm{in}(i)}(s) = -\chi(i)E_0^{(i)} f^{(i)}(s). \tag{3.65b}$$

If port(i) is the excited port we require that the fields for $z < 0$ are extinguished and the fields for $z > 0$ represent the TE_{10} mode traveling in the positive z-direction. Following Oseen's extinction theorem, we choose $J_y = 0$ and $M_x = 2M_x^{\mathrm{in}(i)}$ as the equivalent electric and magnetic surface currents at port(i_1). The corresponding expansion coefficients $D_{\mathrm{el},n}^{\mathrm{in}(i)}$ and $D_{\mathrm{mag},n}^{\mathrm{in}(i)}$ are calculated by taking the inner products on $[-1, 1]$ of (3.51a) with the rooftop functions $\Lambda_m^{(i)}$. Then,

$$D_{\mathrm{el}}^{\mathrm{in}(i)} = 0, \tag{3.66a}$$

$$D_{\mathrm{mag}}^{\mathrm{in}(i)} = -2\chi(i)E_0^{(i)}(G^{(i)})^{-1}W^{(i)}, \tag{3.66b}$$

where $W_m^{(i)} = \langle \Lambda_m^{(i)}, f^{(i)} \rangle_{[-1,1]}$ and $G^{(i)}$ is the Gram matrix of the functions $\Lambda_m^{(i)}$. These inner products and the Gram matrix can be calculated analytically. The Gram matrix is given by (D.5). For the inner products we distinguish the following cases: for $s_{m-1}^{(i)} \geq w_g^{(i)}/d_{\mathrm{port}(i)}$ or $s_{m+1}^{(i)} \leq -w_g^{(i)}/d_{\mathrm{port}(i)}$, $W_m^{(i)} = 0$. Otherwise, for $s_{m-1}^{(i)} < w_g^{(i)}/d_{\mathrm{port}(i)}$ and $s_{m+1}^{(i)} > -w_g^{(i)}/d_{\mathrm{port}(i)}$, we distinguish three cases

$$W_m^{(i)} = \Upsilon^-(s)\Big|_{-w_g^{(i)}/d_{\mathrm{port}(i)}}^{\min(s_{m+1}^{(i)}, w_g^{(i)}/d_{\mathrm{port}(i)})}, \qquad s_m^{(i)} \leq -w_g^{(i)}/d_{\mathrm{port}(i)}, \tag{3.67a}$$

$$W_m^{(i)} = \Upsilon^+(s)\Big|_{\max(s_{m-1}^{(i)}, -w_g^{(i)}/d_{\mathrm{port}(i)})}^{w_g^{(i)}/d_{\mathrm{port}}(i)}, \qquad s_m^{(i)} \geq w_g^{(i)}/d_{\mathrm{port}(i)}, \tag{3.67b}$$

$$W_m^{(i)} = \Upsilon^+(s)\Big|_{\max(s_{m-1}^{(i)}, -w_g^{(i)}/d_{\mathrm{port}(i)})}^{s_m^{(i)}} + \Upsilon^-(s)\Big|_{s_m^{(i)}}^{\min(s_{m+1}^{(i)}, w_g^{(i)}/d_{\mathrm{port}(i)})}, \qquad -w_g^{(i)}/d_{\mathrm{port}(i)} < s_m^{(i)} < w_g^{(i)}/d_{\mathrm{port}(i)}, \tag{3.67c}$$

where

$$\Upsilon^{\pm}(s) = \left(1 \mp \frac{s_m^{(i)}}{\Delta_{\mathrm{exp}}^{(i)}}\right)\frac{2w_g^{(i)}}{\pi d_{\mathrm{port}(i)}}\sin\left(\frac{\pi d_{\mathrm{port}(i)}}{2w_g^{(i)}}s\right) \pm \frac{1}{\Delta_{\mathrm{exp}}^{(i)}}\left(\frac{2w_g^{(i)}}{\pi d_{\mathrm{port}(i)}}\right)^2\left\{\cos\left(\frac{\pi d_{\mathrm{port}(i)}}{2w_g^{(i)}}s\right) + \frac{\pi d_{\mathrm{port}(i)}}{2w_g^{(i)}}s\sin\left(\frac{\pi d_{\mathrm{port}(i)}}{2w_g^{(i)}}s\right)\right\}. \tag{3.67d}$$

Let us consider the case that only port(i_1) is excited. Then, $D_{\mathrm{el}}^{\mathrm{in}(i_2)} = D_{\mathrm{mag}}^{\mathrm{in}(i_2)} = 0$ for port(i_2). We compute the expansion coefficients $D_{\mathrm{el},n}^{i,\mathrm{out}(i)}$ and $D_{\mathrm{mag},n}^{i,\mathrm{out}(i)}$ of the electric and magnetic output surface currents by multiplying the expansion coefficients in (3.66) where $i = i_1$ by the current matrix. The output surface currents are then given by (3.51b). The y-component of the electric field corresponding to the output surface current at port(i) is $M_x^{\mathrm{out}(i)}$. The projection of this component on the y-component of the electric field of the TE_{10} modes on the ports, as described

by (3.64), is

$$\frac{\langle E^{(i)}, M_x^{\mathrm{out}(i)}\rangle_{[-1,1]}}{\langle E^{(i)}, E^{(i)}\rangle_{[-1,1]}} E^{(i)}. \tag{3.68}$$

The inner product in the numerator can be written as

$$\langle E^{(i)}, M_x^{\mathrm{out}(i)}\rangle_{[-1,1]} = (E_0^{(i)})^* D_{\mathrm{mag}}^{i,\mathrm{out}(i)} \bullet W^{(i)}, \tag{3.69}$$

where we employ (3.51a), (3.65b) and (3.66b). The inner product in the denominator is given by

$$\langle E^{(i)}, E^{(i)}\rangle_{[-1,1]} = \left|E_0^{(i)}\right|^2 \frac{w_g^{(i)}}{d_{\mathrm{port}(i)}}. \tag{3.70}$$

The expansion coefficients of the output magnetic surface currents in (3.69) are proportional to the modal amplitude $E_0^{(i_1)}$. Thus the coefficient in (3.68) incorporates the unspecified amplitudes $E_0^{(i_1)}$ and $E_0^{(i)}$. To specify $E_0^{(i)}, i = 1, 2$, we require that the modal power at the ports should be equalized and hence $\langle E^{(1)}, E^{(1)}\rangle_{[-1,1]} = \langle E^{(2)}, E^{(2)}\rangle_{[-1,1]}$. By (3.70) we find

$$\left|E_0^{(2)}\right|^2 = \left|E_0^{(1)}\right|^2 \frac{w_g^{(1)}}{d_{\mathrm{port}(1)}} \frac{d_{\mathrm{port}(2)}}{w_g^{(2)}}. \tag{3.71}$$

Requiring also that the TE_{10} modes at the ports have equal phase, we obtain

$$E_0^{(2)} = E_0^{(1)} \sqrt{\frac{w_g^{(1)}}{w_g^{(2)}} \frac{d_{\mathrm{port}(2)}}{d_{\mathrm{port}(1)}}}. \tag{3.72}$$

Introducing $\hat{D}_{\mathrm{mag}}^{\mathrm{out}(i)} = D_{\mathrm{mag}}^{\mathrm{out}(i)} / E_0^{(i)}$ we can write (3.68) as

$$\sqrt{\frac{d_{\mathrm{port}(i_1)}}{w_g^{(i_1)}} \frac{d_{\mathrm{port}(i)}}{w_g^{(i)}}} \hat{D}_{\mathrm{mag}}^{\mathrm{out}(i)} \bullet W^{(i)} E_y^{(i)}. \tag{3.73}$$

The coefficient of $E_y^{(i)}$ is the scattering parameter S_{i,i_1},

$$S_{i,i_1} = \sqrt{\frac{d_{\mathrm{port}(i_1)}}{w_g^{(i_1)}} \frac{d_{\mathrm{port}(i)}}{w_g^{(i)}}} \hat{D}_{\mathrm{mag}}^{\mathrm{out}(i)} \bullet W^{(i)}. \tag{3.74}$$

This completes the calculation of the scattering parameters of a PWWG section with parallel input ports. These scattering parameters serve as input for a multi-line calibration to determine the propagation constant of uniform PWWG transmission lines, as has also been carried out for sets of uniform PWWG transmission lines simulated by HFSS in Section 3.2.

Chapter 4

Uniform Post-Wall Waveguides

In this chapter we verify experimentally the characteristics of PWWGs. In order to do so, test sets of uniform post-spacing PWWG transmission lines of different kinds are designed, manufactured and characterized. The results are then interpreted and compared with the simulation results. We investigate three different PWWG geometries:

- two types of PWWG in a high-permittivity substrate ($\varepsilon_{r,1} = 9.8$) with either,
  - metallic posts, or
  - dielectric posts ($\varepsilon_{r,2} = 1.0$), and
- one type of PWWG with metallic posts in a (relatively) low-permittivity substrate ($\varepsilon_{r,1} = 3.55$).

For the low-permittivity substrate we only consider metallic posts, since the dielectric contrast with air is too small to realize a PWWG with dielectric posts with acceptable loss and dimensions. In Section 4.1 design of these PWWG transmission lines is considered and all the dimensions of the structures are determined. In Section 4.2 the measurement procedure and the multi-line calibration used to extract the propagation constant from scattering-parameter measurements are considered. In Section 4.3 we present measurement setups for the various manufactured samples and we discuss particular setup aspects. Finally, results from the measurements are presented in Section 4.4 and these results are discussed and compared with simulation in Section 4.5.

4.1 Design

This section treats printed circuit board (PCB) designs for the aforementioned types of uniform PWWG transmission lines. A set of uniform transmission lines of different lengths is required when using the multi-line calibration method to determine the propagation constant. The choice for and the details of this calibration method will be explained in Section 4.2. We designed the test sets for operation at 10 GHz, because in this band

- the measurement accuracy is high due to good repeatability and low (cable) losses,

- the waveguide dimensions are sufficiently small, so that a large number of components fit on a test panel that is easy to handle,
- the waveguide dimensions are sufficiently large, so that the manufacturing tolerances have a minor influence on the characteristics, and
- high performance 10 GHz coaxial connectors for PCB mounting exist.

The standard air-filled waveguide for the 10 GHz frequency band is WR-90, which has inner dimensions of $w_g = 22.87$ mm and $h_g = 10.16$ mm and, consequently, a cut-off frequency for the dominant TE_{10} mode of $f_{co} = 6.55$ GHz; the operational band of this mode is 8.2–12.4 GHz. We use these specifications as a starting point in our designs. We select two substrates with high and low permittivity, respectively, such that it is possible to manufacture the samples in a glass/epoxy-based printed circuit board facility: Rogers TMM10i laminate as the high-permittivity substrate ($\varepsilon_{r,1} = 9.80$) and Rogers RO4003C as the low-permittivity substrate ($\varepsilon_{r,1} = 3.55$). The high-permittivity substrate is required for PWWGs with dielectric posts in order to create sufficient dielectric contrast for guided-wave propagation.

4.1.1 High-Permittivity Substrate

Accounting for the high relative permittivity $\varepsilon_{r,1} = 9.8$, the scaled width of WR-90 waveguide is 7.3 mm. As described in Section 3.2 the width of a corresponding PWWG is determined by first specifying the effective width (see e.g. (3.10)) and next by determining the width by simulations or empirically derived expressions (see e.g. (3.13)).

Metallic Posts

For the metallic posts in the high-permittivity substrate we choose $w_{g,\text{eff}} = 8.05$ mm as the effective width of the PWWG, which corresponds to $w_g = 8.91$ mm. We require that the ratio of the thickness of the PCB layer and the effective waveguide width be close to the ratio of WR-90 waveguide, i.e., 2.25. Hence the most suited thickness of Rogers TMM10i is $h_g = 3.81$ mm.

Dielectric Posts

For the dielectric posts we choose the same PWWG width $w_g = 8.91$ mm and the same PWWG height h_g. The dielectric posts in the waveguide are (air-filled) holes that are drilled in the circuit board. The dielectric contrast between the central guiding region and the post-wall regions dictates the amount of scattering at the waveguide walls. In maximizing this scattering, we minimize the leakage loss of the propagating wave. The dielectric contrast is determined by both the permittivity of the circuit board and by the *effective* permittivity of the post-walls which is dependent on the relative dielectric and air volumes. Given the fixed permittivity of the circuit board, $\varepsilon_{r,1} = 9.8$, we can further increase the dielectric contrast by

- increasing the post diameter,
- increasing the number of parallel rows of posts per side-wall, or
- decreasing the distance between the posts in a side-wall.

Frequency	Attenuation (dB/m)			
	$L = 1$	$L = 2$	$L = 3$	$L = 4$
8 GHz	146	22.4	5.95	2.96
10 GHz	70.9	11.3	6.24	6.93
12 GHz	37.4	9.73	9.37	7.82

Table 4.1 — Computed attenuation at 8, 10, and 12 GHz for three PWWGs with $L = 1, 2, 3, 4$ linear arrays of posts per side wall. Computations with our approach described in Section 3.4 and 3.5 combined with multi-line calibration. Simulation parameters: $\varepsilon_{r,1} = 9.8$, $\varepsilon_{r,2} = 1.0$, $a = 1.50$ mm, $d_x = 4.09$ mm, $d_z = 3.30$ mm, $d_{\text{port}(i)} = 12$ mm, $w_g = 8.9$ mm and $N_{\text{exp}} = 25$.

On the other hand the maximum distance between the posts is bounded by the grating condition and the post diameter is bounded by this distance and by manufacturing restrictions. For a post spacing of $d_z = 3.30$ mm along the direction of propagation, the frequency is bounded by $f_{\text{stop}} = 14.51$ GHz. This bound is acceptable since our band of operation is centered around 10 GHz and ranges up to 12.4 GHz. We choose a post radius $a = 1.50$ mm such that a distance of 0.15 mm exists between posts. This radius is the maximum feasible radius for the chosen production technology in combination with the spacing $d_z = 3.30$ mm. To achieve sufficient isolation we have chosen three linear arrays of posts per side wall. The distance between these linear arrays is $d_x = 4.09$ mm. The choice of four linear arrays per side wall is based on the computed attenuation of PWWGs with one, two, and three linear arrays per side wall, the results of which are listed in Table 4.1. For three parallel linear arrays per side wall ($L = 3$), the attenuation is below 10 dB/m and of approximately the same order as in the case of the PWWG with metallic posts.

Figure E.1 in Appendix E shows the layer stack of the circuit board. In the same appendix the specifications of the materials used are given. We constructed the PWWGs inside the thick Rogers TMM10i dielectric layer, i.e., the lower layer in Figure E.1. We designed PWWGs with metallic and dielectric posts, both by drilling through holes in the dielectric, which are electroplated with copper to form the metallic posts. Table 4.2 summarizes the final specification for the PWWG designs with metallic and dielectric posts. We refer to Figure 2.1 for an explanation of the different parameters. Note that f_{co} is the cut-off frequency of the TE_{10} mode and f_{stop} is the frequency at which the first stop band due to the periodicity starts.

To couple power into the PWWGs we use slot-coupled excitation to form a transition from microstrip line to PWWG. The details of this excitation are described in Section 5.2 and the details of connecting coaxial cables to the microstrip lines by means of coaxial connectors or probes are described in Section 4.4.1.

4.1.2 Low-Permittivity Substrate

Taking the low permittivity of the RO4003C dielectric into account for the metallic PWWGs, we find an effective width of $w_{g,\text{eff}} = 12.14$ mm for the PWWG with the same cut-off frequency as WR-90 waveguide. Posts with a radius $a = 0.50$ mm and an inter-post spacing of $d_z = 2.0$ mm can easily be manufactured. Using the approach described in Section 4.1.1, we find

Parameter	Symbol	Value		Unit
		Metal. posts	Diel. posts	
Rel. permittivity of PCB	$\varepsilon_{r,1}$	9.80	9.80	–
Rel. permittivity of posts	$\varepsilon_{r,2}$	–	1.00	–
Post radius	a	0.65	1.50	mm
Post spacing	d_z	2.57	3.30	mm
Inter-wall post spacing	d_x	–	4.09	mm
Number of rows per sidewall	L	1	3	–
Waveguide width	w_g	8.91	8.91	mm
Waveguide height	h_g	3.81	3.81	mm
Effective waveguide width	$w_{g,\text{eff}}$	8.05	–	mm
Cut-off frequency	f_{co}	5.95	–	GHz
First stop band frequency	f_{stop}	18.63	14.51	GHz
Loss tangent of PCB	$\tan\delta_1$	0.0020	0.0020	–

Table 4.2 — Specifications of the PWWGs, with metallic and dielectric posts in a high-permittivity substrate.

the PWWG width w_g to be 12.63 mm. Calculating the height of the PWWG directly from WR-90 rectangular waveguide dimensions, we arrive at a height h_g of 5.39 mm. At the upper limit of the frequency band (12.4 GHz) the waveguide is 0.42 wavelengths high. Since this can lead to unwanted resonances in the GCPW feed line that we intend to use and that shares the same dielectric slab as that of the PWWG, we need to reduce the waveguide height h_g. For h_g = 1.524 mm, which is one of the standard heights of the RO4003C material, the waveguide is 0.12 wavelengths high at 12.4 GHz, which is sufficiently small to avoid resonances in the GCPW feed line. A reduction in waveguide height will not affect the phase characteristics of the propagating TE_{n0} modes, but it will increase the losses due to the finite conductivity of the waveguide walls and an increase of the electric-field strength. Figure 4.1 shows the contribution of the conductor losses to the total losses of a rectangular waveguide filled with RO4003C dielectric material, copper walls, and three different heights. The losses caused by the dielectric material are dominant. For a waveguide with a height h_g = 1.524 mm the conductor losses stay below 10 percent of the total losses within the 8.2 to 12.4 GHz frequency range. This percentage is twice the conductor-loss contribution for a waveguide with height h_g = 5.39 mm, but it is still sufficiently small to consider the dielectric losses to be dominant.

The detailed layer stack and manufacturing information for the low-permittivity boards are given in Figure E.1 in Appendix E. Table 4.2 summarizes the specifications for the PWWG designs with metallic posts. The PWWGs are constructed in a Rogers RO4003C layer by drilling and plating holes within the slab, which is enclosed by a top and bottom ground plane. The excitation structure has been integrated in the top ground plane, see Section 5.3 for an extensive description.

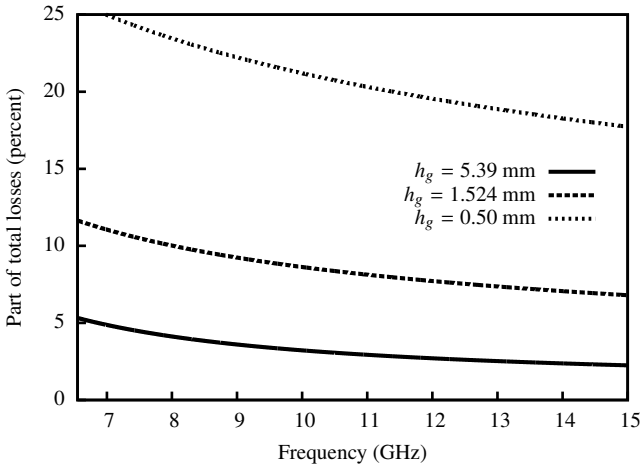

Figure 4.1 — Contribution of the conductor losses to the total losses of the TE_{10} mode in a rectangular waveguide with annealed copper walls as a function of frequency. Total loss: loss of dielectric filling and loss of conducting walls. Waveguide dimensions and material specifications: $w_g = 12.14$ mm, $\varepsilon_{r,1} = 3.55$, $\tan\delta = 0.0027$, and $\sigma = 5.8 \cdot 10^7$ S·m^{-1}. Plots for three different waveguide heights h_g.

Parameter	Symbol	Value	Unit
Rel. permittivity of PCB	$\varepsilon_{r,1}$	3.55	–
Post radius	a	0.5	mm
Post spacing	d_z	2.0	mm
Waveguide width	w_g	12.63	mm
Waveguide height	h_g	1.524	mm
Effective width	$w_{g,\mathrm{eff}}$	12.14	mm
Cut-off frequency	f_{co}	6.55	GHz
First stop band frequency	f_{stop}	39.78	GHz
Loss tangent of PCB	$\tan\delta_1$	0.0027	–

Table 4.3 — Specifications of the PWWG with metallic posts in a low-permittivity substrate.

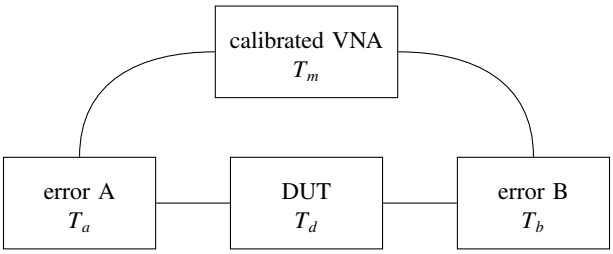

Figure 4.2 — A specific error model of a two-port scattering-parameter measurement with a calibrated VNA. For the multi-line calibration, transmission lines of different lengths are inserted as the device under test. T matrices: wave-transmission matrices associated to the blocks.

4.2 Measurement Procedure

We measure the scattering parameters of the test samples with a vector network analyzer (VNA) that is first calibrated using SOLT (short-open-load-through) standards, following applicable equipment procedures. This places the reference planes at the connection of the mounted connectors on the test structure and those at the outer ends of the VNA coaxial cables. The procedure accounts for the systematic errors introduced by the VNA itself. From the measured scattering parameters (after the SOLT calibration) we need to extract the complex propagation constant k_z of the propagating mode. In [74], Marks proposes multi-line calibration as a method to extract the propagation constant per frequency point from the scattering parameters of a set of transmission lines. We use this method to determine the propagation constant of the PWWG transmission lines. In the following we discuss the method and our implementation to extract the propagation constant of PWWGs from their scattering parameters.

Figure 4.2 depicts the error-box formulation for a two-port scattering parameter measurement with a VNA [75]. The VNA in the figure represents an ideal error free vector network analyzer. The error boxes A and B represent all the perturbations of the measurement result that occur due to the connectors, transmission lines, and transitions. In our formulation we assume perfectly isolated error boxes, or in other words, we assume that the levels of direct coupling between the two ports are negligible with respect to the coupling through the device under test (DUT). Consequently, in our formulation the coupling between A and B occurs solely through the DUT. We further assume that the error boxes A and B are constant, also in case a new sample is inserted as DUT. This assumption is only approximately satisfied for a real measurement setup, because connector connections and disconnections and manufacturing differences between samples introduce variations in the error boxes. We assume that these variations are also negligible.

We consider a set of transmission lines where the length of the ith line is l_i; each line is inserted as a DUT in the model of Figure 4.2. We characterize each block in the figure by a wave-transmission matrix, where T_a and T_b represent error box A and B, respectively, T_m^i is the wave-transmission matrix measured by the calibrated VNA and T_d^i is the theoretical wave-transmission matrix of line i. The reason to work with wave-transmission matrices instead of scattering matrices is the straightforward description of multi-line calibration in terms of

cascadable wave-transmission matrices. The wave-transmission matrices T_m, T_a, T_d, and T_b are related to their respective scattering matrices by the relationship

$$T = \frac{1}{S_{21}} \begin{pmatrix} S_{12}S_{21} - S_{11}S_{22} & S_{11} \\ -S_{22} & 1 \end{pmatrix}. \tag{4.1}$$

and they are related to each other by

$$T_m^i = T_a T_d^i T_b. \tag{4.2}$$

For a pair of measured transmission lines i and j we define the matrices T_m^{ij} and T_d^{ij} by

$$T_m^{ij} T_m^j = T_m^i, \qquad T_d^{ij} T_d^j = T_d^i. \tag{4.3}$$

Substituting these two expressions in (4.2) we obtain $T_m^{ij} T_m^j = T_a T_d^{ij} T_d^j T_b$. By (4.2) with i replaced by j we can write this relation as $T_m^{ij} T_a T_d^j T_b = T_a T_d^{ij} T_d^j T_b$. In practice, $T_d^j T_b$ is invertible and it follows that

$$T_m^{ij} T_a = T_a T_d^{ij}. \tag{4.4}$$

Let us assume for the moment perfectly-matched uniform transmission lines. The wave-transmission matrix of such an ideal transmission line of length l_i is a diagonal matrix with diagonal elements $e^{jk_z l_i}$ and $e^{-jk_z l_i}$, T_d^{ij} is a diagonal matrix given by

$$T_d^{ij} = \begin{pmatrix} e^{jk_z(l_i - l_j)} & 0 \\ 0 & e^{-jk_z(l_i - l_j)} \end{pmatrix}. \tag{4.5}$$

From (4.4) it follows that T_m^{ij} and T_d^{ij} share the same eigenvalues (provided that T_a is invertible). Therefore, the diagonal elements of the matrix T_d^{ij} are the eigenvalues of the matrix T_m^{ij}. We observe that $N + 1$ measurements of transmission lines yield N independent measurements, which is the number of transmission line pairs. We use the average of the eigenvalues λ_1^{ij} and λ_2^{ij} of T_m^{ij} to estimate the phase difference between the lines i and j,

$$\phi^{ij} = -j \ln \left[\frac{1}{2} \left(\lambda_1^{ij} + \frac{1}{\lambda_2^{ij}} \right) \right]. \tag{4.6}$$

If the transmission line is not ideal, the matrix T_d^{ij} is not a diagonal matrix and all elements will exhibit perturbations. From Marks [74] we know that

- the error in k_z is reduced by enlarging the difference in line lengths $l_i - l_j$,
- small reflections in the transmission lines do not influence k_z; the errors in the transmission coefficients determine predominantly the errors in the eigenvalues, and
- the Gauss-Markov theorem states that the best linear unbiased estimate (BLUE) of k_z is the weighted least squares solution to the phase differences ϕ^{ij} and the length differences $l_i - l_j$.

Since the measured scattering parameters are represented by phasors, the value of the phase difference estimate in (4.6) represents the phase difference modulo 2π. Hence, we have a solution ambiguity. To resolve this ambiguity we estimate first the number of 2π transitions for each line pair $(1, i)$ based on the difference in geometrical length of line 1 and line i and the wavelength in the dielectric. Here, 1 indicates the line with the shortest length. We observe that the number of phase transitions for line pair $(1, i)$ is always equal to or larger than for line pair $(1, j)$ when $l_i > l_j$. We set a maximum number of phase transitions for the line pair $(1, i)$ with i the line with the largest length. In this way we limit the possible combinations of phase transitions for the set of transmission-line pairs that we need to investigate to resolve the ambiguity. For each combination of phase transitions of the pairs we calculate the variance of the least squares approximation and we select the combination with the lowest sum of squares of the residuals.

To perform the multi-line calibration we use our own numerical implementation.We note that this program uses an equally-weighted linear least-squares procedure to determine the propagation constant. Finally, we emphasize that the multi-line procedure extracts the propagation constant only if there is one dominant propagating mode. If multiple modes propagate simultaneously in the transmission line under test, the model based on the T_d^{ij} matrix in (4.5) is no longer valid. To overcome this limitation, the multi-line calibration can be formulated in terms of generalized scattering matrices [76] such that a multi-modal calibration can be performed [77].

4.3 Measurement Setup

The setup that we use for all our measurements of uniform PWWGs, is a standard two-port VNA setup. Figure 4.3 depicts this generic setup. Three configurations, one for each of the three different PWWG types considered, with differently specified blocks in the measurement setup have been measured. The block specifications for each configuration are listed in the table of Figure 4.3. All the VNAs used exhibit similar performance and the choice of instruments was based on availability. In all cases a short-open-load-through (SOLT) calibration is carried out with the reference planes as indicated by the diagram. We discuss the details and further aspects of the three configurations in this section.

4.3.1 Measurements with Connectors on the High-Permittivity Substrate

The design of the high-permittivity PCBs is based on straight-angle surface-mount SMP connectors (Tensolite P703-2CC) connecting the coaxial cable to the microstrip line on the PCB. This connector is intended for use on relatively low-permittivity material (Rogers 4350; $\varepsilon_r = 3.66$). HFSS [15] was used to improve the connector footprint design for high-permittivity material. The two port scattering parameters for the coaxial-to-microstrip-line transition are depicted in Figure 4.5(a). Up to 12 GHz the match is better than -12 dB, which is much worse than the connector specification of -23 dB up to 18 GHz for the low-permittivity material. Although such a match is poor for a practical system, it is, nevertheless, adequate for the extraction of the PWWG characteristics when using multi-line calibration, since a considerable portion of the total power is transferred from the PWWG to the microstrip line.

Figure 4.4(a) shows a photograph of the measurement setup. The settings of the VNA are: intermediate frequency bandwidth (IFBW) 20 Hz, 1201 frequency points, frequency range 4–16 GHz, source power 7 dBm and SOLT calibration with Rosenberger SMP-19CK10A-150

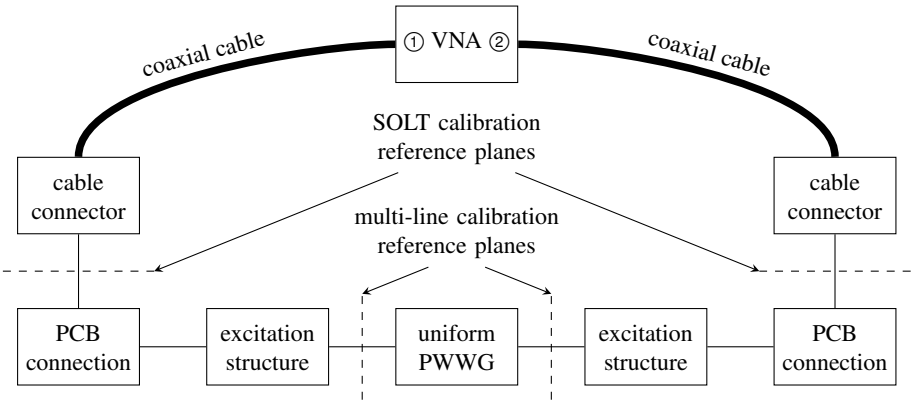

No.	VNA	Cable connector	PCB connection	Excitation structure	Uniform PWWG
1	Agilent N5230A PNA	SMP	Tensolite P703-2CC SMP	Microstrip to PWWG	High-permittivity substrate
2	Agilent E8361A PNA	SMA	Picoprobe 40A-GSG-1000-P probe	Microstrip to PWWG	High-permittivity substrate
3	Agilent N5242A PNA	SMA	Johnson-Emerson 142-0701-801 SMA	GCPW to PWWG	Low-permittivity substrate

Figure 4.3 — Measurement setup used in all three measurement configurations (high-permittivity substrate with coaxial connectors, high-permittivity substrate with probes and low-permittivity substrate with coaxial connectors) with details of implementation of the sub-blocks for each of the configurations.

calibration kit. As a consequence of the poor fit and the excessive play in the SMP connector parameters, we observe a substantial variation in the magnitude of the measured scattering parameters (±0.5 dB) and, therefore, the repeatability of the measurements is poor.

4.3.2 Probed Measurements on the High-Permittivity Substrate

The poor repeatability renders the measurement results practically useless, in particular to determine the losses of the PWWGs. To overcome the repeatability issues, we removed the connectors from the circuit boards and used ground-signal-ground (GSG) probes to connect directly to the microstrip lines near the connector footprints. The probes have a 1000 μm spacing (Picoprobe 40A-GSG-1000-P). Since the microstrip line does not extend inside the footprint ground, the PCB needs to be positioned under an angle such that the probe tips connect to the signal and to ground (see the photograph of Figure 4.4(c)); only one probe tip connects to ground via the connector footprint, the other is isolated and touches a metal-free part of the PCB. Because the designs were optimized for the SMP connectors, we expect the matching to be extremely poor. On the other hand we anticipate an improved repeatability and, despite the poor matching of the probes, this setup will yield more stable measurement results than the setup with the SMP

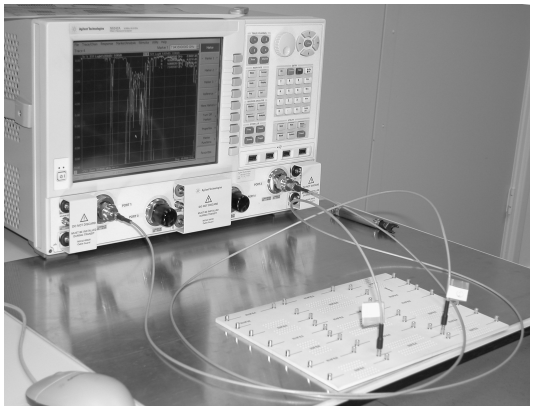

(a) SMP connector measurement setup

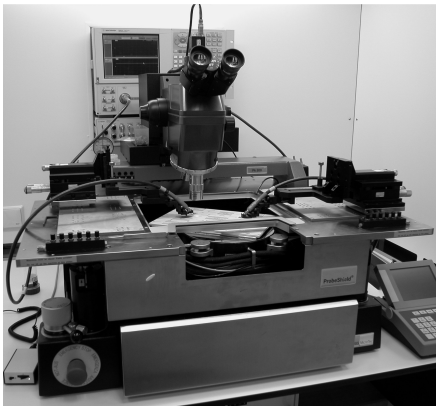

(b) Probe measurement setup

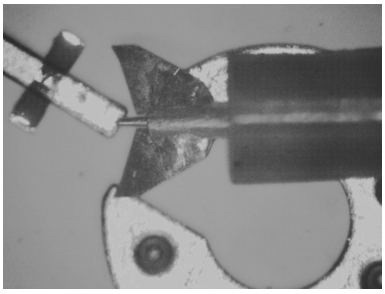

(c) Probe detail

Figure 4.4 — Photographs of the measurement setups for the high-permittivity PCBs. (a) Setup with the surface-mounted SMP connectors. (b) Probe station used for the probed measurements. (c) Microphotograph of the Picoprobe GSG probe at the microstrip connector footprint during the probed measurements.

connectors.

We performed the measurements on a probe station (Süss MicroTec PA 200). A photograph of the measurement setup is shown in Figure 4.4(b). The settings of the VNA are: IFBW 500 Hz, 1001 frequency points, frequency range 5–15 GHz, source power 5 dBm and SOLT calibration (SOLT101000) with Picoprobe CS10 calibration substrate and reference plane on the probe tips.

4.3.3 Low-Permittivity Substrate

The measurement setups for the high-permittivity substrates revealed two problem areas: poor matching and poor repeatability. To avoid these issues, we chose end-launch connectors of the SMA type (Johnson-Emerson 142-0701-801) for the low-permittivity designs. These connectors have better matching characteristics than straight-angle connectors, which ensures higher repeatability of the connections.

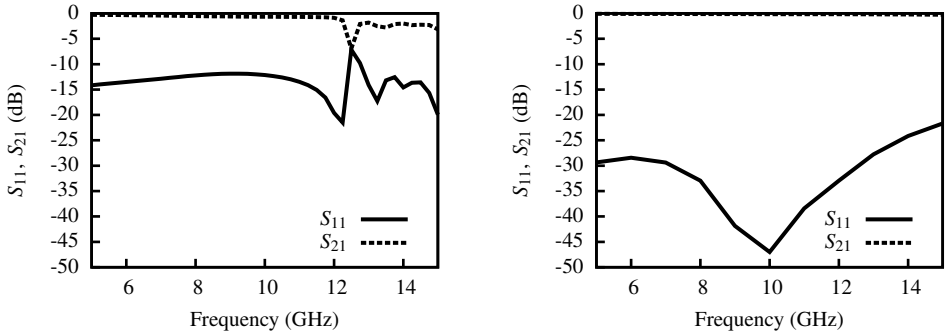

(a) SMP to microstrip

(b) SMA to GCPW

Figure 4.5 — Simulated results (HFSS) for the scattering parameters of a surface mounted Tensolite P703-2CC SMP connector on a high-permittivity substrate connected to a microstrip line and a Johnson-Emerson 142-0701-801 SMA connector on a low-permittivity substrate connected to a GCPW.

The simulated scattering parameters (HFSS) of the Johnson connector mounted on the low-permittivity substrate and connected to a GCPW transmission line are given in the graph of Figure 4.5(b) as a function of frequency. The performance ($|S_{11}|$ below -21 dB to 15 GHz) is much better than that of the SMP connector on the high-permittivity substrate.

The settings of the VNA are: IFBW 500 Hz, 901 frequency points, frequency range 0.01–18.01 GHz, source power 5 dBm and SOLT calibration with electronic calibration module (Agilent N4691-60004) fitted with SMA connectors.

4.4 Measurement Results

4.4.1 High-Permittivity Substrate

As mentioned in Section 4.3.1, the measurements of the high-permittivity substrates with the SMP connectors exhibited poor repeatability. The measurement uncertainty is unacceptably high for the connectorized measurements and, therefore, we present only the results that are based on the probed measurements of the high-permittivity substrate. In Chapter 5 we discuss the excitation of the PWWGs: for the high-permittivity substrates we use three different microstrip to PWWG transition designs to cover the complete bandwidth of the TE_{10} mode. Out of these three microstrip to PWWG transitions, only the lowest band (F1, centered at 8 GHz) matches sufficiently well to the probes to obtain useful results, which we present in this section. In this respect we emphasize that the high-permittivity substrates were not intended for probed measurements and therefore the matching is poor. Nevertheless, the repeatability of the probed measurements is better than that of the measurements with the SMP connectors.

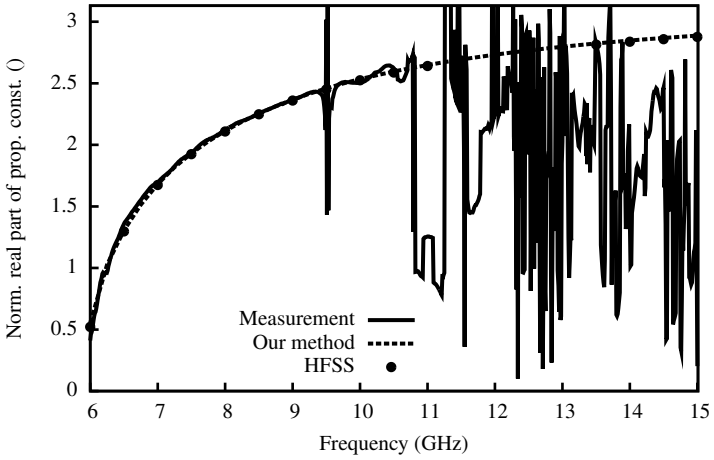

(a) Real part of the propagation constant

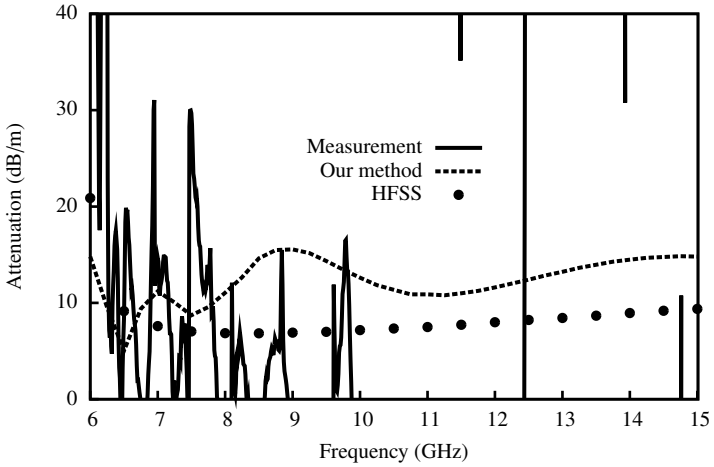

(b) Attenuation

Figure 4.6 — Propagation characteristics of a uniform PWWG with metallic posts in the high-permittivity substrate obtained from multi-line calibration applied to probed measurements, HFSS simulations, and our method. Depicted are the real part of the propagation constant (top graph) and the attenuation as a function of frequency. Normalization is with respect to k_0.

Results for Metallic Posts

Figure 4.6 shows for the dominant mode in the PWWG with metallic posts the normalized real part of the propagation constant and the attenuation in dB/m calculated with (3.18) from the imaginary part of the propagation constant. In the graphs we compare the results obtained through measurement to results obtained with HFSS and our method as described in Chapter 3. In the simulated cases, the scattering parameters of seven lines of 6, 7, 8, 10, 12, 14, and 35 unit-cell lengths are evaluated and used as input for a multi-line calibration. Our method uses a port width $d_{\text{port}(i)} = 10.21$ mm, a TE_{10} mode width $w_g = 8.85$ mm, $N_{\text{exp}} = 25$ expansion functions per port, $N_{\text{int}} = 5$ integration steps per rooftop function, and three expansion coefficients per post.

Results for Dielectric Posts

Figure 4.7 depicts the normalized real part of the propagation constant and the attenuation of the dominant mode in the PWWG with dielectric posts. The computational results are based on a set of seven lines with the same number of unit cells as in the case of metallic-post lines, namely 6, 7, 8, 10, 12, 14, and 35 unit-cells. Our method uses a port width $d_{\text{port}(i)} = 12.00$ mm, a TE_{10} mode width $w_g = 8.90$ mm, $N_{\text{exp}} = 25$ expansion functions per port, $N_{\text{int}} = 5$ integration steps per rooftop function, and three expansion coefficients per post.

4.4.2 Low-Permittivity Substrate

Figure 4.8 depicts the normalized real part of the propagation constant and the attenuation of the dominant mode in the low-permittivity samples. The simulated results (both HFSS and our method) are based on seven lines with lengths of 10, 11, 13, 15, 19, 33, and 55 unit cells. The settings used in our method are a port width $d_{\text{port}(i)} = 12.14$ mm, TE_{10} mode width $w_g = 12.14$ mm, $N_{\text{exp}} = 15$ expansion functions per port, $N_{\text{int}} = 10$ integration steps per rooftop function, and three expansion coefficients per post.

4.5 Discussion of Measured and Computed Results

4.5.1 High-Permittivity Substrate

Metallic Posts

Figure 4.6(a) shows a reasonable agreement (within 3 percent) between the simulated and measured results for the real part of the propagation constant up to 10.75 GHz, except for a spike at 9.5 GHz and a deviation of our method close to the cut-off frequency. Figure 4.6(b) shows that the variations in the measured results for the attenuation constant are quite large compared to the simulated results. Hence, the measured values are practically useless. Comparing our method to HFSS, we observe a different trend close to cut-off, where the HFSS results better meet our expectations. Possible explanations are: 1. loss of accuracy near cut-off caused by a critical sensitivity of the results with respect to the port parameters near cut-off in our implementation and 2. a problem related to the calculation of nonnormalized scattering parameters in our method.

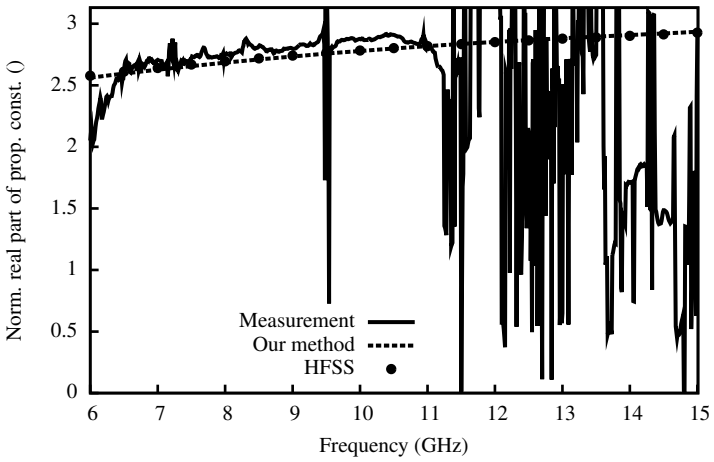

(a) Real part of the propagation constant

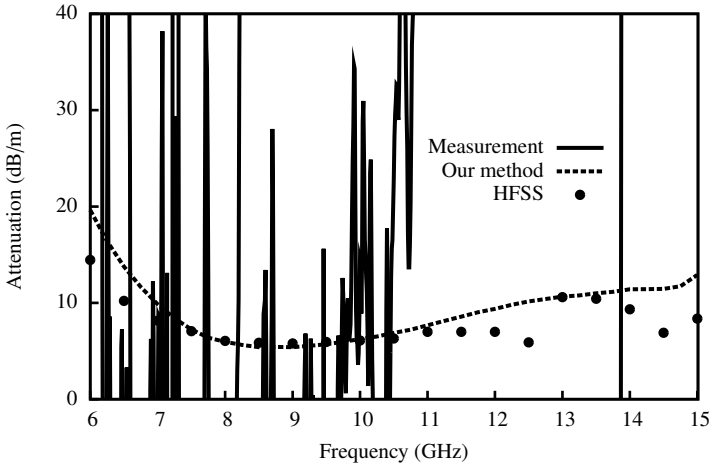

(b) Attenuation

Figure 4.7 — Propagation characteristics of a uniform PWWG with dielectric posts in the high-permittivity substrate obtained from multi-line calibration applied to probed measurements, HFSS simulations, and our method. Depicted are the real part of the propagation constant (top graph) and the attenuation as a function of frequency. Normalization is with respect to k_0.

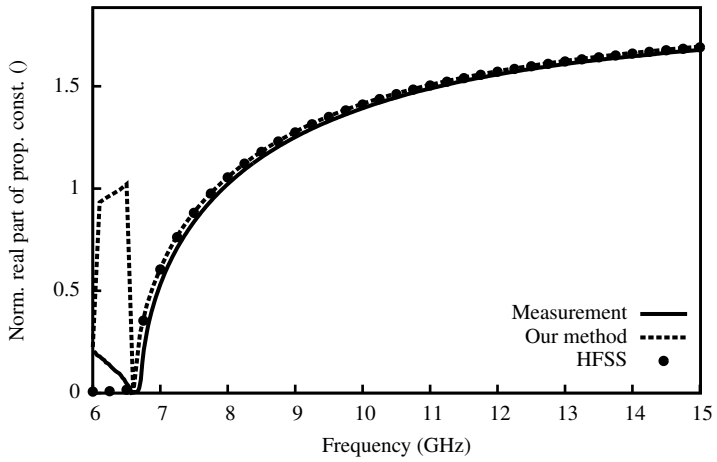

(a) Real part of the propagation constant

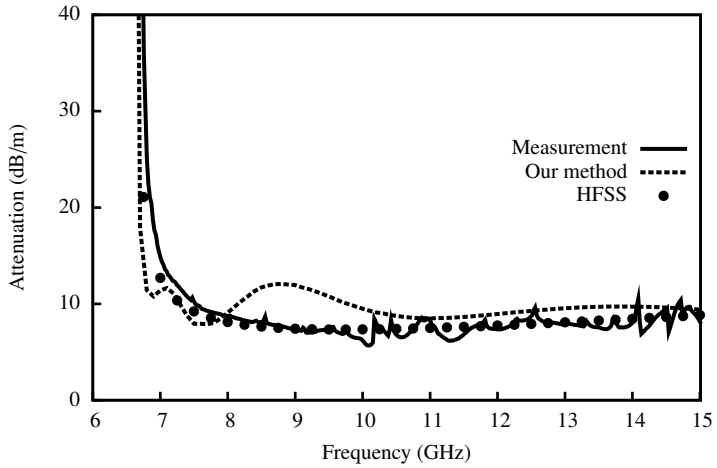

(b) Attenuation

Figure 4.8 — Propagation characteristics of a uniform PWWG in the low-permittivity substrate obtained from multi-line calibration applied to measurements, HFSS simulations, and our method. Depicted are the real part of the propagation constant (top graph) and the attenuation as a function of frequency. Normalization is with respect to k_0.

Dielectric Posts

The results for the PWWGs with dielectric posts are plotted in Figure 4.7. We observe that the computational results for the real part of the propagation constant in Figure 4.7(a) almost coincide; the differences are less than a percent. The measured values are structurally higher than the computed values, up to 4 percent in comparison to our method. Comparing the simulated and measured attenuation in Figure 4.7(b), we observe that the measurements demonstrate little or no correlation to the computed values. The two computational methods show a maximum difference of 5 dB/m (at 12.5 GHz). The attenuation curve obtained by HFSS appears less smooth than the curve obtained by our method, especially above 12 GHz. This could originate from the propagation of higher-order modes and the difference in field discretization approach of each method.

It is apparent that the measurement accuracy for high-permittivity structures is poor, which is especially prominent when extracting the attenuation constant. We list a number of issues that can contribute to this result.

- The matching of the probes to the microstrip line is extremely poor. In the band of operation almost total reflection occurs at the interfaces and no power is transmitted into the microstrip lines (see Figure 4.9). This explains the spikes in the results at 9.5 GHz and shows also severe limitations of the measurement accuracy.

- The absolute value of the imaginary part of $k_z l$ is much smaller than the absolute value of its real part (typically a factor 500), but both parts are affected by the same absolute error. Consequently, the effect of this error is much more severe for the imaginary part. To obtain the same accuracy that we find for the real part, we should consider the imaginary part of a proportionally longer line. This is, in general, not practically feasible.

- Multi-modal propagation affects the accuracy of the measurements, since we assume single-mode propagation. Above 12 GHz the disturbed response of the real parts is caused by the TE_{20} mode propagating in the PWWG with the metallic posts. The rough behavior of the results for the PWWG with dielectric posts may also be explained by the propagation of other modes beside the TE_{10} and TE_{20} modes.

- The transition design with three different frequency sub-bands in order to cover the complete waveguide band is far from optimal (see Chapter 5). The measurement results are affected by the poor match of the probes and the mediocre performance of in particular the two transitions at the highest sub-bands (F2 and F3).

- The manufactured boards show cracks in the substrate layer that arose during the manufacturing process. The cracks may introduce an additional variation among the different lines that leads to increased measurement uncertainty.

- The largest length difference between two lines is 10 unit cells (Δl = 25.7 mm for metallic posts and Δl = 33.0 mm for dielectric posts). This length difference corresponds to an approximate attenuation difference of 0.3 dB, which is in the order of the measurement accuracy and the contributions of the disturbances. This observation is a further indication that the measurements with the SMP connectors, with a non-repeatable variation of ±0.5 dB, are useless.

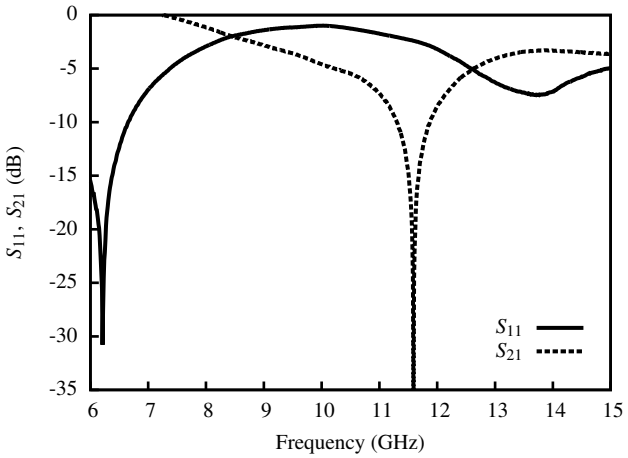

Figure 4.9 — Measured scattering parameters of a probed microstrip through line on a high-permittivity substrate with the reference plane of the SOLT calibration at the probe tips. The results are the scattering parameters of error box at port 1 resulting from TRL calibration using the microstrip TRL standards on the high-permittivity PCB.

- Manufacturing and material tolerances contribute to the variation of the measured results.

Concerning the poor match of the probes to the microstrip line, as shown in Figure 4.9, we note the following contributions to the poor match in the case of the probed measurements:

- the GSG probes are used with one ground unterminated (touching the dielectric), and
- the connector footprints contribute parasitics.

4.5.2 Low-Permittivity Substrate

Figure 4.8 shows that the measurement accuracy on the low-permittivity substrate is much higher than that on the high-permittivity substrate. All measured curves show a much smoother behavior and the attenuation curve shows a clear trend. The measured and computed (HFSS) real parts of the propagation constants in Figure 4.8(a) agree within 5 percent. The attenuation in Figure 4.8(b) shows similar behavior. The measurements and the HFSS results agree within 1.5 dB/m.

As a demonstration of the repeatability and as a measure for the measurement floor, we plot the reflection coefficients of the transmission lines that we use in the multi-line calibration in Figure 4.10. The plotted data is de-embedded with a TRL calibration and the reference planes are at the center of the shortest line (L0) in all three cases. We observe that the measured reflection is below −18.5 dB over the 8.2–12.4 GHz frequency range. The differences between the reflections of different samples are the result of variations between samples that originate from manufacturing, connector soldering, and connector mounting. $|S_{11}|$ computed by HFSS is

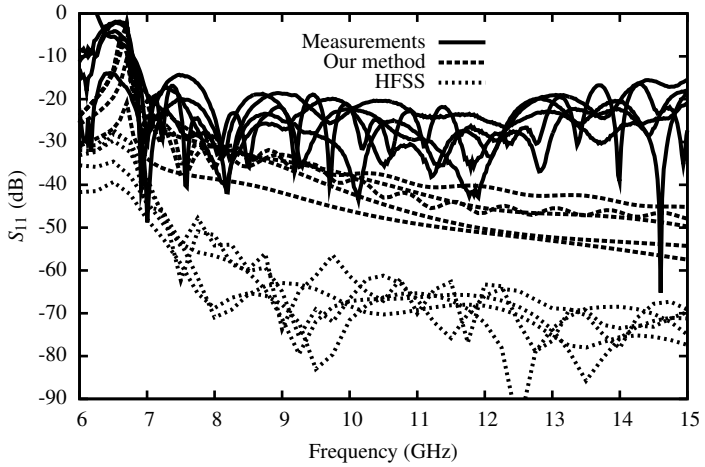

Figure 4.10 — Simulated by HFSS (lower curves) and measured (upper curves) reflection coefficients of the low-permittivity PWWGs with lengths $L_2 = 6$ mm, $L_3 = 10$ mm, $L_4 = 18$ mm, $L_5 = 46$ mm, and $L_6 = 90$ mm.

below −54 dB in this band. This value is determined by the meshing of the different samples and the numerical precision of HFSS and, hence, it is a measure for the overall numerical accuracy of the HFSS simulations. The same is valid for our own method. $|S_{11}|$ is below −30 dB.

CHAPTER 5

Excitation of Post-Wall Waveguides

An important aspect in the use of PWWG components is the excitation that couples power from a feed line into the PWWG. The excitation structure is a transition between two different transmission line types. Commonly, the feed line is of a (quasi-) TEM type, e.g. a coaxial line, a microstrip line, or a co-planar waveguide. These lines operate over very wide bands due to the nature of TEM propagation. The fractional bandwidth (FBW), where single-mode (TE_{10}) behavior of a PWWG can be achieved, is typically larger than 40 percent, while the bandwidth of (resonant) transitions is generally smaller. The transition will limit the overall bandwidth and its design must thus be properly attended to.

In Section 5.1 we review a variety of waveguide transitions described in the literature. Sections 5.2 and 5.3 treat the design of a microstrip line to PWWG transition and of a grounded co-planar waveguide (GCPW) to PWWG transition, respectively. A transition from a PWWG with metallic posts to a PWWG with dielectric posts is discussed in Section 5.4.

5.1 Literature Overview

Similarities between rectangular waveguide and PWWG (see Section 3.2) lead us to first consider classical transitions to rectangular waveguide in Section 5.1.1. Subsequently, we review the literature on different types of PWWG excitation structures in Section 5.1.2.

5.1.1 Transitions to Rectangular Waveguide

In the literature, three types of transitions are distinguished: probe-fed transitions (e.g. [78, Sec. 4.7], [79, Sec. 7–1a], [70, Sec. 7.1,7.2], and [80, Ch. 3]), slot-fed transitions (e.g. [78, Sec. 4.8] and [70, Sec. 7.3,7.4]) and tapered line transitions (e.g. [79, Sec. 4–2c]). Probe-fed transitions are the most often used type for rectangular waveguides. Slot-fed transitions have the disadvantage of a small bandwidth, especially if the strong coupling of resonant slots is used to obtain low insertion loss. The tapered-line transition can only be used if the two transmission lines can be smoothly reshaped. Generally it has the disadvantage of being long in terms of wavelength.

- In [81] a vertical voltage probe is proposed, that consists of a metal track –the extended

center conductor of a CPW– on a PCB that is inserted in the center of the waveguide. The probe couples power to the electric field of the TE_{10} mode. The transition operates over the full WR-90 band (8.2–12.4 GHz) with $|S_{11}|$ below −17 dB and $|S_{21}|$ above −0.5 dB. It exhibits a $FBW_{(17\ dB)}$ of 42 percent.

- In [82] a tapered line transition is described, where a CPW line ends in a tapered slot. In the rectangular waveguide underneath, a tapered ridge has been positioned in alignment with the slot in the top wall. This transition has $|S_{11}|$ below −11 dB and $|S_{21}|$ above −1 dB in the 18–26.5 GHz frequency range. It exhibits a $FBW_{(15\ dB)}$ of 3.7 percent.

- The transition in [83] consists of a rectangular slot to couple the fields of a microstrip line to the TE_{10} mode of a rectangular waveguide. The coupling is, in this specific case, very small (below −30 dB) and therefore the configuration is not suitable as transmission-line transition. In [84] and [85] the same concept is used to construct a back-to-back structure consisting of two microstrip lines coupled through a rectangular cavity.

- In [86] a tapered microstrip line to rectangular waveguide transition is presented, where the microstrip signal conductor connects to the top wall of the waveguide through an impedance taper. The measured $|S_{11}|$ is below −15 dB and $|S_{21}|$ is above −1 dB in the 9.6–10 GHz range for a back-to-back structure. The transition exhibits a $FBW_{(15\ dB)}$ of 4.1 percent.

- In [87] and [88] a non-radiative dielectric guide is coupled to a microstrip line through an aperture in the top metal wall. In the first reference a measured $|S_{11}|$ below −15 dB and $|S_{21}|$ above −2 dB for the back-to-back structure in the 18.7–19.2 GHz range is reported as well as a $FBW_{(15\ dB)}$ of 2.6 percent.

In summary, only the voltage-probe transition shows a bandwidth that is commensurate with the bandwidth of the TE_{10} mode in a rectangular waveguide.

5.1.2 Transitions to Post-Wall Waveguide

In virtually all reported configurations, PWWGs consist of (stacked) printed circuit boards with (metallized) holes that define the side walls. Hence, PWWG transitions are preferably planar or semi-planar structures with vias as the only vertical elements. As was the case for transitions to a rectangular waveguide, we encounter probe-fed and slot-fed transitions as well as a third type of transition, the tapered transition, where the feed line gradually transforms into the PWWG. In this section, we distinguish transitions to PWWG based on the feed line: rectangular waveguide, microstrip line, (G)CPW, and coaxial line.

Rectangular Waveguide

Transitions from rectangular waveguide are often used to feed PWWGs with dielectric posts. The critical design step is the matching of the air-filled rectangular waveguide to the dielectric-filled PWWG. In the literature, various implementations are described.

- In [29, 89] a tapered dielectric insert in a WR-10 waveguide is used. This insert is combined with one half of a pyramidal horn to connect to a PWWG with alumina or high-resistivity silicon as a dielectric medium and air holes as posts. A mean $|S_{21}|$ of 1.6 dB for a 20 mm long line, including the two transitions to a WR-10 waveguide, is reported for the silicon guide in the frequency range 85–105 GHz. The transition exhibits a FBW of 21 percent.

- In [24] a transition from a rectangular-slab waveguide to a PWWG is described, which consists of gallium arsenide (GaAs) dielectric with air holes. The dimensions of the feeding waveguide are related to the dimensions of the PWWG. The paper describes a qualitative and theoretical study; no conclusions as to bandwidth and loss are drawn.

- In [52] height tapering is applied to connect a WR-28 waveguide to a PWWG with a relative permittivity $\varepsilon_{r,1} = 10.2$. Since the air-dielectric interface is not tapered but straight, the performance of the transition is presumably poor, but is not explicitly specified in the paper.

- The authors of [90] use a two-step transformer with a dielectric probe to match the impedance of a WR-10 waveguide to a PWWG fabricated in alumina. The measured $|S_{11}|$ of the back-to-back transitions is below −15 dB and $|S_{21}|$ is between −3 and −8 dB in the 93–96.5 GHz frequency range. The transition exhibits a $\mathrm{FBW}_{(15\ \mathrm{dB})}$ of 3.7 percent.

- In [91], a ridged waveguide quarter-wavelength impedance transformer is used for impedance matching. The measurement of a back-to-back structure shows a $|S_{11}|$ below −20 dB and a $|S_{21}|$ above −0.8 dB between 20–26.5 GHz. A $\mathrm{FBW}_{(20\ \mathrm{dB})}$ of 26 percent is achieved.

- The transition described in [92, 93] consists of a 90° E-plane aperture coupler, where the width of the two waveguides is adjusted such that two impedance transforming sections are constructed. The measured $|S_{11}|$ is below −15 dB in the 53–68.1 GHz range. The transition exhibits a $\mathrm{FBW}_{(15\ \mathrm{dB})}$ of 25 percent.

Microstrip lines

Microstrip lines are popular transmission lines for the excitation of PWWGs as they offer easy compatibility with the semi-planar PWWG structures. The most popular configuration consists of a tapered microstrip that connects to the top plane of the PWWG. This structure has the advantage of being a very simple single-layer structure, but in planar technology the height of the waveguide is fixed by the height of the microstrip line. An alternative configuration consists of a slot-coupled microstrip line. We list a number of microstrip line to PWWG transitions.

- The tapered microstrip line transition presented in [20] ensures field matching between the TEM mode and the TE_{10} mode. The transition structure obtains a measured $|S_{21}|$ above −0.3 dB and $|S_{11}|$ below −15 dB over the 26–30.5 GHz range for a back-to-back configuration. Moreover, it exhibits a $\mathrm{FBW}_{(15\ \mathrm{dB})}$ of 16 percent. The same, or very similar structures, have been used in several other references, e.g., in [68], [94], [95], [96], [97] and [98].

- In [26] the transition of [20] is used to feed a PWWG with both metallic and dielectric posts. The measured $|S_{21}|$ is above −0.75 dB with $|S_{11}|$ below −15 dB in the 8–18 GHz range for a back-to-back structure. The transition exhibits a $\text{FBW}_{(15\text{ dB})}$ of 83 percent.

- The authors of [99] use an adjusted microstrip insert line to obtain a specified external quality factor required for the realization of a number of band pass filters.

- In [100], a microstrip line couples to a post-wall cavity resonator via a rectangular slot in the shared bottom microstrip ground plane and cavity top wall. This transition results in a back-to-back cavity structure with $|S_{21}|$ is −0.84 dB at 59.2 GHz, a 3 dB bandwidth of 0.89 GHz, and a $\text{FBW}_{(15\text{ dB})}$ of 1.5 percent.

Co-Planar Waveguide

Transitions from CPW have an advantage over microstrip lines in that the height of the substrate is less critical to the wave-guiding properties and that all the metallization is in a single plane. The first advantage is also true for grounded co-planar waveguides. A disadvantage of co-planar waveguides is the easy excitation of parasitic modes at discontinuities such as corners and bends. There is variety in coupling methods; voltage probes, current probes and slot couplers can be found.

- In [37] and [18] the coupling structure is a metallic post inside the PWWG. The post extends from the top wall to somewhere halfway the bottom wall and is electrically isolated from the top wall. A ground-signal-ground probe on top feeds the post that acts as a voltage probe and couples power to the TE_{10} mode through the electric field. In [18] a measured $|S_{21}|$ above −2 dB and $|S_{11}|$ below −15 dB over a frequency range of 75–90 GHz are reported for a back-to-back structure. The transition exhibits a $\text{FBW}_{(15\text{ dB})}$ of 18 percent.

- A CPW that feeds a rectangular slot in the top wall of a PWWG is the proposed structure in [19]. The bottom wall has only been metallized beneath the PWWG section and, therefore, the field distribution of the slot only couples efficiently to the TE_{10} mode in the PWWG. For the back-to-back structure, the measured $|S_{11}|$ is below −15 dB and the measured $|S_{21}|$ is above −3.5 dB in the 27.5–29.7 GHz range. The transition exhibits a $\text{FBW}_{(15\text{ dB})}$ of 7.7 percent.

- An improved version of the slot-coupled structure of [19], where the slot is strongly coupled to a post-wall cavity, is described in [101]. The measured $|S_{11}|$ is above −1.2 dB with $|S_{11}|$ below −15 dB over the 39–59 GHz frequency range. The transition exhibits a $\text{FBW}_{(15\text{ dB})}$ of 42 percent. A similar transition is proposed in [102], but there the transition is used to excite a PWWG with dielectric posts.

- The authors of [103] propose a current-probe transition. A GCPW that is shorted through a via to the bottom wall of a PWWG excites the TE_{10} mode by coupling to the magnetic field of the mode. The measured back-to-back transition exhibits $|S_{11}|$ below −15 dB and $|S_{21}|$ above −0.9 dB in the 26.5–30.2 GHz range. The transition exhibits a $\text{FBW}_{(15\text{ dB})}$ of 13 percent.

- For the current-probe transition in [104] the vertical probe is interrupted by a short horizontal strip halfway the probe, realizing a stepped transition with a more gradual field matching. The back-to-back structure has a $|S_{11}|$ below -15 dB and a $|S_{21}|$ above -1.9 dB in the 19.5–29.3 GHz frequency band. Moreover, it exhibits a $\text{FBW}_{(15\text{ dB})}$ of 41 percent.

Coaxial Line

Excitation structures based on coaxial lines consist mostly of a standard coaxial connector where the center conductor extends into the PWWG to act as a probe. The choice for coaxial structures of this kind is often based on avoiding an additional transition to the (measurement) equipment.

- In [105] and [106] the authors use SMA connectors that have been attached to the top wall of a PWWG. The center conductor is fed through a hole in the top wall and is electrically connected to the opposing bottom wall, effectively forming a current probe. No information on either the insertion or the return loss of the measured structures is provided.

- The power dividers in [107], [108], and [109] have similar transitions. The extended center conductor of a SMA connector is used as a current probe that excites the TE_{10} mode through the magnetic field. In [108] the authors report a measured $|S_{11}|$ below -15 dB combined with $|S_{21}|$ above -0.7 dB for a four-way coupler in the 7.5–11.5 GHz frequency range. The transition exhibits a $\text{FBW}_{(15\text{ dB})}$ of 40 percent. The measured eight-way divider in [107] yields $|S_{11}|$ below -15 dB with $|S_{21}|$ above -0.5 dB in the 4.9–5.5 GHz frequency range. Moreover, it has a $\text{FBW}_{(15\text{ dB})}$ of 12 percent.

- The coaxial line implemented in [110] consists of a stripline transmission line bounded on the sides by two rows of posts and so forming a coaxial line integrated in a printed circuit board. The line is used to feed a current-probe post in a PWWG from the side. Only simulation results, for a single transition, are presented. The $|S_{11}|$ is below -15 dB, while the $|S_{21}|$ is above -0.3 dB in the 25.5–40 GHz range. The transition exhibits a $\text{FBW}_{(15\text{ dB})}$ of 45 percent.

5.2 The Microstrip Line to Post-Wall Waveguide Transition

As discussed in Section 5.1.2, various methods have been proposed in the literature to excite PWWGs with microstrip lines. Based on the reported performance we formulate requirements for such a transition:

- compatibility with (standard) printed circuit board technology,
- minimal dependence on the microstrip and PWWG substrate heights, and
- a minimum bandwidth of 10–15 percent around 10 GHz.

Based on these requirements we conclude that the aperture-coupled microstrip line fits well. It is a planar structure, the conducting plane with the aperture isolates the two transmission lines, and based on results obtained with aperture-coupled antennas [111], a fractional bandwidth of 10–15 percent can be obtained.

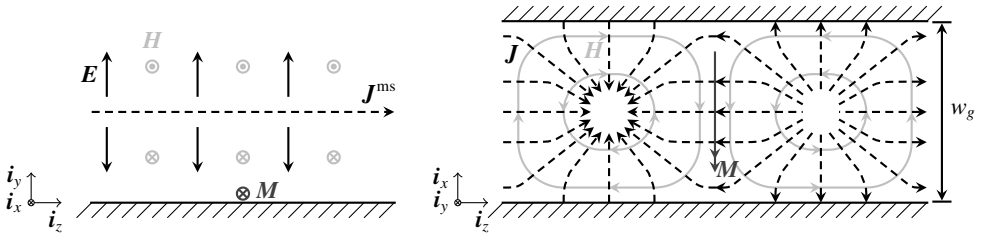

(a) microstrip (b) waveguide

Figure 5.1 — Fields and currents for a microstrip line, represented by an electric current filament above a perfect ground plane (side view) and the TE_{10} mode in a PWWG, represented by a rectangular waveguide (top view).

5.2.1 Transition Concept and Analysis

With the use of Love's equivalence principle, we can split the transition problem into two separate parts: a microstrip line above a perfect ground plane with a magnetic current at the ground plane and a PWWG with the same –but reversely directed– equivalent magnetic current at the top wall.

We start the analysis of the structure by regarding an infinitely long microstrip line and we assume that we can represent this configuration by an electric current filament $\boldsymbol{J}^{\mathrm{ms}} = J_z^{\mathrm{ms}}\boldsymbol{i}_z$ above a perfectly conducting ground plane. This configuration is depicted in Figure 5.1(a). The tangential electric field at the ground plane must vanish ($E_z = E_x = 0$) and only the current J_z exists. The z-component of Maxwell's equation (2.4b) is

$$\frac{\partial H_y}{\partial x} - \frac{\partial H_x}{\partial y} = j\omega\varepsilon E_z + J_z, \tag{5.1}$$

where $E_z = 0$ at the ground plane. Next we assume a (non-conductive) aperture in the ground plane, which is narrow in the z direction. At the aperture no electric current exists ($J_z = 0$) and the right-hand side of (5.1) reduces to $j\omega\varepsilon E_z$. Since the aperture is narrow, E_x is negligible and, hence, the aperture can be represented by a magnetic current $\boldsymbol{M} = \boldsymbol{n} \times E_z\boldsymbol{i}_z = E_z\boldsymbol{i}_x$, with $\boldsymbol{n} = \boldsymbol{i}_y$, the unit vector normal to the ground plane.

In the previous paragraph, we have represented the microstrip line by an electric current filament. For an infinite microstrip line (with a traveling wave in one direction) the current distribution is uniform, $I(z) = I_0^+ e^{-jk_z z}$. In the case of an open-ended microstrip line, the traveling wave will reflect at the open end. The result is a standing wave, with an associated current $I(z) = I_0^+ e^{-jk_z z} - I_0^- e^{jk_z z}$. The current is minimal at the open end ($z = 0$) and will exhibit a first maximum at $k_z z = \pi/2$, which is located a quarter wavelength from the open end. In order to obtain maximum excitation of the aperture, we need to position the center of the aperture a quarter wavelength from the open end of the microstrip line.

The TE_{10} mode is the dominant mode in the PWWG. The electromagnetic field associated with this mode is of the form

$$\boldsymbol{H} = H_x\boldsymbol{i}_x + H_z\boldsymbol{i}_z \qquad\qquad \boldsymbol{E} = E_y\boldsymbol{i}_y. \tag{5.2}$$

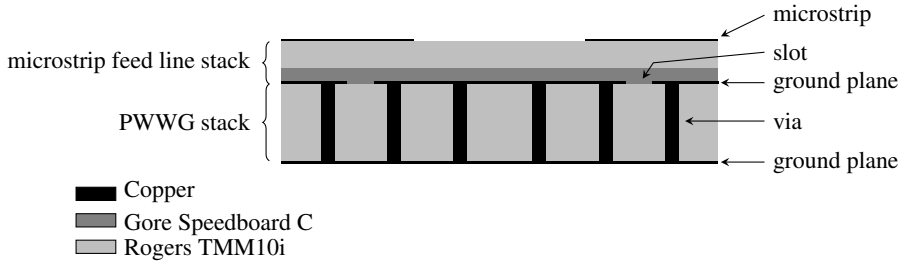

Figure 5.2 — Side view of the (back-to-back) microstrip line to PWWG transition, including the layer stack.

The tangential magnetic field at the waveguide top wall will generate an electric current $\boldsymbol{J} = \boldsymbol{n} \times \boldsymbol{H}$. Substitution of $\boldsymbol{n} = \boldsymbol{i}_y$ results in

$$\boldsymbol{J} = H_x \boldsymbol{i}_z + H_z \boldsymbol{i}_x. \tag{5.3}$$

From [36, Sec. 2.2] we find that for the TE_{10} mode (in a rectangular waveguide)

$$H_x \sim I(z) \sin \frac{\pi x}{w_g}, \qquad 0 \le x \le w_g, \tag{5.4a}$$

$$H_z \sim V(z) \cos \frac{\pi x}{w_g}, \qquad 0 \le x \le w_g. \tag{5.4b}$$

Figure 5.1(b) visualizes the magnetic fields and the surface currents in the top wall of a rectangular waveguide. The electric field at the aperture, and thus the electric currents near the aperture, must equal the fields and currents that are generated by the microstrip line in order to ensure good matching. Consequently, $\boldsymbol{J} = J_z \boldsymbol{i}_z$ close to the aperture. From (5.3) we observe that $\boldsymbol{J} = J_z \boldsymbol{i}_z$ requires that H_x is maximum and H_z is minimum, which occurs when $x = w_g/2$ in (5.4a) and (5.4b). Thus the current attains its maximum for $x = w_g/2$. To determine the corresponding z-coordinate, we follow a similar reasoning as with the open-ended microstrip line. For a shorted waveguide $I(z) = I_0^+ e^{-jk_z z} + I_0^- e^{jk_z z}$, and the current is maximum at the short position ($z = 0$). The next maximum occurs for $k_z z = \pi$, i.e., a half wavelength from the short position. We choose to position the aperture in the center of the waveguide and a half wavelength from the short position.

5.2.2 Implementation

We designed the microstrip line to PWWG transition with the aid of the finite-element solver Ansoft HFSS [15]. We tune the dimensions of the transmission lines and the aperture starting from the initial geometry as described in the preceding section and in [112].

The layer stack is specified in detail in Appendix E. Figure 5.2 shows the side view of the transition and the layer stack. The microstrip line has a 50 Ω characteristic impedance when $w_{\mathrm{ms}} = 0.430$ mm. The PWWG has been designed with $w_{\mathrm{g,eff}} = 8.00$ mm, which results in $w_{\mathrm{g}} = 8.91$ mm and $f_{\mathrm{co}} = 5.98$ GHz for the TE_{10} mode. The bandwidth of the TE_{10} mode is generally

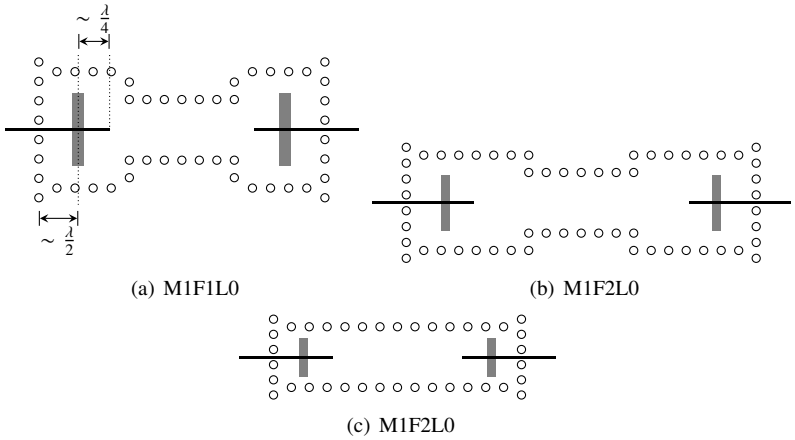

(a) M1F1L0 (b) M1F2L0

(c) M1F2L0

Figure 5.3 — Top views of the microstrip line to PWWG transitions, operating at 8 GHz (M1F1L0), 10 GHz (M1F2L0) and 11.5 GHz (M1F3L0). The microstrip feed lines with quarter wavelength open-circuit stubs are depicted in black, the aperture in the combined microstrip ground and PWWG top wall is depicted in gray, and the metallized posts with the short circuit at half a wavelength from the aperture are depicted by circles.

defined from $1.25 f_{\mathrm{co}}$ to $1.90 f_{\mathrm{co}}$, which is 7.48–11.36 GHz for f_{co} = 5.98 GHz. The design has been tuned to a center frequency of 10 GHz and we find $\mathrm{FBW}_{(15\ \mathrm{dB})}$ = 12.16 percent (ranging from 9.36–10.57 GHz, see Figure 5.4(a)) for a back-to-back structure. To approximately cover the whole band of the PWWG, the transition is also designed for lower (8 GHz) and higher (11.5 GHz) center frequencies. Thus we obtain three separate designs, each optimized for a part of the PWWG band. The top view of the layouts of the three transitions is shown in Figure 5.3. Figure 5.4 depicts the simulated and measured scattering parameters as a function of frequency for the three transitions in the back-to-back configuration. An overview of the characteristic data from these plots is given in Table 5.1.

5.3 The Grounded Co-Planar Waveguide to Post-Wall Waveguide Transition

Reviewing the microstrip line to PWWG transition of Section 5.2, we encounter two main disadvantages. Firstly, the fractional bandwidth of 7.07–16.4 percent is small compared to the bandwidth of the TE_{10} mode (typically more than 40 percent). Secondly, the structure is (relatively) complex to manufacture, since it consists of multiple circuit boards that need to be glued together. With respect to the limited bandwidth we observe that

- the open-ended microstrip-line stub is a resonating structure and therefore operates over a limited bandwidth,
- this holds equally for the shorted waveguide stub, and

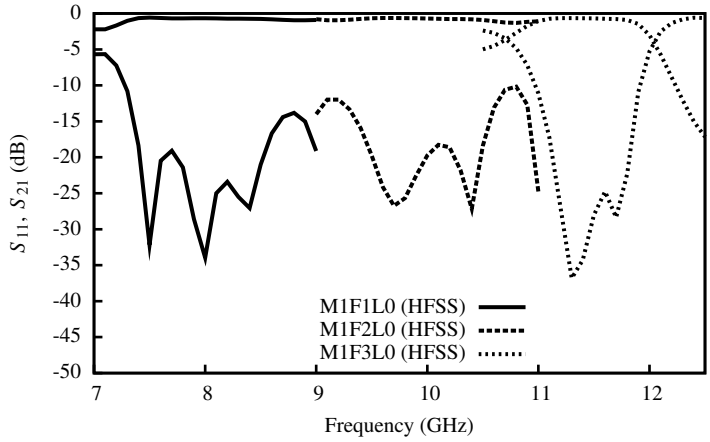

(a) simulation (HFSS)

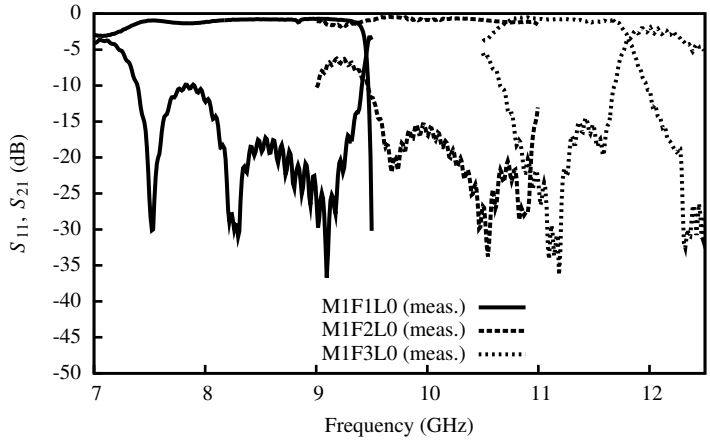

(b) measurement

Figure 5.4 — Simulated and measured scattering parameters for microstrip line to PWWG transitions in a back-to-back configuration. The three transitions are optimized at 8 GHz (M1F1L0), 10 GHz (M1F2L0) and 11.5 GHz (M1F3L0).

- the rectangular aperture operates close to its resonance frequency, which further limits the bandwidth of the transition.

From these observations we conclude that we need to remove all resonating structures from our design, in order to obtain a wide-band transition.

The second issue –the complexity of the multi-layer structure– can be overcome by integrating the feed line and the PWWG into a single printed circuit board. The heights of both transmission lines are then necessarily equal. This constrains the choice of PWWG geometry; for the specific considerations regarding the PWWG we refer to Section 6.2.

Transition		Freq. Range GHz	$FBW_{(15\ dB)}$ percent	Max. IL dB
M1F1L0	(measured)	7.38–9.37	23.93	1.36
M1F1L0	(simulated)	7.36–8.67	16.40	0.87
M1F2L0[1]	(measured)	8.69–10.10	15.05	1.79
M1F2L0	(simulated)	9.36–10.57	12.16	1.02
M1F3L0	(measured)	10.67–11.72	9.39	1.68
M1F3L0	(simulated)	11.06–11.87	7.07	1.30

[1] $FBW_{(10\ dB)}$ instead of $FBW_{(15\ dB)}$.

Table 5.1 — Measured and simulated performance of microstrip line to PWWG transitions. The data for the transition has been obtained from a back-to-back structure with reference planes at the microstrip line. For the M1F2L0 transition, the FBW is specified for $|S_{11}| = -10$ dB instead of $|S_{11}| = -15$ dB because of a small peak of $|S_{11}|$ just above -15 dB in the center of the band.

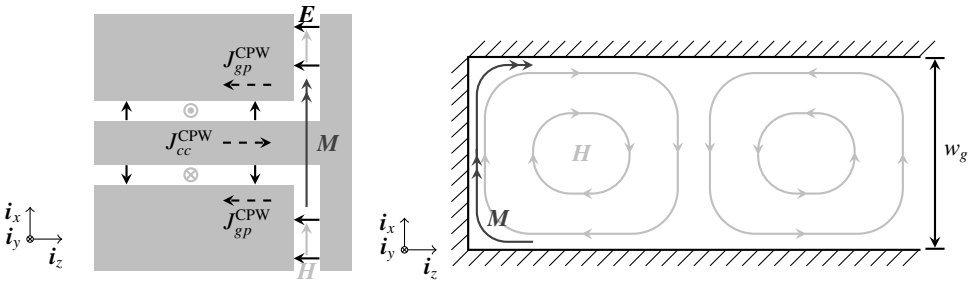

(a) CPW (b) RWG

Figure 5.5 — Fields and currents for a co-planar waveguide feeding an aperture (top view) and the TE_{10} mode in a shorted rectangular waveguide (top view).

5.3.1 Transition Concept and Analysis

The electric current induced in the ground plane by the microstrip line, as visualized in Figure 5.1(a), can be generated directly by a (G)CPW line that is aligned with the ground plane. Its center conductor passes through the center of the aperture and terminates in a short circuit at the other end of the aperture. This excites a maximum electric current J_{cc}^{CPW} at the aperture center. The counter-directed electric currents in the co-planar grounds, depicted in Figure 5.5(a) as J_{gp}^{CPW}, are perturbed by the gap that is formed by the aperture and from (5.1) we learn that this will be accounted for by an electric field at the aperture. The aperture can exactly like in Section 5.2 be represented by an equivalent magnetic current on the ground plane and this current excites the waveguide through the top wall.

Transition		Freq. Range GHz	$\mathrm{FBW}_{(15\ \mathrm{dB})}$ percent	Max. IL dB
MLCL0	(simulated)	7.60–13.46	57.94	0.63
MLCL0	(measured)	7.57–10.07	28.63	1.97
MLCL0[1]	(measured)	7.19–14.10	68.62	2.96

[1] $\mathrm{FBW}_{(10\ \mathrm{dB})}$ instead of $\mathrm{FBW}_{(15\ \mathrm{dB})}$.

Table 5.2 — Measured and simulated performance of the GCPW to PWWG transitions. The data is based on a single transition with the reference plane at a connected SMA coaxial connector. The FBW is specified for $|S_{11}| = -10$ dB for the measured transition because of a small peak of $|S_{11}|$ just above -15 dB in the center of the band.

The electric and magnetic fields at the aperture are parallel to the xz-plane and since

$$\boldsymbol{M} = \boldsymbol{i}_y \times \boldsymbol{E}, \qquad \boldsymbol{J} = \boldsymbol{i}_y \times \boldsymbol{H}, \tag{5.5}$$

$\boldsymbol{J}$ and $\boldsymbol{E}$ are aligned, as well as $\boldsymbol{M}$ and $\boldsymbol{H}$. If we look at the expression for the magnetic field of the TE_{10} mode at the top wall of a rectangular waveguide, given in (5.4), we notice that the direction of the fields becomes parallel to $\boldsymbol{i}_z$ near the side walls. By the introduction of a curve in the aperture we can deform the magnetic current $\boldsymbol{M}$ such that it aligns with the direction of the magnetic field. This is depicted in Figure 5.5(b) for a shorted rectangular waveguide. From this we also observe that the aperture can be positioned very close to the short location, to circumvent the resonating half-wavelength waveguide stub.

5.3.2 Implementation

We optimize and tune the design with Ansoft HFSS [15]. The circuit board is Rogers 4003C with a thickness of 1.524 mm, a relative permittivity of 3.55 and copper metallization on top and bottom. The dimensions of the grounded CPW with a characteristic impedance of 50 Ω are $h_{\mathrm{g}} = 1.52$ mm, $w_{\mathrm{gap}} = 0.25$ mm and $w_{\mathrm{cc}} = 1.20$ mm for the substrate height, the gap width and the center conductor width, respectively. The PWWG has been designed with $w_{\mathrm{g,eff}} = 12.15$ mm; this results in $w_{\mathrm{g}} = 12.63$ mm and $f_{\mathrm{co}} = 6.55$ GHz, for the TE_{10} mode and a usable frequency band 8.2–12.4 GHz. The top view of a back-to-back transition is depicted in Figure 5.6 and the simulated and measured scattering parameters for the de-embedded half of this structure are plotted in Figure 5.7; an overview of the characteristic data from the plot is given in Table 5.2.

5.4 The Metallic-to-Dielectric Post-Wall Waveguide Transition

The excitation of a PWWG with metal posts by a PWWG with dielectric posts is, basically, a matching problem where we need to minimize the reflection at the transition. In both PWWGs, the TE_{10} mode is the dominant propagating mode. The characteristic impedance of a TE mode

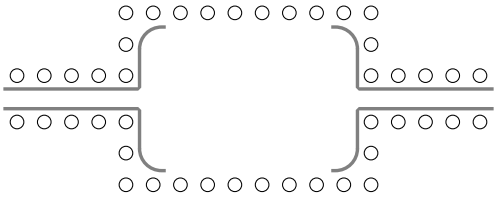

Figure 5.6 — Top view of the grounded CPW to PWWG transition. The GCPW gap and the coupling aperture are drawn in gray.

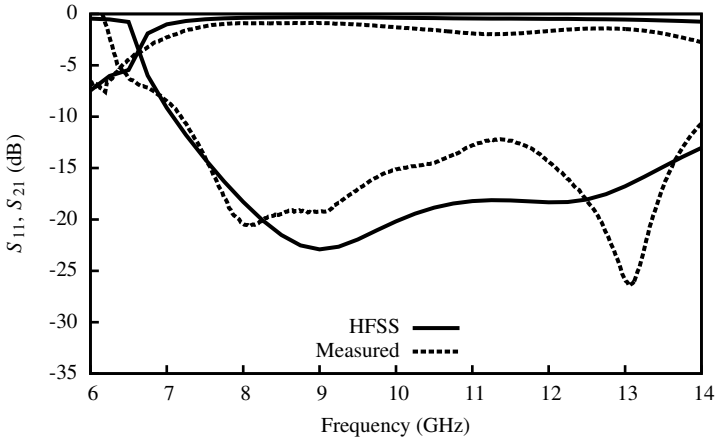

Figure 5.7 — Simulated and measured scattering parameters for the GCPW to PWWG transition in a single transition configuration. The measured results are obtained from the TRL calibration data of a back-to-back transition.

is related to its propagation constant

$$Z_{\mathrm{TE}} = \frac{\omega\mu}{k_z}. \tag{5.6}$$

This implies that we need to equalize the propagation constants of both types of PWWG in order to match their impedances. We use the procedure described in Section 3.1, which uses the infinite periodic array formulation to determine the propagation constant of a uniform PWWG. As an example, we formulate the design steps for a transition optimized at 11.5 GHz (based on the high-permittivity PWWGs as described in Section 4.1):

1. calculate the real part of the propagation constant of the PWWG with the dielectric posts ($k_z = 2.84k_0$ at 11.5 GHz),

2. determine, using an iterative approach, the width of a PWWG with metal posts that has the same propagation constant at 11.5 GHz ($w_g = 10.2$ mm), and

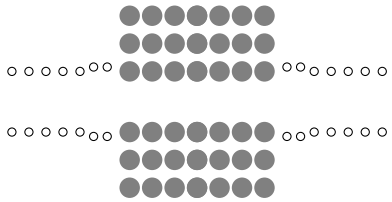

Figure 5.8 — Top view of a tapered PWWG with metallic posts to a PWWG with dielectric posts transition. The dielectric posts are depicted in gray and the metallic posts are depicted by the black circles.

3. design a smoothly tapered transition from the original width of the PWWG with metal posts (w_g = 8.91 mm) to the newly calculated width.

Figure 5.8 depicts the top view of such a tapered transition. We remark that

- the width difference (1.29 mm) is relatively small, hence the tapered section can be short,
- the transition has been optimized at a single frequency and since the dispersion curves of the two types of PWWG do not coincide, a mismatch will occur at other frequencies, and
- this is a (simple) matching procedure exploiting the infinite PWWG model; more classical matching introducing reactive elements in the waveguides could also be applied. This procedure will typically be more complicated.

A more systematic approach, possibly including the software developed in this project can be used to refine this design.

CHAPTER 6

Post-Wall Waveguide Components

In Chapter 4, we focused on the design of straight PWWGs. PWWG bends, T-junctions and other components can be designed starting from straight PWWGs in a manner conceptually analogous to rectangular waveguides. Components can be constructed and their scattering parameters can be tuned by combining several different sections of PWWG, adding or removing posts or making other modifications. In turn, these components can be combined to create more complex structures, such as a Butler matrix or filters. To design such PWWG-based structures, we would like to have at our disposal a component library similar to those existing for conventional transmission lines and discontinuities. This library can then be integrated with a circuit simulator such as Agilent's Advanced Design System (ADS). A numerical method that can calculate the scattering matrices of different types of components, is described in Chapter 2 and 3. We will validate this basis for our future library implementation by comparison with the literature, by simulations with other solvers and experimentally. The experimental validation requires a test set of PWWG components whose design and measurement is described in this chapter. We use both our own software code and Ansoft HFSS for the simulations and we compare the results.

In Section 6.1 we briefly review PWWG components that have been described in the literature with the aim to be representative rather than complete. Next, in Section 6.2, we discuss the design of a set of components including differential phase-shift sections, bends, a T-junction, couplers and a Butler matrix. The measurement setup is described in Section 6.3 followed by a comparison with the measurement results in Section 6.4. We conclude this chapter with an outlook to future requirements to improve the flexibility and to facilitate the integration of our numerical method with a circuit simulator.

6.1 Literature Overview

In the literature on PWWGs, we observe a shift of focus from uniform lines in the early publications to components in more recent work. In the last few years the number of papers on components has rapidly increased. Most of the work is based on PWWGs with metal posts. Some work on PWWG components with dielectric posts has been published, in part originating in the optical community. We distinguish in this overview four major categories of PWWG components, and discuss for each category some illustrative examples.

Bends are important components in complex networks, since they are often crucial to the efficient interconnection of components. The planar nature of typical PWWG manufacturing processes limits bends to be mostly of H-plane type. In [18, 94] 90° curved PWWG bends are presented, whose outer walls consist of a regular distribution of posts on a quarter circle trajectory. In [94], a mitered bend is presented; measurement results show poor matching compared to the rounded bend. In [113, 114] bends of 60° and 120° in a PWWG with dielectric posts are optimized for minimum leakage at the bends.

Splitters and combiners are used to distribute, or combine, power from one transmission line to multiple transmission lines or vice versa. Most power dividers are based on T- or Y-shaped junctions, see for example [18, 113, 115, 116]. The first three papers concern PWWGs with metal posts and the last discusses a T-shaped power divider with dielectric posts. In most cases these 1:2 dividers are combined into larger 1:N dividers. A slightly different approach can be found in [107, 117], which describe respectively the design of a 1:8 power divider and a magic-T based power divider.

Couplers selectively transfer part of the excitation power to a number of ports depending on the design specifications and the direction of propagation. Examples of a 90° and a 180° hybrid coupler with metal posts can be found in [90] and [97], respectively. In [59, 113, 118] examples of PWWG couplers with dielectric posts are discussed.

Filters and resonators are used to introduce frequency selectivity. The most used form is the bandpass filter. In [95, 96, 119] bandpass filtering is obtained through the introduction of metal posts inside a PWWG section. In [59, 113] the introduction of dielectric posts in a PWWG also yields a bandpass effect. Coupled post-wall cavities form the basic components of the bandpass filters described in [99, 100]. In [99] a cross-coupled filter with an elliptic filter function and operation around 20 GHz is designed and measured. Another use of PWWGs can be found in the oscillator designs of [120, 121], where post-wall cavities with high quality factors are used as the frequency determining elements.

Finally, aside from the categories described, we cite the three-port circulator in [91] as an example of a PWWG component integrated with a non-reciprocal element and, as an example of a complex combined system, the 4x4 Butler matrix with integrated slotted waveguide antenna array operating around 40 GHz discussed in [51].

6.2 Design of a Set of Test Components

The component test set that we design and characterize in this chapter consists of: a number of straight lines, a short, two phase-delay lines, a bend, a T-junction, a single and a cascaded Riblet short-slot coupler, a 5 dB coupler, two neighboring isolated lines, and a 4x4 Butler matrix. An overview of the test set components with designated name codes and brief component descriptions is given in Table E.3 of Appendix E. Pictures of the manufactured hardware samples are shown in Figure E.6. The uniform transmission lines in this set are described in Chapter 4. Here, we address the general design and measurement aspects of the other components in the set: the phase-delay lines, the bend, the junction, the couplers and the Butler matrix.

The test set is realized using standard microwave PCB material (Rogers RO4003C) with a low dielectric constant ($\varepsilon_r = 3.55$). The components are designed for operation from 8.2–12.4 GHz (the operational band of WR-90 waveguide), exploiting the high measurement accuracy, the convenient waveguide dimensions facilitating the realization of all the components on a single panel, and the availability of well-documented coaxial connectors (SMA). The choice of the PWWG dimensions is discussed in detail in Section 4.1.2 and the excitation structure with a GCPW feed line is discussed in Section 5.3.

We emphasize that the component designs in this chapter are not optimized designs and that our main purpose was to manufacture a set of components whose measurement results can be used for comparison with other characterization methods. In retrospect, our method for calculating the scattering parameters of PWWG components, as described in Sections 3.4 and 3.5, turns out to be unable to simulate some of the manufactured designs with the present implementation, as it puts some constraints on the types of PWWGs that can be handled:

- only two-port problems can be solved,
- both port planes must be in parallel,
- scattering parameter calculation has been based on the TE_{10} mode in a rectangular waveguide, and
- the cascading of sub-blocks of components at current-matrix level has been implemented but not yet been used (see Section 6.5 for details).

None of these constraints is inherent to our method; they emanate from the current implementation and are open to resolution.

For comparison of the scattering parameters obtained using our method, HFSS and the measurements, we use TRL calibration to normalize the scattering parameters to the impedance of the dominant mode.

6.2.1 Phase-Delay Lines

In microwave networks, a phase-shifting component is often required. Different PWWG geometries can be used to introduce phase shift. The phase delay ϕ of a transmission line depends linearly on the propagation constant k_z of the propagating mode and the length of the line l_g as

$$\phi = k_z l_g. \tag{6.1}$$

The propagation constant of a PWWG depends on the geometry of the unit cell, see Chapter 3. If we want to introduce a phase delay between two transmission lines of equal length l_g, but with different geometries and consequently two different propagation constants $k_{z,1}$ and $k_{z,2}$, the phase difference at the end of the transmission lines is

$$\Delta\phi = (k_{z,2} - k_{z,1}) l_g. \tag{6.2}$$

This relation is non-linear with frequency, since the propagation constant in a PWWG is a non-linear function of the frequency (see Section 3.1). The propagation constant in a rectangular waveguide is a function of the waveguide width, while the propagation constant of a PWWG

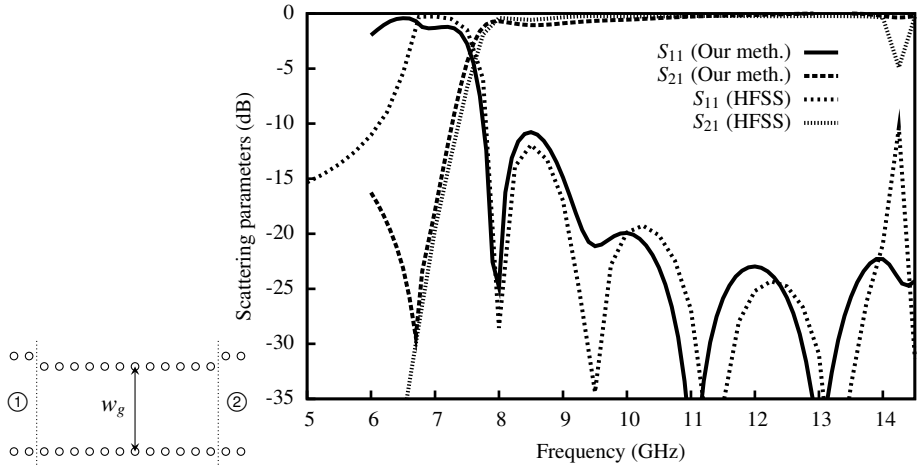

(a) Top view (b) Scattering parameters

Figure 6.1 — Top view and simulated scattering parameters (our method and HFSS) for a phase-delay line with w_g = 11.25 mm and l_g = 26.0 mm (CMPP1).

depends on the *effective width* of the guide. As demonstrated in Section 3.2, the effective width of a PWWG is determined by the waveguide width w_g, the post spacing d_z, the post radius a, and the number of side walls and their spacing d_y. For equal-length PWWGs, the width of the guides is the easiest parameter to control.

We design two phase-delay lines P1 and P2 such that they provide the phase shifts required by the Butler matrix in Section 6.2.4. In that section we describe in more detail how we determine the required phase shifts.

Decreasing the waveguide width lowers the propagation constant and thereby increasing the phase delay. At the same time, the cut-off frequency of the TE_{10} mode increases and, as a result, the operational frequency range reduces to 9.5–12.4 GHz. To calculate the phase delay we use two methods: one is based on the calculation of the propagation constant in an infinitely long PWWG using the modal representation as discussed in Section 3.1 and the other on the calculation of the phase of the scattering parameters with the finite-element method (HFSS). Figure 6.1(a) and 6.2(a) show the top views of the phase-delay lines with widths w_g = 11.25 mm and w_g = 10.75 mm. The centers of the narrow PWWGs are not aligned with the center of the feed-line PWWGs. This allows better integration with the Butler matrix as discussed in Section 6.2.4. The accompanying plots of Figure 6.1(b) and 6.2(b) show the calculated magnitudes of the scattering parameters. The plots compare the results based on our method with the results from Ansoft HFSS. $|S_{11}|$ computed by both our method and HFSS follow a similar trend: in the range 9.5–12.4 GHz they are below −19 dB; for our method the $|S_{21}|$ is above −0.67 dB and for HFSS above −0.27 dB. The second line has a $|S_{11}|$ below −17 dB combined with a $|S_{21}|$ above −0.82 dB in the 9.5–12.4 GHz frequency range, for our method as well as for HFSS. We also observe in this case that the two methods result in similar curves. The phase differences between the two phase-delay lines and a reference line of width

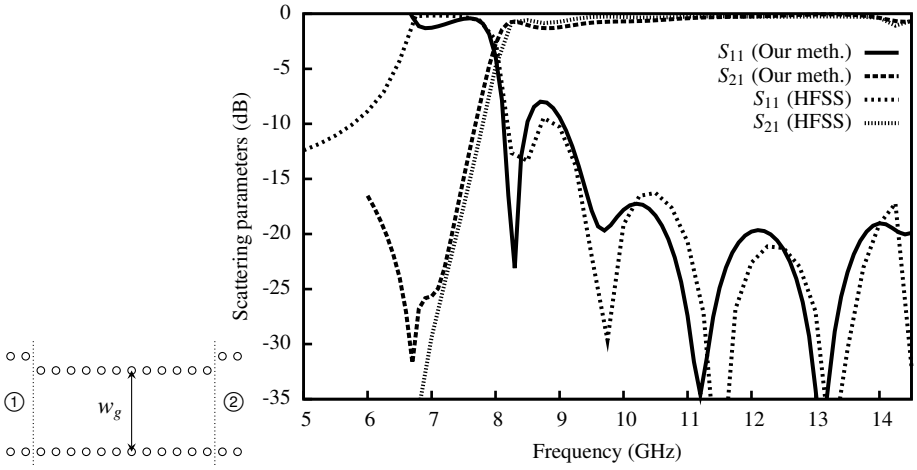

(a) Top view (b) Scattering parameters

Figure 6.2 — Top view and simulated scattering parameters (our method and HFSS) for a phase-delay line with w_g = 10.75 mm and l_g = 26.0 mm. (CMPP2)

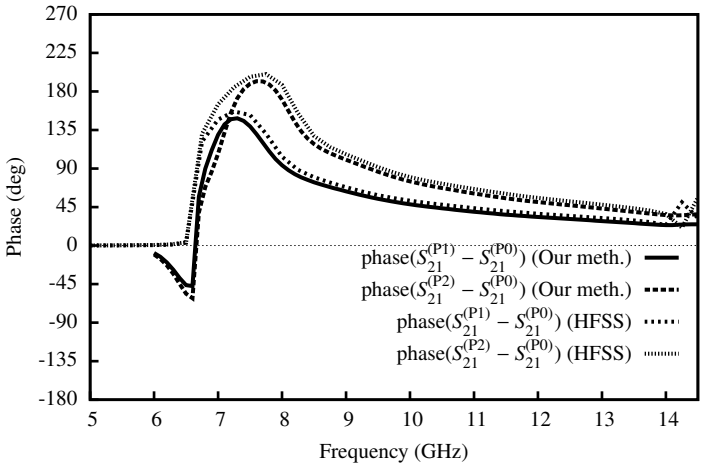

Figure 6.3 — Phase difference for two phase-delay lines P1 and P2 with w_g = 11.25 mm and w_g = 10.75 mm compared to a reference line P0 with w_g = 12.63 mm as obtained with our method and HFSS. All lines have length l_g = 26.0 mm. (P0: CMPC4, P1: CMPP1, and P2: CMPP2)

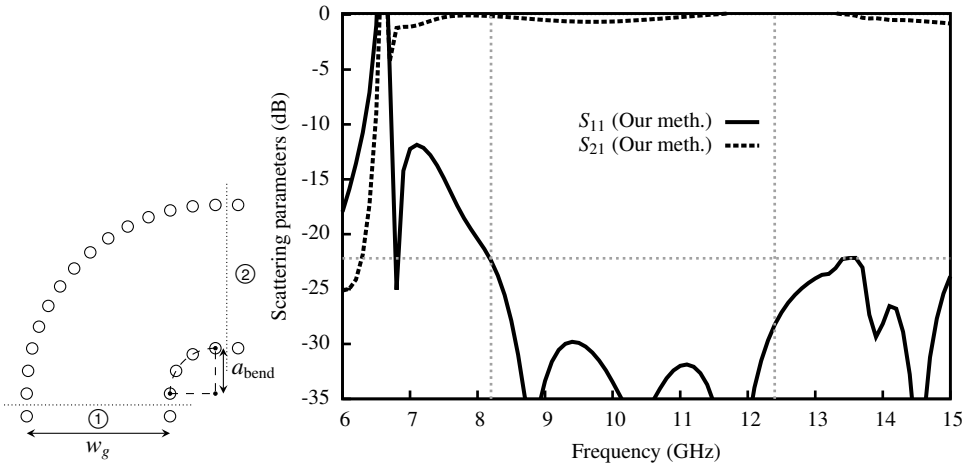

(a) Top view (single bend)

(b) Calculated scattering parameters (two bends)

Figure 6.4 — Top view of a single 90° H-plane bend with $a_{\text{bend}} = 4$ mm and $w_g = 12.63$ mm (CMPB) and simulated scattering parameters for two cascaded 90° H-plane bends. The results have been obtained with our method.

$w_g = 12.63$ mm and equal length $l_g = 26.0$ mm are plotted in Figure 6.3. We observe that the differences between our method and Ansoft HFSS are less than 5.8° in the 9.5–12.4 GHz range.

6.2.2 Bends and Junctions

A 90° H-plane bend and a H-plane T-junction using the same bend are designed.

The 90° H-plane bend

Figure 6.4(a) shows a schematic representation of a 90° H-plane bend. Since the bend is an asymmetric structure, undesired asymmetric modes like the TE_{20} can be excited, especially if the inner radius of the bend is small with respect to the waveguide width. For our design we chose $a_{\text{bend}} = 4$ mm. The outer and inner walls of the bend consist of 14 and 4 equally spaced posts.

The two port planes of the 90° bend are not in parallel and the current implementation of our method cannot be used to simulate the scattering parameters of a single bend. Instead, we can cascade two bends such that the port planes are in parallel. The calculated scattering parameters are shown in Figure 6.4(b). In the 8.2–12.4 GHz range the $|S_{11}|$ for the two cascaded bends is below −22 dB and the $|S_{21}|$ is above −0.7 dB. The fact that $|S_{21}|$ is larger than 0 dB around 12 GHz is ascribed to the existence of higher-order modes at the ports. These parasitic modes are easily excited in bends because of the curved trajectory of the TE_{10} mode.

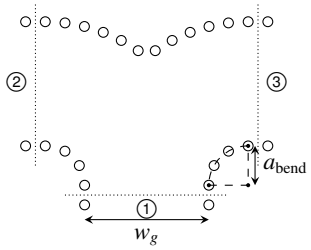

Figure 6.5 — Top view of the H-plane T-junction, derived from two superimposed 90° H-plane bends with $a_{\text{bend}} = 4$ mm and $w_g = 12.63$ mm (component name CMPT1).

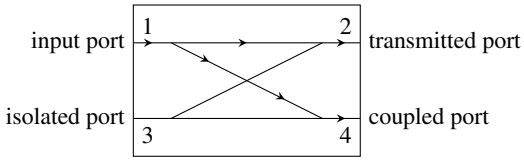

Figure 6.6 — Schematic diagram of a general four-port hybrid coupler and the names of its ports.

The H-plane T-junction

An H-plane T-junction as illustrated in Figure 6.5 is derived from two superimposed H-plane bends. The junction is a three-port structure whose port planes are not parallel. Therefore, the scattering parameters cannot be calculated with our present implementation. Instead we use Ansoft HFSS to compute the scattering parameters of the T-junction. From the simulation results in Figure 6.17, we observe that the reflectivity at the input port is high ($|S_{11}|$ between −6 and −10 dB in the 8.2–12.4 GHz band). In this respect, we note that a lossless reciprocal three-port network cannot be matched at all ports simultaneously [79, App. D], which explains the high reflectivity.

6.2.3 Hybrid Couplers

All couplers considered are four-port components with an input port (port 1), a transmission port (port 2), an isolated port (port 3), and a coupled port (port 4) as depicted in Figure 6.6. The power at the input port is divided over the transmission port and the coupled port by a ratio that is imposed by the coupling parameter. In a non-ideal coupler a (small) part of the input power is also coupled to the isolated port or reflected back at the input port of the component. A detailed introduction to hybrid couplers can be found in the literature, e.g. in [79, Ch. 8] and in [122, Ch. 5].

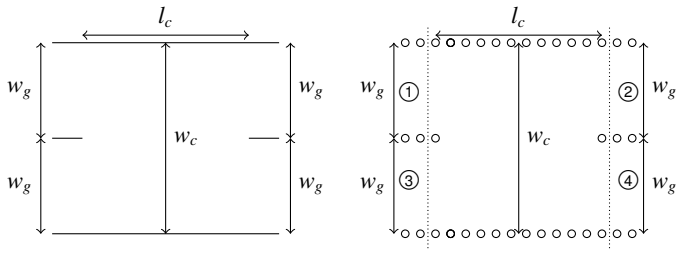

(a) Rectangular waveguide (b) Post-wall waveguide

Figure 6.7 — Geometry of a rectangular and a PWWG Riblet short-slot coupler. The coupling region has length $l_c = 22.0$ mm and width $w_c = 2w_g$. The horizontal spacing of the posts $d_z = 2.00$ mm and the width of the waveguides at the four ports is $w_g = 12.63$ mm (component name CMPC2).

The Riblet Short-Slot Coupler

The Riblet short-slot coupler is a 3 dB coupler that consists of two waveguides with coinciding H-planes and a common side wall. The common wall is removed over a distance l_c in order to obtain coupling between the waves in both waveguides. The output signals of the coupler are 90° out of phase. A device with these properties is termed a 90° or quadrature hybrid. The Riblet short-slot coupler is discussed in [123] and [79, pp.388-390] and a schematic view of a rectangular waveguide coupler is depicted in Figure 6.7(a). The geometry of the coupler is determined based on an even/odd mode analysis, where the even mode is the TE_{10} mode and the odd mode is the TE_{20} mode. The phase difference $\Delta\phi$ between the two modes is expressed by

$$\Delta\phi = (\beta_e - \beta_o)l_c, \tag{6.3}$$

where β_e and β_o are the propagation constants of the TE_{10} and TE_{20} modes, respectively. In the band of operation, the condition $\Delta\phi = \pi/2$ needs to be satisfied.

We base the design of the coupler on a PWWG with $w_g = 12.63$ mm, $a = 0.5$ mm and $d_z = 2.0$ mm. To avoid a step in the side wall of the waveguide, we set $w_c = 2w_g$ for the design of the PWWG Riblet short-slot coupler. At the center frequency of 10 GHz we calculate the real part of the propagation constant β_e of the TE_{10} mode for a PWWG with $w_g = 12.63$ mm. With $\beta_e = 373.9$ m^{-1} and $\beta_o = 302.6$ m^{-1}, we arrive at a coupler length $l_c = 22.0$ mm, which corresponds to 10 posts spaced at a distance of $d_z = 2.0$ mm. Figure 6.7(b) shows the resulting geometry of the PWWG Riblet short-slot coupler.

Figure 6.18 shows the results of simulations with HFSS. In the range 8.2–11 GHz $|S_{11}|$ and $|S_{31}|$ are both below −16 dB. The input at port 1 is not equally split: $|S_{21}|$ is between −5.4 and −3.8 dB while $|S_{41}|$ is between −2.0 and −2.6 dB. The computed result for the phase difference between port 2 and port 4, with the coupler exited at port 1, has been plotted in Figure 6.18(b). This difference is between 89.9° and 92.5° in the 8.2–11 GHz frequency range and this confirms that the coupler operates as a 90° hybrid. Around 11.5 GHz, we observe that the functionality of the coupler is disturbed. $|S_{11}|$ increases, which limits the bandwidth of the component. This

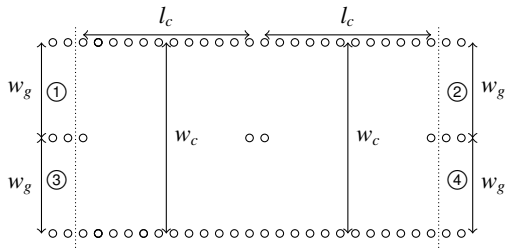

Figure 6.8 — Geometry of two cascaded PWWG Riblet short-slot couplers. Signals at port 1 are fully coupled to port 4 and the signals at port 3 are fully coupled to port 2 (CMPC3).

disturbance originates from TE_{30}-mode excitation in the broad coupling section. To suppress this spurious effect, the design could be altered by narrowing the coupling region, and so effectively shifting the effect to a higher frequency. Since the band from 8.2–11 GHz is sufficient for our purpose, we did not change the design.

The Cascaded Riblet Short-Slot Coupler

Two Riblet short-slot couplers were cascaded by connecting the transmission port and the coupled port of the first coupler to the input port and the isolated port of the second coupler. We obtain the four-port device that is depicted in Figure 6.8. The component is a 0 dB coupler: the signal at port 1 is transferred to port 4 and the signal from port 3 is transferred to port 2. The 0 dB coupler, or cross-over junction, is a useful component in planar antenna feed networks where two signals have to cross each other. We will need this functionality in the Butler-matrix feed network to be discussed in Section 6.2.4. Figure 6.19 shows the scattering parameters for the cascade of two Riblet short-slot couplers obtained with HFSS as a function of the frequency. $|S_{21}|$ is below -10 dB in the 8.2–11 GHz range, while $|S_{41}|$ is above -1.3 dB. $|S_{31}|$ is below -13 dB and $|S_{11}|$ is below -15 dB. Since the coupler is constructed from two Riblet short-slot couplers, the same parasitic behavior, caused by the TE_{30}-mode excitation occurs around 11.5 GHz.

Line Isolation

If a PWWG is close to another PWWG, energy will leak from one into the other and vice versa. The worst-case situation entails two PWWGs sharing a sidewall. To characterize the isolation between such transmission lines, we consider the coupling between the lines in the geometry of Figure 6.9. Figure 6.20 shows the computed scattering parameters for this configuration. Both $|S_{11}|$ and $|S_{31}|$ are below -53 dB in the 8.2–12.4 GHz band. $|S_{41}|$ is below -35 dB, while $|S_{21}|$ is higher than -0.18 dB.

6.2.4 Butler Matrix

A Butler matrix is an antenna feed network for a switched-beam phased array system. By applying a signal at one of the input ports of the matrix, the phasing on the output ports corresponds

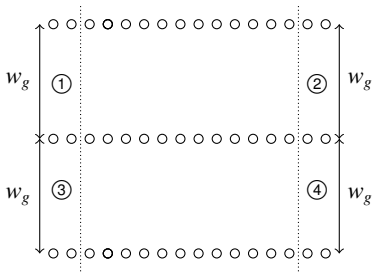

Figure 6.9 — Geometry of two PWWG transmission lines with a common sidewall. The coupling between ports 1 and 4, is a measure for the worst-case isolation between two parallel transmission lines (CMPC4).

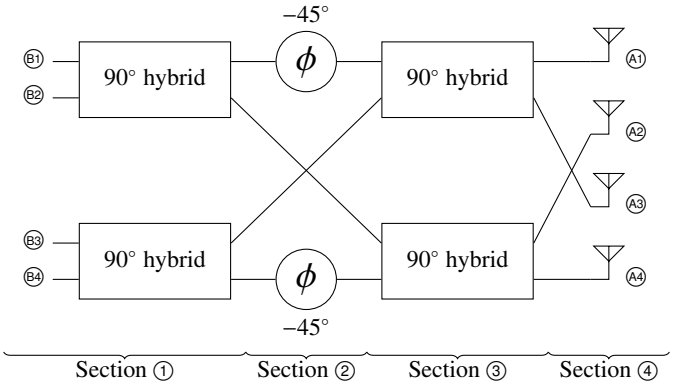

Figure 6.10 — Block diagram of a 4x4 Butler matrix (CMPBM). The names B1 to B4 correspond to the four input ports and the names A1 to A4 correspond to the four output ports. The sections 1 to 4 correspond to the sections in the PWWG Butler matrix geometry depicted in Figure 6.11.

in linear-array theory to a beam with specific direction determined by the excited input port. A block schematic of a 4x4 Butler matrix is depicted in Figure 6.10. For a 4x4 PWWG Butler matrix we need four 90° hybrids (the Riblet short-slot coupler of Figure 6.7(b)), two cross-over junctions (the cascaded Riblet short-slot couplers of Figure 6.8), two −45° phase shifters (with respect to the cross-over junction) and two 0° phase shifters (with respect to a cross-over junction). Combining these building blocks leads to the PWWG Butler matrix of Figure 6.11. From Figure 6.11 it is clear that compared to the previous PWWG structures, a 4x4 PWWG Butler matrix is a large and complex structure. The simulation in a general-purpose simulator is troublesome; simulations are extremely time consuming. Optimization of the complete structure is, therefore, not practical, and we have to resort to simulation of building blocks in order to estimate the behavior of the complete system. The building blocks are simulated by HFSS and characterized by single-mode scattering parameters, which are transferred to a circuit

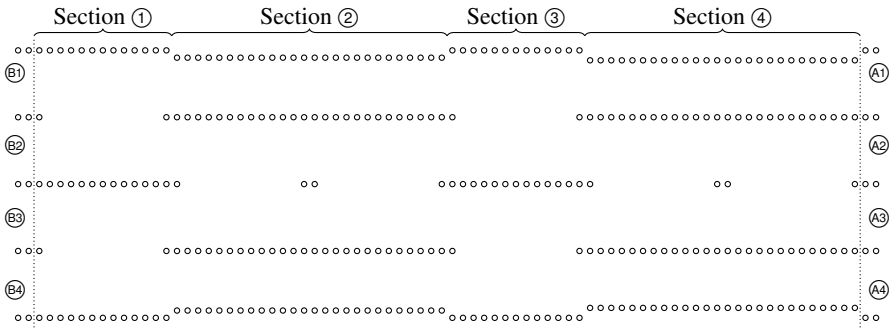

Figure 6.11 — Top view of a PWWG 4x4 Butler matrix (component name CMPBM).

simulator (ADS). The results from these simulations provided an estimate of the response of the Butler matrix and allowed us to select the best-fitting building-block geometries from a discrete set of field simulations. Following this approach, the widths of the delay-lines presented in Section 6.2.1 are selected from a set of simulations for different waveguide widths. The accuracy of this approach is low, especially if the number of building blocks is large. To improve the design process it would be useful to:

- extract multi-modal scattering parameters (generalized scattering matrix) from the field simulations, such that the coupling of the higher order modes between the sub-components is accounted for,
- improve the software implementation of our method, such that it can handle multi-port components and the cascading of multi-modal components, and
- optimize the designs of the sub-components.

The two $-45°$ phase shifters in section ② of the Butler matrix are formed by the phase delay lines of Section 6.2.1. They consist of two PWWG transmission lines with width w_g = 11.25 mm and length l = 52.0 mm and give rise to a $-45°$ phase difference with respect to the output signal of the cross-over junction at the design frequency of 10 GHz. In section ④, we achieve a $0°$ phase difference between the cross-over junction and the lines to A1 and A4 with a transmission line of width w_g = 10.75 mm and length l = 52.00 mm.

6.3 Measurement Setup

All PWWG components described in Section 6.2 have been manufactured and measured. The scattering parameters of the components were measured using an Agilent N5242A four-port network analyzer. The measurement setup is given in Figure 6.12. All four ports are calibrated to the SMA connector reference planes using an Agilent N4691B 3.5 mm two-port electronic calibration module. Calibration has been carried out over the frequency range from 10 MHz to 18 GHz with an intermediate frequency bandwidth (IFBW) of 500 Hz.

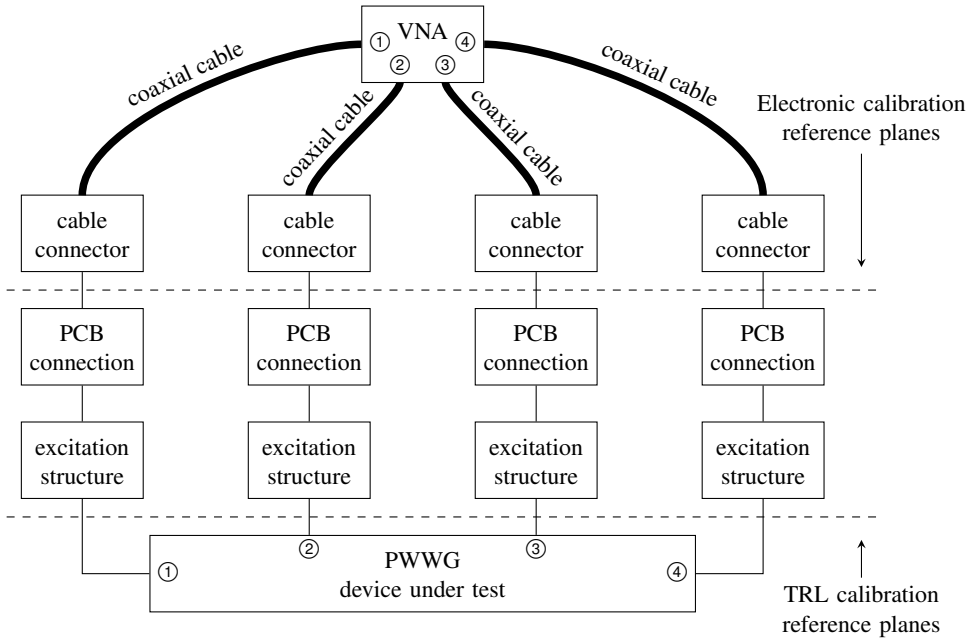

Figure 6.12 — Measurement setup with a four-port VNA, as used for all component measurements.

Following measurement of the scattering parameters at the SMA connector reference planes, we use the TRL algorithm [124] to de-embed the measurement results and determine the characteristics of the PWWG component. This de-embedding removes the contribution of the transition structures and shifts the reference plane from the SMA connector to the PWWG.

For the measurement of the one-, two-, three– and four-port components in our set of test components, we can directly determine all scattering parameters with the four-port network analyzer following the schematic of Figure 6.12. If the number of ports of the component under test is less than four, we leave the ports of the network analyzer that are not needed disconnected. For the eight-port Butler matrix, we cannot simultaneously measure all 64 scattering parameters. Therefore, we perform a number of measurements, each with four ports of the Butler matrix connected to the VNA and the other four ports terminated in a 50 Ω load. By choosing ten different combinations of connected ports (B1A1A2A3, B2A1A2A3, B3A1A2A3, B4A1A2A3, B1A2A3A4, B2A2A3A4, B3A2A3A4, B4A2A3A4, B1A2B3A4 and B1A1B3A3), we can measure all 64 scattering parameters, with which we can reconstruct the 8x8 scattering matrix, assuming a negligible influence from the non-idealities of the 50 Ω terminations.

6.4 Measurement Results

The measurements of the PWWG components in this chapter are performed with the same setup as the measurements of the uniform lines on the low-dielectric substrate in Chapter 4. In

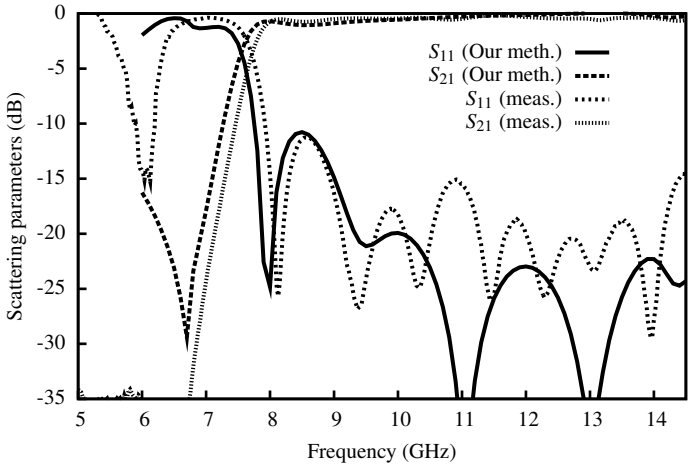

Figure 6.13 — Measured and simulated (our method) scattering parameters for a phase-delay line with w_g = 11.25 mm and l_g = 26.0 mm (CMPP1).

Section 4.5.2 we discussed the measurement accuracy of these measurements and observed that the measurement floor was around −18.5 dB over the 8.2–12.5 GHz band (see Figure 4.10). The measurements presented in this section suffer from the same measurement floor.

6.4.1 Phase-Delay Lines

In Figures 6.13 and 6.14 the measured magnitude of the scattering parameters is plotted for the phase-delay lines with w_g = 11.25 mm and w_g = 10.75 mm, respectively. The results from our method have been plotted in the same graphs. The $|S_{11}|$ of the widest line (CMPP1) is below −15 dB and $|S_{21}|$ is above −0.55 dB in the 9.5–12.4 GHz range. The second line (CMPP2) exhibits a $|S_{11}|$ below −13 dB and a $|S_{21}|$ above −0.49 dB measured over the same frequency range. We observe that below approximately $1.25 f_{\text{co}}$ the S_{11} and the S_{21} calculated by our method can become larger than 0 dB. The difference between measurements and simulations for low values of S_{11} can be explained by the measurement inaccuracy at low coupling levels.

Figure 6.15 shows the phase differences of the phase-delay lines with respect to the reference line (w_g = 12.63 mm). For CMPP1 the difference between measurement and simulation can amount to 11.3° and for CMPP2 to 16.1° in the 9.5–12.4 GHz range.

6.4.2 Bends and Junctions

The measured scattering parameters of the single 90° H-plane bend are shown in Figure 6.16 together with results from Ansoft HFSS. The measured $|S_{11}|$ is below −20 dB with an $|S_{21}|$ above −0.36 dB in the 8.2–12.4 GHz frequency band.

In the measurements of the H-plane T-junction shown in Figure 6.17, we observe an oscillation in the magnitude of the scattering parameters. Aside from this oscillation, the simulation

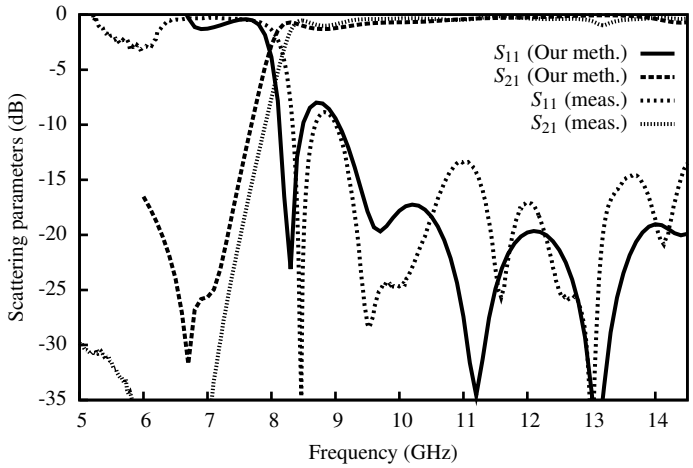

Figure 6.14 — Measured and simulated (our method) scattering parameters for a phase-delay line with w_g = 10.75 mm and l_g = 26.0 mm (CMPP2).

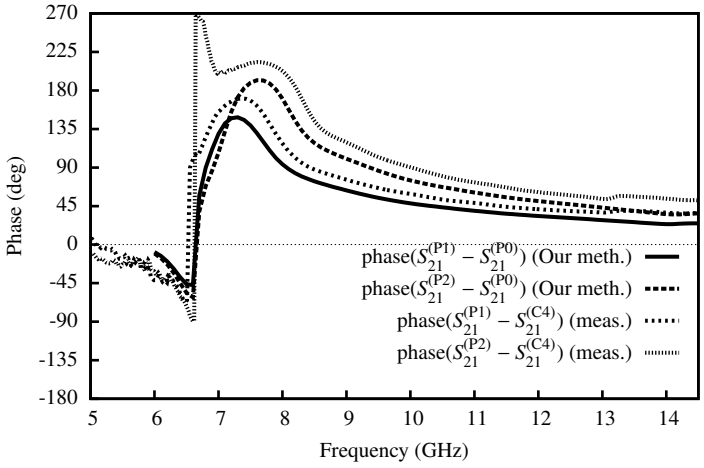

Figure 6.15 — Phase difference for two phase-delay lines P1 and P2 with w_g = 11.25 mm and w_g = 10.75 mm compared to a reference line P0 with w_g = 12.63 mm. Measurements and results from our method are compared. The reference line P0 for the measurements is one line of the isolated lines (component name CMPC4). All lines have length l_g = 26.0 mm.

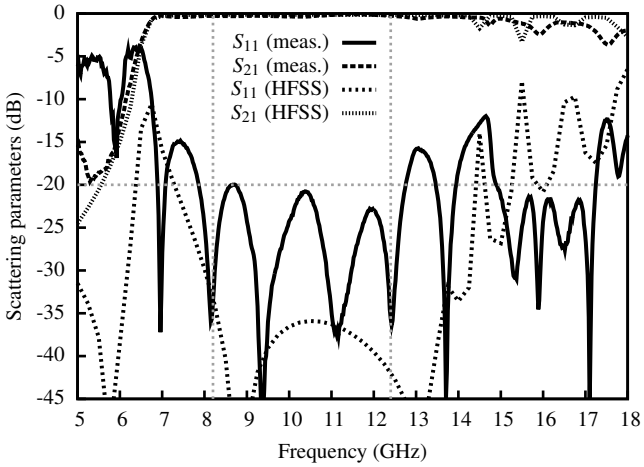

Figure 6.16 — Top view and simulated and measured magnitude of the scattering parameters for a single 90° H-plane bend with $a_{\text{bend}} = 4$ mm and $w_g = 12.63$ mm (CMPB). The simulation results have been obtained with HFSS.

and measurement trends are similar. The oscillation might well be caused by the excitation of higher-order modes inside the structure. In simulation we only observe at the ports the projection of the fields on the TE_{10} mode, while in the measurement setup the modes at the ports cannot be distinguished. The measurement results are, therefore, distorted if the power in the higher-order modes is high relative to the dominant mode, which is the reference mode for the TRL calibration. This distortion does not occur for the simulation results, since here the power in the higher-order modes is ignored at the ports.

6.4.3 Hybrid Couplers

All manufactured hybrid couplers are four-port components, and are measured in accordance with the measurement setup in Figure 6.12.

The Riblet Short-Slot Coupler

Figure 6.18 shows the measured and simulated scattering parameters of the Riblet short-slot coupler depicted in Figure 6.7(b). The computed and measured $|S_{21}|$ and $|S_{41}|$ in Figure 6.18 almost coincide (difference is less than 0.65 dB) within the 8.2–11 GHz frequency range. The measured $|S_{11}|$ is below -15 dB while the measured $|S_{31}|$ is below -12 dB. Both values are higher than the simulated values which may be explained by the specific measurement floor of the measurements. The phase difference between port 2 and port 4, as shown in Figure 6.18(b), is close to 90° over the 8.2–11 GHz range: the difference between the measured and calculated values is less than 4°.

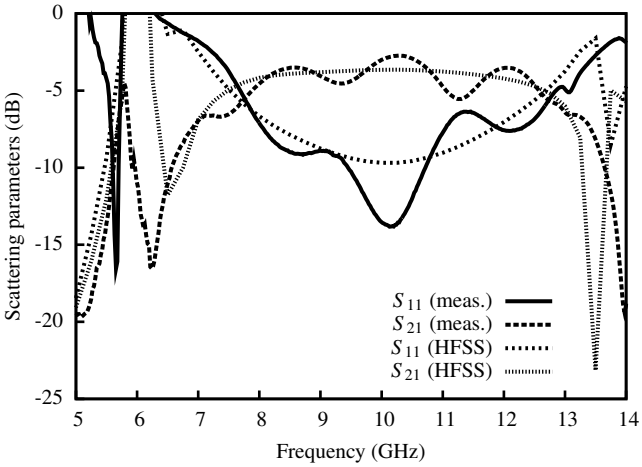

Figure 6.17 — Simulated and measured magnitude of the scattering parameters of a H-plane T-junction, derived from two superimposed 90° H-plane bends with $a_{\text{bend}} = 4$ mm and $w_g = 12.63$ mm (CMPT). The simulation results have been obtained with HFSS.

The Cascaded Riblet Short-Slot Coupler

The measured results for the cascaded Riblet short-slot coupler are given in Figure 6.19. The match between the measurements and the simulations in the 8.2–11 GHz range, is good for $|S_{21}|$ and $|S_{41}|$, the difference is less than 1.15 dB and 0.42 dB, respectively. $|S_{11}|$ and $|S_{31}|$ show larger differences than in the case of the single Riblet short-slot coupler: $|S_{11}|$ is below −13 dB and $|S_{31}|$ is below −10 dB. This is most likely a result of the mismatch between the two cascaded couplers. The slope of $|S_{31}|$ is steep around 8.2 GHz, and thus $|S_{31}|$ is below −19 dB in the 8.5–11 GHz range.

Line Isolation

In Figure 6.20 the measured results for the pair of isolated lines show that the $|S_{11}|$, $|S_{31}|$, and $|S_{41}|$ are higher for the measurement case than for the simulation case. Since the measurement floor is at the level of the measured values, it is difficult to assess if the values are real or a measurement setup artifact.

6.4.4 Butler Matrix

The measurements of the Butler matrix are split into two cases: in Figure 6.21 and 6.22 the input is at port B1 of the matrix and in Figure 6.23 and 6.24 the input is at port B2. The Butler matrix is designed at a center frequency of 10 GHz and we specify performance over the 9.5–10.5 GHz frequency range.

In the first case, we observe in Figure 6.21 that $|S_{B1,B1}|$ is below −14 dB, while the transmissions to the output ports ($|S_{A1,B2}|$, $|S_{A2,B2}|$, $|S_{A3,B2}|$ and $|S_{A4,B2}|$) are between −5.8 dB and

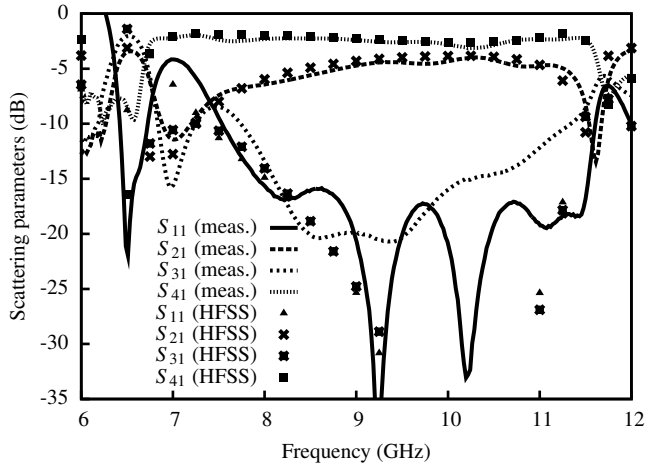

(a) Magnitude

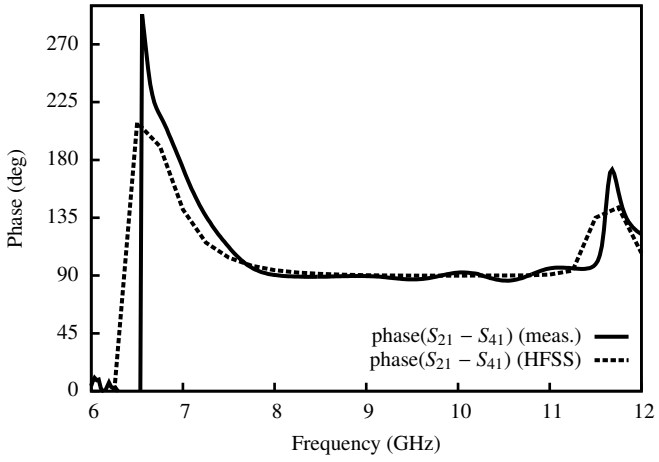

(b) Phase

Figure 6.18 — Measured and simulated scattering parameters (top graph: magnitude, bottom graph: phase) of a PWWG Riblet short-slot coupler (CMPC2) as a function of the frequency. Simulations using HFSS.

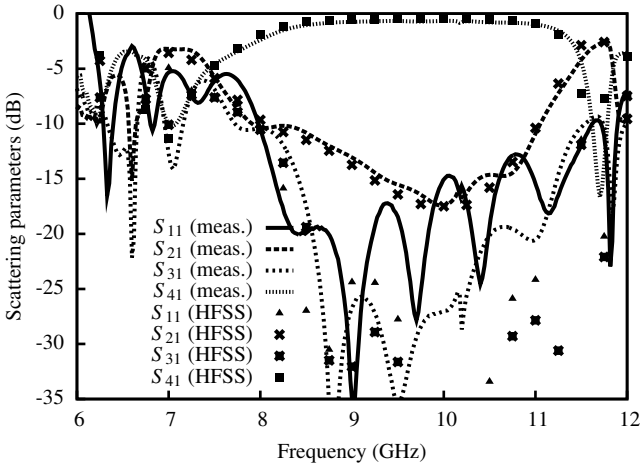

Figure 6.19 — Measured and simulated scattering parameters of a cascade of two Riblet short-slot couplers (CMPC3) as a function of the frequency.

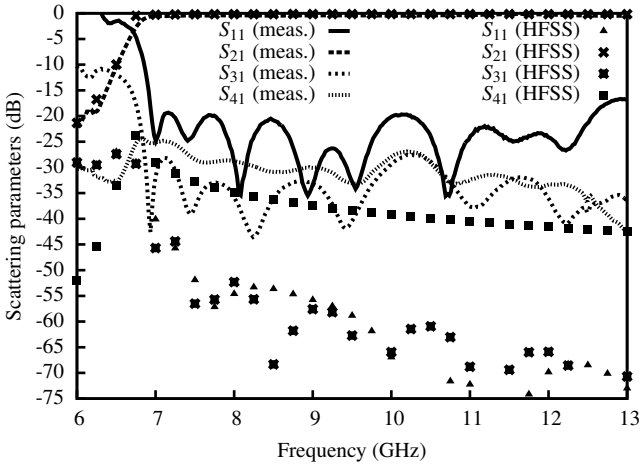

Figure 6.20 — Measured and simulated scattering parameters of two PWWG transmission lines with a common sidewall (CMPC4) as a function of the frequency.

−10.8 dB. Thus the variation is relatively large and relative to the nominal −6 dB the excess loss is between −0.2 dB and 4.8 dB. The variation of the excess loss is less then 1.4 dB over the considered frequency range for each output port. Considering the phase response in Figure 6.22, we note that the differential phase shift between the output ports exhibits a significant frequency dependence. The nominal value for the differential phase shift is 45°, but in the figure we observe that the closest match for all output ports occurs around 10.6 GHz, where the phase differences are between 34° and 50°.

In the second case, we note from Figure 6.23 that the magnitudes of the scattering parameters for the transmission from the input port to the output ports ($|S_{A1,B2}|$, $|S_{A2,B2}|$, $|S_{A3,B2}|$ and $|S_{A4,B2}|$) are closer to the nominal −6 dB. with all four magnitudes between −6.2 dB and −9.1 dB, the excess loss varies from 0.2 dB to 3.1 dB over the specified frequency range. The variation of the excess loss is less then 1.7 dB over the considered frequency range for each output port. At port B2 $|S_{B2,B2}|$ is below −19.5 dB. The differential phase shifts at the output ports are shown in Figure 6.24. The nominal value for the input at port B2 is −135°, which is almost obtained at 9.9 GHz where all phase differences are between −136° and −139°. The strong frequency dependence of the phase response of the Butler matrix is enhanced by the use of delay lines instead of phase shifters. The phase-delay lines do not exhibit a constant phase shift as a function of the frequency, leading to excessive frequency dependence of the overall system.

From the previous discussion we can conclude that the general performance of the Butler matrix is poor. This is a result of not optimizing the design of the structure as we described in Section 6.2.4. The simulation of a structure with the complexity of the complete Butler matrix poses computational problems for current general-purpose simulation systems and the single-mode cascading of components in a circuit simulator results in a poor design. To avoid this performance degradation extra lengths of single-mode PWWG could be inserted between the components in the Butler matrix. This will reduce the coupling of higher-order modes between the cascaded components, but it will considerably enlarge the size of the system. Needless to say, for the optimization of the current design we need a fast and accurate simulation tool.

6.5 Methodological Component and Feed Network Design Extensions

The pros and cons of our numerical method for the design of PWWG components and feed networks have extensively been discussed and larded with examples in this chapter. We observe that general-purpose simulators are extremely accurate, but generally too slow for an optimization of complex systems. Our method can overcome all of these issues. In its present implementation, this is already true for a number of problem setups. In this section, we propose three (methodological) extensions, to largely extend the application space.

Multi-Port Components Extension

The first improvement only requires a straightforward extension of the scattering parameter calculation described in Section 3.5. If we take the PWWG Riblet short-slot coupler in Figure 6.7(b) as an example, we can define two port regions that we mesh with rooftop functions: one covering both port 1 and 3 and the other covering port 2 and 4. Following the same steps as in Section 3.5, we can excite with a TE_{10} mode that is centered at port 1 and then calculate its projection on other TE_{10} modes centered at the other three ports. We repeat this procedure for

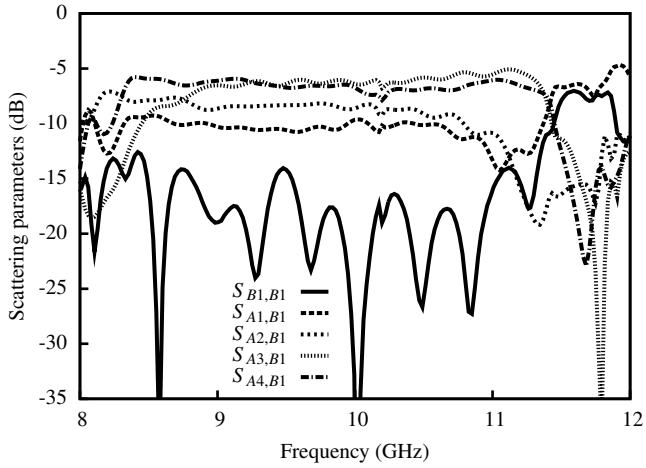

Figure 6.21 — Measured magnitude of the scattering parameters as a function of the frequency for the Butler matrix with input at port B1. The ideal nominal value for the input to output transmission ($|S_{A1,B1}|$, $|S_{A2,B1}|$, $|S_{A3,B1}|$ and $|S_{A4,B1}|$) is −6 dB.

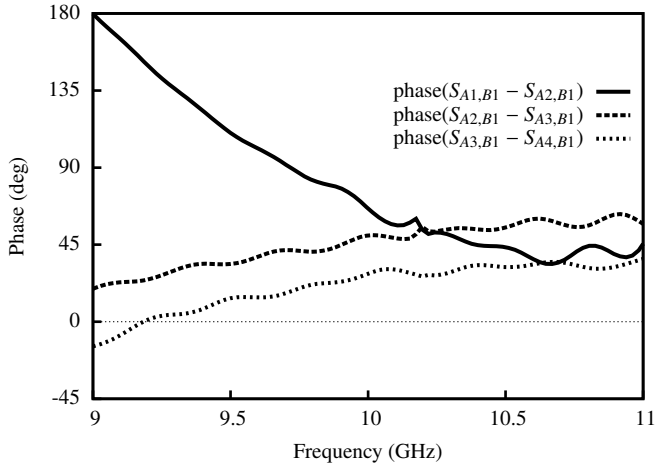

Figure 6.22 — Measured differential phase shift as a function of the frequency for the Butler matrix with a source on port B1. The nominal value of the differential phase shift is 45°.

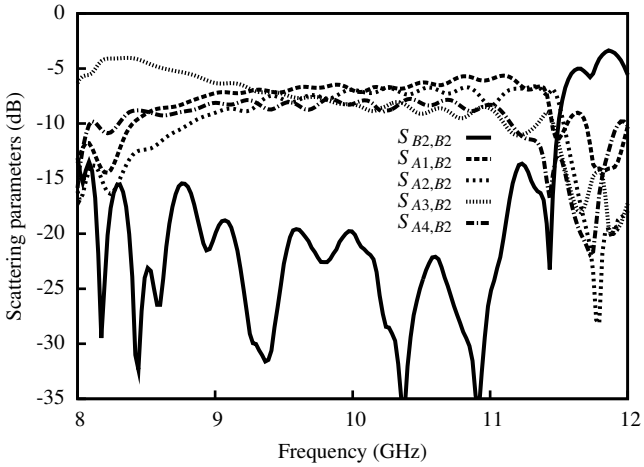

Figure 6.23 — Measured magnitude of the scattering parameters as a function of the frequency for the Butler matrix with input at port B2. The ideal nominal value for the input to output transmission ($|S_{A1,B2}|$, $|S_{A2,B2}|$, $|S_{A3,B2}|$ and $|S_{A4,B2}|$) is −6 dB.

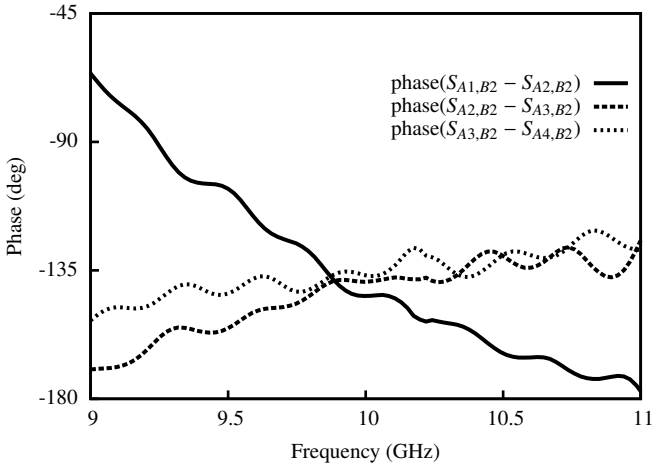

Figure 6.24 — Measured differential phase shift as a function of the frequency for the Butler matrix with a source on port B2. The nominal value of the differential phase shift is −135°.

the other three ports to determine the complete four-port scattering matrix of the component. The cascading of current matrices can be carried out unchanged, since it does not depend on the projection of the waveguide modes at the ports. In this way we can straightforwardly determine the response of the cascaded Riblet short-slot coupler.

Cascaded-Components Extension

The second suggestion refers to the cascading procedure based on Redheffer's star product described in Section 3.4. This procedure enables the design of sub-components or sub-sections of PWWGs that can be cascaded in a computationally fast and efficient manner. It paves the road for the integration of our method in circuit simulators, thus facilitating the interconnection of components so that the performance of complex systems such as a Butler matrix can be evaluated and optimized. In our first investigation of the application of the cascading procedure we observed that the cascade of the current matrices of two sub-blocks composing a component cannot be compared directly to the current matrix of the complete component. Differences in matrix elements occur in particular far off the central elements of the matrix blocks $T^{u(i_i),v(i_2)}$ or, in other words, in the coupling of rooftops that are close to the ends of the ports. These differences occur because the coupling of these rooftops to the surrounding area outside the port is ignored, which leads to errors in the cascading procedure. To estimate the quality of the cascaded result we should not examine the current matrix itself, but rather the product of the current matrix and the coefficient vector $(D_{\mathrm{el}}^{\mathrm{in}(1)}, D_{\mathrm{mag}}^{\mathrm{in}(1)}, D_{\mathrm{el}}^{\mathrm{in}(2)}, D_{\mathrm{mag}}^{\mathrm{in}(2)})^T$. Here the vector components corresponding to rooftops located outside the TE_{10} port with size $w_g^{(i)} < d_{\mathrm{port}(i)}$ as introduced in Section 3.5 are set to zero. This additional step is justified since the power is assumed to be mainly transfered through the TE_{10} ports.

Parallel-Plane Ports Extension

Regarding the third extension, there is no intrinsic limitation to our method that inhibits the use of non-parallel ports. However, we need to be extremely cautious at the intersection of ports. We can choose the length of the ports d_{port} small enough, such that different ports do not intersect or overlap. But since the ports need to be sufficiently large to accurately characterize the fields incident on them, this can lead to a problem choosing proper port size. To overcome this, one could use extra sections of uniform transmission lines inserted at the port locations that effectively increase the distance between the ports. The extra sections of transmission line can then later be de-embedded numerically, to find the response at the original ports. Another approach would be to define a closed boundary around the complete component and then calculate the equivalent magnetic and electric currents on this boundary as in [49, 50]. The disadvantage of such an approach is that the step toward a classical circuit simulator that handles a finite number of discrete ports requires considerable analysis of the component boundary.

The implementation of these three suggestions, would facilitate the integration of our method in a circuit simulator, such that PWWG sub-components can be accurately characterized by (computationally more intensive) simulations based on a reduced electromagnetic model and subsequently be cascaded with the (computationally fast) Redheffer's star product. This com-

putational procedure promises a relatively fast evaluation of composite systems and enables the use of optimization schemes, that can simplify and improve system design.

Computation Times

In order to compare computation times we consider a single uniform PWWG that consists of a single row of 55 conducting posts per sidewall with the geometry specified in Section 4.1.2. All simulations have been performed for a single frequency (10 GHz) and are executed on a HP xw8200 workstation with two 3.40 GHz Intel Xeon dual core CPUs, 8 GB RAM and running Windows XP Professional x64 version 2003. For all simulations a single core of one CPU is used. The implementation of our method in Fortran has been compiled with Intel's 32-bit Fortran compiler version 9.1.033. We note that calculation times vary between runs with equal parameters: we estimate that this variation is ±0.5 seconds.

We analyze the execution times of our implementation for two simulation approaches: a brute-force simulation of the complete structure containing 110 posts and a simulation of a unit cell consisting of two posts that is cascaded 54 times. The PWWG with 110 posts is analyzed with HFSS with default settings: the total simulation time is 881 seconds. In Table 6.1 and Table 6.2 we specify for different values of N_{exp} the computation times of the computationally intensive steps as well as the total execution times for the 110 and 2 post cases, respectively. As is to be expected from our calculational scheme in Appendix D, we observe that the relations between computation time and N_{exp} are approximately

- constant for the C-matrix calculations,
- linear for the A and B calculation,
- quadratic for the combined Ξ, F, and $\tilde{T}$ calculations, and
- quadratic for the matrix cascading.

This means that for small N_{exp} all steps contribute significantly to the total execution time, but for large N_{exp} the contributions of the quadratic operations become dominant.

For the cascading of short sections, the port widths, and therefore N_{exp}, must be chosen sufficiently large to account for the coupling of the (accessible) modes that are present at the port interfaces. In the case of a long line the number of rooftops can be considerably smaller, since the field does not need to be approximated at the interfaces between the consecutive unit cells.

Step	Description	$N_{\text{exp}} = 7$	$N_{\text{exp}} = 15$	$N_{\text{exp}} = 30$	$N_{\text{exp}} = 45$
I	Fill and invert matrix C	21.8	21.6	21.3	21.7
II.A–II.D	Calculate coefficients A and B	28.8	61.5	123.0	184.6
II.E	Calculate $\Xi_{1,2,3,4}$, F, and $\tilde{T}$	19.8	84.0	324.5	722.0
TOTAL	Total time per frequency point	70.4	167.2	469.2	928.6

Table 6.1 — Computation times in seconds of our implementation for a uniform 55 unit cell (110 posts) PWWG without cascading. Only computationally intensive steps are specified, but total accounts for *all* steps. The numbering of the steps is according to the scheme of Appendix D. Geometry based on Table 4.3 with $f = 10$ GHz, $N_{\text{int}} = 10$, and $d_{\text{port}} = 12.14$ mm.

Step	Description	$N_{\text{exp}} = 7$	$N_{\text{exp}} = 15$	$N_{\text{exp}} = 30$	$N_{\text{exp}} = 45$
I	Fill and invert matrix C	0.1	0.1	0.1	0.6
II.A–II.D	Calculate coefficients A and B	0.5	1.1	2.0	3.0
II.E	Calculate $\Xi_{1,2,3,4}$, F, and $\tilde{T}$	0.5	1.9	7.4	17.0
Cascade	54 matrix cascading steps	1.6	4.6	19.2	49.0
TOTAL	Total time per frequency point	2.6	7.7	29.0	69.9

Table 6.2 — Computation times in seconds of our implementation for a uniform PWWG of one unit cell (two posts) and 54 current-matrix cascading steps. All other settings equal to the settings used in Table 6.1

CHAPTER 7

Conclusions, Perspectives and Recommendations

In this chapter, an outline of the basic results and conclusions of this thesis are presented and a number of recommendations are made.

7.1 Conclusions

The three aims of this thesis as formulated in Section 1.4 are:

1. to systematically inventory the key PWWG characteristics,

2. to develop a model to link subsystem specifications directly to PWWG characteristics and design, and

3. to work out issues related to implementation and manufacturing.

Regarding the first aim, we identified the propagation constant, the effective width, the losses and the scattering parameters as the key characteristics of PWWGs, and we demonstrated that the first three characteristics can be determined from the scattering parameters. Evidently, a procedure to determine the scattering parameters of a PWWG is essential in relating subsystem specifications to the PWWG geometry.

To achieve the second aim, we developed an electromagnetic model starting from Lorentz's reciprocity theorem that enables us to calculate the fields in (sections of) PWWGs with metallic or dielectric posts. The projection of these fields on equivalent currents defined on bounded segments of specified interfaces allows for the characterization of a PWWG with current matrices. Current matrices are related to the scattering parameters, which in turn facilitate interfacing with microwave design software and determining key PWWG characteristics.

In relation to the third aim, implementation and manufacturing issues are primarily related to developing suitable excitation structures as well as optimally employing third party capabilities for the applicable technology. We have shown that, in standard PCB technology, GCPW excitation structures that cover the full TE_{10} mono-modal band of the PWWG can be realized. The grating condition limits the maximum usable frequency of PWWGs. In standard PCB technology this limit is around 100 GHz. GCPW excitation also provides a simpler PCB layer stack

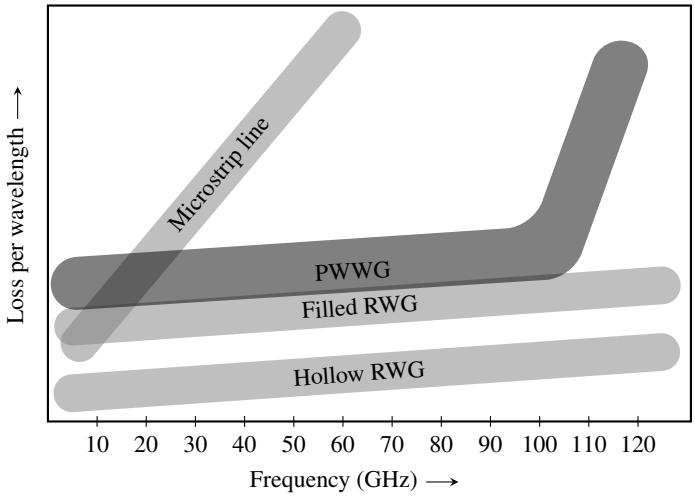

Figure 7.1 — Characteristic loss for a PWWG with respect to loss in traditional microwave transmission lines.

than slot-based excitation. For dielectric post PWWGs we demonstrated that three rows of relatively large posts are necessary to sufficiently confine power to the guide, which may make the structure bulky and too large for phased array feed networks.

In PWWGs with metallic posts dielectric losses are dominant if the post radii and spacings are well-chosen. The loss in PWWGs is comparable to the loss in filled RWG and therefore the loss per wavelength will be lower than for microstrip transmission lines for higher frequencies. Figure 7.1 places the loss of PWWGs in perspective with loss in traditional microwave transmission lines (microstrip line and hollow RWG). Around 100 GHz PWWG operation is limited by high losses since standard PCB technology does not allow more closely spaced posts. It is evident that PWWG transmission lines are advantageous over microstrip lines in the region above ±10 GHz.

In the remainder of this section, we refine our conclusions on a per-chapter basis. In Chapter 2 we start from general electromagnetic theory to model wave propagation in PWWGs. The dominant wave behavior in PWWGs with limited height is similar to the TE_{m0} modal behavior of rectangular waveguides. We describe two different approaches to solve the resulting field equations: one based on the modal representation in Section 2.4 and the other, in Section 2.5, based on an integral-equation formulation that follows from Lorentz's reciprocity theorem. For metallic posts these solutions are equivalent: we do not implement the integral-equation formulation for dielectric posts. We characterize the wave propagation in uniform PWWGs by means of infinitely long periodic PWWGs and we introduce an acceleration procedure to accurately calculate the slowly converging infinite series. We demonstrate the (spatial) evaluation of the electric field in a PWWG in Section 2.7.

In Section 3.1 the propagation constant of uniform PWWGs is determined by means of an optimization procedure applied to the periodic-array model described in Section 2.6. For real

propagation constants the computed infinite series converges, but not for complex constants. Thus, the infinite-array approach is suitable for determining the phase constant of PWWGs, but not for determining the attenuation constant or loss. The concept of a fixed effective width relates a PWWG to a RWG with the same dispersion characteristic. The concept provides a valid description of wave propagation in PWWGs in case the posts are sufficiently closely spaced. The concept is not valid for multiple parallel rows of posts per side wall, PWWG with multiple modes or very small or dielectric posts. For the configuration presented by Hirokawa and Ando [17], our method based on the infinite-array approach demonstrates a difference smaller than 2 percent with respect to HFSS for the relationship between waveguide width and post spacing: this is better than other methods found in the literature. We relate the electromagnetic model of Chapter 2 to the excitation at specified ports, through a current matrix that describes the output electric and magnetic currents at the ports in terms of prescribed input electric and magnetic currents. Both input and output currents are, in our case, described by rooftop functions. The scattering parameters of PWWGs are derived from the current matrices by prescribing a TE_{10} mode at the port interfaces. While this mode is defined on a segment whose size is the effective width of the PWWG, the equivalent electric currents on the interfaces are defined on larger segments to account for radiation loss. The current matrix concept is a powerful tool for characterizing the behavior of PWWG components, because small, separately characterized, subsections can be rapidly cascaded to form a long PWWG. Moreover, a library of computed current matrices of PWWG sections can be compiled.

In Chapter 4 we apply multi-line calibration to extract the propagation constant from scattering-parameter measurements. Measurements and simulations demonstrate that wave propagation is possible in PWWGs with metallic or dielectric posts in a high-permittivity substrate ($\varepsilon_{r,1} = 9.8$). The measurement accuracy for the high-permittivity structures is poor, especially regarding the attenuation. Comparing the results of our method to those obtained by HFSS, we observe, for the most part, similar trends. The issues that led to the low accuracy of the measurements of the structures on the high-permittivity substrate are identified and addressed successfully in the design on the low-permittivity substrate ($\varepsilon_{r,1} = 3.55$): the measurement accuracy on the low-permittivity substrate is much higher than that on the high-permittivity substrate. In this respect we note that we applied a different excitation structure for the low-permittivity structures as discussed in Chapter 5 and that we employed connectors with better performance.

In Section 5.2 we present an aperture-coupled microstrip-line excitation that is compatible with PCB technology and exhibits an average measured bandwidth of 14 percent, which is much smaller than the 40 percent bandwidth of the TE_{10} mode. The resonating elements in this excitation structure limit the bandwidth and manufacturing is complex due to the multi-layer construction. In Section 5.3 we present a GCPW to PWWG transition operating over a large bandwidth (simulated 58 percent, measured 29 percent) that exhibits non-resonant behavior. The transition is easy to manufacture and has been realized in a single PCB layer. Our simulations and measurements demonstrate that the excitation structure can operate over a bandwidth that is commensurate with the bandwidth of the TE_{10} mode. In Section 5.4 a metallic-to-dielectric PWWG transition based on width tapering is designed. The transition equalizes the propagation constants of both types of PWWG in order to match their impedances.

The design, manufacturing, and characterization of a set of functional components, including phase-shift lines, bends, a T-junction, couplers and a Butler-matrix, are described in

Chapter 6. The design of components is carried out by combining several different sections of PWWG, selectively adding or removing posts, or adding slots or other perturbations. We perform a coarse tuning of the scattering parameters of (multi-port) component building blocks. These blocks are combined to create more complex structures, such as bends, splitters, and couplers. For the fine-tuning we employ both our own simulation method, as far as components are described by two parallel interfaces, and HFSS. The simulations and measurements of our test set of components show reasonable agreement in practice and should in the future be used as validation for extensions to our own implementation as discussed in Section 7.3.

7.2 Perspectives

The full potential of SIW components and transmission lines emerges at the lower millimeter-wave frequencies (roughly 30–110 GHz). At these frequencies the loss is lower than in planar transmission lines and standard PCB technology can still be used for manufacturing. In the current development of millimeter-wave components and systems we discern a trend toward three major applications: high data rate communication systems, automotive radar systems, and imaging systems.

High data rate communication systems primarily operate in a license-free band around 60 GHz most frequently used for short-range communications (wireless personal area networks, WPANs). The high path loss at millimeter-wave frequencies requires high-gain antennas that are often realized through the use of an antenna array. PWWGs are well-suited to minimize the loss in the feed network of such an array, while at the same time they provide a low-cost integrated solution in large-volume PCB production.

Parallel to the development of high data rate communication systems, collision-avoidance and vehicle-guidance radar are emerging as systems with high growth potential in the near future. Automotive radar systems are in general based on FMCW front-ends with linear antenna arrays. The integration of PWWGs in these systems will lower loss compared to current planar solutions, while low-cost PCB techniques can still be employed.

A fast-developing millimeter-wave application is imaging. Imaging systems are used for the detection of concealed objects at high-security sites, such as airports. Many of the systems under development operate at 94 GHz. Contrary to the first two millimeter-wave applications, imaging is not based on classical phased-array theory but on the principle that the antennas constitute pixels in an image. The acquisition time, that is inversely proportional to the number of pixels, is currently a major obstacle in the practical application of imaging systems. PWWG technology can be used to integrate many pixels on a PCB and, hence, help to decrease the acquisition time of imaging systems.

7.3 Recommendations

We concluded that our current PWWG implementation has a number of limitations. In order to increase versatility, the software should be extended through:

1. implementation of multi-port components,
2. implementation of non-parallel ports, and

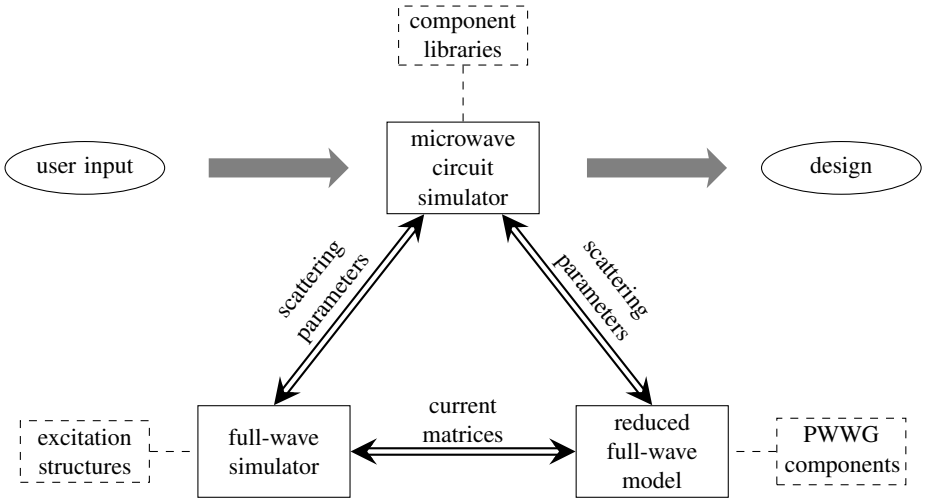

Figure 7.2 — Implementation of a reduced full-wave model with existing full-wave and circuit simulation tools to facilitate practical microwave system design.

3. integration of our method into a microwave circuit simulator.

These improvements, combined with the cascading of components, will make the software suitable for practical system design. The block diagram of Figure 7.2 depicts our vision of the interaction between a circuit simulator, a full-wave electromagnetic simulator, and our software based on a reduced full-wave model. The integration of our software in a circuit simulator (such as ADS) will provide designers a user interface that they are familiar with, will facilitate the integration of PWWGs with other microwave components, and will make available powerful optimization algorithms. Integration is unquestionably an essential step for the application of PWWGs in practical microwave systems.

Beside optimizing the design procedure in PWWG-based systems, the simulated performance of such systems needs to be supported by measurements. We therefore propose the manufacturing of a set of new and more complex hardware demonstrators:

1. PWWG samples that operate at 60 GHz and/or higher frequencies,

2. complex fully-optimized PWWG components, and

3. a complete integrated PWWG (phased) array front-end combining front-end electronics, feed network and antennas.

The first item is meant to demonstrate that PWWGs manufactured in standard PCB technology can be used at higher frequencies and to verify by measurement that PWWGs exhibit lower loss than conventional planar transmission lines in the millimeter frequency range. Considerable effort has to be put into accurate characterization of the samples, since measurements at millimeter-wave frequencies suffer from a higher measurement floor and greater repeatability

error. In manufacturing complex component demonstrators, we wish to establish, in practice, the ability of our method to rapidly and accurately calculate the performance of PWWG systems compared to general-purpose field simulators which require orders of magnitude greater computation times. A complete front-end should prove the feasibility of active component integration with PWWG technology.

APPENDIX A

Rectangular Waveguide Dimensions

Frequency band	Standard	Frequency range (GHz)	Width (mm)	Height (mm)
L	WR-770	0.96–1.50	196	86.0
D	WR-340	2.20–3.30	86.4	43.2
S	WR-284	2.60–3.95	72.2	34.0
C	WR-137	5.85–8.20	34.9	15.8
X	WR-90	8.20–12.4	22.9	10.2
Ku	WR-62	12.4–18.0	15.8	7.90
K	WR-42	18.0–26.5	10.7	4.32
Ka	WR-28	26.5–40.0	7.11	3.56
V	WR-15	50.0–75.0	3.76	1.88
W	WR-10	75.0–110	2.54	1.27

Appendix B

Graf's Summation Theorem

Gradshteyn [125, Sec. 8.53] and Watson [61, Sec. 11.3] give Graf's summation theorem for general solutions of the Bessel equation $\mathscr{C}_\nu$ as

$$\mathscr{C}_\nu(r_{BA})e^{-j\nu\psi} = \sum_{m=-\infty}^{\infty} \mathscr{C}_{\nu+m}(r_A)J_m(r_B)e^{-jm\phi}, \qquad (r_A > r_B). \tag{B.1}$$

From Figure B.1 we see that in case $r_A < r_B$, we need only to exchange r_A and r_B and the angle Ψ becomes the angle between OB and AB instead of OA and AB. In [61], the signs of ϕ and ψ are not fixed, but according to $Rr_B \sin\phi = r_{BA} \sin\psi$ they must have the same sign. Continuity at $r_A = r_B$ is guaranteed, since ϕ remains unchanged and at $r_A = r_B$, $L(OB, AB) = L(OA, AB)$.

Fixing OA and moving B, we can say that ϕ and ψ are both measured with respect to OA in clockwise and counter-clockwise direction, respectively. Then, they are either both positive or both negative.

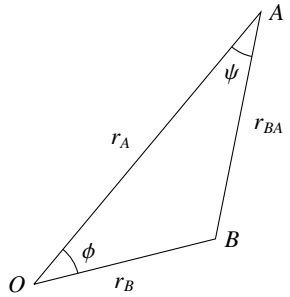

Figure B.1 — Notation used in Graf's summation theorem.

Appendix C

Divergence Transfer

For the numerical evaluation of the magnetic field it can be useful to transfer the divergence in the first term of (2.56) to the surface current. To accomplish this transfer, we reverse first the divergence and the integral and we apply the vector identity $\operatorname{div}(f\boldsymbol{v}) = f\operatorname{div}\boldsymbol{v} + \operatorname{grad} f \cdot \boldsymbol{v}$ to obtain

$$\text{first term in RHS of (2.57)} = \operatorname{grad}_{\boldsymbol{x}} \int_{\partial\Omega} \operatorname{grad}_{\boldsymbol{x}} H_0^{(2)}(k_i|\boldsymbol{x}_t - \boldsymbol{x}_t'|) \cdot \boldsymbol{M}^{\text{surf}}(\boldsymbol{x}_t')\, d\partial\Omega', \tag{C.1}$$

where we use $\operatorname{div}_{\boldsymbol{x}} \boldsymbol{M}^{\text{surf}}(\boldsymbol{x}_t') = 0$. We write $\boldsymbol{M}^{\text{surf}}$ as $-\boldsymbol{n}_t \times (\boldsymbol{n}_t \times \boldsymbol{M}^{\text{surf}})$, apply cyclic rotation to the dot product in (C.1) with this expression for $\boldsymbol{M}^{\text{surf}}$, and apply the gradient to $\boldsymbol{x}'$ instead of $\boldsymbol{x}$. Then,

$$\text{first term in RHS of (2.57)} = \operatorname{grad}_{\boldsymbol{x}} \int_{\partial\Omega} \boldsymbol{n}_t \cdot \Big((\boldsymbol{n}_t \times \boldsymbol{M}^{\text{surf}}(\boldsymbol{x}_t')) \times \operatorname{grad}_{\boldsymbol{x}'} H_0^{(2)}(k_i|\boldsymbol{x}_t - \boldsymbol{x}_t'|) \Big)\, d\partial\Omega'. \tag{C.2}$$

We observe in this expression that the gradient is twice applied to an argument of the Hankel function. We can transfer the gradient with respect to $\boldsymbol{x}'$, to the surface current. To accomplish this transfer, it is tempting to apply the vector identity $\boldsymbol{v} \times \operatorname{grad} f = f\operatorname{curl}\boldsymbol{v} - \operatorname{curl}(f\boldsymbol{f})$ to the cross product in the integrand, but we have to realize that $\boldsymbol{n}_t$ and $\boldsymbol{M}^{\text{surf}}$ are only defined at $\partial\Omega$. We know that $\boldsymbol{M}^{\text{surf}} = \boldsymbol{n}_t \times \boldsymbol{E}|_{\partial\Omega}$, where $\boldsymbol{E}$ is an electric field that satisfies the source free Maxwell's equations either in Ω or in $\overline{\Omega}$ with corresponding magnetic field $\boldsymbol{H}$. Then, $\boldsymbol{n}_t \times \boldsymbol{M}^{\text{surf}} = \boldsymbol{n}_t \times (\boldsymbol{n}_t \times \boldsymbol{E}|_{\partial\Omega}) = -\boldsymbol{E}|_{\partial\Omega}$. Substituting this expression in (C.2) we can omit the restriction to $\partial\Omega$, since the integral is over $\partial\Omega$. Next, we apply the vector identity $\boldsymbol{v} \times \operatorname{grad} f = f\operatorname{curl}\boldsymbol{v} - \operatorname{curl}(f\boldsymbol{v})$ to obtain

$$\begin{aligned}&\text{first term in RHS of (2.57)} = \\ &-\operatorname{grad}_{\boldsymbol{x}} \int_{\partial\Omega} \boldsymbol{n}_t \cdot \Big[H_0^{(2)}(k_i|\boldsymbol{x}_t - \boldsymbol{x}_t'|)\operatorname{curl}_{\boldsymbol{x}'} \boldsymbol{E}(\boldsymbol{x}_t') - \operatorname{curl}_{\boldsymbol{x}'} \left(H_0^{(2)}(k_i|\boldsymbol{x}_t - \boldsymbol{x}_t'|)\boldsymbol{E}(\boldsymbol{x}_t') \right) \Big]\, d\partial\Omega'.\end{aligned} \tag{C.3}$$

With Gauss' theorem in two dimensions it follows that the integral over the dot product of $\boldsymbol{n}_t$ and the second term between brackets vanishes, since $\operatorname{div}\operatorname{curl} = 0$. To calculate the first integral we

recall that $\boldsymbol{E} = e_y \boldsymbol{i}_y$. Applying the vector identity $\operatorname{curl}(f\boldsymbol{v}) = f\operatorname{curl}\boldsymbol{v} + \operatorname{grad} f \times \boldsymbol{v}$ to the curl of $\boldsymbol{E}$ and applying cyclic rotation, we find

$$\text{first term in RHS of (2.57)} = -\operatorname{grad}_{\boldsymbol{x}} \int_{\partial\Omega} H_0^{(2)}(k_i|\boldsymbol{x}_t - \boldsymbol{x}_t'|)\operatorname{grad}_{\boldsymbol{x}'} E_y(\boldsymbol{x}_t') \cdot (\boldsymbol{i}_y \times \boldsymbol{n}_t)\, d\partial\Omega'. \quad \text{(C.4)}$$

Define the vector $\boldsymbol{\tau}$ by $\boldsymbol{\tau}(\boldsymbol{x}_t) = \boldsymbol{i}_y \times \boldsymbol{n}_t(\boldsymbol{x}_t),\ \boldsymbol{x}_t \in \partial\Omega$. Then $\boldsymbol{\tau}$ is the tangential vector at $\partial\Omega$. Hence the dot product in (C.4) is the tangential derivative of E_y along $\partial\Omega$. Since $\boldsymbol{M}^{\text{surf}} = \boldsymbol{n}_t \times \boldsymbol{E}|_{\partial\Omega} = -E_y\boldsymbol{\tau}$, we can interpret the dot product as minus the derivative of $\boldsymbol{M}^{\text{surf}} \cdot \boldsymbol{\tau}$.

Appendix D

Calculation of the Current Matrix

To calculate the blocks of the current matrix (3.52) we first compute the coupling matrix C of the posts between the two parallel interfaces, as shown in Figure 3.6. The blocks C_{pq} of C are defined by (2.31) for metallic posts and by (2.38) for dielectric posts. We consider the blocks $T^{v(i),\mathrm{el}(i_1)}$, $v = \mathrm{el}, \mathrm{mag}$. The components $T^{v(i),\mathrm{el}(i_1)}_{\cdot n}$ correspond to the nth rooftop acting as an electric input surface current. The corresponding expansion coefficients of the incident fields on the posts are according to (3.37)

$$B^{\mathrm{el}(i_1,n)}_{p,\nu} = -\frac{k_1\zeta_1 d_{\mathrm{port}(i_1)}}{16\pi J_\nu(k_1 a_p)} \int_{-\pi}^{\pi} \int_{s^{(i_1)}_{n-1}}^{s^{(i_1)}_{n+1}} e^{j\nu\varphi} H_0^{(2)}(k_1 R_p^{(i_1)}(\varphi, s')) \Lambda_n^{(i_1)}(s') ds' d\varphi. \tag{D.1}$$

The expansion coefficients of the corresponding scattered field are computed from the matrix-vector product $A^{\mathrm{el}(i_1,n)} = C^{-1} B^{\mathrm{el}(i_1,n)}$. The output surface currents follow from (3.44). By (3.45)–(3.49)

$$J_y^{\mathrm{out}(i),\mathrm{el}(i_1,n)}(s) = \chi(i)\Bigg\{ \frac{jk_1 d_{\mathrm{port}(i_1)}}{8} \int_{s^{(i_1)}_{n-1}}^{s^{(i_1)}_{n+1}} H_1^{(2)}(k_1 R^{(i,i_1)}(s,s')) \frac{c_{\mathrm{port}(i),z} - c_{\mathrm{port}(i_1),z}}{R^{(i,i_1)}(s,s')} \Lambda_n^{(i_1)}(s') ds' + \sum_{q=1}^{Q} F_{H,q}^{i,\mathrm{el}(i_1,n)}(s) \Bigg\}, \tag{D.2a}$$

$$M_x^{\mathrm{out}(i),\mathrm{el}(i_1,n)}(s) = \chi(i)\Bigg\{ \frac{k_1\zeta_1 d_{\mathrm{port}(i_1)}}{8} \int_{s^{(i_1)}_{n-1}}^{s^{(i_1)}_{n+1}} H_0^{(2)}(k_1 R^{(i,i_1)}(s,s')) \Lambda_n^{(i_1)}(s') ds' + \sum_{q=1}^{Q} F_{E,q}^{i,\mathrm{el}(i_1,n)}(s) \Bigg\}, \tag{D.2b}$$

where

$$F_{H,q}^{i,u(i_1,n)}(s) = -\frac{\omega\varepsilon_1}{k_1^2 r_q^{(i)}(s)} \sum_{\nu=-N}^{N} \nu A_{q,\nu}^{u(i_1,n)} H_\nu^{(2)}(k_1 r_q^{(i)}(s)) e^{j\nu\varphi_q^{(i)}(s)} \sin\varphi_q^{(i)}(s) - \frac{j\omega\varepsilon_1}{k_1} \sum_{\nu=-N}^{N} A_{q,\nu}^{u(i_1,n)} H_\nu^{(2)\prime}(k_1 r_q^{(i)}(s)) e^{j\nu\varphi_q^{(i)}(s)} \cos\varphi_q^{(i)}(s), \quad \text{(D.3a)}$$

and

$$F_{E,q}^{i,u(i_1,n)}(s) = \sum_{\nu=-N}^{N} A_{q,\nu}^{u(i_1,n)} H_\nu^{(2)}(k_1 r_q^{(i)}(s)) e^{j\nu\varphi_q^{(i)}(s)}, \quad \text{(D.3b)}$$

with $u = \text{el}, \text{mag}$. The components of $T_{\cdot n}^{\text{el}(i),\text{el}(i_1)}$ are the expansion coefficients of $J_y^{\text{out}(i),\text{el}(i_1,n)}$ expanded in terms of $\Lambda_n^{(i)}$, and the components of $T_{\cdot n}^{\text{mag}(i),\text{el}(i_1)}$ are those of $M_x^{\text{out}(i),\text{el}(i_1,n)}$. By taking inner products of these expansions with $\Lambda_m^{(i)}$ it follows that

$$T^{v(i),u(i_1)} = \left(G^{(i)}\right)^{-1} \tilde{T}^{v(i),u(i_1)}, \quad \text{(D.4)}$$

where $v = \text{el}, \text{mag}$ and $u = \text{el}$ and where $G^{(i)}$ is the (tri-diagonal) Gram matrix of the functions $\Lambda_m^{(i)}$,

$$G_{mn}^{(i)} = \langle \Lambda_m^{(i)}, \Lambda_n^{(i)} \rangle_{[-1,1]} = \begin{cases} 2\Delta_{\text{exp}}^{(i)}/3, & m = n, \\ \Delta_{\text{exp}}^{(i)}/6, & |m-n| = 1, \\ 0, & |m-n| > 1, \end{cases} \quad \text{(D.5)}$$

and $\tilde{T}^{\text{el}(i),\text{el}(i_1)}$ and $\tilde{T}^{\text{mag}(i),\text{el}(i_1)}$ are defined by

$$\tilde{T}_{mn}^{\text{el}(i),\text{el}(i_1)} = \langle \Lambda_m^{(i)}, J_y^{\text{out}(i),\text{el}(i_1,n)} \rangle_{[-1,1]} = \chi(i) \left\{ \frac{jk_1 d_{\text{port}(i_1)}}{8} \Xi_1^{i,m,i_1,n} + \sum_{q=1}^{Q} \int_{s_{n-1}^{(i)}}^{s_{n+1}^{(i)}} \Lambda_m^{(i)}(s) F_{H,q}^{i,\text{el}(i_1,n)}(s) ds \right\}, \quad \text{(D.6a)}$$

$$\tilde{T}_{mn}^{\text{mag}(i),\text{el}(i_1)} = \langle \Lambda_m^{(i)}, M_x^{\text{out}(i),\text{el}(i_1,n)} \rangle_{[-1,1]} = \chi(i) \left\{ \frac{k_1\zeta_1 d_{\text{port}(i_1)}}{8} \Xi_2^{i,m,i_1,n} + \sum_{q=1}^{Q} \int_{s_{n-1}^{(i)}}^{s_{n+1}^{(i)}} \Lambda_m^{(i)}(s) F_{E,q}^{i,\text{el}(i_1,n)}(s) ds \right\}. \quad \text{(D.6b)}$$

The integrals $\Xi_1^{i,m,i_1,n}$ and $\Xi_2^{i,m,i_1,n}$ are given by

$$\Xi_1^{i,m,i_1,n} = \int_{s_{m-1}^{(i)}}^{s_{m+1}^{(i)}} \int_{s_{n-1}^{(i_1)}}^{s_{n+1}^{(i_1)}} H_1^{(2)}(k_1 R^{(i,i_1)}(s,s')) \frac{c_{\mathrm{port}(i),z} - c_{\mathrm{port}(i_1),z}}{R^{(i,i_1)}(s,s')} \Lambda_m^{(i)}(s) \Lambda_n^{(i_1)}(s') ds' ds, \tag{D.7a}$$

$$\Xi_2^{i,m,i_1,n} = \int_{s_{m-1}^{(i)}}^{s_{m+1}^{(i)}} \int_{s_{n-1}^{(i_1)}}^{s_{n+1}^{(i_1)}} H_0^{(2)}(k_1 R^{(i,i_1)}(s,s')) \Lambda_m^{(i)}(s) \Lambda_n^{(i_1)}(s') ds' ds. \tag{D.7b}$$

Finally we consider the blocks $T^{v(i),\mathrm{mag}(i_1)}$, $v = \mathrm{el}, \mathrm{mag}$. The components $T_{\cdot n}^{v(i),\mathrm{mag}(i_1)}$ correspond to the nth rooftop acting as a magnetic input surface current. The corresponding expansion coefficients of the incident fields on the posts are according to (3.37)

$$B_{p,\nu}^{\mathrm{mag}(i_1,n)} = -\frac{jk_1 d_{\mathrm{port}(i_1)}}{16\pi J_\nu(k_1 a_p)} \int_{-\pi}^{\pi} \int_{s_{n-1}^{(i_1)}}^{s_{n+1}^{(i_1)}} e^{j\nu\varphi} H_1^{(2)}(k_1 R_p^{(i_1)}(\varphi, s')) \frac{c_{p,z} + a_p \cos\varphi - c_{\mathrm{port}(i_1),z}}{R_p^{(i_1)}(\varphi, s')} \Lambda_n^{(i_1)}(s') ds' d\varphi. \tag{D.8}$$

The expansion coefficients of the corresponding scattered field are computed from the matrix-vector product $A^{\mathrm{mag}(i_1,n)} = C^{-1} B^{\mathrm{mag}(i_1,n)}$. The output surface currents follow from (3.44). By (3.45)–(3.49) and the definitions of (D.3) we find

$$J_y^{\mathrm{out}(i),\mathrm{mag}(i_1,n)}(s) = \chi(i) \Bigg\{ \frac{k_1 d_{\mathrm{port}(i_1)}}{8\zeta_1} \int_{s_{n-1}^{(i_1)}}^{s_{n+1}^{(i_1)}} H_0^{(2)}(k_1 R^{(i,i_1)}(s,s')) \Lambda_n^{(i_1)}(s') ds' + \frac{4}{k_1^2 d_{\mathrm{port}(i_1)} d_{\mathrm{port}(i)}} \frac{d}{ds} \int_{s_{n-1}^{(i_1)}}^{s_{n+1}^{(i_1)}} H_0^{(2)}(k_1 R^{(i,i_1)}(s,s')) \Lambda_n^{(i_1)'}(s') ds' + \sum_{q=1}^{Q} F_{H,q}^{i,\mathrm{mag}(i_1,n)}(s) \Bigg\}, \tag{D.9a}$$

$$M_x^{\mathrm{out}(i),\mathrm{mag}(i_1,n)}(s) = \chi(i) \Bigg\{ \frac{jk_1\zeta_1 d_{\mathrm{port}(i_1)}}{8} \int_{s_{n-1}^{(i_1)}}^{s_{n+1}^{(i_1)}} H_1^{(2)}(k_1 R^{(i,i_1)}(s,s')) \frac{c_{\mathrm{port}(i),z} - c_{\mathrm{port}(i_1),z}}{R^{(i,i_1)}(s,s')} \Lambda_n^{(i_1)}(s') ds' + \sum_{q=1}^{Q} F_{E,q}^{i,\mathrm{mag}(i_1,n)}(s) \Bigg\}. \tag{D.9b}$$

The components of $T_{\cdot n}^{\mathrm{el}(i),\mathrm{mag}(i_1)}$ are the expansion coefficients of $J_y^{\mathrm{out}(i),\mathrm{mag}(i_1,n)}$ expanded in terms of $\Lambda_n^{(i)}$, and the components of $T_{\cdot n}^{\mathrm{mag}(i),\mathrm{mag}(i_1)}$ are those of $M_x^{\mathrm{out}(i),\mathrm{mag}(i_1,n)}$. By taking inner products of the expansions with $\Lambda_m^{(i)}$ it follows that $T^{\mathrm{el}(i),\mathrm{mag}(i_1)}$ and $T^{\mathrm{mag}(i),\mathrm{mag}(i_1)}$ are given by (D.4) with

$v = \mathrm{el}, \mathrm{mag}$ and $u = \mathrm{mag}$, and $\tilde{T}^{\mathrm{el}(i),\mathrm{mag}(i_1)}$ and $\tilde{T}^{\mathrm{mag}(i),\mathrm{mag}(i_1)}$ are defined by

$$\tilde{T}^{\mathrm{el}(i),\mathrm{mag}(i_1)}_{mn} = \langle \Lambda^{(i)}_m, J_y^{\mathrm{out}(i),\mathrm{mag}(i_1,n)} \rangle_{[-1,1]} =$$

$$\chi(i)\left\{ \frac{k_1 d_{\mathrm{port}(i_1)}}{8\zeta_1} \left(\Xi_2^{i,m,i_1,n} - \frac{4}{k_1^2 d_{\mathrm{port}(i_1)} d_{\mathrm{port}(i)}} \Xi_3^{i,m,i_1,n} \right) + \sum_{q=1}^{Q} \int_{s^{(i)}_{m-1}}^{s^{(i)}_{m+1}} \Lambda^{(i)}_m(s) F_{H,q}^{i,\mathrm{mag}(i_1,n)}(s) ds \right\}, \quad \text{(D.10a)}$$

$$\tilde{T}^{\mathrm{mag}(i),\mathrm{mag}(i_1)}_{mn} = \langle \Lambda^{(i)}_m, M_x^{\mathrm{out}(i),\mathrm{mag}(i_1,n)} \rangle_{[-1,1]} =$$

$$\chi(i)\left\{ \frac{jk_1 d_{\mathrm{port}(i_1)}}{8} \Xi_1^{i,m,i_1,n} + \sum_{q=1}^{Q} \int_{s^{(i)}_{m-1}}^{s^{(i)}_{m+1}} \Lambda^{(i)}_m(s) F_{E,q}^{i,\mathrm{mag}(i_1,n)}(s) ds \right\}. \quad \text{(D.10b)}$$

The integral $\Xi_3^{i,m,i_1,n}$ is defined by

$$\Xi_3^{i,m,i_1,n} = \int_{s^{(i)}_{m-1}}^{s^{(i)}_{m+1}} \int_{s^{(i_1)}_{n-1}}^{s^{(i_1)}_{n+1}} H_0^{(2)}(k_1 R^{(i,i_1)}(s,s')) \Lambda^{(i)\prime}_m(s) \Lambda^{(i_1)\prime}_n(s') ds' ds. \quad \text{(D.11)}$$

We note that in (D.10a) and (D.11) we transferred the derivative d/ds in (D.9a) to the functions $\Lambda^{(i)}_m$ by integration by parts and, moreover,

$$\Lambda^{(i)\prime}_n(s) = \frac{1}{\Delta^{(i)}_{\mathrm{exp}}} \Lambda' \left(\frac{s - s^{(i)}_n}{\Delta^{(i)}_{\mathrm{exp}}} \right), \qquad s \neq s^{(i)}_{n-1}, s^{(i)}_n, s^{(i)}_{n+1}. \quad \text{(D.12)}$$

The next step is to numerically evaluate the integrals in (D.1),(D.6),(D.8) and (D.10). Let us first consider the integrals

$$\Xi_{4,v,u,q}^{i,m,i_1,n} = \int_{s^{(i)}_{m-1}}^{s^{(i)}_{m+1}} \Lambda^{(i)}_m(s) F_{w(v),q}^{i,u(i_1,n)}(s) ds, \quad \text{(D.13)}$$

where $u, v = \mathrm{el}, \mathrm{mag}$, $w(\mathrm{el}) = H$, $w(\mathrm{mag}) = E$. For fixed i, i_1, n, q, u and w we evaluate the integral by first computing the function $F_{w,q}^{i,u(i_1,n)}$ in the points $s^{(i)}_{n,\kappa} = s^{(i)}_n + \kappa \Delta^{(i)}_{\mathrm{exp}}/N^{(i)}_{\mathrm{int}}$, $\kappa = 0, 1, \ldots, N^{(i)}_{\mathrm{int}} - 1$, $n = 0, 1, \ldots, N^{(i)}_{\mathrm{exp}}$, and $s^{(i)}_{N^{(i)}_{\mathrm{exp}}+1} = 1$. Next we compute the integrals by a composite Simpson rule, which is given by

$$\int_a^b f(x) dx = \frac{b-a}{6N_{\mathrm{int}}} \sum_{\kappa=0}^{2N_{\mathrm{int}}} W^{[N_{\mathrm{int}}]}_{\kappa+1} f(x_\kappa), \quad \text{(D.14)}$$

where $x_\kappa = a + \kappa(b-a)/2N_{\mathrm{int}}$ and the weighting vector $W^{[N_{\mathrm{int}}]}$ of length $2N_{\mathrm{int}} + 1$ is defined by $W^{[N_{\mathrm{int}}]} = (1, 4, 2, 4, 2, \ldots, 4, 1)$. In the specific case of the integrals (D.13), $a = s^{(i)}_{m-1}$, $b = s^{(i)}_{m+1}$,

$b - a = 2\Delta_{\text{exp}}^{(i)}$, $N_{\text{int}} = N_{\text{int}}^{(i)}$, f is the integrand in (D.13) and $x_\kappa = s_{m-1,\kappa}^{(i)}$ where we use that $s_{m,\kappa}^{(i)} = s_{m-1,\kappa}^{(i)} + (N_{\text{int}}^{(i)} + \kappa)\Delta_{\text{exp}}^{(i)}/N_{\text{int}}^{(i)}$.

The integrals $\Xi_{\kappa'}^{i,m,i_1,n}$, $\kappa' = 1, 2, 3$ are all of the following type

$$\Xi_{\kappa'}^{i,m,i_1,n} = \int_{s_{m-1}^{(i)}}^{s_{m+1}^{(i)}} \int_{s_{n-1}^{(i_1)}}^{s_{n+1}^{(i_1)}} f_{\kappa'}(k_1 R^{(i,i_1)}(s,s'))\Lambda_m^{(i)}(s)\Lambda_n^{(i_1)}(s')ds'ds, \tag{D.15}$$

where $\Lambda_m^{(i)}$ and $\Lambda_n^{(i_1)}$ are replaced by their derivatives for $\kappa' = 3$. We write the distance measure of (3.46) as

$$R^{(i,i_1)}(s,s') = \left|\boldsymbol{c}_{\text{port}(i)} - \boldsymbol{c}_{\text{port}(i_1)} + \boldsymbol{i}_x d_{\text{port}(i_1)}\left(s\frac{d_{\text{port}(i)}}{d_{\text{port}(i_1)}} - s'\right)/2\right|. \tag{D.16}$$

Next we introduce $\hat{s} = d_{\text{port}(i)}s/d_{\text{port}(i_1)}$ in D.15. Then

$$\Xi_{\kappa'}^{i,m,i_1,n} = \frac{d_{\text{port}(i_1)}}{d_{\text{port}(i)}} \int_{\hat{s}_{m-1}^{(i)}}^{\hat{s}_{m+1}^{(i)}} \int_{s_{n-1}^{(i_1)}}^{s_{n+1}^{(i_1)}} f_{\kappa'}(k_1 \hat{R}^{(i,i_1)}(\hat{s} - s'))\Lambda_m^{(i)}(\hat{s})\Lambda_n^{(i_1)}(s')ds'd\hat{s}, \tag{D.17}$$

where $\hat{s}_m^{(i)} = d_{\text{port}(i)}s_m^{(i)}/d_{\text{port}(i_1)}$ and

$$\hat{R}^{(i,i_1)}(s) = |\boldsymbol{c}_{\text{port}(i)} - \boldsymbol{c}_{\text{port}(i_1)} + \boldsymbol{i}_x d_{\text{port}(i_1)}s/2|. \tag{D.18}$$

Introducing the transformations $\xi = (s - s_m^{(i)})/\Delta_{\text{exp}}^{(i)}$ and $\xi' = (s' - s_m^{(i)})/\Delta_{\text{exp}}^{(i)}$ we obtain

$$\begin{aligned}\hat{R}^{(i,i_1)}(\hat{s} - s') = \Big|&\boldsymbol{c}_{\text{port}(i)} - \boldsymbol{c}_{\text{port}(i_1)} + \boldsymbol{i}_x d_{\text{port}(i_1)}\Delta_{\text{exp}}^{(i_1)} \\ &\times\left(\frac{\Delta_{\text{exp}}^{(i)}}{\Delta_{\text{exp}}^{(i_1)}}\xi - \xi' + \frac{1}{\Delta_{\text{exp}}^{(i_1)}}\left(1 - \frac{d_{\text{port}(i)}}{d_{\text{port}(i_1)}}\right) + \frac{d_{\text{port}(i)}}{d_{\text{port}(i_1)}}\frac{\Delta_{\text{exp}}^{(i)}}{\Delta_{\text{exp}}^{(i_1)}}m - n\right)/2\Big|.\end{aligned} \tag{D.19}$$

For $\Xi_{\kappa'}^{i,m,i_1,n}$ we find

$$\begin{aligned}\Xi_{\kappa'}^{i,m,i_1,n} = \frac{d_{\text{port}(i_1)}}{d_{\text{port}(i)}}\left(\Delta_{\text{exp}}^{(i_1)}\right)^2 \int_{-\Delta^{(i,i_1)}}^{\Delta^{(i,i_1)}} f_{\kappa'}\Bigg(k_1\Big|&\boldsymbol{c}_{\text{port}(i)} - \boldsymbol{c}_{\text{port}(i_1)} + \boldsymbol{i}_x d_{\text{port}(i_1)}\Delta_{\text{exp}}^{(i_1)} \\ &\times\left(\hat{\xi} - \xi' + \frac{1}{\Delta_{\text{exp}}^{(i_1)}}\left(1 - \frac{d_{\text{port}(i)}}{d_{\text{port}(i_1)}}\right) + \Delta^{(i,i_1)}m - n\right)/2\Big|\Bigg)\Lambda_m^{(i)}(\hat{\xi})\Lambda_n^{(i_1)}(\xi')d\xi'd\hat{\xi},\end{aligned} \tag{D.20}$$

where we set $\hat{\xi} = \Delta_{\text{exp}}^{(i)}\xi/\Delta_{\text{exp}}^{(i_1)}$ and $\Delta^{(i,i_1)} = d_{\text{port}(i)}\Delta_{\text{exp}}^{(i)}/d_{\text{port}(i_1)}\Delta_{\text{exp}}^{(i_1)}$. This integral can be interpreted as an inner product and a convolution. We introduce the convolution $*$ and the inner product $\langle\cdot,\cdot\rangle_\infty$ by

$$(f * g)(x) = \int_{-\infty}^{\infty} f(x')g(x - x')dx', \qquad \langle f, g\rangle_\infty = \int_{-\infty}^{\infty} f^*(x)g(x)dx. \tag{D.21}$$

Then we can write (D.20) as

$$\Xi_{\kappa'}^{i,m,i_1,n} = \frac{d_{\mathrm{port}(i_1)}}{d_{\mathrm{port}(i)}} \left(\Delta_{\mathrm{exp}}^{(i_1)}\right)^2 \left\langle \Lambda 1_{[-\Delta^{(i,i_1)},\Delta^{(i,i_1)}]}, \Lambda * f_{\kappa'}\left(k_1 \left| \boldsymbol{c}_{\mathrm{port}(i)} - \boldsymbol{c}_{\mathrm{port}(i_1)} + \boldsymbol{i}_x d_{\mathrm{port}(i_1)} \Delta_{\mathrm{exp}}^{(i_1)} \right.\right.\right.$$
$$\left.\left.\left. \times \left(\cdot + \frac{1}{\Delta_{\mathrm{exp}}^{(i_1)}} \left(1 - \frac{d_{\mathrm{port}(i)}}{d_{\mathrm{port}(i_1)}}\right) + \Delta^{(i,i_1)} m - n \right) /2 \right| \right) \right\rangle_\infty . \quad \text{(D.22)}$$

Note that Λ is defined as in (3.50). Employing the identity $\langle f, g * h\rangle_\infty = \langle h^*, f^* * g^\vee\rangle_\infty$ where $f^\vee(x) = g(-x)$, we obtain

$$\Xi_{\kappa'}^{i,m,i_1,n} = \frac{d_{\mathrm{port}(i_1)}}{d_{\mathrm{port}(i)}} \left(\Delta_{\mathrm{exp}}^{(i_1)}\right)^2 \int_{-(1+\min(1,\Delta^{(i,i_1)}))}^{1+\min(1,\Delta^{(i,i_1)})} f_{\kappa'}\left(k_1 \left| \boldsymbol{c}_{\mathrm{port}(i)} - \boldsymbol{c}_{\mathrm{port}(i_1)} + \boldsymbol{i}_x d_{\mathrm{port}(i_1)} \Delta_{\mathrm{exp}}^{(i_1)} \right.\right.$$
$$\left.\left. \times \left(\xi + \frac{1}{\Delta_{\mathrm{exp}}^{(i_1)}} \left(1 - \frac{d_{\mathrm{port}(i)}}{d_{\mathrm{port}(i_1)}}\right) + \Delta^{(i,i_1)} m - n \right) /2 \right| \right)$$
$$\times (\Lambda 1_{[-\Delta^{(i,i_1)},\Delta^{(i,i_1)}]} * \Lambda^\vee)(\xi) d\xi. \quad \text{(D.23)}$$

For the case $\kappa' = 1, 2$ we use that $\Lambda^\vee = \Lambda$, consequently the convolution in (D.23) is given by

$$(\Lambda 1_{[-\Delta^{(i,i_1)},\Delta^{(i,i_1)}]} * \Lambda^\vee)(\xi) =$$

$$\begin{cases} -v(1 + v - (1 + \frac{1}{2}v)|\xi| + \frac{1}{3}v^2) + u(1 - u + (1 - \frac{1}{2}u)|\xi| + \frac{1}{3}u^2) - \xi^2 + \frac{1}{3}|\xi|^3, & |\xi| \le u, \\ -v(1 - v - (1 - \frac{1}{2}v)|\xi| - \frac{1}{3}v^2) + u(1 - (1 - \frac{1}{2}u)|\xi| - \frac{1}{3}u^2), & u \le |\xi| \le 1, \\ \frac{2}{3} + (1 - \frac{1}{3}u^2)u - (\frac{3}{2} + (1 - \frac{1}{2}u)u)|\xi| + \xi^2 - \frac{1}{6}|\xi|^3, & 1 \le |\xi| \le 1 + u, \\ 0, & |\xi| > 1 + u, \end{cases} \quad \text{(D.24)}$$

where $u = \min(1, \Delta^{(i,i_1)})$ and $v = \max(-u, -1 + |\xi|)$. For the case $\kappa' = 3$, $\Lambda_m^{(i)}$ and $\Lambda_n^{(i_1)}$ are replaced by their derivatives. We use that $(\Lambda')^\vee = -\Lambda'$ and we express the convolution as

$$(\Lambda' 1_{[-\Delta^{(i,i_1)},\Delta^{(i,i_1)}]} * (\Lambda')^\vee)(\xi) = \begin{cases} u - 2|\xi| - v, & |\xi| \le u, \\ -u - v, & u \le |\xi| \le 1, \\ |\xi| - u - 1, & 1 \le |\xi| \le 1 + u, \\ 0, & |\xi| > 1 + u, \end{cases} \quad \text{(D.25)}$$

with u and v equally defined as for $\kappa' = 1, 2$.

In the case $i \neq i_1$ the integrand of integral (D.23) is regular for $\kappa' = 1, 2, 3$. We compute the integral by the composite Simpson rule (D.14), where $a = -(1 + \min(1, \Delta^{(i,i_1)}))$, $b = 1 + \min(1, \Delta^{(i,i_1)})$, f is the integrand in (D.23) and $x_\kappa = \xi_\kappa = -2 + 2\kappa/N_{\text{int}}$, $\kappa = 0, 1, \ldots, 2N_{\text{int}}$.

For the self-coupling case $i = i_1$ the integral $\Xi_1^{i,m,i_1,n}$ vanishes, thus there is no electric-to-electric and magnetic-to-magnetic self-coupling of a port. For the self-coupling cases with $\kappa' = 2, 3$ we substitute $\Delta^{(i,i_1)} = 1$ and $f = H_0^{(2)}$ in (D.23) to obtain

$$\Xi_{\kappa'}^{i,m,i,n} = \left(\Delta_{\text{exp}}^{(i)}\right)^2 \int_{-2}^{2} H_0^{(2)}(k_1 d_{\text{port}(i)} \Delta_{\text{exp}}^{(i)} |\xi + m - n|/2)(\Lambda * \Lambda^\vee)(\xi) d\xi = \tilde{\Xi}_{\kappa'}^{i,m-n}, \tag{D.26}$$

where for the case $\kappa' = 3$, Λ is replaced by its derivative Λ'. By substitution of $\Delta^{(i,i_1)} = 1$, $u = 1$ and $v = -1 + |\xi|$ the convolutions (D.24) and (D.25) simplify to

$$(\Lambda * \Lambda^\vee)(\xi) = \begin{cases} \frac{2}{3} - \xi^2 + \frac{1}{2}|\xi|^3, & |\xi| \leq 1, \\ \frac{4}{3} - 2|\xi| + \xi^2 - \frac{1}{6}|\xi|^3, & 1 \leq |\xi| \leq 2, \\ 0, & |\xi| > 2, \end{cases} \tag{D.27}$$

and

$$(\Lambda' * (\Lambda')^\vee)(\xi) = \begin{cases} 2 - 3|\xi|, & |\xi| \leq 1, \\ |\xi| - 2, & 1 \leq |\xi| \leq 2, \\ 0, & |\xi| > 2, \end{cases} \tag{D.28}$$

respectively.

We observe that $\tilde{\Xi}_{\kappa'}^{i,-n} = \tilde{\Xi}_{\kappa'}^{i,n}$, thus we only need to compute $\tilde{\Xi}_{\kappa'}^{i,n}$ for $n \geq 0$. For $n \geq 3$ the integrand of $\tilde{\Xi}_{\kappa'}^{i,n}$ is regular. In that case we compute the integral by the composite Simpson rule (D.14), where $a = -2$, $b = 2$, f is the integrand in (D.26) and $x_\kappa = \xi_\kappa = -2 + 2\kappa/N_{\text{int}}$, $\kappa = 0, 1, \ldots, 2N_{\text{int}}$. The integrand of $\tilde{\Xi}_{\kappa'}^{i,n}$ is logarithmically singular for $n = 0, 1, 2$ at $\xi = -n$. We write $\tilde{\Xi}_{\kappa'}^{i,n}$ as

$$\begin{aligned} \tilde{\Xi}_{\kappa'}^{i,n} = \left(\Delta_{\text{exp}}^{(i)}\right)^2 \Bigg\{ & -\frac{2j}{\pi}(\Lambda * \Lambda^\vee)(-n) \int_{-2}^{2} \log(\dagger) d\xi \\ & + \int_{-2}^{2} H_0^{(2)}(2\dagger)(\Lambda * \Lambda^\vee)(\xi) + \frac{2j}{\pi}(\Lambda * \Lambda^\vee)(-n) \log(\dagger) d\xi \Bigg\}, \\ & \dagger = k_1 d_{\text{port}(i)} \Delta_{\text{exp}}^{(i)} |\xi + n|/4, \end{aligned} \tag{D.29}$$

where for the case $\kappa' = 3$, Λ is replaced by Λ'.

The integrand of the second integral is regular at $\xi = -n$ and hence we can compute the integral by the composite Simpson rule (D.14). The first integral can be calculated analytically

$$\int_{-2}^{2} \log(\dagger|\xi + n|)d\xi = (n+2)\log(\dagger(n+2)) - (n-2)\log(\dagger(2-n)) - 4,$$

$$\dagger = k_1 d_{\mathrm{port}(i)} \Delta_{\mathrm{exp}}^{(i)}/4. \quad \text{(D.30)}$$

Finally we consider the integrals in (D.1) and (D.8). Both integrals have regular integrands since there is always a significant distance between the ports and the posts. We compute the integrals by a 2D composite Simpson rule, which is given by

$$\int_a^b \int_c^d f(x,y)dydx = \frac{(b-a)(d-c)}{36N_{\mathrm{int},x}N_{\mathrm{int},y}} \sum_{\kappa=0}^{2N_{\mathrm{int},x}} \sum_{\kappa'=0}^{2N_{\mathrm{int},y}} W_{\kappa+1,\kappa'+1}^{[N_{\mathrm{int},x},N_{\mathrm{int},y}]} f(x_\kappa, y_{\kappa'}). \quad \text{(D.31)}$$

Having described all the calculational ingredients to construct the current matrix, we summarize the steps that have to be carried out for the actual computation.

I. Compute the blocks C_{pq} $(p,q = 1,2,\ldots,Q)$ of the coupling matrix C of the posts between the interfaces; these blocks are defined by (2.31) for metallic posts and (2.38) for dielectric posts. Store the inverse C^{-1} of C.

II. For each combination (i_1, n) with $i_1 = 1,2$, $n = 1,2,\ldots,N_{\mathrm{exp}}^{(i)}$:

   A. Compute the components $B_{p,\nu}^{\mathrm{el}(i_1,n)}$, $p = 1,2,\ldots,Q$, $\nu = -N, -N+1, \ldots, N$ of the column vector $B^{\mathrm{el}(i_1,n)}$ by evaluating the integrals (D.1).

   B. Compute the matrix-vector product $A^{\mathrm{el}(i_1,n)} = C^{-1}B^{\mathrm{el}(i_1,n)}$.

   C. Compute the components $B_{p,\nu}^{\mathrm{mag}(i_1,n)}$, $p = 1,2,\ldots,Q$, $\nu = -N, -N+1, \ldots, N$ of the column vector $B^{\mathrm{mag}(i_1,n)}$ by evaluating the integrals (D.8).

   D. Compute the matrix-vector product $A^{\mathrm{mag}(i_1,n)} = C^{-1}B^{\mathrm{mag}(i_1,n)}$.

   E. For each value of $i = 1,2$:

      i. Compute the integrals $\Xi_{\tilde{\kappa}}^{i,m,i_1,n}$ for $m = 1,2,\ldots,N_{\mathrm{exp}}^{(i)}$ and $\tilde{\kappa} = 1,2,3$ by (D.7a), (D.7b) and (D.11).

      ii. For each combination (v,u) with $v,u = \mathrm{el}, \mathrm{mag}$:

         a. Set $\mathrm{Sum}[m] = 0$ for $m = 1,2,\ldots,N_{\mathrm{exp}}^{(i)}$.

         b. For $q = 1$ to Q

            - Compute $F_{w(v),q}^{i,u(i_1,n)}$ in the points $s_{n,\kappa}^{(i)} = s_n^{(i)} + \kappa\Delta_{\mathrm{exp}}^{(i)}/N_{\mathrm{int}}^{(i)}$, $\kappa = 0,1,\ldots,N_{\mathrm{int}}^{(i)} - 1$, $n = 0,1,\ldots,N_{\mathrm{exp}}^{(i)}$, and $s_{N_{\mathrm{exp}}^{(i)}+1}^{(i)} = 1$ from (D.3a) for $w(v) = H$ and from (D.3b) for $w(v) = E$.
            - Compute the integrals $\Xi_{4,v,u,q}^{i,m,i_1,n}$ for $m = 1,2,\ldots,N_{\mathrm{exp}}^{(i)}$ from (D.13).
            - Set $\mathrm{Sum}[m] = \mathrm{Sum}[m] + \Xi_{4,v,u,q}^{i,m,i_1,n}$ for $m = 1,2,\ldots,N_{\mathrm{exp}}^{(i)}$.

- Compute $\tilde{T}^{v(i),u(i_1)}$ from (D.6a) for $(u, v) = (\mathrm{el}, \mathrm{el})$, from (D.6b) for $(u, v) = (\mathrm{mag}, \mathrm{el})$, from (D.10a) for $(u, v) = (\mathrm{el}, \mathrm{mag})$ and from (D.10b) for $(u, v) = (\mathrm{mag}, \mathrm{mag})$, for each $m = 0, 1, \ldots, N_{\mathrm{exp}}^{(i)}$. Note that the sum from $q = 1$ to Q in (D.6) and (D.10) is Sum$[m]$.

III. For $i = 1, 2$: compute the Gram matrix $G^{(i)}$ as defined by (D.4).

IV. For each combination (i, v, i_1, u) with $i, i_1 = 1, 2$ and $v, u = \mathrm{el}, \mathrm{mag}$: compute the matrix products $T^{v(i),u(i_1)} = (G^{(i)})^{-1} \tilde{T}^{v(i),u(i_1)}$.

V. Compose the current matrix from the blocks $T^{v(i),u(i_1)}$ as in (3.52).

Appendix E

Manufactured Boards

E.1 Material specifications

The material specifications of the high and low-permittivity circuit boards discussed in Chapter 4 are presented in Table E.1.

		value			
Parameter	Symbol	Rogers TMM10i	Rogers RO4003C	Gore Speedboard C	Unit
Dielectric constant	ϵ_r	9.80 ± 0.245	3.38 ± 0.05	2.6	
Loss tangent	$\tan\delta$	0.0020	0.0027	0.004	
Thickness	h	0.381 and 3.810	1.524	0.038	mm

Table E.1 — Material properties of the used materials.

E.2 Board layer stack and layouts of the High-Permittivity Circuit Boards

The picture and the table of Figure E.1 give a detailed overview of the board stacks, copper patterns, and via holes of the high-permittivity circuit boards. Etched copper patterns are only present at the top of the thin TMM10i dielectric (layer Ⓐ) and at the top of the thick TMM10i dielectric (layer Ⓑ). At the bottom of the thin TMM10i dielectric no copper is present and the bottom of the thick TMM10i dielectric is completely covered with a copper layer. In the design two types of plated vias (Ⓘ and Ⓘⓘ) are used, the first consisting of through holes with an outer diameter of d=1.3 mm and the second consisting of blind holes with a outer diameter of d = 0.5 mm. Furthermore one type of non-plated holes (Ⓜ) is used with diameter d = 3.0 mm for the dielectric posts On the top of the layer stack a solder mask is applied (layer Ⓒ) directly on the bare copper. At the bottom of the layer stack no special finish is applied. The final layout of the manufactured boards is depicted in Figure E.3. Figure E.4 shows a photograph of the final manufactured board. The codes of the different transmission lines are clarified in Table E.2.

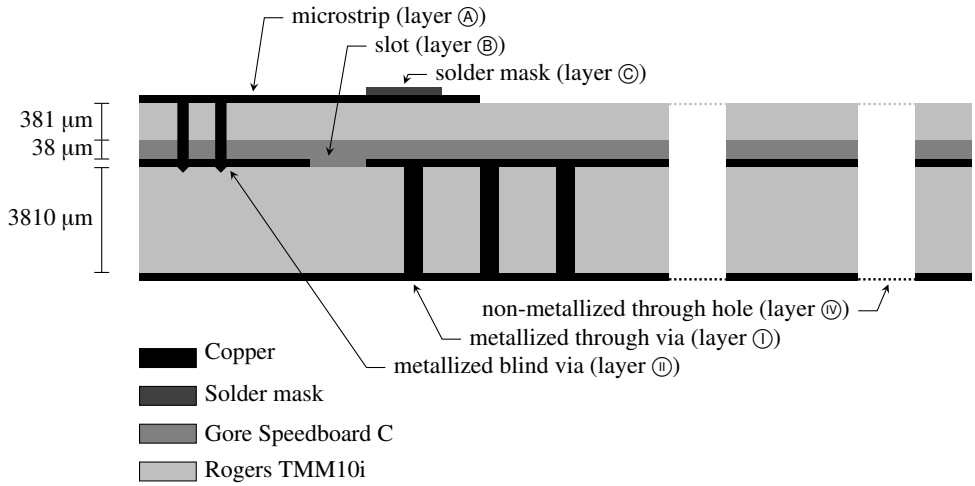

Layer	Description	Definition
Ⓐ	copper pattern	tracks (positive)
Ⓑ	copper pattern	slots (negative)
Ⓒ	solder mask	presence (positive)
Ⅰ	plated through hole	T01, d = 1.3 mm
Ⅱ	plated blind hole	T02, d = 0.6 mm
Ⅳ	non-plated blind hole	T04, d = 3.0 mm

Figure E.1 — Detailed layer stack and detailed specifications of the layer and via patterns of the manufactured high-permittivity boards.

Name	Description	Name	Description
D2F1L0	Through line	M1F1L0	Through line
D2F1L1	Line (Δl = 6.60 mm)	M1F1L1	Line (Δl = 5.14 mm)
D2F1L2	Line (Δl = 13.20 mm)	M1F1L2	Line (Δl = 10.28 mm)
D2F1L3	Line (Δl = 19.80 mm)	M1F1L3	Line (Δl = 15.42 mm)
D2F1L4	Line (Δl = 26.40 mm)	M1F1L4	Line (Δl = 20.56 mm)
D2F1L5	Line (Δl = 33.00 mm)	M1F1L5	Line (Δl = 25.70 mm)
D2F2L0	Through line	M1F2L0	Line (Δl = 0 mm)
D2F2L1	Line (Δl = 6.60 mm)	M1F2L1	Line (Δl = 5.14 mm)
D2F2L2	Line (Δl = 13.20 mm)	M1F2L2	Line (Δl = 10.28 mm)
D2F2L3	Line (Δl = 19.80 mm)	M1F2L3	Line (Δl = 15.42 mm)
D2F2L4	Line (Δl = 26.40 mm)	M1F2L4	Line (Δl = 20.56 mm)
D2F2L5	Line (Δl = 33.00 mm)	M1F2L5	Line (Δl = 25.70 mm)
D2F3L0	Through line	M1F3L0	Through line
D2F3L1	Line (Δl = 6.60 mm)	M1F3L1	Line (Δl = 5.14 mm)
D2F3L2	Line (Δl = 13.20 mm)	M1F3L2	Line (Δl = 10.28 mm)
D2F3L3	Line (Δl = 19.80 mm)	M1F3L3	Line (Δl = 15.42 mm)
D2F3L4	Line (Δl = 26.40 mm)	M1F3L4	Line (Δl = 20.56 mm)
D2F3L5	Line (Δl = 33.00 mm)	M1F3L5	Line (Δl = 25.70 mm)
T	Microstrip through	M1F1R	Reflect
R1	Microstrip short	M1F2R	Reflect
R2	Microstrip open	M1F3R	Reflect
LF1	Microstrip line (Δl = 3.89 mm)		
LF2	Microstrip line (Δl = 3.10 mm)		
LF3	Microstrip line (Δl = 2.69 mm)		

Table E.2 — List of the manufactured high-permittivity test samples with their assigned names. The indications M and D correspond to PWWGs with metallic and dielectric posts respectively. The samples are designed with three microstrip to PWWG transitions each with a different center frequency. The indication F1 corresponds to f_c = 8 GHz, F2 to f_c = 10 GHz, and F3 to f_c = 11.5 GHz.

E.3 Board layer stack and layouts of the Low-Permittivity Circuit Boards

The picture and the table of Figure E.2 give a detailed overview of the board stacks, copper patterns, and via holes of the high-permittivity circuit boards. The codes of the different components are clarified in Table E.3. The top and bottom of the RO4003C PCB are completely covered with a copper layer, but etched slot patterns in the copper are present at the top of the RO4003C PCB (layer Ⓐ). There is one type of plated via (①), that runs completely through the RO4003C PCB and has an outer diameter of d = 1.0 mm. Furthermore, the outlines of the sub-boards are drawn in layer ©: milling must be carried out around the contours defined in this layer. On the top of the layer stack a solder mask has to be applied (layer Ⓑ) directly on the bare copper. For the bottom of the PCB no special finish is needed: the bare copper is sufficient. Figure E.6 shows top-view photographs of the manufactured low-permittivity PWWG components.

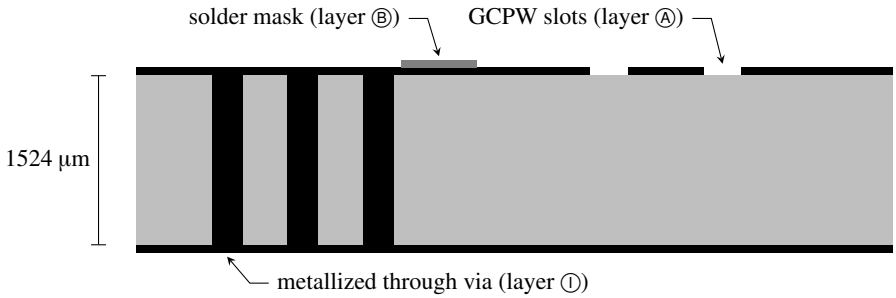

Layer	Description	Definition
Ⓐ	copper pattern	tracks (positive)
Ⓑ	solder mask	presence (positive)
Ⓒ	sub-board outline	milling outline
①	plated through hole	T01, d = 1 mm

Figure E.2 — Detailed layer stack and detailed specifications of the layer and via patterns of the manufactured low-permittivity boards.

Name	Description	Name	Description
MLCL0	Through line	CMPP1	Phase delay (w_g = 11.25 mm)
MLCL1	Line (Δl = 2.00 mm)	CMPP2	Phase delay (w_g = 10.75 mm)
MLCL2	Line (Δl = 6.00 mm)	CMPT1	H-plane tee
MLCL3	Line (Δl = 10.00 mm)	CMPC1	5 dB coupler
MLCL4	Line (Δl = 18.00 mm)	CMPC2	Riblet short-slot coupler
MLCL5	Line (Δl = 46.00 mm)	CMPC3	Cascaded Riblet short-slot coupler
MLCL6	Line (Δl = 90.00 mm)	CMPC4	Isolated lines
TRLR	Reflect (short)	CMPBM	4x4 Butler matrix
CMPB	H-plane bend		

Table E.3 — Overview of all manufactured low-permittivity PWWG components with the designated code name and a brief description.

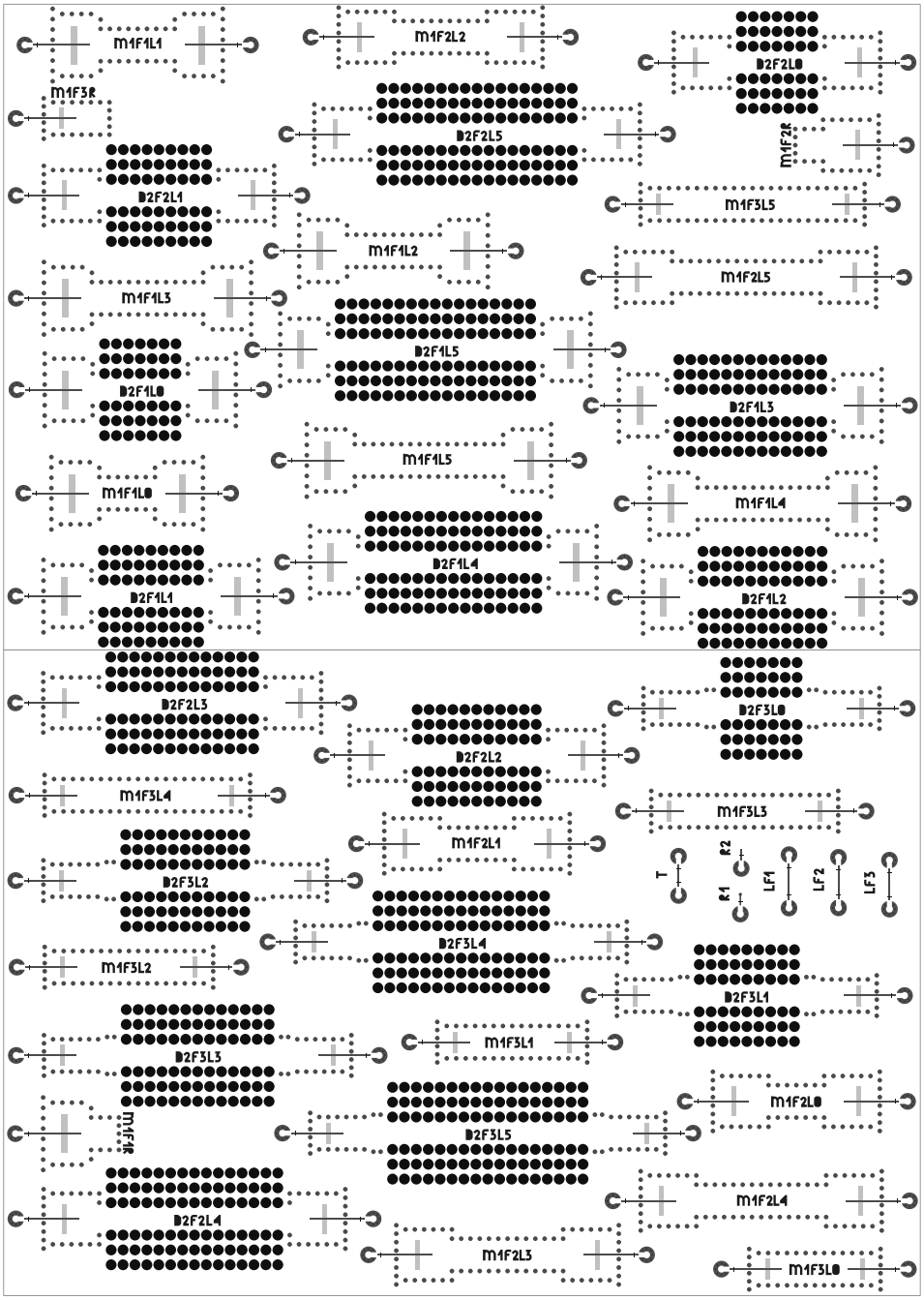

Figure E.3 — Top view of the layout design of the complete printed circuit board.

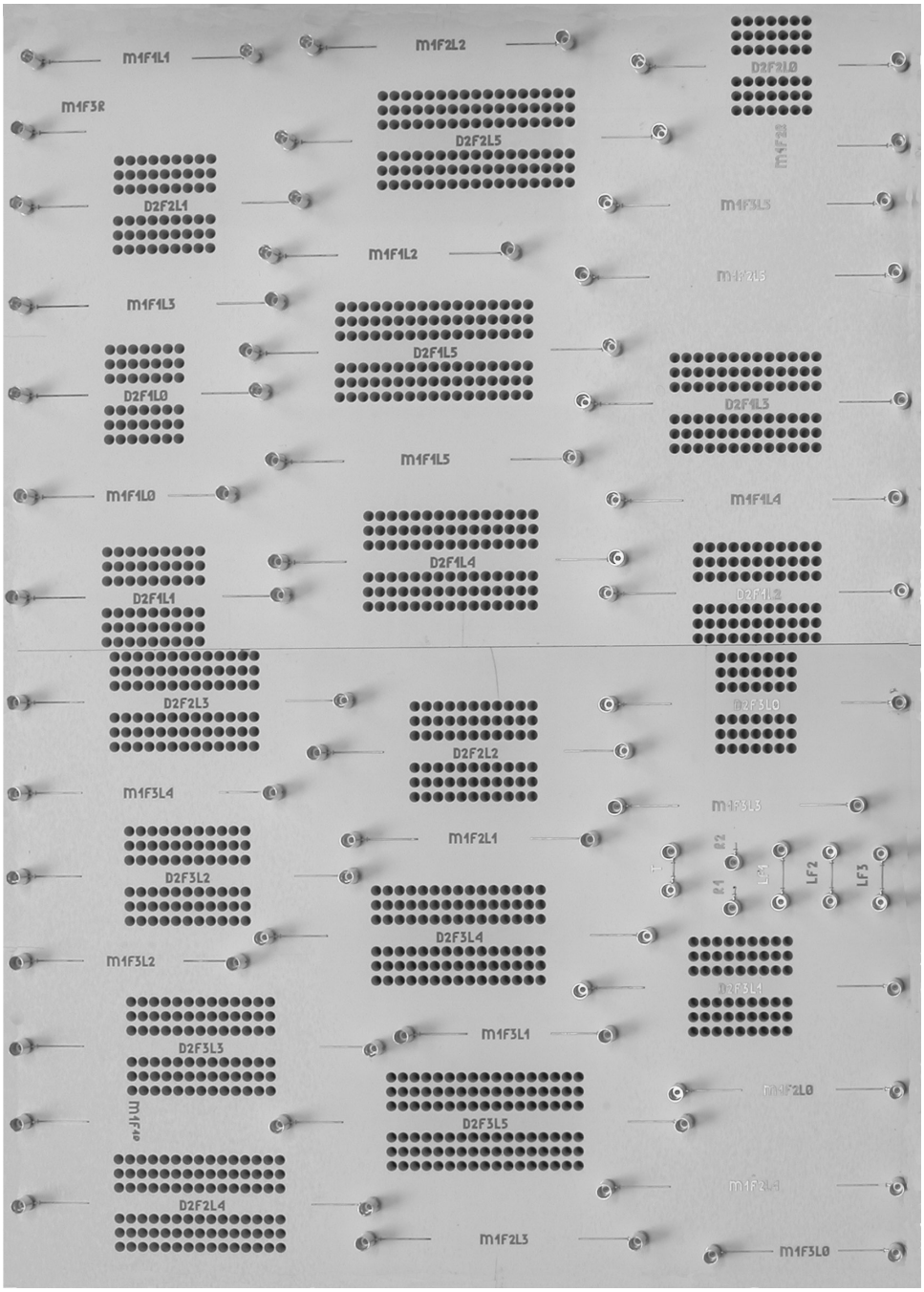

Figure E.4 — Top view of the manufactured and soldered printed circuit board.

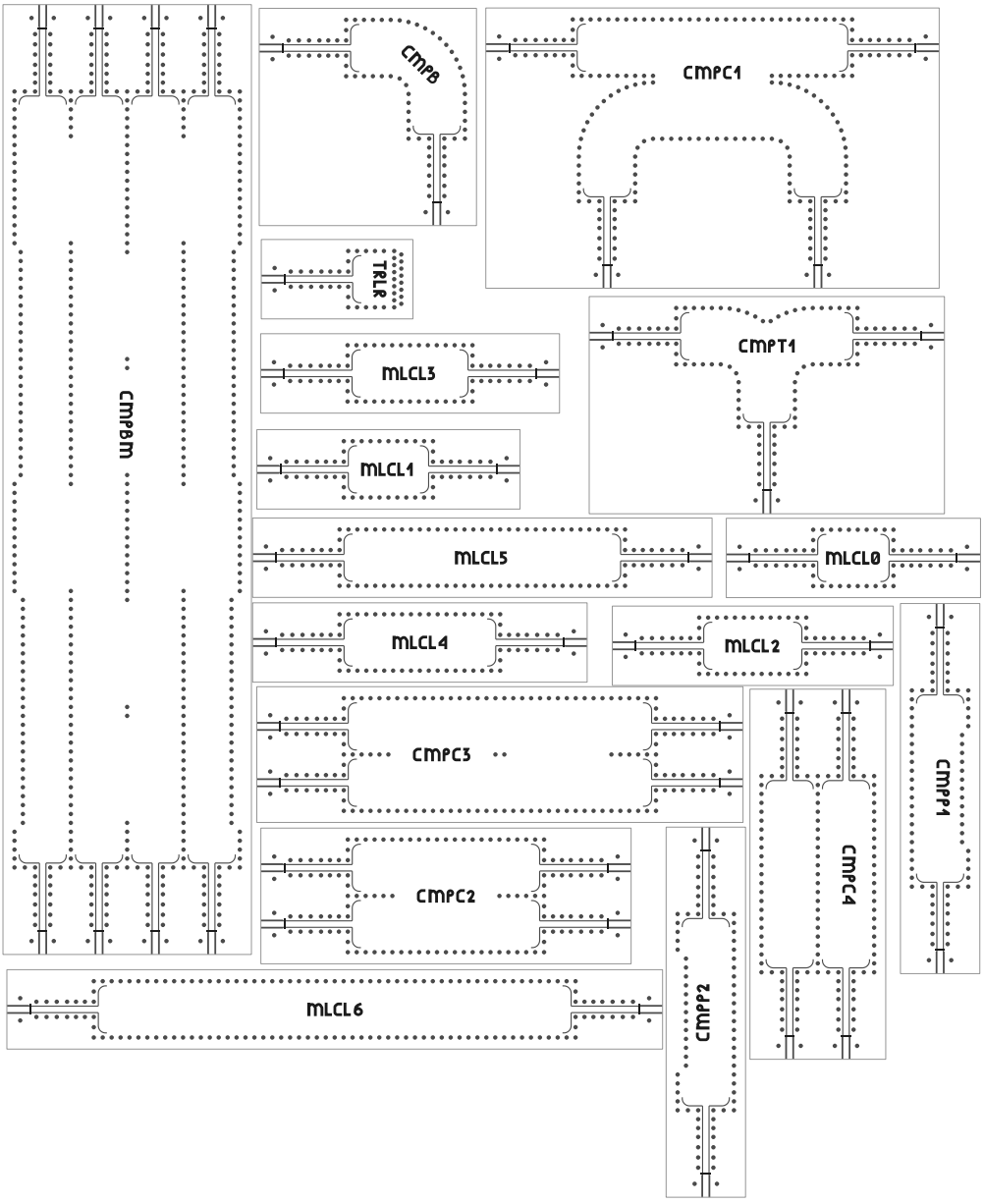

Figure E.5 — Top view of the layout design of the complete low-permittivity printed circuit board.

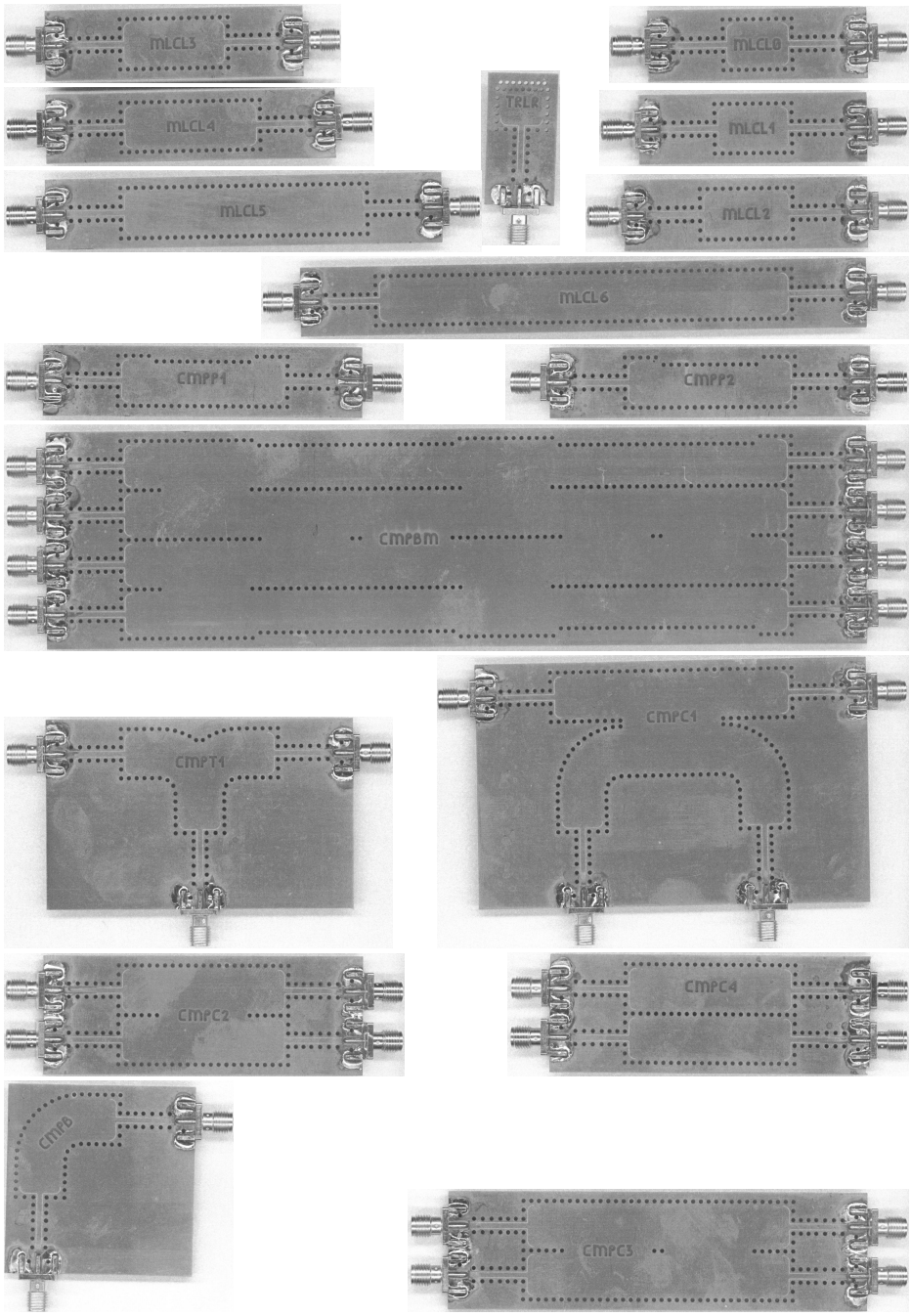

Figure E.6 — Top-view photographs of all manufactured low-permittivity PWWG components.

Bibliography

[1] A. Jentzsch and W. Heinrich, "Theory and measurements of flip-chip interconnects for frequencies up to 100 GHz," *IEEE Trans. Microwave Theory Techn.*, vol. 49, pp. 871–878, May 2001.

[2] P.-S. Kildal, A. A. Khisk, and S. Maci, eds., *Special issue on artificial magnetic conductors, soft/hard surfaces, and other complex surfaces*, vol. 53, IEEE Trans. Antennas Propagat., Jan. 2005.

[3] R. W. Ziolkowski and N. Engetha, eds., *Special issue on metamaterials*, vol. 51, IEEE Trans. Antennas Propagat., Oct. 2003.

[4] E. Yablonivitch, ed., *Mini-special issue on electromagnetic crystal structures, design, synthesis, and applications*, vol. 47, IEEE Trans. Microw. Theory Techn., Nov. 1999.

[5] N. Llombart, A. Neto, G. Gerini, and P. de Maagt, "Planar circularly symmetric EBG structures for reducing surface waves in printed antennas," *IEEE Trans. Antennas Propagat.*, vol. 53, Oct. 2005.

[6] K. S. Packard, "The origin of waveguides: A case of multiple rediscovery," *IEEE Trans. Microwave Theory Techn.*, vol. 32, pp. 961–969, Sep. 1984.

[7] R. M. Barrett, "Microwave printed circuits–the early years," *IEEE Trans. Microwave Theory Techn.*, vol. 32, pp. 983–990, Sep. 1984.

[8] D. J. Bekers, *Finite Antenna Systems: an Eigencurrent Approach*. PhD thesis, Technische Universiteit Eindhoven, The Netherlands, 2004. [Online: `http://alexandria.tue.nl/extra2/200411410.pdf`].

[9] M. Streetly, ed., *Jane's Radar and Electronic Warfare Systems*, p. 172. Jane's Information Group Limited, eighth ed., 1996.

[10] A. Lamminen, J. Saily, and A. R. Vimpari, "60-GHz patch antennas and arrays on LTCC with embedded-cavity substrates," *IEEE Trans. Antennas Propagat.*, vol. 56, pp. 2865–2874, Sep. 2008.

[11] B. Morsink, *Fast Modeling of Electromagnetic Fields for the Design of Phased Array Antennas in Radar Systems*. PhD thesis, Technische Universiteit Eindhoven, The Netherlands, 2005. [Online: `http://alexandria.tue.nl/extra2/200513119.pdf`].

[12] M. Streetly, ed., *Jane's Radar and Electronic Warfare Systems*, pp. 157–158. Jane's Information Group Limited, eight ed., 1996.

[13] D. Parker and D. C. Zimmermann, "Phased arrays - part I: theory and architectures," *IEEE Trans. Microwave Theory Techn.*, vol. 50, pp. 678–687, Mar. 2002.

[14] D. Parker and D. C. Zimmermann, "Phased arrays-part II: implementations, applications, and future trends," *IEEE Trans. Microwave Theory Techn.*, vol. 50, pp. 688–698, Mar. 2002.

[15] Ansoft Corporation, *High Frequency Structure Simulator User's Guide*, 2008. (HFSS version 11.1.3).

[16] F. Shigeki, "Waveguide line," Feb. 1994. Japanese Patent No. JP6053711.

[17] J. Hirokawa and M. Ando, "Single-layer feed waveguide consisting of posts for plane TEM wave excitation in parallel plates," *IEEE Trans. Antennas Propagat.*, vol. 46, pp. 625–630, May 1998.

[18] H. Uchimura, T. Takenoshita, and M. Fujii, "Development of a "Laminated Waveguide"," *IEEE Trans. Microwave Theory Techn.*, vol. 46, pp. 2438–2443, Dec. 1998.

[19] D. Deslandes and K. Wu, "Integrated transition of coplanar to rectangular waveguides," in *IEEE MTT-S Int. Microwave Symp. Dig.*, (Phoenix, AZ), pp. 619–620, May 2001.

[20] D. Deslandes and K. Wu, "Integrated microstrip and rectangular waveguide in planar form," *IEEE Microw. Guided Wave Lett.*, vol. 11, pp. 68–70, Feb. 2001.

[21] E. Yablonovitch, "Inhibited spontaneous emission in solid state physics and electronics," *Phys. Rev. Lett.*, vol. 58, pp. 2059–2062, 1987.

[22] H. Benisty, "Modal analysis of optical guides with two-dimensional photonic band-gap boundaries," *J. Appl. Phys.*, vol. 79, pp. 7483–7492, May 1996.

[23] I. El-Kady, M. M. Sigalas, R. Biswas, and K. M. Ho, "Dielectric waveguides in two-dimensional photonic bandgap materials," *J. Lightwave Technol.*, vol. 17, pp. 2042–2049, Nov. 1999.

[24] A. Adibi, Y. Xu, R. Lee, A. Yariv, and A. Scherer, "Properties of the slab modes in photonic crystal optical waveguides," *J. Lightwave Technol.*, vol. 18, pp. 1554–1564, Nov. 2000.

[25] M. Lončar, T. Doll, J. Vučković, and A. Scherer, "Design and fabrication of silicon photonic crystal optical waveguides," *J. Lightwave Technol.*, vol. 18, pp. 1402–1411, Oct 2000.

[26] D. Deslandes and K. Wu, "Substrate integrated slab waveguide (SISW) for wideband microwave applications," in *IEEE MTT-S Int. Microwave Symp. Dig.*, (Philadelphia, PA), pp. 1103–1106, Jun. 2003.

[27] K. Wu, D. Deslandes, and Y. Cassivi, "The substrate integrated circuits - a new concept for high-frequency electronics and optoelectronics," *Telecommunications in Modern Satellite, Cable and Broadcasting Service, 2003. TELSIKS 2003. 6th International Conference on*, vol. 1, pp. P–III–P–X, Oct. 2003.

[28] M. Bozzi, D. Deslandes, P. Arcioni, L. Perregrini, K. Wu, and G. Conciauro, "Analysis of substrate integrated slab waveguides (SISW) by the BI-RME method," in *IEEE MTT-S Int. Microwave Symp. Dig.*, (Philadelphia, PA), pp. 1975–1978, Jun. 2003.

[29] A. Patrovsky and K. Wu, "94-GHz planar dielectric rod antenna with substrate integrated image guide (SIIG) feeding," *IEEE Ant. Wireless Prop. Lett.*, vol. 5, pp. 435–437, 2006.

[30] T. J. Coenen, D. J. Bekers, A. Mazzinghi, and J. L. Tauritz, "Integrated metallic and dielectric post-wall waveguides for microwave and MM-wave feed networks," in *Proc. URSI Benelux Meeting*, (Eindhoven, The Netherlands), p. 8, May 2006.

[31] T. J. Coenen, A. Mazzinghi, D. J. Bekers, A. Neto, J. L. Tauritz, A. Freni, and G. Gerini, "Design and analysis of EBG based integrated waveguide structures for microwave and MM-wave feed networks," in *Proc. IEEE AP-S Int. Symp. Dig.*, (Albuquerque, NM), p. 654, Jul. 2006.

[32] T. J. Coenen, D. J. Bekers, J. L. Tauritz, and F. E. van Vliet, "Design of post-wall waveguides with metal and dielectric posts," in *Proc. 37th Eur. Microw. Conf.*, (Munich, Germany), pp. 20–23, Oct. 2007.

[33] T. J. Coenen, D. J. Bekers, J. L. Tauritz, and F. E. van Vliet, "An analysis technique for post-wall waveguides," in *Proc. 38th Eur. Microw. Conf.*, (Amsterdam, The Netherlands), pp. 1006–1009, Oct. 2008.

[34] T. J. Coenen, D. J. Bekers, F. E. van Vliet, and J. L. Tauritz, "Analysis and design of metallic and dielectric post-wall waveguides for antenna feeds," in *Proc. URSI Benelux Meeting*, (Brussels, Belgium), p. 42, May 2008.

[35] T. J. Coenen, D. J. Bekers, J. L. Tauritz, and F. E. van Vliet, "Design and measurement of metallic post-wall waveguide components," in *IEEE MTT-S Int. Microwave Symp. Dig.*, (Boston, MA), pp. 261–264, Jun. 2009.

[36] N. Marcuvitz, *Waveguide Handbook*. McGraw-Hill, 1951.

[37] J. R. Bray and L. Roy, "Resonant frequencies of post-wall waveguide cavities," *IEE Proc.-Microw. Antennas Propag.*, vol. 150, pp. 365–368, Oct. 2003.

[38] R. Levy, "Derivation of equivalent circuits of microwave structures using numerical techniques," *IEEE Trans. Microw. Theory Techn.*, vol. 47, pp. 1688–1695, Sept. 1999.

[39] G. O. Olaofe, "Scattering cross section for two cylinders," *IEEE Trans. Antennas Propagat.*, vol. 18, pp. 823–825, Nov. 1970.

[40] A. Z. Elsherbeni and M. Hamid, "Scattering by parallel conducting circular cylinders," *IEEE Trans. Antennas Propagat.*, vol. 35, pp. 355–358, March 1987.

[41] A. Z. Elsherbeni and A. A. Kishk, "Modeling of cylindrical objects by circular dielectric and conducting cylinders," *IEEE Trans. Antennas Propagat.*, vol. 40, pp. 96–99, Jan. 1992.

[42] N. Llombart, *Development of integrated printed array antennas using EBG substrates*. PhD thesis, Universidad Politécnica de Valencia, Spain, 2006.

[43] S. Monni, *Frequency Selective Surfaces Integrated with Phased Array Antennas*. PhD thesis, Technische Universiteit Eindhoven, The Netherlands, 2005. [Online: http://alexandria.tue.nl/extra2/200511922.pdf].

[44] S. Monni, G. Gerini, A. Neto, and A. Tijhuis, "Multimode equivalent networks for the design and analysis of frequency selective surfaces," *IEEE Trans. Antennas Propagat.*, vol. 55, pp. 2824–2835, Oct. 2007.

[45] S. Bruni, *Wide band leaky wave radiation for integrated antennas and arrays*. PhD thesis, Università degli Studi di Siena, Italy, 2005.

[46] D. J. Bekers, S. J. L. van Eijndhoven, and A. G. Tijhuis, "An eigencurrent description of finite arrays of electromagnetically characterized elements," *Radio Science*, vol. 44, no. RS2S90, doi:10.1029/2007RS003797, 2009.

[47] G. Conciauro, M. Guglielmi, and R. Sorrentino, *Advanced Modal Analysis*. Wiley, 1st ed. ed., 2000.

[48] M. Bozzi, L. Perregrini, K. Wu, and G. Conciauro, "Multi-mode equivalent circuit models for substrate-integrated waveguide discontinuities," *XVI Riunione Nazionale di Elettromagnetismo (XVI RiNEm), Genova*, 18-21 Sep. 2006.

[49] A. M. van de Water, B. P. de Hon, M. C. van Beurden, A. G. Tijhuis, and P. J. I. de Maagt, "Linear embedding via Green's operators: A modeling technique for finite electromagnetic band-gap structures," *Physical Review E: Statistical, Nonlinear, and Soft Matter Physics*, vol. 72, no. 5, pp. 056704–1/11, 2005.

[50] A. M. van de Water, *LEGO – Linear embedding via Green's operators*. PhD thesis, Technische Universiteit Eindhoven, The Netherlands, 2007. [Online: http://alexandria.tue.nl/extra2/200711874.pdf].

[51] J. Hirokawa and M. Ando, "Complex propagation constant of post-wall waveguide and beam-switching slot array antennas for modern communications," in *Proc. EMTS 2007 - Int. URSI Comm. B*, (Ottawa, Canada), p. EMTS174, Jul. 2007.

[52] F. Xu, Y. Zhang, W. Hung, K. Wu, and T. J. Cui, "Finite-difference frequency-domain algorithm for modelling guided-wave properties of substrate integrated waveguide," *IEEE Trans. Microwave Theory Techn.*, vol. 51, pp. 2221–2227, Nov. 2003.

[53] Y. Cassivi, L. Perregrini, P. Arcioni, M. Bressan, K. Wu, and G. Conciauro, "Dispersion characteristics of substrate integrated rectangular waveguide," *IEEE Microw. Wireless Comp. Lett.*, vol. 12, pp. 333–335, Sep. 2002.

[54] D. Pissoort and F. Olyslager, "Study of eigenmodes in periodic waveguides using the Lorentz reciprocity theorem," *IEEE Trans. Microwave Theory Techn.*, vol. 52, pp. 542–553, Feb. 2004.

[55] D. Deslandes and K. Wu, "Accurate modelling, wave mechanisms, and design considerations of a substrate integrated waveguide," *IEEE Trans. Microwave Theory Techn.*, vol. 54, pp. 2516–2526, June 2006.

[56] A. Mazzinghi, "Analisi e caratterizzazione di guide basate su strutture EBG," Master's thesis, Università degli Studi di Firenze, Apr 2006. (in English).

[57] N. Ranjkesh, M. Shahabadi, and D. Busuioc, "Effect of dielectric losses on the propagation characteristics of the substrate integrated waveguide," *APMC Asia-Pacific Microw. Conf. Proc.*, vol. 3, pp. 4–7, Dec. 2005.

[58] A. Patrovsky and K. Wu, "Substrate integrated image guide (SIIG)—a low-loss waveguide for millimetre-wave applications," in *Proc. 35th Eur. Microw. Conf.*, (Paris, France), pp. 897–900, Oct. 2005.

[59] Y. Cassivi and K. Wu, "Substrate integrated circuits concept applied to the nonradiative dielectric guide," *IEE Proceedings - Microw., Ant. and Propagat.*, pp. 424–433, Dec. 2005.

[60] A. T. de Hoop, *Handbook of Radiation and Scattering of Waves*. Academic Press Limited, electronic reproduction ed., 2008. [Online: `http://www.atdehoop.com/`].

[61] G. N. Watson, *A Treatise on the Theory of Bessel Functions*. Cambridge University Press, second ed., 1966.

[62] C. Lanczos, *Linear Differential Operators*. D. Van Nostrand Company, 1961.

[63] V. H. Rumsey, "Reaction concept in electromagnetic theory," *Phys. Rev.*, vol. 94, pp. 1483–1491, 1954.

[64] A. J. Poggio and E. K. Miller, *Integral Equation Solutions of Three-Dimensional Scattering Problems*. Springer-Verlag, 1987.

[65] W. H. Press, S. A. Teukolsky, W. T. Vetterling, and B. P. Flannery, *Numerical Recipes in C*. Cambridge University Press, second ed., 1995.

[66] T. Weise, *Global Optimization Algorithms - Theory and Application*. Self-Published, second ed., Jan. 14, 2009. [Online: `http://www.it-weise.de/`].

[67] M. Anis, A. Jöstingmeier, and A. Omar, "Introduction of an effective waveguide width in transmission/reflection methods for dielectric measurements," in *Proc. IEEE AP-S Int. Symp. Dig.*, (Honolulu, HI), pp. 281–284, Jun. 2007.

[68] C. H. Tseng and T. H. Chu, "Measurement of frequency-dependent equivalent width of substrate integrated waveguide," *IEEE Trans. Microwave Theory Techn.*, vol. 54, pp. 1431–1437, Apr. 2006.

[69] F. Xu and K. Wu, "Guided-wave and leakage characteristics of substrate integrated waveguide," *IEEE Trans. Microwave Theory Techn.*, vol. 53, pp. 66–73, Jan. 2005.

[70] R. E. Collin, *Field Theory of Guided Waves*. IEEE Press, second ed., 1991.

[71] R. S. Elliott, *Antenna Theory and Design*. Prentice-Hall, Inc., 1981.

[72] Thales Nederland B.V., *Bare boards & Substrates Product Brochure*, 2003. [Online: `http://www.thales-nederland.nl/nl/bbs/`].

[73] J. C. Vardaxoglou, *Frequency Selective Surfaces, Analysis and Design*. Wiley, 1997.

[74] R. B. Marks, "A multiline method of network analyzer calibration," *IEEE Trans. Microwave Theory Techn.*, vol. 39, pp. 1205–1215, Jul. 1991.

[75] R. B. Marks, "Formulations of the basic vector network analyzer error model including switch-terms," in *50th ARFTG Conf. Dig.*, vol. 32, pp. 115–126, Dec. 1997.

[76] G. V. Eleftheriades, A. S. Omar, L. P. B. Katehi, and G. M. Rebeiz, "Some important properties of waveguide junction generalized scattering matrices in the context of the mode matching technique," *IEEE Trans. Microwave Theory Techn.*, vol. 42, pp. 1896–1903, Oct 1994.

[77] C. Seguinot, P. Kennis, J.-F. Legier, F. Huret, E. Paleczny, and L. Hayden, "Multimode TRL. a new concept in microwave measurements: theory and experimental verification," *IEEE Trans. Microwave Theory Techn.*, vol. 46, pp. 536–542, May 1998.

[78] D. M. Pozar, *Microwave Engineering*. John Wiley & Sons, Inc., second ed., 1998.

[79] P. A. Rizzi, *Microwave Engineering*. Prentice-Hall, 1998.

[80] J. S. Izadian and S. M. Izadian, *Microwave Transition Design*. Artech House, Inc., 1988.

[81] V. S. Möttönen and A. V. Räisänen, "Novel wide-band coplanar waveguide-to-rectangular waveguide transition," *IEEE Trans. Microwave Theory Techn.*, vol. 52, pp. 1836–1842, Aug. 2004.

[82] G. E. Ponchak and R. N. Simons, "A new rectangular waveguide to coplanar waveguide transition," in *IEEE MTT-S Int. Microwave Symp. Dig.*, vol. 1, (Dallas, TX), pp. 491–492, May 1990.

[83] J. S. Rao, K. K. Joshi, and B. N. Das, "Analysis of small aperture coupling between rectangular waveguide and microstrip line," *IEEE Trans. Microwave Theory Techn.*, vol. 29, pp. 150–154, Feb. 1981.

[84] E. S. Li, J.-C. Cheng, and C. C. Lai, "Designs for broad-band microstrip vertical transitions using cavity couplers," *IEEE Trans. Microwave Theory Techn.*, vol. 54, pp. 464–472, Jan. 2006.

[85] M. Davidovitz, R. A. Sainati, and S. J. Fraasch, "A non-contact interconnection through an electrically thick ground plate common to two microstrip lines," *IEEE Trans. Microwave Theory Techn.*, vol. 43, pp. 753–759, Apr. 1995.

[86] C.-K. C. Tzuang, K.-C. Chen, C.-J. Lee, C.-C. Ho, and H.-S. Wu, "H-plane mode conversion and application in printed microwave integrated circuit," in *Proc. 30th Eur. Microw. Conf.*, (Paris, France), pp. 1–4, Oct. 2000.

[87] A. Bacha and K. Wu, "Toward an optimum design of NRD-guide and microstrip-line transition for hybrid-integration technology," *IEEE Trans. Microwave Theory Techn.*, vol. 46, pp. 1796–1800, Nov. 1998.

[88] Y. Cassivi, D. Deslandes, and K. Wu, "Engraved NRD-guide for milimetre-wave integrated circuits," in *IEEE MTT-S Int. Microwave Symp. Dig.*, vol. 2, (Boston, MA), pp. 605–608, May 2001.

[89] A. Patrovsky and K. Wu, "Substrate integrated image guide (SIIG)—a planar dielectric waveguide technology for millimeter-wave applications," *IEEE Trans. Microwave Theory Techn.*, vol. 54, pp. 2872–2879, Jun. 2006.

[90] E. Moldovan, R. G. Bosisio, and K. Wu, "*W*-band multiport substrate-integrated waveguide circuits," *IEEE Trans. Microwave Theory Techn.*, vol. 54, pp. 625–632, Feb. 2006.

[91] W. D'Orazio and K. Wu, "Substrate-integrated-waveguide circulators suitable for millimeter-wave integration," *IEEE Trans. Microwave Theory Techn.*, vol. 54, pp. 3675–3680, Oct. 2006.

[92] T. Kai, J. Hirokawa, and M. Ando, "A stepped post-wall waveguide with aperture interface to standard waveguide," in *Proc. IEEE AP-S Int. Symp. Dig.*, vol. 2, (Monterey, CA), pp. 1527–1530, Jun. 2004.

[93] T. Kai, J. Hirokawa, and M. Ando, "Feed through an aperture to a post-wall waveguide with step structure," *IEICE Trans. Communications*, vol. E88-B, pp. 1298–1302, Mar. 2005.

[94] D. Deslandes and K. Wu, "Design consideration and performance analysis of substrate integrated waveguide components," in *Proc. 32th Eur. Microw. Conf.*, vol. 2, (Milan, Italy), pp. 881–884, Sep. 2002.

[95] D. Deslandes and K. Wu, "Single-substrate integration technique of planar circuits and waveguide filters," *IEEE Trans. Microwave Theory Techn.*, vol. 51, pp. 593–596, Feb. 2003.

[96] F. Mira, A. A. S. Blasy, V. E. Boriaz, and B. Gimenox, "Fast and accurate analysis and design of substrate integrated waveguide (SIW) filters," in *Proc. 37th Eur. Microw. Conf.*, (Munich, Germany), pp. 170–173, Oct. 2007.

[97] Y. Cheng, W. Hong, and K. Wu, "Novel substrate integrated waveguide fixed phase shifter for 180-degree directional coupler," in *IEEE MTT-S Int. Microwave Symp. Dig.*, (Honolulu, HI), pp. 189–192, Jun 2007.

[98] D. Busuioc, M. Shahabadi, A. Borji, G. Shaker, and S. Safavi-Naeini, "Substrate integrated waveguide antenna feed – design methodology and validation," in *Proc. IEEE AP-S Int. Symp. Dig.*, (Honolulu, HI), pp. 2666–2669, Jun. 2007.

[99] X.-P. Chen and K. Wu, "Substrate integrated waveguide cross-coupled filter with negative coupling structure," *IEEE Trans. Microwave Theory Techn.*, vol. 56, pp. 142–149, Jan. 2008.

[100] J. H. Lee, S. Pinel, J. Papapolymerou, J. Laskar, and M. M. Tentzeris, "Low-loss LTCC cavity filters using system-on-package technology at 60 GHz," *IEEE Trans. Microwave Theory Techn.*, vol. 53, pp. 3817–3824, Dec. 2005.

[101] A. Patrovsky, M. Daigle, and K. Wu, "Millimeter-wave wideband transition from CPW to substrate integrated waveguide on electrically thick high-permittivity substrates," in *Proc. 37th Eur. Microw. Conf.*, (Munich, Germany), pp. 138–141, Oct. 2007.

[102] A. Patrovsky and K. Wu, "Substrate integrated image guide array antenna for the upper millimeter-wave spectrum," *IEEE Trans. Antennas Propagat.*, vol. 55, pp. 2994–3001, Nov. 2007.

[103] D. Deslandes and K. Wu, "Analysis and design of current probe transition from grounded coplanar to substrate integrated rectangular waveguides," *IEEE Trans. Microwave Theory Techn.*, vol. 53, pp. 2487–2494, August 2005.

[104] S. Lee, S. Jung, and H.-Y. Lee, "Ultra-wideband cpw-to-substrate integrated waveguide transition using an elevated-cpw section," *IEEE Microw. Wireless Comp. Lett.*, vol. 18, pp. 746–748, Nov. 2008.

[105] J. J. Simpson, A. Taflove, J. A. Mix, and H. Heck, "Computational and experimental study of a microwave electromagnetic bandgap structure with waveguiding defect for potential use as a bandpass wireless interconnect," *IEEE Microw. Wireless Comp. Lett.*, vol. 14, pp. 343–345, Jul. 2004.

[106] J. J. Simpson, A. Taflove, J. A. Mix, and H. Heck, "Substrate integrated waveguides optimized for ultrahigh-speed digital interconnects," *IEEE Trans. Microwave Theory Techn.*, vol. 54, pp. 1983–1990, May 2006.

[107] K. Song, Y. Fan, and Y. Zhang, "Eight-way substrate integrated waveguide," *IEEE Trans. Microwave Theory Techn.*, vol. 56, pp. 1473–1477, Jun. 2008.

[108] K. Song, Y. Fan, and X. Zhou, "X-band broadband substrate integrated rectangular waveguide power divider," *Electronic Letters*, vol. 44, pp. 211–213, Jan. 2008.

[109] K. Song, Y. Fan, and Y. Zhang, "Design of low-profile millimeter-wave substrate integrated waveguide power divider/combiner," *Int. J. Infrared Milli. Waves*, vol. 28, pp. 473–478, Jun. 2007.

[110] M. Wong, B. MacIntosh-Hobson, and A. R. Sebak, "A coaxial to waveguide transition feeding method for substrate integrated waveguides," in *Proc. EMTS 2007 - Int. URSI Comm. B*, (Ottawa, Canada), p. EMTS174, Jul. 2007.

[111] D. M. Pozar, "A review of aperture coupled microstrip antenna: History, operation, development, and applications," review article, University of Massachusetts at Amherst, May 1996. [Online: `http://www.ecs.umass.edu/ece/pozar/aperture.pdf`].

[112] G. Rosati, "Design of an EBG-based feed for a cylindrical reflector antenna using PCB technology," Master's thesis, Università degli Studi di Firenze, 2006.

[113] D. Pissoort, E. Michielssen, and A. Grbic, "An electromagnetic crystal Green function multiple scattering technique for arbitrary polarizations, lattices, and defects," *J. Lightwave Technol.*, vol. 25, pp. 571–583, Feb. 2007.

[114] D. Pissoort, E. Michielssen, D. Vande Ginste, and F. Olyslager, "Fast-multipole analysis of electromagnetic scattering by photonic crystal slabs," *J. Lightwave Technol.*, vol. 25, pp. 2847–2863, Sep. 2007.

[115] S. Germain, D. Deslandes, and K. Wu, "Development of substrate integrated waveguide power dividers," in *IEEE CCECE 2003, Can. Conf. on Electr. and Comp. Eng.*, vol. 3, pp. 1921–1924, May 2003.

[116] S. Park, Y. Okajima, J. Hirokawa, and M. Ando, "A slotted post-wall waveguide array with interdigital structure for 45° linear and dual polarization," *IEEE Trans. Antennas Propagat.*, vol. 53, pp. 2865–2871, Sep. 2005.

[117] L. Han, K. Wu, and S. Winkler, "Singly balanced mixer using substrate integrated waveguide magic-T structure," in *EuWiT 2008, Proc. 38th Eur. Microw. Conf.*, (Amsterdam, The Netherlands), Oct. 2008.

[118] D. Pissoort, D. Vande Ginste, and F. Olyslager, "Including PML-based absorbing boundary conditions in the MLFMA," *IEEE Ant. Wireless Prop. Lett.*, vol. 4, no. 1, pp. 312–315, 2005.

[119] M. Bozzi, L. Perregrini, and K. Wu, "Modeling of conductor, dielectric, and radiation losses in substrate integrated waveguide by the boundary integral-resonant mode expansion method," *IEEE Trans. Microwave Theory Techn.*, vol. 56, pp. 3153–3161, Dec. 2008.

[120] J. Mojica, Y. Cassivi, and K. Wu, "Low-cost RF and microwave source design using substrate integrated waveguide technique," in *Proc. IEEE Radio and Wireless Conf.*, pp. 447–450, Sep. 2004.

[121] J. Xu and K. Wu, "A subharmonic self-oscillating mixer using substrate integrated waveguide cavity for millimeter-wave application," in *IEEE MTT-S Int. Microwave Symp. Dig.*, (Long Beach, CA), pp. 2019–2022, Jun 2005.

[122] S. A. Maas, *Nonlinear Microwave Circuits*. Artech House, 1988.

[123] H. J. Riblet, "The short-slot hybrid junction," *Proc. IRE*, vol. 40, pp. 180–184, Feb. 1952.

[124] P. Colestock and M. Foley, "A generalized TRL algorithm for S-parameter deembedding," Technical Memo TM-1781, Fermi National Accelerator Laboratory, Apr. 1993.

[125] I. S. Gradshteyn and I. M. Ryzhik, *Table of Integrals, Series and Products*. Academic Press, fifth ed., 1994.

Summary

The number of wireless devices that plays a role in our daily live has considerably increased in the last years. These devices are used in communication, navigation and sensor systems and often contain microwave components. A recently introduced type of microwave transmission line, the post-wall waveguide (PWWG), combines integrability with printed circuit board technology with a small, compared to planar transmission lines, increase in loss at millimeter-wave bands. The side walls of a PWWG do not consist of flat surfaces, as in a rectangular waveguide, but of a set of cylindrical posts. The aims of this thesis are to provide a systematic inventory of the key PWWG characteristics, to develop a model to link subsystem specifications directly to PWWG characteristics and design, and to work out the issues related to implementation and manufacturing.

The first part of this thesis discusses the modeling of PWWG structures. To characterize PWWGs electromagnetically we use a model based on a 2D formulation of Maxwell's equations. A modal expansion of the fields around the cylindrical posts in the PWWG results in a matrix equation from which the scattered field as a result of the applied field can be determined. As an alternative, we formulate a solution in integral form. Using Lorentz's reciprocity theorem, we derive integral equations that relate the electromagnetic fields to the surface currents. These currents can then be computed by means of the method of moments. We only calculate the moment matrix for the case of perfectly conducting posts.

The propagation constant, the effective width, the losses and the scattering parameters are the key PWWG characteristics. The propagation constant can be determined by considering an infinitely-long PWWG, i.e. an infinite row of identical unit cells positioned along a line. The matrix in the corresponding modal or moment equation is described by a slowly converging series; the use of convergence acceleration strongly reduces the number of required summation terms. The propagation constant is determined by an iterative procedure that minimizes the determinant of the matrix. Since the series does not converge for a propagation constant with an imaginary part, this method can only be used to estimate the real part of the propagation constant. This estimation gives immediate insight in the effective width of the PWWG. This is the width of a rectangular waveguide which has a dispersion curve that is identical to that of the PWWG. The effective widths that we have determined show, in comparison with the literature, the smallest deviation compared to the values that have been determined with a commercial simulator. The losses of a PWWG are composed of dielectric loss, conductor loss and radiation loss. We propose several approximative expressions to determine these losses. However, due to convergence problems the accurate calculation of the losses (the imaginary part of the propagation constant) requires an alternative model, through which the scattering parameters of a PWWG can also be determined. By combining the modal formulation and the integral formulation we can adequately describe the electromagnetic behavior of a PWWG component by electric and magnetic surface currents at port planes. The transfer from port to port can be calculated using this characterization and from this the scattering parameters of a PWWG com-

ponent can be determined. Finally the propagation constant, the effective width and the losses can be determined from the scattering parameters of a straight PWWG.

The second part of this thesis is concerned with the design, realization and measurement of PWWG structures. We first consider three sets of uniform, straight PWWG transmission lines. Two sets have been manufactured on a substrate with high permittivity (one based on metallic posts and the other based on dielectric posts) and a third set has been manufactured on a substrate with low permittivity. All dimensions have been chosen such that the samples operate optimally around 10 GHz. These three sets consist of transmission lines of different length, such that the propagation constant can be determined from the (measured) scattering parameters using multiline calibration. The measurement results for the two sets with the high permittivity are inaccurate, in particular the results for the attenuation. This is caused by a poor match of the samples to the coaxial cables of the measurement equipment and by the narrow bandwidth of the excitation structures. The accuracy of the measurements of the third set of samples is much higher since the matching and the excitation structure have been considerably improved. The design of an excitations structure which couples power to the PWWG, can limit the usable bandwidth of the PWWG. In the case of the high-permittivity substrate a microstrip line is coupled to the PWWG through a slot in the combined ground plane. This excitation structure is usable over only one third of the bandwidth of the main mode of the PWWG. Moreover, the manufacturing is complicated since two PCBs need to be glued together. This has been taking into account during the design of the excitation structure for the low-permittivity substrate. Therefore, a slot-coupled grounded co-planar waveguide positioned in the top ground plane of the PWWG has been selected. The excitation structure and the PWWG are located in one single PCB and the main mode of the PWWG is excited over almost it's full bandwidth. Similar to rectangular waveguides, straight parts of PWWG can be the basis for the design of bends and splitters. By combining such components and by selectively adding and removing posts, complex components such as Butler matrices or filters can be realized. To compare simulation results for PWWG components with measurement results a set of test components has been manufactured. This set includes phase shifters, a bend, a T-splitter, different types of couplers and a 4x4 Butler matrix.

Samenvatting

Het aantal draadloze apparaten dat een rol speelt in ons dagelijks leven is de afgelopen jaren sterk gestegen. Deze apparaten vinden hun toepassing in o.a. communicatie-, navigatie-, en sensorsystemen en bevatten veelal microgolfcomponenten. Een vrij recent geïntroduceerd type microgolftransmissielijn, de paalwandgolfpijp (post-wall waveguide, PWWG), combineert een goede integreerbaarheid met printplaattechnologie met een, in vergelijking met planaire transmissielijnen, geringere toename van de verliezen op de millimetergolfbanden. De zijwanden van een PWWG bestaan niet uit een vlakke wand, zoals in een rechthoekige golfpijp, maar uit een verzameling cilindervormige palen. Het doel van dit proefschrift is het geven van een systematische inventarisatie van de voornaamste PWWG-karakteristieken, het ontwikkelen van een model waarmee subsysteemspecificaties direct aan PWWG-karakteristieken kunnen worden gerelateerd en het in kaart brengen van knelpunten bij de implementatie en fabricage.

Het eerste deel van dit proefschrift behandelt de modellering van PWWG-structuren. Voor de elektromagnetische karakterisering van PWWG gebruiken we een model op basis van een 2D-formulering van Maxwells vergelijkingen. Een modale expansie van de velden rondom de cilindrische palen van de golfpijp levert een matrixvergelijking op waarmee het verstrooide veld als gevolg van een aangelegd veld kan worden berekend. Als alternatief hiervoor, formuleren we een oplossing in integraalvorm. Met behulp van Lorentz' reciprociteittheorema leiden we integraalvergelijkingen af die de elektromagnetische velden relateren aan de oppervlaktestromen. Deze stromen kunnen vervolgens worden berekend door middel van de momentenmethode. Alleen voor perfect geleidende palen werken we de componenten van de momentenmatrix uit.

De propagatieconstante, de effectieve breedte, de verliezen en de verstrooiingsparameters zijn de belangrijkste PWWG-karakteristieken. De propagatieconstante kan worden bepaald door een oneindig lange PWWG te beschouwen, d.w.z. een oneindige rij van op één lijn geplaatste identieke eenheidscellen. De matrix in de bijbehorende modale vergelijking of momentenvergelijking wordt beschreven door een langzaam convergerende reeks; het toepassen van convergentieacceleratie reduceert het aantal benodigde sommatietermen sterk. De propagatieconstante wordt berekend met een iteratieve procedure waarbij de determinant van de matrix wordt geminimaliseerd. Aangezien de reeks niet convergeert voor propagatieconstantes met een imaginair deel kan deze rekenmethode alleen gebruikt worden om het reële deel te schatten. Met deze schatting kan snel inzicht worden verkregen in de effectieve breedte van de PWWG. Dat is de breedte van een equivalente rechthoekige golfpijp waarvan de dispersiecurve identitiek is aan die van de PWWG. De door ons bepaalde effectieve breedtes vertonen, in vergelijking met resultaten uit de literatuur, de kleinste afwijking met door een commerciële simulator berekende waarden. De verliezen van een PWWG zijn samengesteld uit de diëlektische verliezen, de geleidingsverliezen en de stralingsverliezen. Voor het bepalen van deze verliezen worden enkele benaderingsuitdrukkingen voorgesteld. Echter, vanwege het beschreven divergentieprobleem is voor een nauwkeurige berekening van de verliezen (het imaginaire deel van de propagatieconstante) een alternatief model vereist, waarmee tevens de verstrooiingsparameters van een

PWWG kunnen worden bepaald. Door de modale formulering en de integraalformulering te combineren kunnen we het elektromagnetisch gedrag van een PWWG-component afdoende beschrijven met elektrische en magnetische oppervlaktestromen op poortvlakken. De overdracht van poort op poort kan met deze beschrijving worden berekend en uit de overdracht kunnen de verstrooiingsparameters van een PWWG-component worden bepaald. Tenslotte kunnen de propagatieconstante, de effectieve breedte en de verliezen worden bepaald uit de verstrooiingsparameters van een rechte PWWG.

Het tweede deel van dit proefschrift behandelt het ontwerp, de realisatie en de meting van PWWG-structuren. We beschouwen allereerst drie sets van uniforme, rechte PWWG-transmissielijnen. Twee sets zijn vervaardigd in een substraat met een hoge permittiviteit (één gebaseerd op metalen palen en de ander gebaseerd op diëlektrische palen) en een derde set is vervaardigd in een substraat met een lage permittiviteit. Alle afmetingen zijn gekozen zodat de structuren rond 10 GHz optimaal functioneren. De drie sets bestaan uit transmissielijnen van verschillende lengte, zodat de propagatieconstante kan worden bepaald uit de (gemeten) verstrooiingsparameters door middel van een multilijncalibratie. De meetresultaten voor de twee sets met de hoge permittiviteit zijn onnauwkeurig, met name de resultaten voor de verzwakking. Dit wordt onder andere veroorzaakt door een slechte aanpassing van de structuren op de coaxiale kabels van de meetapparatuur en door de smalbandige ontwerpen van de excitatiestructuren. De nauwkeurigheid van de metingen van de derde set transmissielijnen is groter omdat de aanpassing en de excitatiestructuur sterk verbeterd zijn. Het ontwerp van de excitatiestructuur waarmee vermogen in en uit de PWWG wordt gekoppeld kan de bruikbare bandbreedte van de PWWG beperken. Voor het substraat met hoge permittiviteit is er gekozen voor een microstriplijn die de PWWG exciteert via een spleet in een gemeenschappelijk grondvlak van PWWG en microstriplijn. Deze excitatiestructuur is slechts bruikbaar over één derde van de bandbreedte van de hoofdmodus in de PWWG. Bovendien is de fabricage gecompliceerd, omdat twee printplaten verlijmd moeten worden. Bij het ontwerp van de excitatiestructuur voor het substraat met lage permittiviteit is met deze bevindingen rekening gehouden. Derhalve is gekozen voor een via een spleet gekoppelde en geaarde coplanaire golfgeleider die geplaatst is in de bovenste grondplaat van de PWWG. De excitatiestructuur en de PWWG bevinden zich in één enkele printplaat en de hoofdmodus wordt over (nagenoeg) zijn volle bandbreedte geëxciteerd. Net als bij rechthoekige golfpijp kunnen rechte stukken PWWG als uitgangspunt dienen voor het ontwerp van bochten en splitsingen. Door zulke componenten te combineren en door selectief palen toe te voegen en te verwijderen kunnen complexe schakelingen zoals Butlermatrices of filters worden gerealiseerd. Om simulatieresultaten van PWWG-componenten te vergelijken met meetresultaten is er een set van testcomponenten vervaardigd. Deze set bevat fasedraaiers, een bocht, een T-splitsing, verschillende hybride koppelaars en een 4x4 Butlermatrix.

Acknowledgements

Many people contributed, directly or indirectly, to the successful conclusion of my PhD project. I am very grateful for all their contributions and I would like to thank some of them in particular.

First of all I would like to thank my assistant promotor: Dave's contribution to this project was enormous. Thank you for the very nice cooperation and for speaking the same 'language'. I really appreciated the cooperation. I know you did enjoy working on this PhD project and I hope you enjoyed it as much as I did. Thank you for the nice discussions we had during the many kilometers we ran together. Joe, thank you for being my promotor and for the help, support and advice you gave me in the past years. I really enjoyed the many discussions we had, sometimes related to this work and at other times not, as well as the many anecdotes you told me. Thank you for all the hours you spent on reading and correcting all the manuscripts which I sent you. I would like to thank Frank van Vliet for his efforts to initiate this project, for all the advise he gave me, and for the comments he made and that improved the quality of this work. I appreciated your sincere interest as well as the conversations we had when we took a stroll.

I am thankful to the management of TNO for enabling and supporting this PhD project. In particular I would like to express my gratitude to Frank van den Bogaart, André Verweij, and Jeffrey Vermeer. I also thank Agnese Mazzinghi and Gabriele Rosati for their contribution through their MSc projects which they carried out at TNO. I thank all my colleagues at TNO since they provided a very nice atmosphere. From the antenna team I would like to thank especially Andrea Neto and Giampiero Gerini for the discussions I had with them. Andrea, I will keep up the good work! I enjoyed the lunches we had as 'antenna team'; apart from the people I have already mentioned I would like to mention Stefania Monni, Frans Nennie, Daniele Cavallo, Annalisa Iacono, Nuria Llombart Juan, Simona Bruni, Mauro Ettore, and Iwan Akkermans for their nice company.

During the project I shared a room with a number of people: Guido Visser, Marien Rodenburg, Frank de Wolf, and Christos Pateropoulos. I want to express my gratitude to all of them for their patience (and endurance). Guido, thank you for the discussions we had about all the absurdities in this world, often ending with „Teis, de wereld is gek, dat weet je toch?" Marien, I really appreciate you as a colleague and I hope you enjoyed running together as much as I did. I am grateful to Frank that he gave me the opportunity to outlive him as a room mate; was my company really that bad? Christos has only been my room mate for a few weeks. In these weeks I was not so talkative since I was finalizing my thesis; thank you for your patience.

Finally, I would like to thank my friends, family and relatives for their interest, support, patience and friendship. Especially, my mother and 'Tante Trudi en Oom Ed' for their continuous support throughout my study time, and of course my sister Elien: „Eindelijk heeft je broer dat boekje af!" I hope that my 'paranimfen' Luud and Joachim will support me when the questions get nasty (you better start reading the thesis in time!). Last, I thank someone whose support and love have been invaluable to me. Marloes, I realize that from time-to-time I have been nerve-wracking to you; thank you so much for your persistent support and for the pushes you continuously gave me. I needed it.

Biography

Teis Coenen was born in Nijmegen, The Netherlands, on September 18, 1978. He completed his secondary school at the Elshof-/Kandinskycollege in Nijmegen in 1996 and he moved to Twekkelo to start as a student in Electrical Engineering at the University of Twente in Enschede. As part of his curriculum he selected a minor in Law and a major in Telecommunications. Between December 2002 and June 2003 he worked on low-loss microwave filters during his internship at Thales Nederland in Hengelo. The research of the final project for his MSc thesis was carried out at the Telecommunications Engineering group at on the University of Twente and concerned the realization of compact microwave filters. He received the MSc degree in August 2004.

During his time in Twente he was a member of the university's rowing club Euros where he was a sub-top level race rower. Since then his training intensity decreased, but he still enjoys sports. Currently he prefers mostly running and cycling.

Since November 2004, he has been with TNO Defence, Security, and Safety in Den Haag as a designer of passive microwave components. In April 2005 he started working toward the PhD degree. Currently, he is an employee at TNO Defence, Security, and Safety in Den Haag. In February 2010 he will start as a postdoctoral researcher at Eindhoven University of Technology. His research interest are in electromagnetic modeling, passive microwave filters and components, and microwave antennas and arrays.